Universidade Federal Fluminense
Instituto de Física

First-principles studies on layered materials and their interaction with liquids

Author: Marcelo Fábio Costa Albuquerque Filho
Supervisor: Prof. Pedro Paulo de Mello Venezuela

Niterói-RJ
October / 2021

Universidade Federal Fluminense

Instituto de Física

Marcelo Fábio Costa Albuquerque Filho

First-principles studies on layered materials and their interaction with liquids

Niterói-RJ

2021

MARCELO FÁBIO COSTA ALBUQUERQUE FILHO

FIRST-PRINCIPLES STUDIES ON LAYERED MATERIALS AND THEIR INTERACTION WITH LIQUIDS

Ph.D. Thesis presented to the Physics Graduate Program of Universidade Federal Fluminense as a requirement to obtain the Ph.D. degree in Sciences (Physics). Major Area: Condensed Matter Physics and Nanostructured Systems.

Supervisor: Prof. PEDRO PAULO DE MELLO VENEZUELA

Niterói-RJ

2021

Ficha catalográfica automática - SDC/BIF
Gerada com informações fornecidas pelo autor

A345f Albuquerque filho, Marcelo Fábio Costa
First-principles studies on layered materials and their interaction with liquids / Marcelo Fábio Costa Albuquerque filho ; Pedro Paulo de Mello Venezuela, orientador. Niterói, 2021.
188 f. : il.

Tese (doutorado)-Universidade Federal Fluminense, Niterói, 2021.

DOI: http://dx.doi.org/10.22409/PPGF.2021.d.05557808485

1. Condensed matter physics. 2. Nanostructured systems. 3. First-principles simulations. 4. Bidimensional materials. 5. Produção intelectual. I. Venezuela, Pedro Paulo de Mello, orientador. II. Universidade Federal Fluminense. Instituto de Física. III. Título.

CDD -

Bibliotecário responsável: Debora do Nascimento - CRB7/6368

MARCELO FÁBIO COSTA ALBUQUERQUE FILHO

FIRST-PRINCIPLES STUDIES ON LAYERED MATERIALS AND THEIR INTERACTION WITH LIQUIDS

Ph.D. Thesis presented to the Physics Graduate Program of Universidade Federal Fluminense as a requirement to obtain the Ph.D. degree in Sciences (Physics). Major Area: Condensed Matter Physics and Nanostructured Systems.

Aproved in September 2021.

EXAMINING BOARD

Prof. PEDRO PAULO DE MELLO VENEZUELA - Supervisor
IF-UFF

Prof. WANDERLÃ LUIS SCOPEL
DFIS-UFES

Prof. LUCIANO TAVARES DA COSTA
IQ-UFF

Prof. RODRIGO GARCIA AMORIM
ICEx-UFF

Prof. MARCIO JORGE TELES DA COSTA
IF-UFF

Niterói-RJ
2021

To my beloved family and friends.

"Physical facts could not be ignored. In philosophy, or religion, or ethics, or politics, two and two might make five, but when one was designing a gun or an aeroplane they had to make four."

1984

George Orwell

Acknowledgments

This has been a long way up to this point at which I'm presenting my thesis to a board of competent professors in a well-established institution of incalculable value to society, the Universidade Federal Fluminense. It has been a hard work, full of dedication and employed time, made by many hands, whose names I would like to remember in what follows.

First of all, I must recognize all the invaluable help, patience, support, companionship, and love dedicated to our relationship during this time, especially to me during hard moments I've gone through. I ought to thank my wife for never letting me give up on it, for always cheering me up when I was blue, for always trusting that everything would be OK. She even named my thesis as Mathilda. Such gestures were like food to nourish my dreams, strength when I was weak. Everytime I thought I was bitting off more than I could chew, there was she motivating me.

My family also has supported me in many moments, both goods and bad ones, especially my brother and friend, Moriah, who always spent his time with me affording good conversations and advice. My mother has also, even being way far away from Rio de Janeiro (she's in Pernambuco), backed me with her love.

I can't forget the man who shed light on my future with respect to my life after high-school. During my period in school, the teacher of physics, Mr. André, was the one responsible for my choice in getting into the university to study physics. At first, I wanted to become a teacher as well. In spite of this flame still burn inside me, I found out science in the university, and that made me keen on graduate bachelor of physics and to pursue the master's degree. Now, I'm about to finishing my Ph.D. in physics, and all of that started with Mr. André.

I also would like to mention the invaluable friendship, and professional support I had from my advisor, Professor Pedro Venezuela. We have been working since the senior period of my undergraduate study, and all this period has been of constant apprenticeship and maturation. His words of encouragement, and tips and advice were crucial to keep me cheered up and motivated.

It would be unjustified forgetting friends and colleagues that, in many ways, gave their contribution for this moment of my life:

- Ramon Oliveira, a friend I met in UFF when we were freshmen in the beggining of the undergraduate physics course in 2011, for his advice and support during the moments we were studying and talking about anything.

- Raphael Costa, a friend that encouraged me to follow this path during my final stages of the

undergraduate period;

- Marcela Marques, a friend from Pernambuco since the high-school time, who never let me forget that I'm capable of doing this;

- Max Junior, a Pernambuco friend I met in the first congress I participated back in 2016, in the early of my master's course, for giving me some ideas, and at times talking to me about perspectives for future;

- Many colleagues from UFF with whom I would spend the same time I've spent during the period I've been in there. It was good moments: the cool-off time, coffee-breaks in the afternoon, the meetings, barbecues and shared beers, and also the Friday night football matches. Thanks to Luis Paulista, Gabriel Bezerra (Jake), Rafael Bellas, Renato, Eliel, Gustavo, Jhonny Alejandro, and many others.

Regarding the professional support, I would like to mention a few names that have taught me some techniques, or gave me advice, ideas, and suggestions, which I saw as tools to be applied and used in my researching leaning process:

- Prof. Roberto Hiroki (Departamento de Física da Universidade Federal de Uberlândia) for having me in their lab, and teaching me the nuts and bolts of XANES simulations, as well as for all the time spent with me, talks we have, and ideas he gave;

- Prof. Luciano Costa (Instituto de Química da UFF), and his Ph.D. student, Flávia Assis, for giving all the support and space to learn about Molecula Dynamics, and related techniques, for having invited me to events, and for presenting me research opportunities;

- Prof. Matheus Mattos (Universidade Federal de Ouro Preto) for giving the idea for one of our projects of this thesis, and also for giving valuable support for it.

- Prof. Rodrigo Amorim (UFF, Volta Redonda campus) for giving me many advice and support through talks, materials for study, courses, and opportunity to work in extra projects with him.

Besides those names, and other that I may have forgotten, I would like to mention a few institutions that have given the conditions and facilities that provided my formation:

- Universidade Federal Fluminense for being my place most of the time since 2011. There, I had great experiences and met many people that certainly are worth to be remembered. Also, it gave me opportunities to learn English, which has been thoroughly indispensable to my formation, not to mention the ones in which I could go to congresses, events, and schools that open doors and windows to me;

- Universidade Federal de Uberlândia (UFU) along with FAPEMG, for the financial support during the period I was with Prof. Hiroki learning about XANES.

- Universidade Federal do Rio de Janeiro (UFRJ) for having accepted me to take part in two courses: First-principle calculations based on Density Functional Theory (including hands-on) with Prof. Rodrigo Capaz e Prof. Marcos Menezes in 2016, and a course on many-body theory with Prof. Marcello Neto in 2017.

- PUC-Rio as well for having me in the course on vibrational spectroscopy of carbon-based materials with Prof. Vitor Caruzo in 2018.

- UFABC for having provided excelent events on DFT and beyond techniques, and also a crash-course on AiiDA; both were organized by Prof. Cedric.

- SBF (Physical Brazilian Society) for having organized the EOSBF (Autumn Meeting of the Physical Brazilian Society) each two years, events that certainly represent an important part of my formation.

- I can't forget to mention CNPQ and CAPES for granting me financial support during this graduate time: the former during the master's course, and the latter during the doctoral period.

- And last but for sure not least, I would like to be very grateful to CENAPAD-UNICAMP, the center of computational resources whereon almost – I mean 80% of – all my calculations were run using the equipaments provided by them. I have to mention all the support them gave when necessary.

List of Figures

1.1 New bidimensional materials, and thier later heterostructures . . . 3
1.2 Number of publications . . . 3
1.3 Time and length scales of different computer simulation techniques . . . 4
1.4 Core electron and valence electron levels . . . 5
1.5 Number of XAS-related topics papers published per year . . . 6
1.6 Synchrotron facilities worldwide . . . 7

2.1 The Kohn-Sham *Ansatz*. Comparison to the Hohenberg-Kohn Theorems . . . 18
2.2 Flowchart for the Kohn-Sham Equations . . . 26
2.3 Reciprocal lattice vectors . . . 28
2.4 Pseudopotential chart . . . 37
2.5 Diamondol supercell with the core-hole carbon atom highlighted . . . 40
2.6 Vacuum representation between material surfaces . . . 41

3.1 Schematic view of the XAS process . . . 43
3.2 Schematic of the incident-and-transmitted X-ray beam, and XAS . . . 44
3.3 Flowchart of the steps to the XANES calculations . . . 55

4.1 Periodic boundary conditions pictorial representation on a system . . . 69
4.2 Flowchart of a MD silumation scheme . . . 71

6.1 Structures of cubic diamond, hexagonal diamond, and Bernal graphite . . . 77
6.2 A few results for XAS experiments . . . 78
6.3 Projected density of states for cubic diamonds . . . 79
6.4 XANES spectra for cubic diamond, and experimental results . . . 80
6.5 Projected density of states of both the first-neighboring atoms and X-ray absorbing atom of cubic diamond . . . 81
6.6 Representation of cubic diamond and hexagonal diamond . . . 81
6.7 Projected density of states for hexagonal diamond . . . 82
6.8 XANES spectra for the hexagonal diamond with its experimental result . . . 83
6.9 Projected density of states of both the first-neighboring atoms and X-ray absorbing atom of hexagonal diamond . . . 84

6.10 Schematic representation of the incident X-ray . . . 85
6.11 Experimental results of carbon K-edge absorption spectra for HOPG . . . 86
6.12 XANES depending on the X-ray incindent angle of HG . . . 86
6.13 Projected density of states for hexagonal graphite (HG) and bilayer graphene (BLG) . . . 87
6.14 XANES simulations for both HG and BLG . . . 88
6.15 Projected density of states on both the first-neighboring atoms and X-ray absorbing atom of HG and BLG . . . 88
6.16 Diamond-like structures studied in this work . . . 90
6.17 XANES simulations: general view . . . 92
6.18 XANES spectra decomposed into polarized X-ray beam . . . 93
6.19 XANES decomposition per carbon atom for each diamond-like structure . . . 95
6.20 Spin-polarization analysis for Y atom of diamondol and F-diamane . . . 96
6.21 Local PDOS on p_z orbitals for each analysed structure . . . 97
6.22 Electronic band strcture for both diamondol's and F-diamane's Y atom . . . 98
6.23 Electronic band structure for diamondol's and F-diamane's X probed atom . . . 99
6.24 Workfunction calculation for 2D diamond-like materials . . . 101

7.1 Simulation box containing acetonitrile . . . 104
7.2 Simulation box containing a slab of MoO_3 surrounded by acetonitrile . . . 105
7.3 Density map, and number density for acetonitrile interacting with the MoO_3 solid . . . 107
7.4 Time average of the interaction energies of the acetonitrile-solid systems . . . 108
7.5 Colormap of the number density of ACN molecules . . . 109
7.6 Pictorial representation of Radial Distribution Functions . . . 110
7.7 Radial distribution functions analysis for all the simulation box . . . 111
7.8 Angle distribution for C–N bonds w.r.t. the solid surface . . . 112
7.9 Simulation box containing acetonitrile and water molecules . . . 113
7.10 Number density of ACN molecules for the systems containg either water or oxygen . . . 113
7.11 Sketch for the link between the MD simulations and QM calculations . . . 114
7.12 Integration region for calculation of the charge transfer . . . 115
7.13 Bar plot of the number of electrons in the Mo-based solids . . . 116

B.1 Example of norm-conserving pseudopotential generated for the Mo atom . . . 128
B.2 Comparison of generated pseudopotential for carbon atom . . . 129

G.1 Definition of the Bader volume for Bader analysis . . . 142
G.2 Grids and Bader volume definition . . . 143

H.1 XANES simulations of diamondol along with PDOS . . . 145
H.2 XANES simulations of bidiamondol along with PDOS . . . 146
H.3 XANES simulations of F-diamane along with PDOS . . . 147
H.4 XANES simulations of bi-F-diamane along with PDOS . . . 148

H.5 Density map, number density and charge density for acetonitrile interacting with the MoO_3 solid with different simulation parameters("S3") 149
H.6 Number density of ACN molecules for the systems containg either water or oxygen 149
H.7 Normalized ACN molecule density for the large and small systems 150

List of Tables

6.1 XANES simulations and experimental values 77
6.2 Bond length and angles between the atoms of the diamond-like structures 91
6.3 Magnetic moment per carbon site 96
6.4 Core-level binding energy and core-level shift analysis 100

7.1 Different parameters used for the SD calculations of the slab system 106

List of Symbols

The next list describes several symbols that were employed throughout this document.

Physics constants

ε_0	Vacuum electric permittivity	$8.8541878128 \times 10^{-12}\,\mathrm{F\,m^{-1}}$
c	Speed of light in a vacuum	$299\,792\,458\,\mathrm{m\,s^{-1}}$
k_B	Boltzmann constant	$1.380649 \times 10^{-23}\,\mathrm{J\,K^{-1}}$
m_e	Electron mass	$9.1093837015 \times 10^{-31}\,\mathrm{kg}$
h	Planck constant	$6.62607015 \times 10^{-34}\,\mathrm{J\,Hz^{-1}}$

Other symbols

χ	Ionic many-body wavefunction.
ϵ_i	Kohn-Sham eigenstates.
γ_i	Friction coefficient with respect to atom i.
$\hat{\varepsilon}$	X-ray polarization vector.
μ	Chemical potential.
ϕ_i^σ	Single-particle orbitals on state i with spin configuration σ of a system of independent electron.
Ψ	Many-body wavefunction.
ψ	Electronic many-body wavefunction.
σ_i	X-ray absorption cross-section of atom i.
τ_P	Time constant for pressure coupling.
τ_T	Time constant for temperature coupling.
θ_{ijk}	Equilibrium angle between the atoms i, j, and k.
a_0	Bohr atomic radius.

b_{ij} Equilibrium bond length between the atoms i and j.

c_V Thermal capacity at constant volume.

H_{el-ion} Hamiltonian operator for the interaction between electrons and nuclei.

H_{el} Electronic Hamiltonian operator, comprising the interaction between electrons.

H_{ion} Nuclei Hamiltonian operator, comprising the interaction between the nuclei.

H_{KS} Kohn-Sham Hamiltonian.

k_F Fermi momentum, or the Fermi's wave vector.

k^{φ}_{ijkl} Torsional angle constant between atoms i, j, k, and l.

k^{θ}_{ijk} Angle deformation constant between atoms i, j, and k.

k^{b}_{ij} Spring-like constant that bonds together the atoms i and j.

n Electronic density.

n_0 Ground-state electronic density.

N_{df} Number of degree of freedom of the system.

r_S Wigner-Seitz radius.

T Kinetic energy.

V Potential energy.

V_{xc} Exchange-correlation potential.

Table of Contents

Acknowledgments vi

List of Figures xi

List of Tables xii

List of Symbols xiv

Abstract xviii

1 Introduction 1

1.1 A Word on Material Science . . . 1

1.2 The Problems Addressed in this Thesis . . . 7

2 Density Functional Theory (DFT) 10

2.1 The Crystal Hamiltonian . . . 10

2.1.1 The Born-Oppenheimer Approximation . . . 11

2.1.2 Thomas-Fermi Approximation . . . 13

2.2 The Hohenberg-Kohn Theorems . . . 15

2.3 Kohn-Sham Equations . . . 18

2.3.1 Approximations for the Exchange-Correlation Potential . . . 21

2.3.2 DFT in practice: Solving the Kohn-Sham Equations . . . 24

2.4 Numerical Methods . . . 27

2.4.1 The One-Particle Problem in a Plane-Waves Basis . . . 27

2.4.2 Special k-points for integration within the Brillouin Zone . . . 29

2.5 Pseudopotentials . . . 31

2.5.1 Ultrasoft Pseudopotential (USPP) . . . 32

2.5.2 Projected Augmented Waves (PAW) Method . . . 35

2.6 Supercell Approximation . . . 39

3 X-Ray Absorption Spectroscopy 42

3.1 The X-Ray Absorption Phenomena . . . 43

3.2 X-Ray Absorption Cross-Section . . . 44

3.3 *Ab-initio* Calculation of XANES into a Pseudopotential Scheme . . . 47
3.3.1 PAW Formalism for XANES Calculation in the Impurity Model . . . 48
3.3.2 The Recursion Method . . . 50
3.3.3 The USPP Scheme . . . 51
3.3.4 Practical DFT Calculation . . . 53

4 Dynamical Methods to Atoms and Molecules 56
4.1 Molecular Dynamics . . . 57
4.1.1 Potential Energy Function (Force Field) . . . 58
4.1.2 Intramolecular Potentials . . . 59
4.1.3 Intermolecular Potentials . . . 60
4.2 Stochastic Dynamics . . . 61
4.3 Energy Minimization . . . 62
4.4 Integration Algorithms . . . 63
4.4.1 Verlet Algorithm . . . 63
4.4.2 Leap-Frog Algorithm . . . 64
4.5 Temperature and Pressure Coupling . . . 65
4.5.1 Temperatute Coupling . . . 65
4.5.2 Pressure Coupling . . . 68
4.6 Periodic Boundary Condition and Minimum Image Convention . . . 69
4.7 Molecular Dynamics Simulation Scheme . . . 70

5 Computational Details 72
5.1 Carbon-based Systems . . . 73
5.2 Diamond-like Systems . . . 74
5.3 Molybdenum-Based Systems and Acetonitrile . . . 74
5.4 Water and oxygen molecules . . . 75

6 XANES simulations in diamond-like two-dimensional materials 76
6.1 Probing Diamond Materials . . . 78
6.1.1 Cubic Diamond . . . 78
6.1.2 Hexagonal Diamond . . . 82
6.2 Hexagonal Graphite and Bilayer Graphene . . . 84
6.3 XANES investigation on diamond-like materials . . . 89
6.3.1 Atomic arrangement of the materials . . . 89
6.3.2 XANES simulations . . . 91
6.3.3 Analysis of the electronic structure of the spin-polarized systems . . . 95
6.3.4 1s-core binding energy for carbon atoms . . . 99
6.4 Main conclusions of this chapter . . . 101

7 The interaction of acetonitrile with molybdenum-based layered materials: A computational investigation **103**

7.1 MD simulations . . . 104

7.2 DFT-based Calculations . . . 114

7.3 Main conclusions of this chapter . . . 116

8 Conclusions and Prospects **118**

Appendices **119**

A Orthogonalized Plane Waves (OPWs) Method **120**

B Norm-conserving Pseudopotentials (NCPPs) **124**

B.1 Separable Pseudopotential Operators and Projectors . . . 129

C Gauge Freedom **131**

C.1 Coulomb Gauge . . . 133

C.2 Lorenz Gauge . . . 134

D Proof of Equation (3.39) **135**

E $\hat{S}^{-1}$ Matrix Calculation **136**

F Gauge-Including Projector Augmented-Wave Method **137**

F.1 The All-Electron Hamiltonian . . . 137

F.2 Translation Invariance . . . 139

F.3 GIPAW Method . . . 140

F.4 GIPAW Hamiltonian . . . 140

G Bader Charge Analysis **142**

H Supplementary Results **144**

H.1 Local PDOS for XANES contributions shown in figure 6.18 . . . 144

H.2 Mo-based Systems, and Their Interaction with Acetonitrile . . . 149

Bibliography **150**

Abstract

We have addressed two problems in this thesis. In the first one, we have performed Density Functional Theory (DFT) along with K-edge X-ray Absorption Near-Edge Structure (XANES) calculations in order to probe the local environment of the X-ray absorbing carbon atoms in carbon allotrope systems, as well as in diamond-like systems. We have found that, in addition to the accordance with experimental results regarding both the 1s – π^* and the 1s – σ^* transition of graphitic systems, as well as the 1s–σ^* transition of diamond systems, our results show that the diamond-like ones can be characterized through this technique by observing the X-ray polarized spectra. Moreover, we observed that diamondol changes from a direct to an indirect bandgap material (0.75 eV at Γ-point to 0.68 eV) when the 1s-electron is removed from the carbon atom. Also, we have found that in such a case, the valence band maximum changes from spin-down to spin-up state. Similar results were seen for the fluorinated system. We also observed that the π transition for both the single-covered materials are spin-down polarized. Regarding the double-covered systems (bidiamondol and bi-F-diamane), this is not observed, though bidiamondol does not show π transition, whereas the another one does. Concerning the second problem, the interaction of liquid acetonitrile (ACN) with the surface of Mo-based layered materials, we have approached it through Molecular Dynamics (MD) simulations followed by DFT-based calculations to assess the charge transfer in the solid-liquid interface. We were able to notice that the liquid ACN molecules are more concentrated near the MoS_2 surface, but only physisorbed, and also that their molecular density acquires an ordering due to the solid surface. By DFT, we calculated the charge transfer between the solid surface and the ACN molecules. Our results did not agree with the experimental evidence, as we have seen that the solids lost electrons to the region where there are ACN molecules. In spite of this, qualitatively our results showed that MoS_2 induced higher charge transfer compared to the MoO_3. This trend may change when environmental effects are included in this model.

Keywords: DFT, XANES, Molecular Dynamics, diamondization, charge-transfer, liquid-solid interactions, molybdenum-based solids, hydroxyl, fluorination.

Chapter 1

Introduction

1.1 A Word on Material Science

Since the past centuries, the humankind has been witnessing the arising of new materials, with which humans were able to make up clothes, inks, all sort of instruments and utensils, as well as electronic devices. The great leap into the new era took place in the middle of 1950s with the synthesis of diamond, and its usage as abrasives in industries [1], as well as its characterization via X-ray spectroscopy from synchrotron-radiation [2]. Its usage finds applicability in machining and cutting tools, thermal conductors, among others. By the way, they can be used as gemstones if they are grown by either High Pressure-High Temperature (HPHT) [3] or Chemical Vapor Deposition (CVD) [4] methods. Diamonds synthesized through those techniques also have applicability as optical materials for usage, for instance, in tools for measuring electric and magnetic properties of materials at ultrahigh pressure [5, 6], and also as semiconductors [7] when doped, during its synthesis process, with boron or phosphorus, which turns it into a p- or n-type semiconductor, respectively. Those synthesized diamonds can be used in p-n junctions, which produces light-emitting diodes (LEDs).

Nonetheless, as diamond has experimental indirect energy gap around 5.6 eV, and a lack of states within 7.6 eV range at Γ-point between the valence band maximum and a higher state in the conduction band [8, 9], they have not been used for fabrication of commercial electronic or optoelectronic devices, but have been used to replace silicon as diffraction grating and window material in high-power radiation sources, such as synchroton ones [5, 10, 11]. In the middle of 1900s, the first silicon device was the radio crystal rectifier, and high-purity germanium and silicon crystals were employed in the fabrication of radar microwave detectors during the period of the World War II. In the 1950s, the thermal oxidation of semiconductor surfaces was possible, and in the middle of 1960s this was used to fabricate integrated circuit and devices [12]. In fact, those crystals (and other ones) have been object of studies until current days.

With the emergence of the Bernal graphite [13], a layered material, and in 2004 the exfoliation of graphite [14], one of those layers, a myriade of new materials started to be discovered, due to the remarkable mechanical, optical, and electronic properties of graphene. It would be expected that these

new materials could possibly present electronic and/or mechanical properties as good as those of graphene as they were being discovered. Figure 1.1 shows us an overview of those materials, such as hexagonal boron nitride (h-BN) [15], transition metal dichalcogenides (TMDs) [16–19], layered metal oxides (MO) [20], layered double hydroxides (LDHs) [21], etc. Conveniently, it is also feasible to combine two (or more) of those materials, according to their properties, to build a new stacked material by van der Waals interaction, known as van der Waals heterostructures. They are classified by types, as one can see in figure 1.1(b). The first type (Type I) is related to the vertical growth/deposition of two different materials. The second type, in turn, is a material forming an in-plane 2D heterostruture. Type III is a heterostructure formed by a vertical growth of ultrathin nanosheets as a compact array on another 2D material as substrate. Crystal phase heterostructures, in turn, comprise the fourth type of heterostrustures, which have the same components (for example, MoW_2), but different crystal phases (2H and 1T in the figure). Lastly, the fifth type is a class in which the heterostructure material can have multiple crystal phases.

With such a variety of materials, many experimental and theoretical techniques have been developed since the early 1900s. Regarding the last two decades, the number of papers concerning to 2D materials, comprising a category of bidimensional nanomaterials nanocomposites in the fields of chemistry, materials science and condensed matter physics [22], has increased, as the figure 1.2(a) shows. That search was made in Web of Science's database server using the keywords as shown in the labels of the graph. In spite of the oscillations in the number of publications, it increased in the last years. It can be seen that an exponential trend is observed from 2004, which matches the year of the graphene synthesis.

As the researches on materials science had been increasing since the 1950s, so did the ones on theoretical methods. In fact, computational simulations started to be exploited as a tool to perform heavy calculations in the development of nuclear weapons and code breaking in the frame of the World War II, and only in early 1950s, electronic computers became partially available to non-military use [23]. At the time, the rush of researches on models to study properties of silicon-, carbon-, and germanium-based materials drove the development of theoretical tools onwards. Those tools are used to model a problem one wants to treat. When a model, linked to a theory, is turned into an algorithm, computations can be performed and its results can be compared directly with experiments. If such results does not match, then the model is inadequate, and one needs to reckon other ways to improve that result.

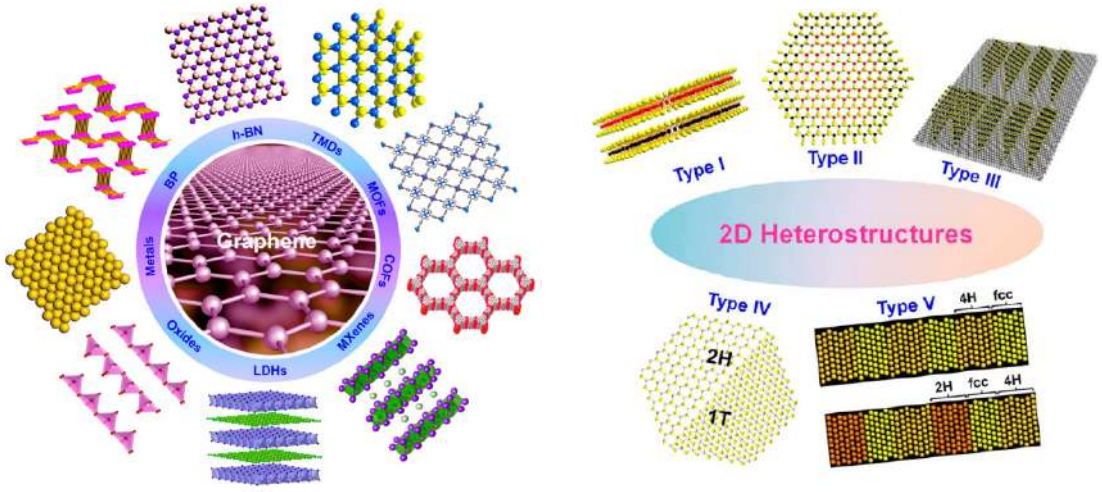

(a) (b)

Figure 1.1: New era of material science: (a) Atomic-thickness material, so-called bidimensional materials, and (b) their later heterostructures built using them. Figures from [24].

Computational simulations can be performed to model small systems, which can consist of thousand of atoms, up to huge systems composed of million of molecules [25, 26]. An overview of existing methods for simulating and modelling molecular interaction, as well as solid and liquid state, according to both the length and time scales, is shown in figure 1.3. Quantum mechanics (QM) methods are suitable for systems with a few hundreds of atoms at most, staying on underneath the nanosecond scale. In the case of Density Functional Theory (DFT) [27, 28] approach, it is typically within the picosecond scale. When the process on which one is working do not include the formation of covalent chemical bonds processes, it can be described by Molecular Mechanics (MM) framework, and its temporal evolution can be addressed by Molecular Dynamics (MD) simulations. In fact, even if chemical bonding actually takes place, physical absorption is primarily recognized as a long-time scale interaction, being, in principle, adequate for such approach.

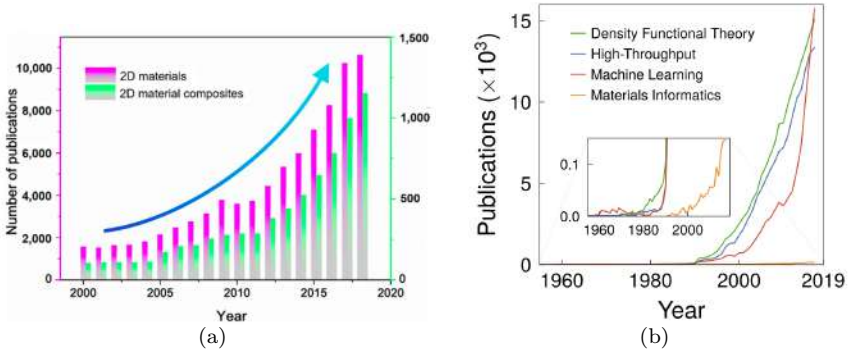

(a) (b)

Figure 1.2: (a) Number of publications in the period of 2000-2018, whose keywords shown as labels were entered on the Web of Science database. This figure was obtained from [22]. (b) Annual number of publications according to the keywords seen as labels of the curves [29].

In this work, we have used QM approach, inside the scope of DFT, along with MM simulations,

specifically in the all-atom Molecular Dynamics (AA-MD)[1], where one is able to perform investigation on dynamic and thermodynamic properties of a system [30]. *Ab-initio* DFT has been the state-of-the-art technique used in material science for calculations of ground-state properties of various types of systems. As one can see in figure 1.2(b), the number of publications that are connected to DFT starts going up drastically from 1990s. As a matter of fact, Walter Kohn [31] and John Pople [32] shared the Nobel prize in chemistry in 1998: the former for devising the DFT, and the latter for developing computational methods in quantum chemistry [33].

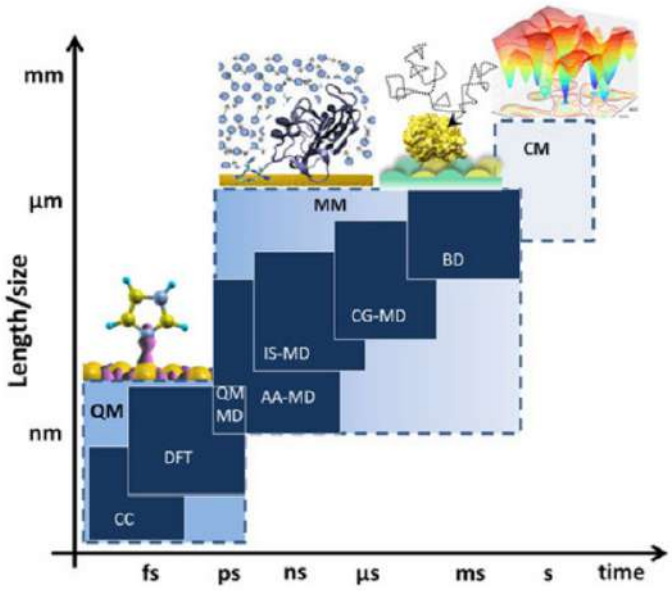

Figure 1.3: Existing computer simulation methods. The abbreviations stand for Quantum Mechanics (QM), which encompasses Coupled Clusters (CC), Density Functional Theory (DFT) (credits for [34]); Molecular Mechanics (MM) comprising all-atom Molecular Dynamics (AA-MD), implicit solvent and coarse grained (IS-MD and CG-MD, respectively), and Brownian Dynamics (BD); and, at last, Continuum Mechanics (CM). This figure was obtained in reference [30].

On the other side, regarding the experimental techniques to characterize materials, there are many complex approaches to synthesize, modify, induce response to electromagnetic fields, among others. Focusing on this last one, we would like to discuss about the core level spectroscopy. However, some basics on solid state needs to be reviewed before we dig into this subject. In figure 1.4(a) we have electron energies of the Mn and O. The core electrons of the former atom are in the orbitals 1s, 2s, 2p, 3s, and 3p (18 electrons), while the latter has two core electrons in the 1s orbital. The valence electrons, in turn, are in the orbitals 3d, 4s, and 4p for Mn, and four 2p electrons for O atom. For a molecule formed by those atoms, MnO, in core electron specroscopy, one of those 18 electrons is excited by incident X-rays and the electronic state of Mn 3d, and O 2p electrons are analyzed, once the character of core electron is well-known [35]. The energy required to excite such a core electron is within the X-ray region of the electromagnetic spectrum, which goes from 2 keV (soft X-rays region) up to 30 keV (hard X-rays region).

Figure 1.4(b) shows a schematic representation of the three main core level spectroscopy techniques. The middle, vertical line represents the Fermi level. The core and valence electrons fully fill up

[1]From here on, it will be addressed only as Molecular Dynamics (MD).

the states on the left-hand side of the vertical line, and the conduction band (CB) is empty (right-hand side of the vertical line). X-ray Photoemission Spectroscopy (XPS), and X-ray Absorption Spectroscopy (XAS) are first order optical process, which only include one photon. In the first process, a core-electron is excited to high-energy continuum states, and detected by a photoelectron apparatus. In XAS, this core-electron is excited to a state with energies (empty states) above the Fermi level. On the other hand, X-ray Emission Spectroscopy (XES) is a second-order optical process, in which a core-electron is excited by the incident X-ray, and the excited state of the system decays emitting X-rays. In this case, when the core-electron is excited to continuum states, one has the Normal XES (NXES). However, if that electron is excited near the Fermi level, the process is called Resonant XES (RXES). In this work, we will only address simulations of XAS, specifically the X-ray Absorption Near-Edge Structure (XANES)[2] spectroscopy.

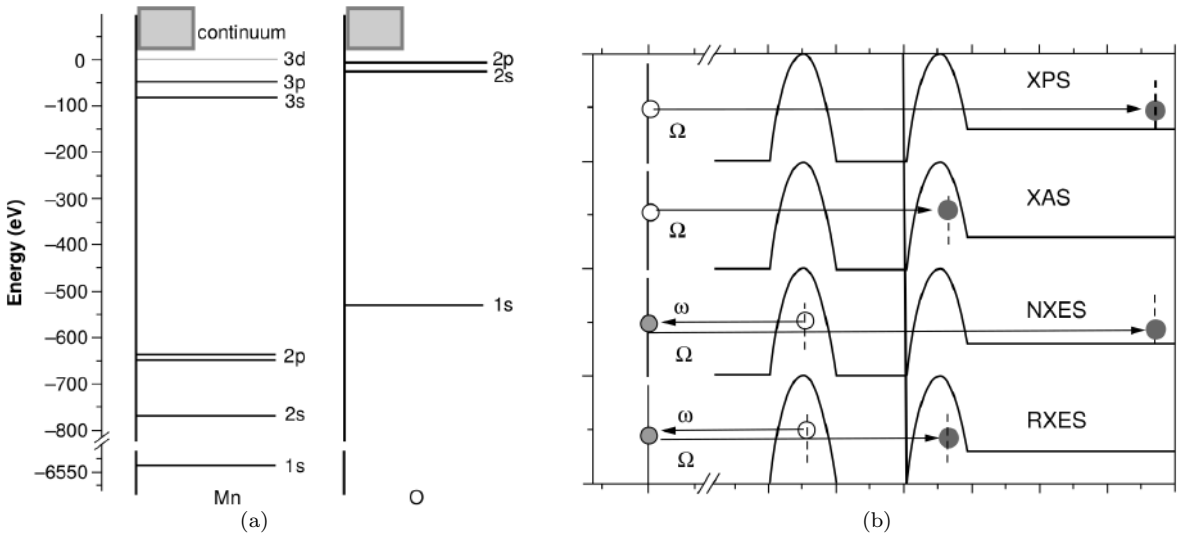

Figure 1.4: (a) Energies of the core level and valence level sates for MnO. (b) Schematic representation of XPS, XAS, and XES. In the figure, Ω refers to the X-ray incoming frequency, and ω is related to the frequency of the X-ray emitted by a radiative decay. Figures extracted from the book [35].

A detailed historical perspective on XAS can be found in [36], chapter one, from which we would like to quote the authors' words on what followed the first Fourier analysis to the point-scattering theory of X-ray absorption fine structure in 1971 [37], which stresses the importance of such analysis:

> "In the 44 years following that key publication, the field developed exponentially. Nowadays it is impossible to imagine frontier research in materials science, solid state physics and chemistry, catalysis, chemistry, biology, medicine, earth science, environmental science, cultural heritage, nanoscience, etc., without the contribution of XAS and related techniques."

From the experimental point of view, silicon crystals were used as monochromator in 1960s, when the first XANES spectra were used to classify trasition metals compounds according to their atomic structure and valence of the metal [38]. Since the 1970s, the continuous increasing on availability of

[2] For more details, please refer to chapter 3.

synchroton radiation sources established the EXAFS (Extended X-ray Absorption Fine Structure) and XANES spectroscopies as a reliable tools for understanding structural and electronic configuration of a wide range of systems [36]. The following two decades would be marked by a wide development and distribution of codes for XAS-based data analysis. In fact, the quote above has been becoming a reality because of three factors: existence of a solid theory for XAS spectra; increasing availability of beamlines in synchrotron facilities; and the development of the mentioned codes. As a consequence, as figure 1.5 portrays, the number of paper published per year has increased vertiginously since 1981, time at which the codes started to be broadly developed.

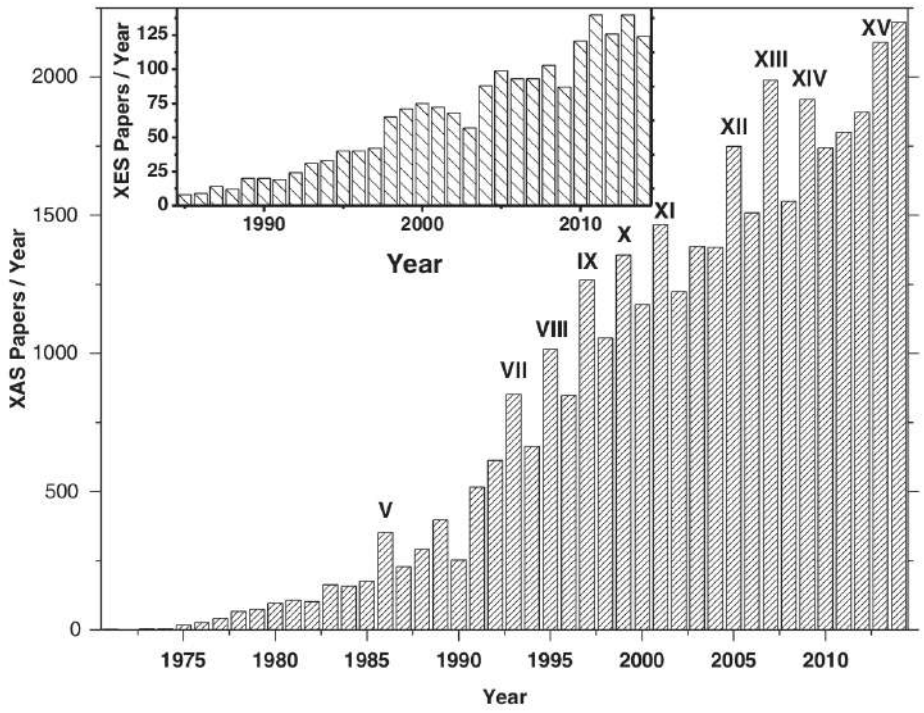

Figure 1.5: Papers published per year using as keyword: XAFS OR EXAFS OR XANES OR x ray absorption spectroscopy OR X-ray absorption spectroscopy OR x ray absorption fine structure OR X-ray fine structure. The Roman numerals indicated the year when proceedings of XAFS conference were published by ISI Web of Science. In the inset, the keywords used were XES OR RIXS OR x ray emission spectroscopy OR X-ray emission spectroscopy. Figure was obtained from [36], figure 1.3.

It is important to mention that nowadays it is possible to perform XANES simulations. Such a method can be used to probe empty states in solids [39]. Furthermore, the use of polarized X-ray allows to probe contribution of different atomic orbital [40], so as to study electronic structure of transition-metal compounds, to probe local environment around an impurity in a crystal, and also to study disordered matter, such as glass and liquids [41], including amorphous materials. Specifically, it can be used to characterize bonding environment of a specific atom, for example, taking part in a functionalization process [42]. We have used, for instance, the code XSpectra from QUANTUM ESPRESSO suite [43]. That fact along with experimentalists working on synchrotron facilities performing XAS spectra is a wide window for atomic core-level research for structural and electronic description of materials.

Presently, there are more than 60 synchrotrons and free electron lasers (FELs) facilities around

the world [44], some of them decommissioned. From those, two are located in Brazil: the LNLS and the Sirius, in Campinas, São Paulo. In figure 1.6, one can see some of the synchrotron facilities' logos, but we cannot see the Sirius one, because this figure was generated in 2014.

Figure 1.6: Synchrotron facilities worldwide. Credits to [45].

1.2 The Problems Addressed in this Thesis

Because of the exquisite properties of graphene, it is natural that new bidimensional candidates arise from layered bulk materials. Many efforts have been employed to obtain carbon allotrope materials, such as graphite by thermal decomposition on SiC surface [46], graphene by mechanical exfoliation of the graphite [14], and also the formation of diamond from shock compression of graphite [47], based on a work back to 1961 [48]. The quest for new 2D materials is a cutting-edge research for, at least, the last twenty years. Properties of a layered materials can considerably change when they are found in a stacked form: bilayer, trilayer, or multilayer graphene, for instance [49]. Also, external factors, such as influence of an external electric field [50, 51], as well as physical-chemical manipulations on graphene [52–55] can drive significant changes in the properties of 2D and layered materials.

Thus, due to the searching in combining a suitable technique to a desirable material, in 2011 Barboza *et al.* synthesized a new-diamond like material from a combination of tailoring process, such as stacking, physical-chemical modifications, and external pressure in the presence of water: a bidimensional hydroxylated diamond-like layer, the diamondol [56]. Their calculations showed that it is a 2D ferromag-

netic semiconductor with spin-polarized energy levels, and a bandgap around 0.6 eV. Also, it presents magnetic momentum of 1.0 Bohr magneton per unit cell. Another diamond-like material was recently synthesized by fluorinating the AB-stacked bilayer graphene grown in a chemical vapor deposition (CVD) approach on a CuNi-(111) surface [57]. This resulted in a fluorinated doubly-covered diamond-like monolayer, coined as F-diamane. However, for simplicity, as we will also study a system with just one side fully covered, we are going to refer to that system as bi-F-diamane, and the later one as F-diamane.

The characterization by electric force microscopy (EFM) experiments was performed, where charge injections into monolayer, bilayer, and mutilayer graphene were monitored through tip-force interaction in an environment with water contents on the surface of the mentioned materials [56]. Recently, a work by L. G. P. Martins *et al.* [58] provided spectroscopic evidence of the formation of such a material by performing Raman spectroscopy on the double-layer graphene under high-pressure conditions and using water as pressure trasmission medium (PTM). Furthermore, experimental evidences were also accomplished for the case of fluorinated bilayer graphene (bi-F-diamane) [57]. The EELS characterization presented the increasing of the carbon K-edge spectrum dominated by 2p(σ^*) transition at 293 eV and 297 eV. Instead, the 2p(π^*) transition is strongly suppressed. Therefore, in this thesis, we would like to provide more evidence through spectroscopy description based on XANES simulations.

As we have already seen, beyond carbon-layered materials, there also exist materials based on other elements, such as trasition metal dichalcogenides (TMDs), black phosphorus (BP) or phosphorene, M-Xanes, among others. Specifically, TMDs [16] present a general chemical formula MX_2, where M is a transition metal (Mo, W, Hf, etc), and X must be one of these chalcogenides: S, Se, or Te. Besides this material, another Mo-based material is also well-known, molybdenum trioxied (MoO_3), a transition metal oxide (TMO), which also can be exfoliated due to disposition of its layers by van der Waals interactions [59, 60]. Likewise, many approaches for synthesizing MoS_2 and MoO_3 are also available, such as hydrothermal [61, 62], chemical vapor deposition [63, 64], decomposition and annealing of precursos [65, 66], reaction between solutions [67], among others.

In spite of that, a method able to yield high-quality materials that can be suitable for large-scale synthesis is necessary. Liquid exfoliation methods based on solvent-based exfoliation by sonication generate stable dispertion of mono and few-layers of TMDs and TMOs [68–72]. Such a method is called Liquid-Liquid Interfacial Route (LLIR), by which the stable, solid dispersion is stabilized and deposited as a thin-film at a liquid-liquid interface, and then the subtrate is removed. A long list of works using that technique can be found in the reference [73].

That method was able to accomplish a simple and efficient route to synthesize, disperse, exfoliate, and process molybdenum-based two-dimensional materials using acetonitrile (ACN) as a tri-functional agent, which acts as a separator of the molybdenum-based material, exfoliator, and stabilizer of the mixture of MoS_2 and MoO_3, which were previously treated in a thermal-controlled inert atmosphere. The result of the LLIR was the formation of both layered MoS_2 and agglomerated MoO_3 solids. Electrokinetics experiments reported that MoS_2 gets negatively charged, whereas, apparently, MoO_3 does not [73]. The origin of these charges is still unclear, albeit some works have reported that those charges must be attibuted to electron tansfer from the solvent itself (ACN), or from byproduct of ACN degradation after

ultrasonication process [74,75]. More details are given in section 7, but basically we would like to address that charge-transfer problem using molecular dynamics simulations (chapter 4), followed by *ab-initio* quantum mechanics based on ground-state density functional theory (chapter 2).

Having presented the introductory aspects of this thesis, we are going to outline what is to come. In the next three chapters, it will be discussed the theoretical fundamentals of this work: the next chapter will address Density Functional Theory (DFT); then, in the chapter 3, we will expose the theory behind X-ray Absorption Near-Edge Strucuture (XANES) simulations; and in the chapter 4, Molecular Dynamics simulations will be addressed. Chapter 5 will show us the computational details to perform the required calculations for this work. Then, both chapters 6 and 7 will disscuss the results addressed in this thesis. Finally, chapter 8 comprises the conclusions of the obtained results, along with some future outlooks.

Chapter 2

Density Functional Theory (DFT)

The early 20th century was marked by great discoveries in the physics area, such as the emergence of the theory of quantum mechanics in 1900 with the Max Planck's solution to the black-body radiation problem. In 1905, Albert Einstein proposed that light is composed by quanta of energy (the light quantization), unveiling the interpretation of light as constituted of particles with well-defined frequencies, which was followed by Louis de Broglie's wave-particle duality that makes up matter in 1924. Being so, quantum mechanics gains fundamental scope to explain natural phenomena. The culmination occurs in 1926, when Erwin Schrödinger proposed an equation to describe quantum-mechanical systems. However, understanding molecules, solids, and even more complex systems is not an easy task due to the many-particles nature of the problem in question. To get a glimpse of that, suppose one wants to study the benzene molecule, which is composed of six carbon atoms and six hydrogen atoms. Each of these atoms has a especific number of electrons, which, in turn, interact with one another. That is a many-body problem impossible to be analytically solved. That's why we resort to the methodologies exposed next.

2.1 The Crystal Hamiltonian

In our case-studies, we are going to address solids and molecules; in describing such systems, it is important to consider them quantum-mechanically, which can be addressed by the corresponding many-body wavefunction Ψ, which can depend on both the electronic and atomic positions, $\mathbf{r_i}$ and $\mathbf{R_j}$, of each i-th electron and j-th atom of the system. According to [76], in the absence of external field, the Hamiltonian is given by[1]

$$H = H_{el} + H_{ion} + H_{el-ion} \tag{2.1}$$

The first term of this equation refers to the electronic part, which is composed by the electronic kinetic energy and the repulsive Coulomb interaction between the electrons:

[1] It is going to be adopted the Hartree atomic units in all equations, unless otherwise indicated: $m_e = e = \hbar = \frac{1}{4\pi\varepsilon_0} = 1$.

$$H_{el} = \sum_i \frac{p_i^2}{2} + \frac{1}{2} \sum_{i \neq i'} \frac{1}{|\mathbf{r}_i - \mathbf{r}_{i'}|}. \tag{2.2}$$

The following term represents the ionic part, given by:

$$H_{ion} = \sum_j \frac{P_j^2}{2M_j} + \frac{1}{2} \sum_{j \neq j'} \frac{Z_j Z_{j'}}{|\mathbf{R}_j - \mathbf{R}_{j'}|}. \tag{2.3}$$

And lastly, the last term refers to the attractive electron-ion interaction:

$$H_{el-ion} = \sum_{ij} V_{el-ion}(\mathbf{r}_i - \mathbf{R}_j). \tag{2.4}$$

A general form for the equation (2.4) is adopted, since the Coulomb interaction of the nuclei is screening by the core electrons. That fact results in a complicated form for that equation, which will be better understood when pseudopotential methods are addressed. If we restricted ourselves to stationary properties of a many-body system, a many-body wavefunction, $\Psi(\{\mathbf{r}_i\}, \{\mathbf{R}_j\})$, labeled by a set of electrons and ions coordinates, $\{\mathbf{r}\}$ and $\{\mathbf{R}\}$, satisfies the time-independent many-body Schrödinger equation:

$$H\,\Psi(\{\mathbf{r}_i\}, \{\mathbf{R}_j\}) = E\,\Psi(\{\mathbf{r}_i\}, \{\mathbf{R}_j\}). \tag{2.5}$$

This problem, comprised by the equations (2.1)–(2.5), is impossible to be solved analytically. Fortunately, it is possible to minimize it out to a simpler problem, allowing one to sort it out numerically. The first approximation to be done is the well-known Born-Oppenheimer approximation (also known, in this context, as the adiabatic approximation). Other approximations will be described in the following topics of this section.

2.1.1 The Born-Oppenheimer Approximation

In any many particles quantum systems, the ions are much heavier than the electrons, since $\frac{M_{ion}}{m_e} \sim 10^4$. That way, electrons turn out to be much faster than the ions, so that $\frac{v_{ion}}{v_e} \sim 10^{-3}$ [77]. Therefore, in the case of the mentioned problem, the decoupling between the ionic and electronic degrees of freedom is done, considering the ions as *almost* frozen for a give electronic configuration. Thus, the ionic coordinates work only as fixed parameters, which account for changes in the electronic configuration in case the ionic one is changed. After solving the electronic problem, one can go back to the ionic dynamics problem and solve it making use of the current electronic state information. That is the Born-Oppenheimer approximation.

Following the appendix C of the reference [78], the kinetic energy of equation (2.3) is too small, so that one can consider it as a perturbation to the steadfast nuclei. Thus, one must define the eigenvalues and eigenfunctions for the electrons, $E_{el}^n(\{\mathbf{R}_j\})$ and $\psi_n(\{\mathbf{r}_i\}, \{\mathbf{R}_j\})$, dependent on nuclei positions $\{\mathbf{R}_j\}$

as parameters. From equation (2.5), if the solutions of this equation form a complete set for a given ionic configuration, then one can expand the many-body wavefunction $\Psi(\{\mathbf{r}_i\},\{\mathbf{R}_j\})$ as:

$$\Psi(\{\mathbf{r}_i\},\{\mathbf{R}_j\}) = \sum_n \chi_n(\{\mathbf{R}_j\})\psi_n(\{\mathbf{r}_i\},\{\mathbf{R}_j\}). \tag{2.6}$$

That lead us to the electronic problem:

$$(H_{el} + H_{el-ion} + E_{ion-ion})\psi_n(\{\mathbf{r}_i\},\{\mathbf{R}_j\}) = E^n_{el}(\{\mathbf{R}_j\})\psi_n(\{\mathbf{r}_i\},\{\mathbf{R}_j\}), \tag{2.7}$$

where the electronic Hamiltonian terms were defined in the equation (2.2) and (2.4), and also

$$E_{ion-ion} = \sum_{j\neq j'} V_{ion}(\{\mathbf{R}_j - \mathbf{R}_{j'}\}) \tag{2.8}$$

is the classical electrostatic energy, which comes in as a constant owing to the "frozen" nuclei approximation. For the elelctronic problem, the significance of this term is to preserve the charge neutrality of the system.

Doing some mathematical manipulations, one finds that

$$[T_{ion} + E^n_{el}(\{\mathbf{R}_j\}) - E]\chi_n(\{\mathbf{R}_j\}) = -\sum_{n'} \beta_{nn'}\chi_{n'}(\{\mathbf{R}_j\}), \tag{2.9}$$

where $T_{ion} = \sum_j -\frac{(\nabla^2_j)}{2M_j}$ is the kinetic energy of the ions. The coeficients $\beta_{nn'}$ are given by

$$\begin{aligned} \beta_{nn'} &= A_{nn'} + B_{nn'}, \\ A_{nn'} &= \sum_j \frac{1}{M_j}\langle\psi_n|\nabla_j|\psi_{n'}\rangle\,\nabla_j, \\ B_{nn'} &= \sum_j \frac{1}{2M_j}\langle\psi_n|\nabla^2_j|\psi_{n'}\rangle. \end{aligned} \tag{2.10}$$

Notice that in $A_{nn'}$ the last gradient acts onto $\psi_{n'}$. The equation (2.9) is a Schrödinger equation for ionic eigenfunctions $\chi_n(\{\mathbf{R}_j\})$ that owns electronic energies of an effective potential for the dynamics of ions. The diagonal elements, β_{nn}, can be added up to the effective potential, while the off-diagonal ones, $\beta_{nn'}$ $(n \neq n')$, couple different electronic states. As a matter of fact, the Born-Oppenheimer approximation arises when one neglects those off-diagonal terms. Hence, this approximation does not take into account electronic transitions that come from interactions with the ions or, more precisely, with their vibrations around their equilibrium position (phonons) [79]. They have their importance for phenomena as Raman scattering and superconductivity.

Our focus will be on the electronic properties of the ground state of systems whose description will be given soon. This can be performed by mean of the electronic problem (2.7), for what the adiabatic approximation is sufficient. Therefore, henceforth, the ionic coordinates of the wavefunctions and the energies will be omitted, as well as their indexes, and the equation (2.7) is now read as

$$(H_{el} + H_{el-ion} + E_{ion-ion})\psi(\{\mathbf{r}_i\}) = E\psi(\{\mathbf{r}_i\}). \tag{2.11}$$

Notice that, doing so, the complete many-body problem is represented by a product of ionic and electronic wavefunctions, $\Psi = \chi\,\psi$.

DFT is an *ab-initio* theory widely used for many-body interacting systems. It is feasible to calculate a range of properties for a broad number of systems such as isolated atoms, molecules, nanostructures, bulk solids, etc. This makes this method to be the most employed presently. The reason for its enormous success is that a variety of properties (formation energy, forces, stress, phonon spectra, reponse functions, among others) of many-body systems that depend on the total energy can be expressed as the ground state functional density, $n_0(\mathbf{r})$. Thereby, at first, only $n_0(\mathbf{r})$ determines all the information of a many-body problem, including excited states and the many-body wavefuntions, making the ground-state density a central variable for the many-body problem instead of a complicated many-body wavefuntion. That rather simplifies the problem.

In practice, what one does is replace a set of wavefunctions dependent on the 3N electron coordinates with a simpler tridimensional function. The proves of those functionals are well documented in [27]; they have stamped the modern wording of the density funcional theory, which will be discussed in the next sections. However, a recipe is not presented for building those functionals. By the way, there is not even a known functional for systems with more than one electron. The practical advantage of DFT usage emerged with the work by Walter Kohn and Lu Jeu Sham in 1965 [28], when they formulated an *ansatz* that replace the interacting many-body problem with an auxiliary problem of independent electrons, in which the effects of the many-body interactions (beyond the classical Coulomb repulsion) are included inside the exchange-correlation functional [78]. This approach leads to the Kohn-Sham equations, which will be discussed in section 2.3. To instance how DFT works, the next subsection will be shown the Thomas-Fermi approximation, starting point of the theory. In the following subsections, it will be show approximations for the exchange-correlation functionals and the way DFT works in practical terms. To address such subjects, the discussions by [78] (chapters 3, and 6 through 9) and original references cited therein will be followed.

2.1.2 Thomas-Fermi Approximation

In 1927, Llewellyn H. Thomas [80] and Enrico Fermi [81] put forward an approximated method able to compute the total energy of quantum systems. That approach shows quite well what would be the use of DFT to treat many-body systems. They realized that the distribution of electrons could statistically be taken as a homogeneous electron gas. Thomas claims that:

> "Electrons are distributed uniformly in the hexadimensional phase space for the motion of an electron at the rate of two for each h^3 of (six) volume. The potential V is itself determined by the nuclear charge and this distribution of electrons."

The phase space is to be considered as translational and rotational degrees of freedom for each spin of electrons. Therefore, he gave us an assumption of how the electronic density formula derivation should be.

In the original Thomas-Fermi method the kinetic energy of electrons is approximated by a density functional of non-interacting electrons, whose value is equal at all the points of space. Thus, they got the functional of energy for all electrons:

$$E_{TF}[n] = c_1 \int d\mathbf{r}\, n(\mathbf{r})^{5/3} + \int d\mathbf{r}\, V_{ext}(\mathbf{r}) n(\mathbf{r}) + c_2 \int d\mathbf{r}\, n(\mathbf{r})^{4/3} + \frac{1}{2} \int d\mathbf{r} d\mathbf{r}'\, \frac{n(\mathbf{r}) n(\mathbf{r}')}{|\mathbf{r} - \mathbf{r}'|}, \tag{2.12}$$

where the first term corresponds to the local approximation for the kinetic energy with $c_1 = \frac{3}{10}(3\pi^2)^{2/3} = 2,871$, the third term is the local exchange (equal spins up and down) with $c_2 = -\frac{3}{4}(\frac{3}{\pi})^{1/3}$, both in atomic units (section 5.1 by [78]). Lastly, the second term is the Hartree classical electrostatic energy.

The ground-state density and energy can be found by minimizing $E_{TF}[n]$ with respect to $n(\mathbf{r})$, and subjected to the condition over which $\int d\mathbf{r} n(\mathbf{r}) = N$. Using the Lagrange's multiplier method, and minimizing the following functional

$$\Omega_{TF}[n] = E_{TF}[n] - \mu \left[\int d\mathbf{r} n(\mathbf{r}) - N \right], \tag{2.13}$$

for any variation of the density $\delta n(\mathbf{r})$, according to appendix A by [78], one gets to the condition for a stationary point:

$$\int d\mathbf{r} \left[\frac{5}{3} c_1 n(\mathbf{r})^{2/3} + V_{eff}(\mathbf{r}) - \mu \right] \delta n(\mathbf{r}) = 0 \tag{2.14}$$

where $V_{eff} = V_{ext}(\mathbf{r}) + V_H(\mathbf{r}) + V_X(\mathbf{r})$ is the total potential, and μ is the Fermi level. If this relations is valid for any $\delta n(\mathbf{r})$, then the funcional is stationay if, and only if, the following relation is satisfied:

$$\frac{1}{2}(3\pi)^{2/3} n(\mathbf{r})^{2/3} + V_{eff}(\mathbf{r}) - \mu = 0. \tag{2.15}$$

There are approaches for corrections of non-homogeneity of the density, in which terms that contain density gradient are included.

It is notorious the enhancement of the handling of systems in terms of density functionals, since one has replaced the 3N many-body Schrödinger equations. Nonetheless, this approach is not effectively beneficial, as the method is an oversimplification of the system, not taking into account the correlation and the exchange effects among the electrons. As a result, it does not provide satisfactory outcomes for cohesion energies of molecules, length of bonds, among other properties due to the lack of essential physical components. After all, the method can be considered a rough approximation for an exact theory proposed by Pierre Hohenberg and Walter Kohn in 1964 [27], the well known density functional theory.

2.2 The Hohenberg-Kohn Theorems

The idea introduced by Thomas and Fermi prompt to possibilities of the usage of the electronic density as a fundamental element in calculations of quantum systems. As a result, the schematic sequence would be as follows:

$$V \rightarrow H \rightarrow \Psi \rightarrow n. \tag{2.16}$$

In other words, one would have to know the potential of the system to solve the Schrödinger equation, then, from the gotten wavefunctions of this system, compute the electronic density. Despite that, because our analytical knowledge of the potential is restricted, one must do many approximations in order to make the computation simpler, fact that leads us to non-physical results. Bearing that in mind, in 1964 Hohenberg and Kohn introduced two theorems, which come to be the DFT basis, that say that the electronic density, besides to define the external potential of the system, also to define its energy. Accordingly, it is appropriate to introduce the density operator:

$$n_{op}(\mathbf{r}) = \sum_{i=1}^{N} \delta(\mathbf{r} - \mathbf{r}_i), \tag{2.17}$$

where $\{\mathbf{r}_i\}$ are the coordinates of the N particles. The particle density, $n(\mathbf{r})$, is given by the expected value of $n_{op}(\mathbf{r})$ in a many-body state $\psi(\mathbf{r}_1, \mathbf{r}_2, \ldots, \mathbf{r}_N)$ as:

$$n(\mathbf{r}) = \frac{\langle\psi|n_{op}|\psi\rangle}{\langle\psi|\psi\rangle} = N\frac{\int d^3r_2 \ldots d^3r_N |\psi(\mathbf{r}, \mathbf{r}_2, \ldots, \mathbf{r}_N)|^2}{\int d^3r_1 d^3r_2 \ldots d^3r_N |\psi(\mathbf{r}_1, \mathbf{r}_2, \ldots, \mathbf{r}_N)|^2}. \tag{2.18}$$

Here we are supposing that the particle are identicals to cut the summation out, inserting the factor N in the expression[2]. The total energy is evaluated from the expected value of the Hamiltonian of the equation (2.11). All in all, we are especially interested in the total external potential:

$$\begin{aligned} \langle V_{ext}\rangle &= \sum_{i=1}^{N} \frac{\langle\psi|V_{ext}(\mathbf{r}_i)|\psi\rangle}{\langle\psi|\psi\rangle} = N\frac{\int d^3r_1 V_{ext}(\mathbf{r}_1) \int d^3r_2 \ldots d^3r_N |\psi(\mathbf{r}_1, \mathbf{r}_2, \ldots, \mathbf{r}_N)|^2}{\int d^3r_1 d^3r_2 \ldots d^3r_N |\psi(\mathbf{r}_1, \mathbf{r}_2, \ldots, \mathbf{r}_N)|^2} \\ &= \int d^3r\, V_{ext}(\mathbf{r}) n(\mathbf{r}), \end{aligned} \tag{2.19}$$

where again we are using the assumption that the particles are identical and the equation (2.18). Being so, the total energy is:

$$E = \frac{\langle\psi|H|\psi\rangle}{\langle\psi|\psi\rangle} = \langle T\rangle + \langle V_{int}\rangle + \int d^3r\, V_{ext}(\mathbf{r}) n(\mathbf{r}) + E_{ion-ion}, \tag{2.20}$$

[2]We are neglecting the spin variable. It could be included by assuming that the integrals contain a summation for each spin variable for each coordinate as well. In that case, the equation (2.18) gives the particle density for a spin component.

with which, submitted to the normalization condition $\langle\psi|\psi\rangle = 1$, the ground-state energy and wave-function can be obtained. The first two terms of this equation are the expected value of kinetic energy of the electrons and the energy of electron-electron interaction whose sum is known as Hohenberg-Kohn universal functional, $F_{HK}[n]$. Observe that it is independent of the material, that is to say, of the external potential.

The energy functional given by the equation (2.20) is the starting point for the Hohenberg-Kohn (HK) theorems. Let's begin with the first one, such as showed by [78]:

Theorem 1 (The fundamental variable: the density) : *Whatever system of interacting particle subjected to a external potential, $V_{ext}(\boldsymbol{r})$, it is possible to find it univocally through the ground-state particle density, $n_0(\boldsymbol{r})$, except for a constant.*

This theorem is proved by contradiction. Knowing that the density and the energy of the system are given by the equations (2.18) and (2.20), let's suppose there are two external potentials, $V^1_{ext}(\mathbf{r})$ and $V^2_{ext}(\mathbf{r})$, which differ by more than a constant; however, they bring about the same ground-state density $n_0(\mathbf{r})$. The two external potentials bring about two different Hamiltonian as well (H^1 e H^2) that, in turn, lead to two different many-body wavefunctions, ψ^1 e ψ^2. Hypothetically, these wavefunctions correspond to the same ground-state density $n_0(\mathbf{r})$. Therefore,

$$E^1 = \langle\psi^1|H^1|\psi^1\rangle < \langle\psi^2|H^1|\psi^2\rangle, \tag{2.21}$$

for ψ^2 is not ground state of H^1. Setting the term after the inquality down as

$$\begin{aligned} \langle\psi^2|H^1|\psi^2\rangle &= \langle\psi^2|H^2|\psi^2\rangle + \langle\psi^2|H^1 - H^2|\psi^2\rangle \\ &= E^2 + \int d\mathbf{r}[V^1_{ext}(\mathbf{r}) - V^2_{ext}(\mathbf{r})]n_0(\mathbf{r}), \end{aligned} \tag{2.22}$$

so that

$$E^1 < E^2 + \int d\mathbf{r}[V^1_{ext}(\mathbf{r}) - V^2_{ext}(\mathbf{r})]n_0(\mathbf{r}). \tag{2.23}$$

Now in light of E^2, and doing the math, we find:

$$E^2 < E^1 + \int d\mathbf{r}[V^2_{ext}(\mathbf{r}) - V^1_{ext}(\mathbf{r})]n_0(\mathbf{r}). \tag{2.24}$$

Summing (2.23) and (2.24) up we get to the absurd inequality $E^1 + E^2 < E^2 + E^1$. We have followed the HK's considerations, supposing that the ground state is not degenerated. Nonetheless, the prove might be extended to degenerated cases [82], in accordance with section 6.1 by [78] and references therein.

As a matter of fact, the external potential is univocally determined by the density, and there is a consequence that comes up from this theorem, which is if all the Hamiltonian terms are determined (except

for a constant), then all many-body wavefunctions are determined, including those excited-state ones. Therefore, in principle, all of the system properties are completely determined from $n_0(\mathbf{r})$. Nevertheless, one would still have to solve the many-body problem with $V_{ext}(\mathbf{r})$.

Although the inclusion of $V_{ext}(\mathbf{r})$ in the problem seems to be tricky, the second theorem tells us that there exists an universal energy functional, $E[n]$, dependent only on the density, from which the ground state could be obtained.

Theorem 2 (Existence of the energy functional and the ground-state obtainment) : *An universal functional to energy $E[n]$ in terms of density $n(\boldsymbol{r})$ can be defined and is valid for any external potential $V_{ext}(\boldsymbol{r})$. For any $V_{ext}(\boldsymbol{r})$, the exact ground-state energy is the global minimum of that functional, and the density, which minimizes this functional, is the ground-state density $n_0(\boldsymbol{r})$.*

HK assumed that the densities $n(\mathbf{r})$ are ground-state densities of the electronic Hamiltonian, constrained to some external potential $V_{ext}(\mathbf{r})$. Thus, defining the space of possible densities in that we can build density functionals (which could be extended to a spectrum of functionals), and recognizing that the system properties are determined if one knows $n(\mathbf{r})$, then we can access the properties using density functionals, as the total energy, for instance.

We define the HK universal functional as:

$$F[n] = T[n] + V_{int}[n] = \langle T \rangle + \langle V_{int} \rangle, \tag{2.25}$$

where the expected values are calculated on the state $\psi(n(\mathbf{r}))$, which corresponds the given density. $F[n]$ depends only on the system particles and on the interactions among them, which is dependent only on the density, being applicable for any V_{ext} (so the term universal). With it, the total energy is given by:

$$E[n] = F[n] + \int d\mathbf{r} V_{ext}(\mathbf{r}) n(\mathbf{r}) + E_{ion-ion}, \tag{2.26}$$

which is also a density functional. $E_{ion-ion}$ above is a constant at the electronic problem. Following the considerations aforementioned, we are going to consider the ground-state density, $n^1(\mathbf{r})$, matching a potential $V^1_{ext}(\mathbf{r})$ and linked to a ground-state wavefunction, ψ^1. The ground-state total energy (equation (2.26)) is given by:

$$E^1 = E[n^1] = \langle \psi^1 | H^1 | \psi^1 \rangle. \tag{2.27}$$

Looking, however, at a density $n^2(\mathbf{r})$, which matches ψ^2, that is not a ground-state wavefunction, the total energy, E^2, is:

$$E^1 = \langle \psi^1 | H^1 | \psi^1 \rangle < \langle \psi^2 | H^1 | \psi^2 \rangle = E^2. \tag{2.28}$$

Hence, the ground-state energy, density functional of the ground state, is less than energy related to any other density. The gound-state energy is the global minimum of the energy functional, and its

density is the exact ground-state one. Although the theorem 2 does not convey anything about the specific form of the HK funcional ($F[n]$), it tells us about the ground-state density and energy, which comes from total energy functional, $E[n]$, and about all the properties related to them. $F[n]$ also contains the kinetic energy of the particles and the effects of the interactions[3]. The usefulness of DFT comes from an *ansatz* thought by Kohn and Sham [28]. It is possible to replace a many-body problem with a set of problems of independent electrons, which can be exactly solved (numerically, in practice). We will see how it works in the following subsection.

2.3 Kohn-Sham Equations

The Kohn-Sham (KS) *ansatz* consists in supposing the ground-state density is the same for both the interacting system and the auxiliary non-interacting system[4]. It leads to equations of independent particles that can be solved by numerical methods. But the trouble lies in the many-body terms, represented by the exchange-correlation functional of the density. That way, one builds a functional of the total energy of the interactiong system, using the information of the auxiliary system. By minimizing it, one obtains both the ground-state energy and density of the original interacting system, but with the accuracy given by the approximation of the exchange-correlation functionals. The KS *ansatz* is based in two assumptions. Firstly, the exact ground-state density can be represented by the ground-state density of a system of non-interacting particles, whose idea the figure 2.1 below perfectly exemplifies. The second assumption says that the auxiliary Hamiltonian has both an ordinary kinetic operator and an effective local potential[5], $V^{\sigma}_{eff}(\mathbf{r})$, acting on an electron with spin σ at $\mathbf{r}$, but with $V_{ext}(\mathbf{r})$ spin-independent.

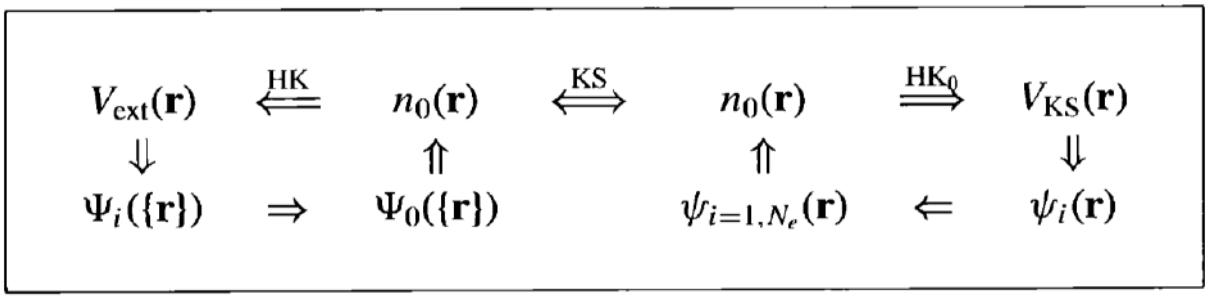

Figure 2.1: Comparison between the problem of an auxiliary system of non-interacting particles (right-hand side) and the complete many-body system, as addressed by the HK theorems (left-hand side). The double arrow with the superscription KS above it represents the link between both the appoaches. The arrow marked as HK_0 represents the HK theorem applied to non–interacting system. Figure has been gotten from [78], figure 7.1.

[3] It does not state anything about the excited states too. This could be done from the ground-state density (theorem 1), but this is still a challenge.

[4] There is still no prove for confirming that to any $n_0(\mathbf{r})$. However, DFT describes very well the properties of a wide reange of systems.

[5] The local form is not important, but it is a quite useful simplification, albeit, on the original article in 1965 [28], KS suggested a non-local form.

The Hamiltonian of an auxiliary particle is:

$$H^{\sigma}_{aux} = -\frac{1}{2}\nabla^2 + V^{\sigma}(\mathbf{r}), \tag{2.29}$$

that satisfies the Schrödinger equation for both the orbitals, $\phi^{\sigma}_i(r)$, and eigenvalues, ϵ_i. We are now taking into account the possibility of configurations of spin-polarization, and, of course, the potential $V^{\sigma}(\mathbf{r})$ is a general potential that depends on the spin, but, as already said, considering the external potential spin-independent. In such case, the density of a non-interacting system is given by

$$n(\mathbf{r}) = \sum_{\sigma} n(\mathbf{r},\sigma) = \sum_{\sigma}\sum_{i=1}^{N^{\sigma}} |\phi^{\sigma}_i(r)|^2, \tag{2.30}$$

where one counts N^{σ} electrons for each spin. Provided that the orbitals can be seen as density functionals, so both the kinetic energy and the Hartree energy (classical Coulomb repulsion energy) can be seen as density functionals as well. So,

$$T_s[n] = -\frac{1}{2}\sum_{\sigma}\sum_{i=1}^{N^{\sigma}}\langle\phi^{\sigma}_i|\nabla^2|\phi^{\sigma}_i\rangle = \frac{1}{2}\sum_{\sigma}\sum_{i=1}^{N^{\sigma}}|\nabla\phi^{\sigma}_i(r)|^2, \tag{2.31}$$

$$E_H[n] = \frac{1}{2}\int d^3r d^3r' \frac{n(\mathbf{r})n(\mathbf{r}')}{|\mathbf{r}-\mathbf{r}'|} \tag{2.32}$$

and thus, the functional of total energy, equations (2.25) and (2.26), can be written as

$$E_{KS}[n] = T_s[n] + \int d^3r V_{ext}(\mathbf{r})n(\mathbf{r}) + E_H[n] + E_{ion-ion} + E_{xc}[n]. \tag{2.33}$$

The many-body effects are embedded in the exchange-correlation functional, $E_{xc}[n]$. The exchange effects arises from Pauli's exclusion principle, included in the Hartree-Fock theory. What there is beyond both the classical and exchange effects is known as correlation effects. Basically, it reflects our lack of knowledge about the most complicated aspects of the interactions. Further, the summation of the terms $\int d^3r V_{ext}(\mathbf{r})n(\mathbf{r})$, E_H and $E_{ion-ion}$ result in a well-defined group, as already said, however with a caveat that, now, the external potential is the potential owing to the nuclei ones and to the external fields. So, we could express $E_{xc}[n]$ as

$$E_{xc}[n] = \langle T\rangle - T_s[n] + \langle V_{int}\rangle - E_H[n], \tag{2.34}$$

which is a functional, because of the functionals lying in the right-hand side. One sees, therefore, that it is not the differencing between both the kinetic and the internal energies of the actual interacting system, and the kinetic and Hartree energies of the auxiliary system.

As one can see from equation (2.33), the kinetic energy of the auxiliary Hamiltonian, $T_s[n]$, is expressed as a functional of the orbitals, and the other terms are density funtionals. Thus, the problem

of the minimization of Kohn-Sham energy functional, $E_{KS}[n]$, comes up, in which, by using the chain rule to vary the wavefunctions, one can derive the variational equation

$$\frac{\delta E_{KS}}{\delta \phi_i^{\sigma *}(\mathbf{r})} = \frac{\delta T_s}{\delta \phi_i^{\sigma *}(\mathbf{r})} + \left[\frac{\delta E_{ext}}{\delta n(\mathbf{r},\sigma)} + \frac{\delta E_H}{\delta n(\mathbf{r},\sigma)} + \frac{\delta E_{xc}}{\delta n(\mathbf{r},\sigma)} \right] \frac{\delta n(\mathbf{r},\sigma)}{\delta \phi_i^{\sigma *}(\mathbf{r})} = 0, \tag{2.35}$$

whose minimization of the functionals must be under the orthonormalization condition of the orbitals

$$\langle \phi_i^{\sigma} | \phi_j^{\sigma'} \rangle = \delta_{i,j} \delta_{\sigma,\sigma'}. \tag{2.36}$$

After some algebra, and making use of the expression

$$\frac{\delta T_s}{\delta \phi_i^{\sigma *}(\mathbf{r})} = -\frac{1}{2} \nabla^2 \phi_i^{\sigma}(\mathbf{r}) \tag{2.37}$$

$$\frac{\delta n(\mathbf{r},\sigma)}{\delta \phi_i^{\sigma *}(\mathbf{r})} = \phi_i^{\sigma}(\mathbf{r}), \tag{2.38}$$

one gets to the Kohn-Sham eigenvalues equations:

$$\left[-\frac{1}{2} \nabla^2 + V_{KS}^{\sigma}(\mathbf{r}) \right] \phi_i^{\sigma}(\mathbf{r}) = \epsilon_i^{\sigma} \phi_i^{\sigma}(\mathbf{r}), \tag{2.39}$$

where the Kohn-Sham potential is given by

$$V_{KS}^{\sigma} = V_{ext}(\mathbf{r}) + V_H(\mathbf{r}) + V_{xc}^{\sigma}(\mathbf{r}). \tag{2.40}$$

The Hartree potential, in turn, is

$$V_H(\mathbf{r}) \equiv \frac{\delta E_H[n]}{\delta n(\mathbf{r},\sigma)} = \int d\mathbf{r}' \frac{n(\mathbf{r}')}{|\mathbf{r} - \mathbf{r}'|}, \tag{2.41}$$

and the exchange-correlation potential is defined as

$$V_{xc}^{\sigma} \equiv \frac{\delta E_{xc}[n]}{\delta n(\mathbf{r},\sigma)}. \tag{2.42}$$

The KS equations are independent-particle equations, whose potential is found from the density self-consistently. The density, in turn, is gotten from the orbitals ϕ_i^{σ}, solution of the equation (2.39). The orbitals provide the ground-state density of the auxiliary system, which is the same as the one of the interacting system. Thenceforth, the ground-state energy and all the properties of the systems are settled. Nonetheless, the potential V_{xc} does not have an anaytical form. Approximations need to be done. Such issues will be discussed up next.

2.3.1 Approximations for the Exchange-Correlation Potential

In view of the recent success of the approximation-by-functionals methods, the exchange-correlation energy, $E_{xc}[n]$, which is a density functional, has gained a very important role in the calculations of many-body systems, for they would have been able to become the outcomes as close to the physical reality as possible. In this work, we have used the GGA approximation (Gradient-Generalized Approximation), specifically the one of Perdew-Burke-Ernzerhof (1996) [83]. There are other approximations indeed, and we also will talk about the LDA (Local Density Approximation), a relatively simpler functional, which was the first one to be developed. In reality, there are countless other approximations, but we will not discuss about them here. But, it is effortless to mention their relevance in treat non-homogeneous systems such as transition metal oxides and rare-earths, which are strongly correlated materials. Among other cases, it is crucial that other functionals are developed, and that is why many researchers have worked hard in finding them.

Local Density Approximation (LDA)

One of the advantages of the Kohn-Sham theory is that one is able to detach the kinetic energy and long-range Hartree interaction energy of independent particle from the part that contais the short-range interaction included in the exchange-corralation functional, $E_{xc}[n]$. In this sense, this functional can be approximated as a local density functional, or nearly local, because the electrons in solids could be considered as a limit case of a homogeneous gas. The most general case would be the inclusion of the spin degree of freedom (LSDA – Local Spin Density Approximation). The simpler expression has the form as

$$E_{xc}^{LSDA}[n^{\uparrow}, n^{\downarrow}] = \int d^3r\, n(\mathbf{r})\epsilon_{xc}(n^{\uparrow}(\mathbf{r}), n^{\downarrow}(\mathbf{r})), \tag{2.43}$$

where ϵ_{xc} is the exchange-correlation energy density, and the arrows denote the spin-up and spin-down labels, respectively, in such a way that $n = n^{\uparrow} + n^{\downarrow}$. The exchange-correlation energy density at each point of the space is given by the density of the homogeneous electron gas, with density in each point as

$$\begin{aligned} E_{xc}^{LSDA}[n^{\uparrow}, n^{\downarrow}] &= \int d^3r\, n(\mathbf{r})\epsilon_{xc}^{hom}(n^{\uparrow}(\mathbf{r}), n^{\downarrow}(\mathbf{r})) \\ &= \int d^3r\, n(\mathbf{r})\big[\epsilon_{x}^{hom}(n^{\uparrow}(\mathbf{r}), n^{\downarrow}(\mathbf{r})) + \epsilon_{c}^{hom}(n^{\uparrow}(\mathbf{r}), n^{\downarrow}(\mathbf{r}))\big]. \end{aligned} \tag{2.44}$$

The exchange energy density of a homogeneous electron gas, ϵ_x^{hom}, is analytically known from the Hartree-Fock theory:

$$\epsilon_x^{hom}(n, \zeta) = \epsilon_x^{hom}(n, 0) + [\epsilon_x^{hom}(n, 1) - \epsilon_x^{hom}(n, 0)]\, f_x(\zeta), \tag{2.45}$$

where $\zeta = (n^{\uparrow} - n^{\downarrow})/n$ is the spin polarization, and the function $f_x(\zeta)$ is given by:

$$f_x(\zeta) = \frac{1}{2}\frac{(1+\zeta)^{4/3} + (1-\zeta)^{4/3} - 2}{2^{1/3} - 1}, \tag{2.46}$$

and the non-polarized exchange energy density (where one has $n^{\uparrow}(\mathbf{r}) = n^{\downarrow}(\mathbf{r}) = n(\mathbf{r})/2$) is

$$\epsilon_x^{hom}(n, 0) = -\frac{3}{4}\left(\frac{6}{\pi}n\right)^{1/3}. \tag{2.47}$$

There is no analytical form for the correlation energy density, ϵ_c^{hom}. Nevertheless, it could be calculated with fine accuracy through the Quantum Monte Carlo stochastic methods [84]. The final expression for the exchange-correlation potential can be obtained from E_{xc} by mean of the equation (2.42).

Curiously, this approximation is very useful in describing systems that evade from homogeneity, such as atoms, molecules and covalent solids, whereby the approximation based on a homogeneous electron gas would not manage to work properly. The most used approximation is the LDA-PZ [85]. Obviously, credits must be given since improved functional features were built, as the GGA ones, which will be considered up next.

Generalized Gradient Approximation (GGA)

The L(S)DA success led to the development of the GGA functionals. In this subsection we will describe briefly some physical ideas, fundamentals of the building of GGA functionals. As the first step in the direction of the improvement over the local approximation, including dependence on the magnitude of the density gradient, $|\nabla n^{\sigma}|$, in ϵ_{xc}, as well as the value of n at each point $\mathbf{r}$, would be a first order expansion. This expansion is known as GEA (Gradient Expansion Approximation) [86]. Nonetheless, it does not lead to consistent results when compared the LDA's ones for these gradients in actual materials are so large that the expansion explodes. The term GGA denotes a range of possibilities of proposing functions that modify the behavior of the mentioned gradients. One could, therefore, include derivatives of higher order so that the equation (2.43) could be generalized as

$$\begin{aligned} E_{xc}^{GGA}[n^{\uparrow}, n^{\downarrow}] &= \int d^3r\, n(\mathbf{r})\epsilon_{xc}(n^{\uparrow}(\mathbf{r}), n^{\downarrow}(\mathbf{r}), |\nabla n^{\uparrow}(\mathbf{r})|, |\nabla n^{\downarrow}(\mathbf{r})|, ...) \\ &= \int d^3r\, n(\mathbf{r})\epsilon_x^{hom}(n(\mathbf{r}))\, F_{xc}\big(n^{\uparrow}(\mathbf{r}), n^{\downarrow}(\mathbf{r}), |\nabla n^{\uparrow}(\mathbf{r})|, |\nabla n^{\downarrow}(\mathbf{r})|, ...\big), \end{aligned} \tag{2.48}$$

where $\epsilon_x(n)$ is the energy density of a non-polarized homogeneous electron-gas, and F_{xc} is a dimensionless function of the densities and their derivatives. For exchange term, there is a scale ratio for $E_x[n]$, in which the density $n(\mathbf{r})$ is non-polarized, so is $F_x(n, |\nabla n|)$. As defined on the references [83, 87], it is convenient using the reduced density gradient, a dimensionless quantity:

$$s_m = \frac{|\nabla^m n|}{(2k_F)^m n} = \frac{|\nabla^m n|}{2^m(3\pi^2)^{m/3}(n)^{(1+m/3)}}. \tag{2.49}$$

where $k_F = 3(2\pi/3)^{1/3}\, r_S^{-1}$ is the Fermi momentum, and r_S is the mean distance between the electrons, also known as local Wigner-Seitz radiusThe Wigner-Seitz radius, named after Eugene Wigner and Freder-

ick Seitz, is the radius of a sphere whose volume is equal to the mean volume per atom in a solid (for first group metals)., which normalizes the m-th variation of the density. The expression for the firts gradient is

$$s_1 \equiv s = \frac{|\nabla n|}{(2k_F)n} = \frac{\nabla r_S}{2(2\pi/3)^{1/3}\, r_S}. \tag{2.50}$$

where $n = 3/4\pi r_S^3$.

For s_1 there are an inifinitude of expressions for F_x, whose three majors are B88 (Becke, [88]), PW91 (Perdew and Wang, [89]) and PBE (Perdew, Burke and Enzerhof, [83]). It is interesting to know that for s within the range $(0, 3)$, region whereby the reduced gradient is small and, because of that, useful for most of the physical applications, distinct F_x have approximately the same form. This betokens that different GGAs contribute in a similar manner on conventional systems. Compared to LDA, the binding energy is decreased. This improves the concordance to the experimental data, which is a highly favorable point of the GGA approximation. Within the range $(3, \infty)$, the F_x result depends on the choice of the physical conditions.

As to the corralation, F_c is more complicated to shape in terms of a functional. However, its contribution to the total energy is much less than that of the exchange. For large values of s, this decrease can be qualitatively understood, because large gradients are connected to the strong potentials of confinement, which increase the spacing and decrease the effects of interactions when compared to the independent electrons terms [78].

In general, GGA provides better results in terms of binding energies when compared to the LDA. In this thesis, we have used the GGA-PBE functional [83], which enhances the description of atoms, molecules and solid compared to the LDA results, even though proposing to mantain their features and combining them with the non-locality of the gradient correction. Therefore, supporting ourselves on the appendix B of [78], the exchange functional is chosen in such a way that the local approximation is recovered ($F_x(0) = 1$ e $F_x \to const.$, whenever $s \to \infty$. Thus, we can write

$$F_x(s) = 1 + \kappa - \frac{\kappa}{(1 + \mu s^2/\kappa)}, \tag{2.51}$$

where $\kappa = 0.804$ to satisfy the Lieb-Oxford limit[6]. In addition, one has chosen $\mu = 0.21951$ in order to recover the linear response form of the local approximation.

The correlation energy, $E_c^{GGA-PBE}$, is the sum of a local correlation term with a term that depends on the gradients and on the spin polarization of the system:

$$E_c^{GGA-PBE}[n^\uparrow, n^\downarrow] = \int d\mathbf{r}\, n \left[\epsilon_c^{hom}(r_S, \zeta) + H(r_S, \zeta, t)\right], \tag{2.52}$$

[6]The Lieb-Oxford inequality has an important role on DFT, in particular regarding the stability of matter. It claims that the difference between the repulsive Coulomb electrostatic energy for the system (indirect part) and the electrostatic energy related to the charge density in a semi-classical approximation (direct part) estimates a lower limit for the indirect part. Details can be found in [90, 91].

where ζ was defined in the equation (2.45), and $t = |\nabla n|/(2\phi k_{TF} n)$ is the dimensionless gradiente defined in [83], but similar to the equation (2.49). Yet we have that $\phi = \Big((1+\zeta)^{2/3} + (1-\zeta)^{2/3}\Big)/2$ is a spin scale factor (SSF, for short)[7]. t in turn is scaled by the Thomas-Fermi wavevector k_{TF} insteade of k_F. Therefore, the final form is

$$H = \gamma\phi^3 ln\left(1 + \frac{\beta}{\gamma}t^2 \frac{1+At^2}{1+At^2+A^2t^4}\right), \tag{2.53}$$

where the function A is given by

$$A = \frac{\beta}{\gamma}\left[exp\left(\frac{-\epsilon_c^{hom}}{\gamma\phi^3}\right) - 1\right]^{-1}. \tag{2.54}$$

Other Approximations

Other approximations are made when one is before systems highly non-homogeneous (to which both the LDA and GGA approximations do not work well), such as transition metal oxides and rare-earths. Very simple types of approximations are the exact exchange functionals (EXX, for short), which come from the Hartree-Fock theory, a general theory, not that from the electron gas case. Another example is the functional LDA+U (the 'U' comes from the interaction term of the Hubbard model). Other class of functionals rather known are those of the hybrid functionals, in which one include a fraction of the exact exchange (the EXX functional of Hartree-Fock) and fractions of the exchange/corralation of local functionals (LDA or GGA) on the final exchange-correlation functional. These functionals are built to work in determined systems of interest, which even solve some DFT problems exactly, such as the energy gap ones, providing more accurate results for beyond-DFT approaches for spectra of light absorption, for instance.

2.3.2 DFT in practice: Solving the Kohn-Sham Equations

The potentials of the equations (2.39)–(2.42) depend on the density, which in turn depend on the one-electron orbitals from the equation (2.30). But the potentials themselves depend on the solutions of the one-electron orbitals equations. Thence, numerically, the equations must be solved in a self-consistent way. At first, one starts with a reasonable "guess" on the density, from which the Kohn-Sham potential is built. Afterward, one solves the KS equations to obtain a new set of one-electron wavefunctions, from which both a new density and a new KS potential are built. So, the new potential enters as input for the next step, and the cycle is repeated until the self-consistency is reached as explained below. This procedure can schematically be represented as

[7] Wang, et. al [92] found that ϕ is the spin scale factor for the term $|\nabla n|^2/n^{4/3}$ of the expansion in terms of the spin density gradient of the exchange energy. And also they perceived that it was a good approximation to the SSF for the correlation energy.

$$V_i \rightarrow n_i \rightarrow V_{i+1} \rightarrow n_{i+1} \rightarrow \ldots \tag{2.55}$$

where the labels represent iterations in self-consistent cycles. The self-consistency is reached when a selected convergency parameter (either total energy or density, for instance) varies by less than a certain threshold, which is the modulus of the difference between two consecutive steps. All the process is ilustrated on the flowchart of the figure **??**. At each step, the KS equations are solved using some based-methods in standard linear algebra. There are many package available on the intertnet that can perform such calculations. In our case, we have used a DFT-based package called QUANTUM ESPRESSO [43], which uses plane-waves basis set and pseudopotential method to make calculations of electronic struture, simulations, optimizations, among other properties. An important fact is that, to reach self-consistency, the program makes use of mixtures of both input and output densities in order to build the potential towards the next step, even using details from more than one previous step. Finally, after self-consistency has been reached the ground-state energy is obtained, as well as all the other ground-state properties that depend on it.

As we have seen, the original expression of the Kohn-Sham energy functional is given by the equation (2.33), which hereby is written in other form to split up the potentials term:

$$\begin{aligned} E_{KS} &= T_s[n] + E_{pot}[n] \\ E_{pot}[n] &= \int d\mathbf{r} V_{ext}(\mathbf{r}) n(\mathbf{r}) + E_H[n] + E_{ion-ion} + E_{xc}[n]. \end{aligned} \tag{2.56}$$

The first three terms of the equation (2.56), added together, correspond the classical Coulomb interaction. The kinetic energy then could be expressed as

$$T_s[n] = E_s - \sum_\sigma \int d\mathbf{r} V^{\sigma,in}(\mathbf{r}) n^{out}(\mathbf{r}), \tag{2.57}$$

where the superscripts *in* and *out* match to the *input* and *output* of both the potential and the density, respectively, as ilustrated on the flowchart showed in the figure **??**; and $E_s = \sum_\sigma \sum_{i=1}^{N^\sigma} \epsilon_i^\sigma$ is the summation of the KS eigenvalues that are given as

$$\epsilon_i^\sigma = \langle \phi_i^\sigma | H_{KS}^\sigma | \phi_i^\sigma \rangle. \tag{2.58}$$

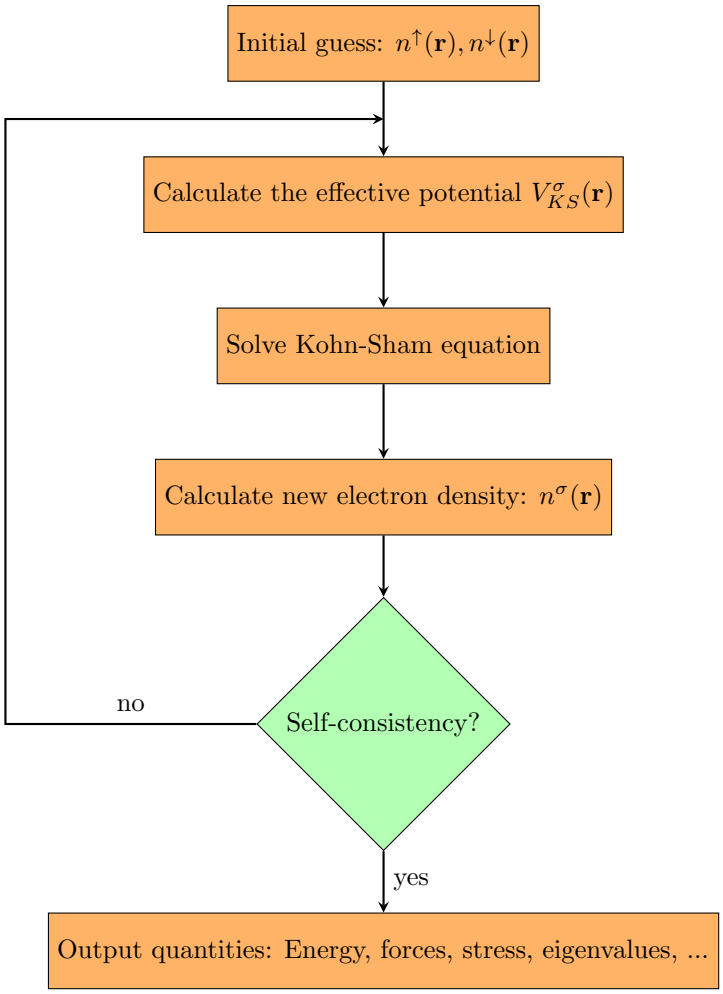

Figure 2.2: Flowchart for the solution of the self-consistent KS equations (credits for [78], figure 9.1).

The Hartree potential is usually determined by solving the Poisson equation in the either the real or reciprocal space for a given density $n(\mathbf{r})$ instead of the equation (2.41). Also one does not use the equation (2.42) to find the solution for exchange-correlation potential. This subject has already been discussed in the subsection 2.3.1. The remaining external potential, which is commonly obtained by the pseudopotential method[8], which will be discussed in the subsection 2.5. It should also be noted that, although the KS energy is a density functional, nothing forecloses one could say that it is a functional of the input potential, since it is it who determines all of the quantities of the equation (2.56), inasmuch as also it determines the output density, whereas energy does not reach its global minimum. Therefore, the solution of the KS equations are related to a potential $V^{in} = V_{KS}$, which minimizes the total energy, and in turn the density $n^{out} = n_0$, which is the ground-state one.

[8]The KS equations are modified when treating the system under this external potential with this method. This is true because this method is, in general, either non-local or semi-local.

2.4 Numerical Methods

In this section we will discuss some numerical methods employed on the solution of the Kohn-Sham equations for realistic systems in any one-particle problem according to the equation (2.39). In the following four subsections, we will discuss both the wavefunction expansion and the one-particle equations in a plane-waves basis, the usage of special k-points for integrations within the Brillouin Zone (BZ), the application of the pseudopotential method for the electron-ion interaction, and, at last, we will talk about the supercell usage to describe defective systems.

2.4.1 The One-Particle Problem in a Plane-Waves Basis

In a problem of crystalline solid, one needs that the wavefunctions are to be reasonably smooth, so that it is convenient to expand them in a plane-waves basis[9], such as

$$\phi_i(\mathbf{r}) = \frac{1}{\sqrt{\Omega}} \sum_{\mathbf{q}} c_{i,\mathbf{q}} e^{i\mathbf{q}.\mathbf{r}} \equiv \sum_{\mathbf{q}} c_{i,\mathbf{q}} \times |\mathbf{q}\rangle, \tag{2.59}$$

where Ω is the volume of the crystal in the reciprocal space, and $c_{i,\mathbf{q}}$ are the coefficients of the expansion of the wavefunctions on an orthonormal plane-waves basis $\{|\mathbf{q}\rangle\}$. The plane waves are represented by their wave vectors, $|\mathbf{q}\rangle$. Taking the orthonormality relation into account, which is $\langle \mathbf{q}'|\mathbf{q}\rangle = \frac{1}{\Omega}\int_\Omega d\mathbf{r}\, exp(-i\mathbf{q}' \cdot \mathbf{r})\, exp(i\mathbf{q}\cdot\mathbf{r}) = \delta_{\mathbf{q}',\mathbf{q}}$, and including the expansion (2.59) inside the equation (2.39), then multiplying it by $\langle \mathbf{q}'|\mathbf{r}\rangle = exp(-i\mathbf{q}'.\mathbf{r})/\sqrt{\Omega}$), and, at last, integrating over all coordinate space, we get

$$\sum_{\mathbf{q}} \langle \mathbf{q}'|H_{eff}|\mathbf{q}\rangle = \epsilon_i \sum_{\mathbf{q}} \langle \mathbf{q}'|\mathbf{q}\rangle c_{i,\mathbf{q}} = \epsilon_i c_{i,\mathbf{q}'}, \tag{2.60}$$

which is the Shrödinger equation in reciprocal space, or also in Fourier space. The matrix element of the kinetic energy operator is

$$\langle \mathbf{q}'|T|\mathbf{q}\rangle = \frac{1}{\Omega}\int_\Omega d\mathbf{r}\, e^{-i\mathbf{q}'\cdot\mathbf{r}}\Big(-\frac{1}{2}\nabla^2 e^{i\mathbf{q}\mathbf{r}}\Big) \longrightarrow \frac{1}{2}q^2\delta_{\mathbf{q},\mathbf{q}'}, \tag{2.61}$$

where we have used orthonormalization relation. The effective potential can be as well expressed in terms of the Fourier components, for they can be periodic:

$$V_{eff}(\mathbf{r}) = \sum_{\mathbf{G}} V_{eff}(\mathbf{G})\, e^{i\mathbf{G}\cdot\mathbf{r}}, \tag{2.62}$$

wherein $\mathbf{G}$ are vectors in reciprocal space, which are defined below and visualized in the figure 2.3. We still have the Fourier transform of $V_{eff}(\mathbf{r})$, with Ω_{cell} being the volume of the primitive unit cell:

[9] Making usage the fact that any periodic function can be expanded in a complete set of Fourier components ([78], chapter 12).

$$V_{eff}(\mathbf{G}) = \frac{1}{\Omega_{cell}} \int_{\Omega_{cell}} d\mathbf{r}\, V_{eff}(\mathbf{r})\, e^{-i\mathbf{G}\cdot\mathbf{r}}. \tag{2.63}$$

Thus, with the orthonormalization relation, the matrix elements are given by

$$\langle \mathbf{q}' | V_{eff} | \mathbf{q} \rangle = \sum_{\mathbf{G}} V_{eff}(\mathbf{G}) \delta_{\mathbf{q}'-\mathbf{q},\mathbf{G}}. \tag{2.64}$$

We have defined that $\mathbf{q} = \mathbf{k} + \mathbf{G}$ and $\mathbf{q}' = \mathbf{k} + \mathbf{G}'$, where $\mathbf{G}$ and $\mathbf{G}'$ are translation vectors of the lattice in reciprocal space, as the figure 2.3 illustrates.

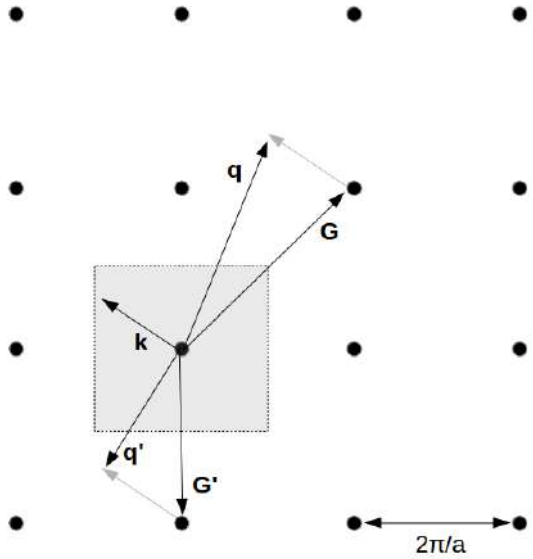

Figure 2.3: Points of an arbitrary, square reciprocal lattice of size $2\pi/a$. The grey region indicates the first Brillouin Zone, in which the vector $\mathbf{k}$ is shown. The translation vectors of the reciprocal lattice, both $\mathbf{G}$ and $\mathbf{G}'$, determines all the points $\mathbf{q}$ and $\mathbf{q}'$ of the reciprocal space.

In this sense, if the kinetic term is defined for $\mathbf{G}$, then the Hamiltonian couples momentum components that differ by $\mathbf{G}$. Moreover, one should bear in mind that the difference between vectors $\mathbf{q}$ and $\mathbf{q}'$ of reciprocal lattice is also a vector of reciprocal lattice. Therefore, one obtains that

$$\sum_{\mathbf{G}'} H_{\mathbf{k}+\mathbf{G},\mathbf{k}+\mathbf{G}'} c_{n,\mathbf{k}+\mathbf{G}'} = \epsilon_{n,\mathbf{k}} c_{n,\mathbf{k}+\mathbf{G}}, \tag{2.65}$$

with

$$H_{\mathbf{k}+\mathbf{G},\mathbf{k}+\mathbf{G}'} = \langle \mathbf{k}+\mathbf{G} | H_{eff} | \mathbf{k}+\mathbf{G}' \rangle = \frac{1}{2} |\mathbf{k}+\mathbf{G}|^2 \delta_{\mathbf{G},\mathbf{G}'} + V_{eff}(\mathbf{G}-\mathbf{G}'). \tag{2.66}$$

This is the final form of the one-particle equation in a plane-waves basis. The indexes n and $\mathbf{k}$ are quantum numbers known as band index and crystal momentum, respectively. Concerning the latter,

a remark ought to be done: it is not a ordinary momentum, for it obeys a discrete set of translation symmetry of the crystal lattice, instead of the complete symmetry of the vacuum. In addition, it suffers a less restrictive limitation as to the conservation law, because it is conserved over any addition of vector of reciprocal lattice **G**.

Making usage of the coefficients $c_{n,\mathbf{k}+\mathbf{G}}$ inside the expasion (2.59), we are going to find that the wavefunctions are labeled by indexes n and $\mathbf{k}$, and the summation will only be limited to the vectors of reciprocal lattice. Therefore, we have

$$\phi_{n,\mathbf{k}}(\mathbf{r}) = \frac{1}{\sqrt{\Omega}} \sum_{\mathbf{G}} c_{n,\mathbf{k}+\mathbf{G}} e^{i(\mathbf{k}+\mathbf{G})\cdot\mathbf{r}} = \frac{1}{\sqrt{N_{cell}}} e^{i\mathbf{k}\cdot\mathbf{r}} u_{n,\mathbf{k}}(\mathbf{r}), \tag{2.67}$$

where N_{cell} is the number of unit cells in the crystal, and

$$u_{n,\mathbf{k}}(\mathbf{r}) = \frac{1}{\sqrt{N_{cell}}} \sum_{\mathbf{G}} c_{n,\mathbf{k}+\mathbf{G}} e^{i\mathbf{G}\cdot\mathbf{r}}. \tag{2.68}$$

Equation (2.67) represents the famous Blöch's theorem ([77], chapter 8), which says that a wavefunction can be written as a product between a phase factor and a function with the lattice periodicity, both defined by the quantum number $\mathbf{k}$ or, equivalently, $\phi_{n,\mathbf{k}}(\mathbf{r}+\mathbf{R}) = exp(i\mathbf{k}\cdot\mathbf{R})\phi_{n,\mathbf{k}}(\mathbf{r})$, for any translation vector $\mathbf{R}$. We can see, yet, from the equations (2.67) and (2.68) that $\phi_{n,\mathbf{k}+\mathbf{G}}(\mathbf{r}) = \phi_{n,\mathbf{k}}(\mathbf{r})$. Thus, both the energies and the Blöch's wavefunctions are periodic functions in reciprocal space. In this sense, we can limit ourselves to the analysis of a primitive unit cell of the reciprocal lattice.

An important parameter in numerical calulation is the cutoff energy E_c. Each expansion (2.67) will have its own cutoff energy to yield efficient computations, as well as to provide wavefunctions as smooth as possible. That parameter is defined as

$$E_c = \frac{1}{2} G_{max}^2, \tag{2.69}$$

where G_{max} is the maximum magnitude from a family of same-size vectors related by symmetry operations of the crystal point group. The purpose is to become the computation as smooth as possible, using appropriate wavefunctions for that, so that to be possible to work with small E_c. This is even the fundamental motivation for the usage of the pseudopotential method, which will be discussed in the subsection 2.5.

All in all, the equations (2.65) and (2.66) are the core of the Kohn-Sham formalism in a plane-waves basis set. There exist other alike expressions for the density, total energy, and related properties, all of them in the reciprocal space (which are related to the wavefunctions expanded in this basis).

2.4.2 Special k-points for integration within the Brillouin Zone

Electronic structure calculations, including total energy, electronic density, density of states, etc, occur commonly at provided estimates either on summation or on averages over the k-points within the

Brillouin Zone (BZ). If it is so, it is essential the choice of wavefunctions that obey the Born-von Karman conditions inside a large crystal volume made up by N_k cells. Thus, it must have exactly a value from $\mathbf{k}$ for each cell. So, for a general function, $f_n(\mathbf{k})$, whose n means discrete set of states for each $\mathbf{k}$, the mean value per cell is

$$\bar{f}_n = \frac{1}{N_k} \sum_{\mathbf{k}} f_n(\mathbf{k}). \tag{2.70}$$

In the thermodynamic limit (infinity crystal), the discrete set of k-points turns into a continuum, and so the summation becomes integrals:

$$\frac{1}{N_k} \sum_{\mathbf{k}} f_n(\mathbf{k}) \to \frac{\Omega_{cell}}{(2\pi)^d} \int_{BZ} d^d k f_n(\mathbf{k}), \tag{2.71}$$

where N_k is the number of k-points within the BZ, and $(2\pi)^d/\Omega_{cell}$ is the BZ's volume of d-dimensions. If the integrand $f_n(\mathbf{k})$ is any periodic function in reciprocal space with vectors $\mathbf{k}$, then we can expand it in plane waves:

$$f_n(\mathbf{k}) = \sum_{\mathbf{R}} \tilde{f}_n(\mathbf{R})\, e^{i\mathbf{k}\cdot\mathbf{R}}, \tag{2.72}$$

where $\mathbf{R}$ is the translation vector in real space, and whose coefficients are given by the Fourier transform of $f_n(\mathbf{k})$:

$$\tilde{f}_n(\mathbf{R}) = \frac{\Omega_{cell}}{(2\pi)^d} \int_{BZ} d^d k\, f_n(\mathbf{k})\, e^{-i\mathbf{k}\cdot\mathbf{R}}, \tag{2.73}$$

from which the equation (2.71) is recovered when $\mathbf{R} = \mathbf{0}$.

In numerical calculations, as periodic functions are smooth, one should approximate the integrals by summations over a suitable set of k-points appropriately chosen. The most normally used is the Monkhorst-Pack (MP) special set of points, [93], a uniform set of points defined by[10]

$$\mathbf{k}_{n_1,n_2,n_3} = \sum_{i=1}^{3} \frac{2n_i - N_i - 1}{2N_i} \mathbf{b}_i, \tag{2.74}$$

where $\{\mathbf{b}_i\}$ are primitive vectors of the reciprocal lattice, and $n_i = 1, 2, \ldots, N_i$. The index i represents directions in space at hand (either reciprocal or real space). One can glance, then, that that defines a uniform grid of size $N_{MP} = N_1 \times N_2 \times N_3$, and still that it represents a reduced version of the reciprocal lattice, with primitive vectors of $\mathbf{b}_i/N_i$ sized on each direction. Ergo, if the grid size, N_i, on each direction is large enough, such that the correspondent truncated expansion yields $f_n(\mathbf{k})$ to the desired accuracy, then the integrals of this function within the BZ are precisely reproduced by the summations over the k-points of the MP grid. In practice, we should test the convergence of the properties one seeks

[10] We have defined a tridimensional MP grid.

(total energy, densities, etc) with respect to the grid size until obtaining the ideal size within the desired accuracy, which varies from system to system.

From equation (2.73), making usage of the MP grid of the equation (2.74), one gets

$$\tilde{f}_n(\mathbf{R}) = \frac{1}{N_{MP}} \sum_{n_1,n_2,n3} f_n(\mathbf{k}_{n_1,n_2,n_3}) e^{-i\mathbf{k}_{n_1,n_2,n_3}\cdot\mathbf{R}}. \tag{2.75}$$

Thus, we observe that a periodic function, (2.72), which contains Fourier components up to $N_i\mathbf{a}_i$ in real space, has its coefficients given exactly by the equation (2.75). Besides, the equation (2.74) represents a reduced-scaled version of the reciprocal lattice, with lattice primitive vectors of size $\mathbf{b}_i/N_i$. Therefore, the more N_i increases on each direction, the more the accuracy of $f_n(\mathbf{k})$ enhances, and the integration of this function over the BZ can precisely be reproduced by summations over the k-points of the MP grid (in other words, we have the equation (2.75) for $\mathbf{R}$).

The symmetry issue is quite important, for if $f_n(\mathbf{k})$ is a scalar, then it is invariant by symmetry operations of the crystal point group. There exist many terms in equation (2.75) that envelops a set of k-point that are equivalents by symmetry for $\tilde{f}_n(\mathbf{0})$. We can gather these terms together, including only one of those points of each set, ascribing to it only a weight $\omega_{\mathbf{k}}$, which corresponds to the number of distinguishable k-points related by symmetry groups on each set of k-points, normalized by the total number of k-points. Hence, the integral of equation (2.71) is evaluated as

$$\frac{\Omega_{cell}}{(2\pi)^3} \int_{BZ} d^3k f_n(\mathbf{k}) = \tilde{f}_n(\mathbf{0}) \approx \sum_{\mathbf{k}_{n_1,n_2,n_3}}^{IBZ} \omega_{\mathbf{k}_{n_1,n_2,n_3}} f_n(\mathbf{k}_{n_1,n_2,n_3}), \tag{2.76}$$

where, now, the summation is restricted to a piece of the BZ, which encompasses the k-point of the grid that are not equivalent to the others by symmetry, lowering too much the computation cost. That piece is known as Irreducible Brillouin Zone (IBZ). QUANTUM ESPRESSO has routines that are able to obtain the MP grid within the IBZ for a given size of the grid along with the corresponding weights.

2.5 Pseudopotentials

Electrons and ions interact through the Coulomb potential. Although we can distinct core electrons from valence electrons, only the latter ones matter for the chemical bonds, since the core electrons have very little significance when it comes to properties of either molecules or solids. Bearing this in mind, the idea of the pseudopotential method is to create a potential that takes into account both the effective interaction of the valence electrons and the interactions that exist among the core electrons, and also the interactions of the latter with the nucleus. That effective potential, or pseudopotential, replaces the Coulomb potential in the Schrödinger equation, whose wavefunctions, also known as pseudo wavefunctions, are smooth (without nodes) for the valence electrons within the core region. These smooth solutions for the valence electrons are suitable for numerical computation. The pseudo wavefunctions are

built in such a way that they maintain the valence properties of all the electrons, which are relevant for describing the bonding properties between atoms.

Pseudopotential methods make use of an effective pseudopotential that replaces the all-electrons (AE) potential with a potential such that the core states are crossed off, and the valence ones are described by nodeless pseudo functions. This is feasible because the core states remain themselves almost unchanged. *Ab-initio* pseudopotentials are derived from a certain atomic state, requiring that the valence eigenstates, both AE and pseudo ones, to be the same outside a chosen cutoff radius. That is illustrated in the figure 2.4. The larger cutoff radius, r_c, the smoother will be the pseudopotential. In other words, it is going to converge more rapidly [94]. They can be generated from atomic calculations and, then, used to compute properties of valence electrons in both molecules or solids. Thus, one may build pseudopotentials that simplify as far as possible both the computation and the interpretation of the outcomes of electronic structure.

There are a big variety of sofisticated pseudopotentials. In spite of that, in our calculations, we have mainly resorted to two types: USPP (Ultrasoft Pseudopotential), introduced by Blöchl [95] and Vanderbilt [96], and also the PAW (Projected Augmented Waves) one [94, 97, 98]. These methods enable performing computations more efficiently by transforming the rapidly oscillating wavefunctions close to the core, computing integrals as combinations of integrals of smooth wavefunctions extending all over the space, along with localized contributions, which are computed by radial integration. In the following, we are going to discuss in detail these methods and their relevance to our research, whose fundamentals originated from the OPW (Orthogonalized Plane Wave) method, [99], and from the conditions hystorically imposed by norm-conserving pseudopotentials (NCPP) [100]. More on these methods can be found in the appendices A and B, respectively.

2.5.1 Ultrasoft Pseudopotential (USPP)

As we had ever seen, in addition to the requirement in creating smooth pseudopotentials, they also needed to be accurate and transferable. As plane-waves-based calculations need Fourier components to describe valence wavefunctions, the computational cost scales as a power of the number of required components. Thus, it would be necessary to maximize "smoothness" whereas minimizing the range of the Fourier space down to a specific accuracy. The latter criterium can be achieved by norm-conserving pseudopotential [100], which is also the startpoint concerning transferability: a pseudopotential constructed in any environment (usually an atom) can faithfully describe the valence properties of atoms, ions, molecules, and condensed matter in different environment [78][11].

The ultrasoft pseudopotential comes into play in trying to solve the accuracy problem. The aim is to re-express the problem in terms of a smooth function and an auxiliary function around each ion core that represents the rapidly varying part of the density ([78], page 222). This pseudopotentials are formaly related to both the OPW equations [99] and the PKA approach [101–103], and are focused upon

[11] Although some errors may occur, this is an excellent approximation for a small, deep core. When it comes to shallow cores, high accuracy is required otherwise this can be the source of the errors.

states that represent great difficulties to be created as smooth as accurate by the OPW, namely the $1s$, $2p$, $3d$, and other states for which the OPW transformation has no effect since there is no core state for the same angular momentum.

An extent of norm-conserving beyond the linear regime is important to be followed, since it spreads the energy range of the original all-electron potential. This is the basis for further generalizations over future pseudopotentials generations. At any energy ϵ_s, the construction of the projectors can be done in order to satisfy the Schrödinger equation at more than one energy for a given (l, m) [95, 104]. Matrices $B_{s,s'} = \langle \psi_s | \chi_{s'} \rangle$ can be formed at any energies ϵ_s if pseudofunctions ψ_s are constructed from all-electrons calculations[12]. Therefore, a generalized non-local potential operator can be written as

$$\delta \hat{V}_{NL} = \sum_{lm} \left[\sum_{s,s'} B_{s,s'} |\beta_s\rangle \langle \beta_{s'}| \right]_{lm}, \tag{2.77}$$

where χ_s are defined in (B.22), and $\beta_s = \sum_{s'} B^{-1}_{s,s'} \chi_{s'}$. And, naturally, ψ_s is solution of $\hat{H}\psi_s = \epsilon_s \psi_s$. With such a modification, the non-local separable pseudopotential can be now generalized, so that it will agree with the all-electron calculations for any accuracy over any energy range.

Then, Blöchl [95] and Vanderbilt [104] rewrote the non-local potential (2.77) in a form involving a smooth function $\tilde{\phi} = r\tilde{\psi}$ that is not norm-conserving. From the norm-conserving function, $\phi = r\psi$, one can calculate the difference in the norm equation (B.4) by

$$\Delta Q_{s,s'} = \int_0^{R_c} \Delta Q_{s,s'}(r), \tag{2.78}$$

where

$$\Delta Q_{s,s'}(r) = \phi^*_s(r)\phi_{s'}(r) - \tilde{\phi}^*_s(r)\tilde{\phi}_{s'}(r), \tag{2.79}$$

which is a constraint in norm-conserving condition.

To relax this constraint, which means that the equation (2.79) is non-null, means that each all-electron wavefunction can be made into a smooth pseudo-wavefunction, $\tilde{\psi}_s$, with the only constraint being the matching of $\tilde{\psi}(R_c) = \psi(R_c)$ at the cutoff radius R_c [104]. This enables to choose the cutoff far beyond the radial wavefunction maximum. Thus, a new non-local potential that operates on $\tilde{\psi}_{s'}$ can now be defined as

$$\delta \hat{V}^{US}_{NL} = \sum_{s,s'} D_{s,s'} |\beta_s\rangle \langle \beta_{s'}|, \tag{2.80}$$

where

$$D_{s,s'} = B_{s,s'} + \epsilon_{s'} \Delta Q_{s,s'}. \tag{2.81}$$

[12] From now on, the superscripts PS and σ, and the subscripts l, m will be omitted for simplicity.

Thus, for each reference atomic state s, the smooth functions $\tilde{\psi}_s$ are solution of the generalized eigenvalue problem:

$$\left[\hat{H} - \epsilon_s \hat{S}\right] \tilde{\psi}_s = 0, \tag{2.82}$$

with $\hat{H} = -\frac{1}{2}\nabla^2 + V_{local} + \delta\hat{V}_{NL}^{US}$, and $\hat{S}$ is an overlap operator:

$$\hat{S} = \hat{\mathbf{1}} + \sum_{s,s'} \Delta Q_{s,s'} |\beta_s\rangle\langle\beta_{s'}|, \tag{2.83}$$

which is non-unitary except only inside the core region. The eigenvalues ϵ_s agree with the all-electron calculations for each s. Thus, it is possible to choose R_c much large than that of the norm-conserving pseudopotential to reache the desired accuracy by adding both the functions $\Delta Q_{s,s'}(r)$ and overlap operator $\hat{S}$.

In calculations using ultrasolf pseudopotential, the smooth functions, $\tilde{\psi}_i(\mathbf{r})$, have the following orthonormalization condition:

$$\langle\tilde{\psi}_i|\hat{S}|\tilde{\psi}_{i'}\rangle = \delta_{i,i'}. \tag{2.84}$$

The valence density is defined as

$$n_v(\mathbf{r}) = \sum_{i}^{occ} \tilde{\psi}_i^*(\mathbf{r})\tilde{\psi}_{i'}(\mathbf{r}) + \sum_{s,s'} \rho_{s,s'} \Delta Q_{s,s'}(\mathbf{r}), \tag{2.85}$$

where

$$\rho_{s,s'} = \sum_{i}^{occ} \langle\tilde{\psi}_i|\beta_{s'}\rangle\langle\beta_s|\tilde{\psi}_i\rangle, \tag{2.86}$$

to compensate the charge shortfall, and whose integral gives the number of valence electrons in the unit cell.

Through the variational theory, the solution is found by minimizing the total energy:

$$E_{total} = \sum_{i}^{occ} \langle\tilde{\psi}_i| -\frac{1}{2}\nabla^2 + V_{local}^{ion} + \sum_{s,s'} D_{s,s'}^{ion} |\beta_s\rangle\langle\beta_{s'}||\tilde{\psi}_i\rangle + E_{Hartree}\left[n_v\right] + E_{ion-ion} + E_{xc}\left[n_v + n_c\right], \tag{2.87}$$

with the normalization condition given by (2.84)[13], and n_c is the frozen-core density included to improve transferability [104, 105].

[13] Also, a non-linear core correction in E_{xc} can be added, as can be done in other methods

The generalized eigenvalue problem can be achieved by defining the "unscreening" bare ion pseudopotential as $V_{local}^{ion} \equiv V_{local} - V_{Hxc}$, where $V_{Hxc} = V_H + V_{xc}$, and similarly $D_{s,s'}^{ion} \equiv D_{s,s'} - D_{s,s'}^{Hxc}$, with

$$D_{s,s'}^{Hxc} = \int d\mathbf{r}\, V_{Hxc}(\mathbf{r})\, \Delta Q_{s,s'}(r), \tag{2.88}$$

whereby we get to

$$\left[-\frac{1}{2}\nabla^2 + V_{local} + \delta\hat{V}_{NL}^{US} - \epsilon_i \hat{S}\right] \tilde{\psi}_i = 0, \tag{2.89}$$

where $\delta\hat{V}_{NL}^{US}$ is given by the sum over ions of (2.80).

2.5.2 Projected Augmented Waves (PAW) Method

This method was developed in the 1990's [94,97,98], but here we will stick together the reference [94] in order to sketch the basic idea of the PAW method for an atom. Later, we will discuss the developments for molecules and solids.

The PAW method reformulates the OPW method, using, like the ultrasoft one, projectors and auxiliary localized functions in order to calculate energy, forces, and stress. It is also an approach to efficiently solve the generalized eigenvalue problem in (2.89). Since the PAW approach keeps the full all-electron wavefunction similarly to OPW-like basis functions (refer to equation (A.1)), and that it varies rapidly near the nucleus, all integrals are evaluated as a combination of integrals of smooth functions extending thoughout the space, along with localized contributions, evaluated by radial intergation. As in the OPW formulation, one can define a smooth part of a valence wavefunction, $\tilde{\psi}_i^v(\mathbf{r})$[14], and a linear transformation, $\psi^v = \mathcal{T}\tilde{\psi}^v$, which relates the set of all-electron valence functions, $\psi_j^v(\mathbf{r})$, to the smooth functions $\tilde{\psi}_i^v(\mathbf{r})$. Henceforward, we will assume the ψ's are all valence states, omitting the labels v, i, and j.

The mentioned tranformation is assumed to be unitary, except on a sphere centered on the nucleus, namely $\mathcal{T} = 1 + \mathcal{T}_0$. In the Dirac notation, within each sphere called augmentation region Ω_R, the expantion of the smooth function $|\tilde{\psi}\rangle$ in plane waves m can be written as

$$|\tilde{\psi}\rangle = \sum_m c_m |\tilde{\psi}_m\rangle, \quad \text{within } \Omega_R, \tag{2.90}$$

with the corresponding all-electron function

$$|\psi\rangle = \mathcal{T}|\tilde{\psi}\rangle = \sum_m c_m |\psi_m\rangle. \tag{2.91}$$

[14] It can be a plane wave (equation (A.1)) or an atomic orbital (as in (A.4)).

Thus, doing the proper substitution, the full wavefunction in all space would be

$$|\psi\rangle = |\tilde{\psi}\rangle + \sum_m c_m \left\{ |\psi_m\rangle - |\tilde{\psi}\rangle \right\}, \tag{2.92}$$

with the same form as the equations (A.4) and (A.8).

The coefficients must be defined as an inner product on each sphere with projector functions $|\tilde{p}_m\rangle$. Since $\mathcal{T}$ is a linear transformation:

$$c_m = \langle \tilde{p}_m | \tilde{\psi} \rangle, \tag{2.93}$$

The core-center expansion $\sum_m |\tilde{\psi}_m\rangle\langle\tilde{p}_m|\tilde{\psi}\rangle$ equals itself if the projection operator satisfy the biorthogonality condition:

$$\langle \tilde{p}_m | \tilde{\psi}_{m'} \rangle = \delta_{m,m'}. \tag{2.94}$$

This biorthogonalization means that the projectors and the smooth wavefunctions are laid on different Hilbert spaces.

Thus, the full all-electron wavefunctions is comprised into the transformation $\mathcal{T}$ as

$$\mathcal{T} = \mathbf{1} + \sum_m \left\{ |\psi_m\rangle - |\tilde{\psi}_m\rangle \right\} \langle \tilde{p}_m |, \tag{2.95}$$

such that it can be equally applied to both the core and the valence states. So, to set things forth properly, the transformation $\mathcal{T}$ is established by three quantities:

1. A set of all-electron partial functions, $|\psi_m\rangle$.
2. A set of partial pseudo-wavefunctions, $|\tilde{\psi}_m\rangle$.
3. A set of projector functions, $|\tilde{p}_m\rangle$.

There are many possible choices for the projectors, but the most important is that the transformation $\mathcal{T}$ involves all-electron wavefunctions. Besides, outside the region Ω_R the partial pseudo-wavefuntion are the same as partial all-electron wavefunction, as one can see in the figure 2.4. Inside the sphere, in turn, they can be any continuous, smooth function, such as a linear combination of polynomial or Bessel functions.

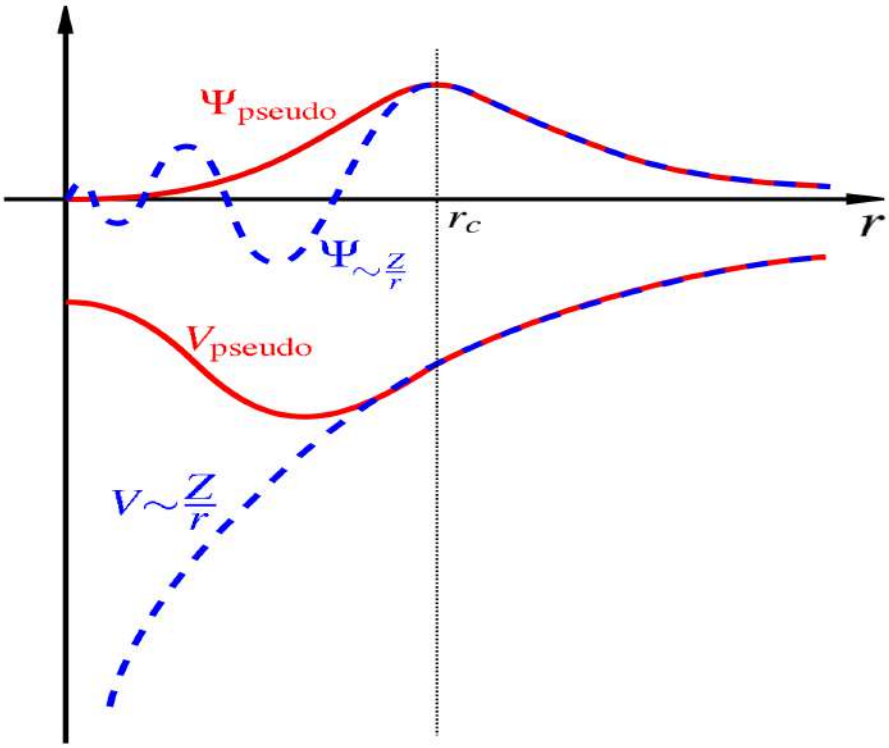

Figure 2.4: Schematic comparison between the wavefunction under the Coulomb potential (blue dashed curve) and under the pseudopotential (red curve). From the chosen cutoff radius, both the full and pseudo wavefunctions, and potentials match themselves up.

For any all-electron operator $\hat{A}$, the equations in PAW method can work as transformations onto $\hat{A}$ so that the resulted operator $\tilde{A}$ operates on the smooth part of the wavefunctions:

$$\tilde{A} = \mathcal{T}^\dagger \hat{A} \mathcal{T} = \hat{A} + \sum_{mm'} |\tilde{p}_m\rangle \left\{ \langle \psi_m | \hat{A} | \psi_{m'} \rangle - \langle \tilde{\psi}_m | \hat{A} | \tilde{\psi}_{m'} \rangle \right\} \langle \tilde{p}_{m'} |, \tag{2.96}$$

which is similar to the separable form (B.19). The total energy, for instance, can be evaluated directly as a functional of the pseudo-wavefunctions, whose modified Kohn-Sham equation can be read as

$$\mathcal{T}^\dagger \hat{H} \mathcal{T} |\tilde{\psi}_i\rangle = \epsilon_i \mathcal{T}^\dagger \mathcal{T} |\tilde{\psi}_i\rangle. \tag{2.97}$$

In addition, there is an additional degree of freedom to add a term of the form:

$$\hat{B} - \sum_{mm'} |\tilde{p}_m\rangle \langle \tilde{\psi}_m | \hat{B} | \tilde{\psi}_{m'} \rangle \langle \tilde{p}_{m'} |, \tag{2.98}$$

to the right side of (2.96) with no change in the expectation value[15]. This freedom is justified when the operator $\hat{A}$ cannot be easily evaluated in a plane-wave expansion. For example, one can remove the Coulomb singularity at the nucleus site for the smooth function, leaving a term that can be dealt with the radial equations about the nucleus, which is less sensitive to a truncation of the number of plane waves.

[15] $\hat{B}$ is an arbitrary operator that is localized within the augmentation region.

Physical quantities in the PAW approach are structured from equations (2.95) and (2.96). The density, for instance, which is the expectation value of the real-space projector operator $|\mathbf{r}\rangle\langle\mathbf{r}|$, is given by

$$n(\mathbf{r}) = \tilde{n}(\mathbf{r}) + n^1(\mathbf{r}) - \tilde{n}^1(\mathbf{r}), \tag{2.99}$$

which can be written in terms of eigenstates labels i with occupations f_i as

$$\tilde{n}(\mathbf{r}) = \sum_i f_i |\tilde{\psi}_i(\mathbf{r})|^2, \tag{2.100}$$

$$n^1(\mathbf{r}) = \sum_i f_i \sum_{mm'} \langle\tilde{\psi}_i|\tilde{\psi}_m\rangle \psi^*_m(\mathbf{r})\psi_{m'}(\mathbf{r})\langle\tilde{\psi}_{m'}|\tilde{\psi}_i\rangle, \tag{2.101}$$

and

$$\tilde{n}^1(\mathbf{r}) = \sum_i f_i \sum_{mm'} \langle\tilde{\psi}_i|\tilde{\psi}_m\rangle \tilde{\psi}^*_m(\mathbf{r})\tilde{\psi}_{m'}(\mathbf{r})\langle\tilde{\psi}_{m'}|\tilde{\psi}_i\rangle. \tag{2.102}$$

These last two terms are localized around each atom, so that the integrals can be done in spherical coordinates.

Therefore, we can see that many aspects of the calculations are identical to pseudopotential calculation. However, since the localized functions keep all the informations on the core states, such as the OPW method, and are rapidly varying around them, augmentation regions around each nucleus help the integration within each sphere in spherical coordinates. That linear transfomation of the all-electron valence functions ψ^v, defined in the second paragraph of this subsection, is assumed to be a sum of non-overlapping atom-centered contribution $\mathcal{T} = \mathbf{1} + \sum_{\mathbf{R}} \mathcal{T}_{\mathbf{R}}$, each localized on a sphere denoted $\Omega_{\mathbf{R}}$. Using the same definitions for smooth wavefunctions and all-electron wavefunction as the equations (2.90) and (2.91), respectively, but now with expansions in spherical harmonics inside each sphere, one has:

$$|\psi\rangle = |\tilde{\psi}\rangle + \sum_{\mathbf{R}m} c_{\mathbf{R}m} \left\{ |\psi_{\mathbf{R}m}\rangle - |\tilde{\psi}_{\mathbf{R}m}\rangle \right\}. \tag{2.103}$$

The biorthogonal projectors, $\langle\tilde{p}_{\mathbf{R}m}|$ in each sphere are the same as in (2.94) since the spheres are non-overlapped.

Still, it is particularly importate to have the PAW form of the total energy. Following [97], the exact Kohn-Sham density functional is

$$E_{total} = \sum_i f_i \langle\psi_i| - \frac{1}{2}\nabla|\psi_i\rangle + E_H[n + n_Z] + E_{xc}[n], \tag{2.104}$$

where $E_H[n+n_Z]$ is the Hartree energy of the electronic charge density n and the point charge densities of the nuclei n_Z, $E_{xc}[n]$ is the electronic exchange-correlation energy, and f_i are the orbital occupation numbers. Also, now, the index i is a shorthand for the atomic site $\mathbf{R}$ and the angular momentum (l,m). As one can see, the total energy can be split up into three terms:

$$E_{total} = \tilde{E}_{total} + E^1_{total} - \tilde{E}^1_{total}, \tag{2.105}$$

where, usign the definitions (2.92) and (2.93), and the densities (2.99)–(2.102),

$$\tilde{E}_{total} = \sum_i f_i \langle \tilde{\psi}_i | -\frac{1}{2}\nabla | \tilde{\psi}_i \rangle + E_{xc}[\tilde{n}+\hat{n}+\tilde{n}_c] + E_H[\tilde{n}+\hat{n}] + \int v_H[\tilde{n}_{Z_c}]\big[\tilde{n}(\mathbf{r})+\hat{n}(\mathbf{r})\big]d\mathbf{r} + U(\mathbf{R}, Z_{ion}), \tag{2.106}$$

$$\tilde{E}^1_{total} = \sum_{m,m'} \rho_{mm'} \langle \tilde{\psi}_m | -\frac{1}{2}\nabla | \tilde{\psi}_{m'} \rangle + \overline{E_{xc}[\tilde{n}^1+\hat{n}+\tilde{n}_c]} + \overline{E_H[\tilde{n}^1+\hat{n}]} + \int_{\Omega_{\mathbf{R}}} v_H[\tilde{n}_{Z_c}] \left\{ \tilde{n}^1(\mathbf{r}) + \hat{n(\mathbf{r})} \right\} d\mathbf{r}, \tag{2.107}$$

$$E^1_{total} = \sum_{m,m'} \rho_{mm'} \langle \psi_m | -\frac{1}{2}\nabla | \psi_{m'} \rangle + \overline{E_{xc}[n^1+n_c]} + \overline{E_H[n^1]} + \int_{\Omega_{\mathbf{R}}} v_H[\tilde{n}_{Z_c}] n^1(\mathbf{r}) dr. \tag{2.108}$$

where $\rho_{mm'}$ are the occupancies of each augmentation channel (m,m') at each site, and they are calculated from the pseudo-wavefunctions applying the projector functions:

$$\rho_{mm'} = \sum_i f_i \langle \tilde{\psi}_i | \tilde{p}_m \rangle \langle \tilde{p}_{m'} | \tilde{\psi}_i \rangle. \tag{2.109}$$

Also, $n_{Z_c} = n_Z + n_c$, where n_Z is the point charge density of the nuclei, and n_c is the frozen core all-electron charge density. The electrostatic potential, v_H, which is a density functional, is given by

$$v_H[n](\mathbf{r}) = \int \frac{n(\mathbf{r}')}{|\mathbf{r}-\mathbf{r}'|} d\mathbf{r}', \tag{2.110}$$

whose electrostatic energy is

$$E_H[n] = \frac{1}{2} \int d\mathbf{r} \int d\mathbf{r}' \, \frac{n(\mathbf{r}) n(\mathbf{r}')}{|\mathbf{r}-\mathbf{r}'|}. \tag{2.111}$$

2.6 Supercell Approximation

In perfect crystal systems, to construct the unit cell, we need to provide both the Bravais lattice and the atomic positions (and/or an atomic basis). Respecting the periodic boundary conditions (PBC),

the crystal is generated by repetitions of the unit cell towards all crystallographic directions. We have made use of both the free software XCRYSDEN [106], which stands for X-windown CRYstalline Structures and DENsities, and also the free program Avogadro [107], which are softwares appointed to visualize crystalline and molecular structures, as well as isosurfaces and contourn on the unit cell, and to edit, design and modeling systems, respectively.

The question that arises is: How can we describe non-periodic systems? Such systems can be regarded to "mimic" real, nearly natural systems, for example, defective systems, nanoribbons, problems between interfaces, oxidation "processes", among others. In our case, our defective system is a simulation of a core-hole deep inside an atom. So, to address this system we need to use the supercell approximation, which means that instead of using a bare, pristine unit cell, we will work on a larger unit cell, so that the atom with a core-hole stands about 7.6 Å from their images. Thus, this suppercell is replicated in all other directions so that if the cell size is large enough, then the interactions between defective atoms from neighboring cells could be neglected.

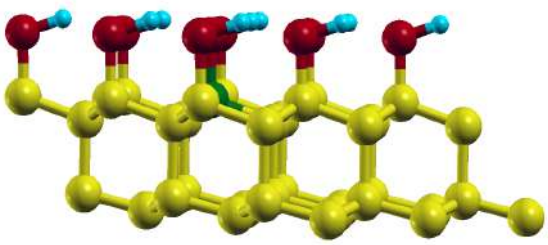

(a)

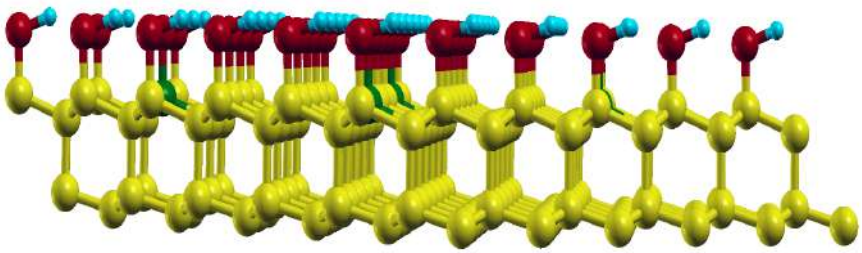

(b)

Figure 2.5: (a): Diamondol supercell with core-hole carbon atom hilighted (green sphere). The hydroxyl groups found themselves bonded to carbon atoms forming dangling bonds. (b): Repetition of the supercell on its in-plane directions, which must represent a real system fairly enough. Each highlighted carbon atom is about 7.6 Å away from the image of the first neighbor. Hydrogen, oxygen, and carbon atoms, except for the core-hole one, are colored as blue, red, and yellow spheres.

Although this is an approximation for studying of both physical and chemical properties of systems, we can think of it as an idealization of what occurs in nature when a high-energy beam shines on a material, for instance. Also, if we think of an exfoliation process, the exfoliated material probably will present a few type of defects in it. Another important consideration concerns the vacuum region.

This “empty” space avoids charge transfer between the surface and its image, which could generate a non-physical electric field inside. Figure 2.5(a) shows a diamondol supercell with a core-hole carbon atom (highlighted) bonded to the hydroxyl group. The figure 2.5(b), in turn, pictures us this supercell repeated on its in-plane directions. The figure 2.6 pictures the mentioned vacuum region.

Taking into account these considerations, it is worth to make an important remark. Since we are dealing with larger cells than those pristine ones, it is to be expected that the corresponding Brillouin Zones are smaller. That leads to the folding process, and it works for any system symmetry. This is useful, for example, to understand the band structure of a supercell with a particular type of defect in a simpler BZ.

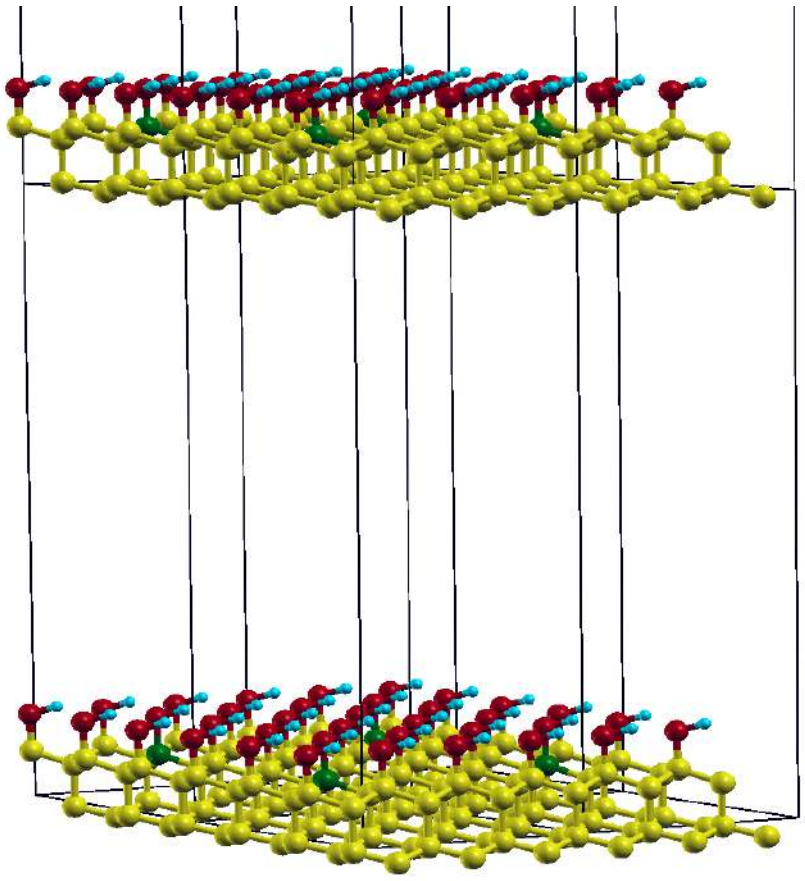

Figure 2.6: Periodicity of the supercell on the direction perpendicular to the surface of the material. The uppermost hydrogen atoms are about 20 Å away from the most lower carbon atom in the neighbor image.

Chapter 3

X-Ray Absorption Spectroscopy

When an electromagnetic ray is absorbed by some material, either in solid or in gasoseous states, or even in liquid state, an energy transfer may occur implying physical, chemical or biological modification. In fact, this kind of information can be used to probe materials. Depending on the type and the thickness of the material, and also, surely, both on the ray energy and on its polarization, absorption will (or will not) be stronger. The photon in the X-ray spectrum can have wavelengths from 0.03 to 3 nanometers, which corresponds to energy range from 100 eV to 200 keV. More specifically, we can subdivide it into two categories: the hard X-rays (below 0.2–0.1 nm, and above 5–10 keV), and those with lower energy and longer wavelengths, which are called soft X-rays [108]. It turns out that when such a photon is absorbed by an atom, there can be a transition of a core electron up to some level, occupying a free orbital or, even, a continuum state [36]. This core electron in this process is now called *photoelectron*. As this phenomenon is local and centered around an *absorbing* atom and possibly depending on its close sorroundings, the corresponding spectroscopy can be applied to any kind of samples, whether ordered or unordered [36].

The study of X-ray absorption versus X-ray energy is named X-Ray Absorption Spectroscopy (XAS). A sudden increase in the absorption probability at a given energy value is called absorption edge, which may chiefly depend on the atomic number of the absorbing atom. Spectra, in general, can cover thousands of electron volts. Focusing on the part of a spectrum at energies larger than 30–50 eV above the edge means that one is making an Extended X-Ray Absorption Fine Structure (EXAFS) study. In this case, the photoelectron has been cast to a free or continuum state. Its analysis depends on the atomic arrangement and does not rely on the chemical bondings between the absorber and its neighbors, thus providing information about the coordination number, interatomic distances, and structural information, being a powerful tool for structural analysis [109]. The region in the lowest part of the spectra, typically the first 50 electron volts, is known as X-Ray Absorption Near Edge Structure (XANES) or Near-Edge X-Ray Absorption Fine Structure (NEXAFS). It has a complicated shape as it is sensitive to chemical bonds, exhibiting, for instance, characteristic features for different oxidation states of the absorbing atom [109], for the photoelectron is promoted to unoccupied bound states. Often, theoretical analysis are compared to the experimental ones in order to study different phases of a crystal, for example. The figures 3.1(a)

and 3.1(b) are a small portrait of this phonomenon.

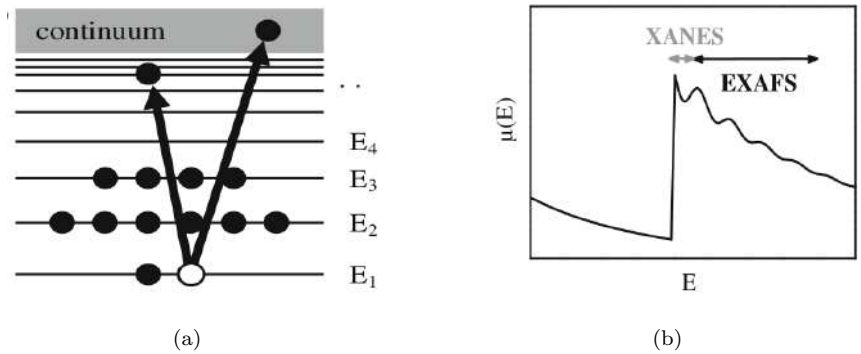

Figure 3.1: (a) A representation scheme of the absorption process. The labels E_1, E_2, etc, on the right-hand side of the figure are the energy levels the electrons are occupying. The Fermi level is not shown here. (b) Absorption coefficient $\mu(E)$ or absorption probability, as written in the text, as a function of the photon energy E. It is also shown the edge (prominent peak), followed by the fine structure regions. Figures extracted from [109], chapter 1.

Being so, we would like to concentrate our efforts on understanding the latter of these two regions of the spectra. As one can notice, the part of the spectrum are very close to the other one, so that the EXAFS theory can be seen as an approximation of the XANES formulation [36]. Thus, the next section will explain the X-ray absorption phenomenon. Subsequently, we will go over the basics of quantum mechanics along with the derivation of the absorption cross-section expression. Thereafter, we will discuss the implementation in DFT, which encompass some techniques [39, 41, 110], along with the GIPAW [111] method, Lanczos method [112], and the recursion method [113–115].

3.1 The X-Ray Absorption Phenomena

Consider the figure 3.2(a) below. Let the sample be a homogeneous isotropic material of thickness t, over which someone launches a X-ray beam of intensity I_0 and energy E. The transmitted beam intensity I_t obbeys the Beer-Lamber law, $ln\,(I_0/I_t) = \mu(E)t$, and decrease exponentially as

$$I_t = I_0 e^{-\mu(E)t}, \tag{3.1}$$

where $\mu(E)$ is the energy-dependent absorption coefficient. For a crystalline solid, it is related to the absorption cross-section, σ_i, of the n different chemical elements of the unit cell:

$$\mu(E) = \frac{1}{V}\sum_{i}^{n}\sigma_i, \tag{3.2}$$

where V is the volume of the unit cell.

,

The energy dependence of the photoelectron absorption cross-section for the interaction of X-rays with a gold foil can be seen in figure 3.2(b). There are three peaks: L_1, L_2, and L_3. These ridges represent the edges of the element that composes the foil. Each peak has nearby oscillations, which have copious information on the vicinity of the absorbing atoms. On the label edges, the letter refers to the principal quantum number n, where the core electron initially is. So, K, L, M, N, O mean $n = 1, 2, 3, 4, 5$, respectively. The subscript of each edge reads as follows: the index 1 is for $\ell = 0$; it is 2 or 3 for $\ell = 1$, and finally, 4 and 5 for $\ell = 2$. The K-edge has energy from 13.6 eV in Hydrogen up to 115.6 keV in Uranium. For $\ell > 1$, the edges are split into two because of the high spin-orbit effect in core states [36]. Sometimes one can observe shifts in the signature of a chemical specie. This is related to the chemical environment in which the absorbent is. The more the oxidation increases, the more the edge tends to shift toward higher energy up to some electron volts. That is important to check the valence state of the atom.

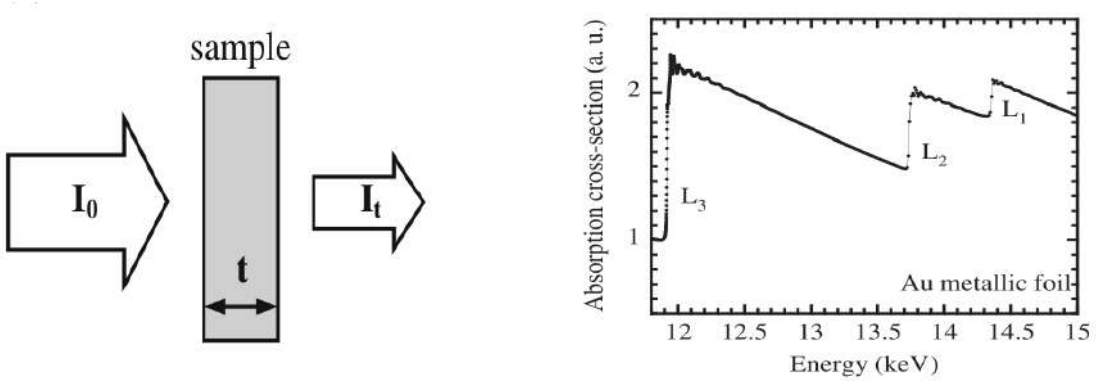

(a) (b)

Figure 3.2: (a) A rough demonstration of the t-thickness sample shined by an incident X-ray beam of intensity I_0. The transmitted intensity I_t is also shown. Credits to [109] (found on page 3). (b) Experimental results by [116] of XAS of Au metallic foil. The huge increase in the absorption cross-section reveals a specific value of the chemical element of the sample. This is the edge. Note that the L_3 edge is about two times higher than the L_2 edge. Figure obtained from [36], chapter 4.

3.2 X-Ray Absorption Cross-Section

In non-relativistic quantum theory in the one-electron framework, a particle with charge q, mass m, gyromagnetic factor g (≈ 2 for electrons) and spin s under a potential $V(\mathbf{r})$, submitted to an external electromagnetic field $(\Phi(\mathbf{r}, t), \mathbf{A}(\mathbf{r}, t))$ is described by the Hamiltonian[1]

$$H = \frac{1}{2m}\left[-i\hbar\boldsymbol{\nabla} - q\mathbf{A}\right]^2 + V(\mathbf{r}) + q\Phi - \left(\frac{gq}{2m}\right)\mathbf{s}\cdot\mathbf{B}, \tag{3.3}$$

[1] To keep consistence with the reference [40], we will use SI units, differently of the chapter 2.

$$H = H_0 + \left(\frac{i\hbar q}{m}\right)\mathbf{A}\cdot\boldsymbol{\nabla} + \left(\frac{i\hbar q}{2m}\right)(\boldsymbol{\nabla}\cdot\mathbf{A}) + \left(\frac{q^2}{2m}\right)A^2 + q\Phi - \left(\frac{gq}{2m}\right)\mathbf{s}\cdot\mathbf{B}, \tag{3.4}$$

where

$$H_0 = -\left(\frac{\hbar^2}{2m}\right)\nabla^2 + V(\mathbf{r}). \tag{3.5}$$

Considering the exciting electromagnetic field as a plane wave in the Coulomb gauge, $\Phi = 0$ and $\boldsymbol{\nabla}\cdot\mathbf{A} = 0$[2]. Thus, $\boldsymbol{\nabla}$ and $\mathbf{A}$ can be considered as commutating operators. Besides, the term $\propto A^2$ is too small for the available X-ray sources [40]. If $I_0(\omega) = (1/2)\epsilon_0 c A^2\omega^2$ is the intensity of a monochromatic X-ray coming from the source, then the ratio of the quadratic term over the linear one is

$$\left|\frac{q^2A^2/2m}{\hbar q\mathbf{A}\cdot\boldsymbol{\nabla}/m}\right| \sim \frac{|qa_0A|}{2\hbar} = \left(\frac{\sqrt{I_0(\omega)}}{\omega}\right)a_0\sqrt{\frac{2\pi\alpha}{\hbar}}, \tag{3.6}$$

where the electron momentum, $|i\hbar\boldsymbol{\nabla}|$ is approximated by $\hbar/a_0$, where a_0 is the Bohr radius. In fact, it was shown in 1984 [117] that a flux of 10^8 photons per second at 9 keV within a 6 mm^2 beam spot, so that $I_0(\omega) \simeq 2.4\times10^{-2}\,W\,m^{-2}$ and $\omega \simeq 1.4\times10^{19}\,s^{-1}$, yields a ratio of about 10^{-14}. It is rather small so the quadratic term can be neglected.

Therefore, we are left with

$$H = H_0 + \left(\frac{i\hbar q}{m}\mathbf{A}\cdot\boldsymbol{\nabla} - \frac{gq}{2m}\mathbf{s}\cdot\mathbf{B}\right). \tag{3.7}$$

The incident plane wave can be written as

$$\mathbf{A}(\mathbf{r},t) = A_0\hat{\varepsilon}e^{[i(\mathbf{k}\cdot\mathbf{r}-\omega t)]} + A_0\hat{\varepsilon}^*e^{[-i(\mathbf{k}\cdot\mathbf{r}-\omega t)]} \tag{3.8}$$

where $\hat{\varepsilon}$ is the polarization vector, $\mathbf{k}$ is the X-ray wavevector, and $\sqrt{2}A_0$ the vector potential amplitute. According to time-dependent perturbation theory, the transition probability per unit of time for a harmonic perturbation $W(t)$, as that of the equation (3.8), is [118]

$$w = \frac{2\pi}{\hbar}\sum_f |\langle f|W|i\rangle|^2\,\delta(E_f - E_i - \hbar\omega). \tag{3.9}$$

Since we have $\mathbf{B} = \boldsymbol{\nabla}\times\mathbf{A}$, then

$$w = \left(\frac{2\pi q^2|A_0|^2}{\hbar m^2}\right)\sum_f \left|\langle f|e^{i(\mathbf{k}\cdot\mathbf{r})}\left\{\hbar\hat{\varepsilon}\cdot\boldsymbol{\nabla} - (g/2)\mathbf{s}\cdot(\mathbf{k}\times\hat{\varepsilon})\right\}|i\rangle\right|^2 \times \delta(E_f - E_i - \hbar\omega). \tag{3.10}$$

[2]You may refer to the appendix C to brush up on this topic.

The absorption cross-section $\sigma(\omega)$ is defined as the ratio of the rate at which energy is removed from the photon beam by the the photoelectric effect ($w\hbar\omega$), divided by the rate at which energy in the photon beam crosses a unit area perpendicular to its propagation direction:

$$I(\omega) = 2\epsilon_0 c|A_0|^2\omega^2. \tag{3.11}$$

Therefore,

$$\sigma(\omega) = \left(\frac{4\pi^2\hbar\alpha}{m^2\omega}\right)\sum_f \left|\langle f|e^{i(\mathbf{k}\cdot\mathbf{r})}\left\{\hbar\hat{\varepsilon}\cdot\boldsymbol{\nabla} - (g/2)\mathbf{s}\cdot(\mathbf{k}\times\hat{\varepsilon})\right\}|i\rangle\right|^2 \times \delta(E_f - E_i - \hbar\omega), \tag{3.12}$$

where $\alpha = q^2/2\epsilon_0 hc = \frac{1}{137}$ is the fine structure constant. The sum over electrons coordinates and spins is tacit since both $|i\rangle$ and $|f\rangle$ are many-electron wavefunctions.

Since the deepest electronic level is located in the 1s orbital of an atom with effective atomic number Z_{eff}, the mean radius of this orbital is a_0/Z_{eff}. So, as the wavelength of the radiation field is far longer than the atomic dimension [119], a fair description of core-level absorption is given by the first terms of the multipole expansion of the term $exp\,[i(\mathbf{k}\cdot\mathbf{r})]$ in equation 3.12. Thus, the transition amplitude with electric dipole, electric quadrupole, and magnetic dipole contibutions is given through the Taylor expansion around $\mathbf{k}\cdot\mathbf{r}\sim 0$:

$$exp\,[i(\mathbf{k}\cdot\mathbf{r})] \simeq 1 + i\mathbf{k}\cdot\mathbf{r} + \cdots . \tag{3.13}$$

One can see that, using the equation of motion of $\mathbf{p}$

$$\mathbf{p} = -i\hbar\boldsymbol{\nabla} = \frac{m}{i\hbar}\left[\mathbf{r}, H_0\right], \tag{3.14}$$

by putting the equation (3.13) in the equation (3.12), the electric dipole matrix elements is

$$\langle f|\hbar\hat{\varepsilon}\cdot\boldsymbol{\nabla}|i\rangle = -\left[\frac{m(E_f - E_i)}{\hbar}\right]\langle f|\hat{\varepsilon}\cdot\boldsymbol{\nabla}|i\rangle. \tag{3.15}$$

Needless to say that both $|i\rangle$ and $|f\rangle$ have to be exact wavefunctions.

Using the following identity [120]:

$$\hbar(\mathbf{k}\cdot\mathbf{r})(\hat{\varepsilon}\cdot\boldsymbol{\nabla}) = \frac{m}{2\hbar}\left[(\hat{\varepsilon}\cdot\mathbf{r})(\mathbf{k}\cdot\mathbf{r}), H_0\right] + \frac{i}{2}(\mathbf{k}\times\hat{\varepsilon})\cdot\mathbf{L}, \tag{3.16}$$

where $\mathbf{L}$ is the angular momentum operator, the transition amplitude for the electric quadrupole term can be obtained. With those terms, the matrix element in (3.12) becomes

$$-\left[\frac{m(E_f-E_i)}{\hbar}\right]\langle f|\hat{\varepsilon}\cdot\mathbf{r}|i\rangle - i\left[\frac{m(E_f-E_i)}{2\hbar}\right]\langle f|(\hat{\varepsilon}\cdot\mathbf{r})(\mathbf{k}\cdot\mathbf{r})|i\rangle - \frac{1}{2}\langle f|(\mathbf{k}\times\hat{\varepsilon})\cdot(\mathbf{L}+g\mathbf{s})|i\rangle, \qquad (3.17)$$

where the first, second, and third terms are the electric dipole, electric quadrupole, and the magnetic dipole transition amplitudes, respectively.

Some aspects of the magnetic dipole term should be accounted for. First of all, it does not have a radial variable, so that if the radial part of the initial and final states are orthogonal, those matrix elements vanish. Secondly, the selection rule for one-electron magnetic dipole transitions, within an atom with spin-orbit $(L-S)$ coupling, are $|\Delta j| \leqslant 0$, $\Delta l = 0$, $\Delta s = 0$, and, $\Delta n = 0$. This means that magnetic dipole absorption occurs at low energies, which means that it would be necessary that the initial and the final states could have a appreciable L-S interaction. However, even if it occurred, it would be neglected because of the large energy differences between the initial and the final states ($\sim 1\,keV$). Taking the one-electron initial state as centered on the absorbing atom, $\langle\mathbf{r}|i\rangle = \langle\mathbf{r}|nlm\rangle$, it does not overlap the states of alike eigenenergies of the neighboring atoms. Also, because these states corresponding to core-level states, all the states corresponding to all values of m are occupied, and the final states $|f\rangle$ are orthogonal to $|nlm\rangle$ for all m. Then, since $\mathbf{L}|nlm\rangle$ are a linear combination of $|nlm-1\rangle$, $|nlm\rangle$, and $|nlm+1\rangle$, which are orthogonal to $|f\rangle$, the terms $\langle f|(\mathbf{k}\times\hat{\varepsilon})\cdot\mathbf{L}|i\rangle = (\mathbf{k}\times\hat{\varepsilon})\cdot\langle f|\mathbf{L}|nlm\rangle = 0$. At last, magnetic dipole trasitions can occur for heavy atoms because $\Delta n = 0$ can be broken due to relativistic effects [121,122]. In case of hafnium (Z=32) [123,124], from the absorption cross-section in the K- and L_1-edges, a changing of the electric dipole density of $5\times10^{-4}\,Ryd^{-1}$ and $10^{-3}\,Ryd^{-1}$ are obtained, respectively. Also the ratio between the magnetic and electric dipoles for hafnium K- and L_1-edges are 2×10^{-4} and 10^{-5}, respectively. Therefore, the magnetic dipole contributions can be neglected, even if relativistic effects are taken into account.

According to foregoing exposed, only the electric and the quadrupole dipoles will contribute to the X-ray absorption spectra. Hence, the absorption cross-section will be

$$\sigma(\omega) = 4\pi^2\alpha\hbar\omega\sum_f\left\{|\langle f|\hat{\varepsilon}\cdot\mathbf{r}|i\rangle|^2 + (1/4)\,|\langle f|(\hat{\varepsilon}\cdot\mathbf{r})(\mathbf{k}\cdot\mathbf{r})|i\rangle|^2\right\}\delta(E_f-E_i-\hbar\omega). \qquad (3.18)$$

3.3 *Ab-initio* Calculation of XANES into a Pseudopotential Scheme

Once someone prepares a XAS experiment and obtains its results, they need to theoretically understand the spectral features of the outcomes. Before we discuss the methodological aspects of the XANES calculations, we would like to sketch the pratical way someone can perform such calculation. According to the user guide of the XSpectra [125], a code of the integrated suite Quantum Espresso [43] we used, to simulate core-effects, a pseudopotential for the photo-absorbing atom (considered as an impurity) with a hole in the core state needs to be generated. Afterwards, this atom is included in a

sufficient large supercell. As one can see from equation (3.18), the core states, $|i\rangle$, need to be a fully all-electron wavefunction. For that, the code uses GIPAW reconstruction of the absorbing atom under the electromagnetic field in order to provide the pseudopotential with those informations. XSpectra program can calculate electric dipole and quadrupole contribution for the spectra since one gets the charge density of the system. The spectrum is calculated using the recursion method as a continued fraction by the Lanczos method.

The choice of the method used to solve the Schrödinger equation for the initial and final states depends on the localized or delocalized character of the final state [39]. For strong electron-electron interaction, or that former type of final states, crystal field multiplet theory is needed ($L_{2,3}$ edges of transition metals and $M_{4,5}$ edges of rare earth). On the other side, for the latter type (K and L_1 edges), single-electron approach based on DFT is enough and commonly employed. Regarding single-electron methods, there are the cluster (real-space) approach and the band-structure (reciprocal-space) approach. The first one [126] is very time-consuming for clusters with up to 50 atoms, plus it is not a first principle approach. Considering the band-structure calculations, local projected density of empty states (LDOS) have been used to interpret XANES spectra [127–129]. Besides this method, there is also another method by Shirley [130], and Soininen and Shirley [131], which incorporate the core-hole interactions in the two-particle Bethe-Salpeter equation (BSE), which is a first principle technique. Nonetheless, in our case (K-edge XANES) the core-hole is frozen at one atomic site, so that the one-particle approach would suffice [39]. Moreover, that method only gives a description of the pre-edge region of the XAS spectra [41]. Bearing that in mind, the real issue now lives in the diagonalization of the Hamiltonian, which is limited by the computational cost of the calculation of several empty states for each **k**-point within the Brillouin zone. The way-out for that nuisance as pointed in [39] (whose work we will follow up next) is to use the recursion method devised by Haydock, Heine, and Kelly [113, 114, 132], which causes the XANES calculation time for large systems (supercell) rather smaller than the self-consistent charge density one.

3.3.1 PAW Formalism for XANES Calculation in the Impurity Model

To begin this discussion, the equation (3.18), and following [39], will be rewritten as

$$\sigma(\omega) = 4\pi^2 \alpha \hbar\omega \sum_f |M_{i\to f}|^2 \, \delta(E_f - E_i - \hbar\omega), \tag{3.19}$$

where $\hbar\omega$ is the incident photon energy, and M_i is the transition amplitude between the initial core state $|\psi_i\rangle$ with energy E_i at the absorbing atom site $\mathbf{R}_0$, and an all-electron final state $|\psi_f\rangle$ with energy E_f, which is

$$M_{i\to f} = \langle \psi_f | \mathcal{O} | \psi_i \rangle, \tag{3.20}$$

where $\mathcal{O} = \hat{\varepsilon} \cdot \mathbf{r}\,[1 + (i/2)\mathbf{k} \cdot \mathbf{r}]$. These two terms here are the electric dipole and the electric quadrupole,

respectively. Also $|\psi_i\rangle$ is a core-state that can be obtained from an all-electron ground-state atomic calculation. In fact, it is the state where there is no electronic core-hole in any atom of the system. The $|\psi_f\rangle$, in turn, is an excited empty state, solution of the Schrödinger equation for a potential that includes a core-hole on the absorbing atom [39], which is achieved in the framework of the PAW method.

In the section 2.5.2, we elaborated on PAW formalism. Here, we will only remind you about its essential aspects in order to better express $M_{i\to f}$. We can recall that the final state all-electron function $|\psi_f\rangle$ are related to the final pseudo wave functions $|\tilde{\psi}_f\rangle$ through

$$|\psi_f\rangle = \mathcal{T}|\tilde{\psi}_f\rangle, \tag{3.21}$$

where

$$\mathcal{T} = \mathbf{1} + \sum_{\mathbf{R},n} \left[|\phi_{\mathbf{R},n}\rangle - |\tilde{\phi}_{\mathbf{R},n}\rangle\right] \langle\tilde{p}_{\mathbf{R},n}|, \tag{3.22}$$

and is equal to identity only outside the augmentation region $\Omega_{\mathbf{R}}$ centered at each atom site $\mathbf{R}$. $|\phi_{\mathbf{R},n}\rangle$ and $|\tilde{\phi}_{\mathbf{R},n}\rangle$ are all-electron and pseudo partial waves, respectively. They are the same outside the region $\Omega_{\mathbf{R}}$. The projector functions $\langle\tilde{p}_{\mathbf{R},n}|$ are null outside $\Omega_{\mathbf{R}}$ and satisfies the orthonormality condition $\langle\tilde{p}_{\mathbf{R},n}|\tilde{\phi}_{\mathbf{R}',n'}\rangle = \delta_{\mathbf{R},\mathbf{R}'}\delta_{n,n'}$. Inside $\Omega_{\mathbf{R}}$, $|\phi_{\mathbf{R},n}\rangle$ form a complete basis for any all-electron wavefunction, so do $|\tilde{\phi}_{\mathbf{R},n}\rangle$ also form a complete basis for pseudowave functions $|\tilde{\psi}\rangle$, that is to say, for any $\langle\mathbf{r}|\chi_{\mathbf{R}}\rangle$ centered at $\mathbf{R}$ and null outside $\Omega_{\mathbf{R}}$:

$$\sum_n \langle\tilde{\psi}|\tilde{p}_{\mathbf{R},n}\rangle\langle\tilde{\phi}_{\mathbf{R},n}|\chi_{\mathbf{R}}\rangle = \langle\tilde{\psi}|\chi_{\mathbf{R}}\rangle. \tag{3.23}$$

Putting (3.22) in (3.21), and then (3.21) in (3.20) one gets

$$M_{i\to f} = \langle\tilde{\psi}_f|\mathcal{O}|\psi_i\rangle + \sum_{\mathbf{R},n}\langle\tilde{\psi}_f|\tilde{p}_{\mathbf{R},n}\rangle\langle\phi_{\mathbf{R},n}|\mathcal{O}|\psi_i\rangle - \sum_{\mathbf{R},n}\langle\tilde{\psi}_f|\tilde{p}_{\mathbf{R},n}\rangle\langle\tilde{\phi}_{\mathbf{R},n}|\mathcal{O}|\psi_i\rangle. \tag{3.24}$$

It has to be noticed that only the $\mathbf{R}_0$ term has to be considered in each sum, because $\langle\mathbf{r}|\psi_i\rangle$ is located at $\mathbf{R}_0$. Thus, the $\langle\mathbf{r}|\mathcal{O}|\psi_i\rangle$ is zero outside $\Omega_{\mathbf{R}_0}$. Moreover, using (3.23) for the third term in (3.24), it cancels with the first one, and $M_{i\to f}$ happens to be an one-term expression. Considering that, we define

$$|\tilde{\phi}_{\mathbf{R}_0}\rangle = \sum_n |\tilde{p}_{\mathbf{R}_0,n}\rangle\langle\phi_{\mathbf{R}_0,n}|\mathcal{O}|\psi_i\rangle. \tag{3.25}$$

In fact, there is an infinity number of projectors, nonetheless, in practical calculations, only a few of them are needed to perform a suitable calculation. Thus, with the support of equation (3.25), the next expression for the X-ray absorption cross-section is obtained:

$$\sigma(\omega) = 4\pi^2\alpha\hbar\omega \sum_f \left|\langle\tilde{\psi}_f|\tilde{\phi}_{\mathbf{R}_0}\rangle\right|^2 \delta(E_f - E_i - \hbar\omega). \tag{3.26}$$

This expression has a remarkable drawback: many empty states to be determined. The recursion method is a clever way to circumvent this issue, which permit us to write the absorption cross-section as a continued fraction. It means that only occupied bands need to be calculated.

3.3.2 The Recursion Method

This method is a powerful recursive algorithm that can be applied to Hermitian matrix to turn it into a tridiagonal form [113,114]. We will assume that the norm of the all-electron partial waves match the pseudopartial waves. However, as we will see shortly in the subsection 3.3.3, that is not always true.

A Green operator is required in order to use the recursion method:

$$\sum_f |\tilde{\psi}_f\rangle\delta(E_f - E_i - \hbar\omega)\langle\tilde{\psi}_f| = -\frac{1}{\pi}\Im\mathfrak{m}\left[\tilde{G}(E)\right], \tag{3.27}$$

with

$$\tilde{G}(E) = \left(E - \tilde{H} + i\gamma\right)^{-1} \tag{3.28}$$

which is the Green operator associated with the Hermitian pseudo-Hamiltonian $\tilde{H} = \mathcal{T}^\dagger H \mathcal{T}$ (refer to equation (2.97)), whose energy E is $E_i + \hbar\omega$, and γ is an infinitesimal positive number[3]. Thus, the equation (3.26) becomes

$$\sigma(\omega) = -4\pi\alpha\hbar\omega\,\Im\mathfrak{m}\left[\langle\tilde{\phi}_{\mathbf{R}_0}|\left(E - \tilde{H} + i\gamma\right)^{-1}|\tilde{\phi}_{\mathbf{R}_0}\rangle\right]. \tag{3.29}$$

As this equation has a pseudo-Hamiltonian, a new basis is required in order to give to $\tilde{H}$ a tridiagonal representation. The recursion method of Lanczos [112,134] sets up this basis, which makes the calculation of the matrix elements in (3.29) very simple. It is obtained by the successive action of $\tilde{H}$ onto the normalized initial vector $|u_0\rangle = |\tilde{\phi}_{R_0}\rangle/\sqrt{\langle\tilde{\phi}_{\mathbf{R}_0}|\tilde{\phi}_{\mathbf{R}_0}\rangle}$[4] through the following recurrence relation

$$\tilde{H}|u_i\rangle = a_i|u_i\rangle + b_{i+1}|u_{i+1}\rangle + b_i|u_{i-1}\rangle, \tag{3.30}$$

where $\{a_i\}$ and $\{b_i\}$ are a set of real parameters defined as [135]

$$a_i = \langle u_i|\tilde{H}|u_i\rangle, \tag{3.31}$$

$$b_i = \left|\tilde{H}|u_i\rangle - a_i|u_i\rangle - b_{i-1}|u_{i-1}\rangle\right|, \tag{3.32}$$

$$|u_{i+1}\rangle = b_i^{-1}\left(\tilde{H}|u_i\rangle - a_i|u_i\rangle - b_{i-1}|u_{i-1}\rangle\right). \tag{3.33}$$

[3] Please, refer to the section 2.3, equations 2.58-59 of [133].

[4] For tight-binding models, it can be any normalized linear combination of localized orbitals [114].

Thus, in the new basis $\{|u_i\rangle\}$, the matrix elements of (3.29) becomes

$$\langle\tilde{\phi}_{\mathbf{R}_0}|\left(\tilde{H}-E-i\gamma\right)^{-1}|\tilde{\phi}_{\mathbf{R}_0}\rangle=\cfrac{\left\langle\tilde{\phi}_{\mathbf{R}_0}\middle|\tilde{\phi}_{\mathbf{R}_0}\right\rangle}{a_0-E-i\gamma-\cfrac{b_1^2}{a_1-E-i\gamma-\cfrac{b_2^2}{\ddots}}} \tag{3.34}$$

One should be aware that a terminator is required to "stop" the continued fraction [135]. Indeed, if the calculation converge after N iteractions, then the coefficients (a_i, b_i) are equal to (a_N, b_N) for $i > N$. As one can see, N strongly depends on the broadening parameter γ. Therefore, this method becomes rather advantageous in face of the direct diagonalization of the equation (3.26), saving a great deal of computational time.

3.3.3 The USPP Scheme

Until now, we have seen a DFT approach using norm-conserving pseudopotentials [39] that permits the XAS calculation up to the far edge region. It also allows further for structural optimization around the absorbing atom in systems with defects or impurities in a supercell [41]. However, one knows that large cutoffs increase the computational time. Although this shortcoming is even more present in both transition metal and rare earth, ultrasoft pseudopotentials (USPP) may demand low cutoffs $(20-40\,Ry)$, as contrast to the norm-conserving ones, which would decrease the computational cost of the supercell calculation by one order of magnitude [41]. Therefore, following the just mentioned reference, we will remember the ultrasoft approach, followed by the reformulation of the continued fraction and the corresponding Lanczos approach.

As mentioned in the subsection 2.5.1, in the ultrasoft approach the norm of the pseudopartial waves is different from the norm of the corresponding all-electron partial waves, so that it is usual to define the integrated augmentation charges $q_{\mathbf{R},nm}$ as

$$q_{\mathbf{R},nm}=\langle\phi_{\mathbf{R},n}|\phi_{\mathbf{R},m}\rangle-\langle\tilde{\phi}_{\mathbf{R},n}|\tilde{\phi}_{\mathbf{R},m}\rangle. \tag{3.35}$$

We also should remember the $\hat{S}$ operator of equation (2.83):

$$\hat{S}=\mathbb{1}+\sum_{\mathbf{R},m,n}|\tilde{p}_{\mathbf{R},n}\rangle q_{\mathbf{R},nm}\langle\tilde{p}_{\mathbf{R},m}|=\mathbb{1}+\sum_{\mathbf{R}}Q_{\mathbf{R}}. \tag{3.36}$$

Now, the pseudo-Hamiltonian $\tilde{H}$ and the pseudo eigenfunctions $|\tilde{\psi}_f\rangle$ satisfy the Schrödinger equation

$$\tilde{H}|\tilde{\psi}_f\rangle=E_f\hat{S}|\tilde{\psi}_f\rangle, \tag{3.37}$$

which by being multiplied by $\hat{S}^{-1/2}$ becomes

$$\hat{S}^{-1/2}\tilde{H}\hat{S}^{-1/2}\hat{S}^{1/2}|\tilde{\psi}_f\rangle = E_f\hat{S}^{1/2}|\tilde{\psi}_f\rangle. \tag{3.38}$$

We will use the follow identity in order to obtain a expression for (3.34):

$$\pi\sum_f |\tilde{\psi}_f\rangle\delta(E_f - x)\langle\tilde{\psi}_f| = \lim_{\gamma\to 0}\mathfrak{Im}\left[\tilde{G}(x)\right], \tag{3.39}$$

where x is a real number[5], and

$$\tilde{G}(x) = \hat{S}^{-1/2}\frac{1}{x - \hat{S}^{-1/2}\tilde{H}\hat{S}^{-1/2} - i\gamma}\hat{S}^{-1/2}. \tag{3.40}$$

Therefore, the XAS cross-section can be written using equations (3.34) and (3.39):

$$\sigma(\omega) = 4\pi\alpha\hbar\omega\lim_{\gamma\to 0}\mathfrak{Im}\left[\langle\tilde{\phi}_{\mathbf{R}_0}|\tilde{G}(\hbar\omega + E_i)|\tilde{\phi}_{\mathbf{R}_0}\rangle\right], \tag{3.41}$$

where E_i is the energy of the initial state. In practical terms, E_i is chosen to be the Fermi level in case of metals, or the highest occupied states, in case of an insulator material.

In fact, as we did in the last section, we will also make usage of the Lanczos recursion method on the matrix elements of equation (3.41):

$$\langle\tilde{\phi}_{\mathbf{R}_0}|\tilde{G}(E)|\tilde{\phi}_{\mathbf{R}_0}\rangle = \frac{\langle\tilde{\phi}_{\mathbf{R}_0}|\hat{S}^{-1}|\tilde{\phi}_{\mathbf{R}_0}\rangle}{a_0 - E - i\gamma - \cfrac{b_1^2}{a_1 - E - i\gamma - \cfrac{b_2^2}{\ddots}}}, \tag{3.42}$$

where the real numbers $\{a_i\}$ and $\{b_i\}$ are computed resursively by defining the set of normalized vectors $\{|u_i\rangle\}$, such that

$$\begin{aligned} |u_0\rangle &= \frac{\hat{S}^{-1/2}|\tilde{\phi}_{\mathbf{R}_0}\rangle}{\sqrt{\langle\tilde{\phi}_{\mathbf{R}_0}|\hat{S}^{-1}|\tilde{\phi}_{\mathbf{R}_0}\rangle}}, \\ \hat{S}^{-1/2}\tilde{H}\hat{S}^{-1/2}|u_i\rangle &= a_i|u_i\rangle + b_{i+1}|u_{i+1}\rangle + b_i|u_{i-1}\rangle. \end{aligned}$$

The coefficients are determined as

$$a_i = \langle u_i|\hat{S}^{-1/2}\tilde{H}\hat{S}^{-1/2}|u_i\rangle, \tag{3.43}$$

$$b_i = \langle u_i|\hat{S}^{-1/2}\tilde{H}\hat{S}^{-1/2}|u_{i-1}\rangle. \tag{3.44}$$

[5]For proof of this equation, please refer to appendix D.

Indeed, the difference here from the standard Lanczos method of the section 3.3.2 is that the initial vector $|u_0\rangle$ and the Hamiltonian $\tilde{H}$ have the operator $\hat{S}$ inside of them. Nonetheless, because the dimension of the matrix $\hat{S}$ is of the same order as the Hamiltonian, in which both depend on the number of plane waves (kinetic energy cutoff), the computational cost of the application of $\hat{S}^{-1/2}$ is as large as the $\tilde{H}$ one.

Therefore, one needs a more efficient way to carry out the Lanczos method, which is obtained by defining the following auxiliary vectors:

$$|t_i\rangle = \hat{S}^{1/2}|u_i\rangle. \tag{3.45}$$

The new basis is, then, obtained by

$$\begin{aligned} |t_0\rangle &= \frac{|\tilde{\phi}_{\mathbf{R}_0}\rangle}{\sqrt{\langle\tilde{\phi}_{\mathbf{R}_0}|\hat{S}^{-1}|\tilde{\phi}_{\mathbf{R}_0}\rangle}}, \\ \tilde{H}\hat{S}^{-1}|t_i\rangle &= a_i|t_i\rangle + b_{i+1}|t_{i+1}\rangle + b_i|t_{i-1}\rangle, \end{aligned}$$

where $\langle t_i|\hat{S}^{-1}|t_j\rangle = \delta_{i,j}$, since $\{|t_i\rangle\}$ are no longer orthogonal. Thus, new vectors $|\tilde{t}_i\rangle = \hat{S}^{-1}|t_i\rangle$ are obtained, and the coefficients $\{a_i\}$ and $\{b_i\}$ are calculated in a more feasible way:

$$a_i = \langle\tilde{t}_i|\tilde{H}|\tilde{t}_i\rangle, \tag{3.46}$$

$$b_i = \langle\tilde{t}_i|\tilde{H}|\tilde{t}_{i-1}\rangle, \tag{3.47}$$

Thus, each iteraction requires only one multiplication by $\hat{S}^{-1}$, one by $\tilde{H}$, and four Lanczos vector $|t_{i-1}\rangle$, $|\tilde{t}_{i-1}\rangle$, $|t_i\rangle$, and $|\tilde{t}_i\rangle$.

A last comment needs to be taken. Through the definintion of the $\hat{S}$ matrix in terms of N_p ultrasoft projectors, the calculations of $\hat{S}^{-1}$ is effectively computed by the products and inversions of matrices of the order $N_p \times N_p$ [136, 137]. The main passages of this matrix calculation are outlined in appendix E.

3.3.4 Practical DFT Calculation

In practical XANES calculations, one needs reconstructing the all-electron wavefunctions for only the X-ray absorbing atom[6]. This information should be included in its pseudopotential in order to perform XANES calculations. In QUANTUM ESPRESSO package [43], the code ld1.x performs this task, while xspectra.x one computes the XANES. The mentioned reconstruction is performed through the GIPAW[7] method [111], which is essential due to the presence of external electromagnetic field from

[6] Non-absorbing atoms accept any kind of pseudopotential.

[7] It stands for Gauge-Included Projector Augmented Waves.

the X-ray radiation. With these informations, the code also requires the radial core wavefunction of the initial core state (without the hole, or the electron extracted from the core level), which can be obtained from a pseudopotential created with GIPAW reconstruction for the atom *without core-hole*. By the way, in appendix F, the GIPAW method is shortly described.

The flowchart below, figure 3.3, pictures us the steps to perform XANES calculations. It is relevant to say that the pseudopotentials built for a specific system can be transfered to another system that has the same atom, under the same condition. This means that, if the environment in which the X-ray absorbent atom is included is "compatible" with the pseudopotential that had already been created, all these information, including the initial core state can be used in this new system.

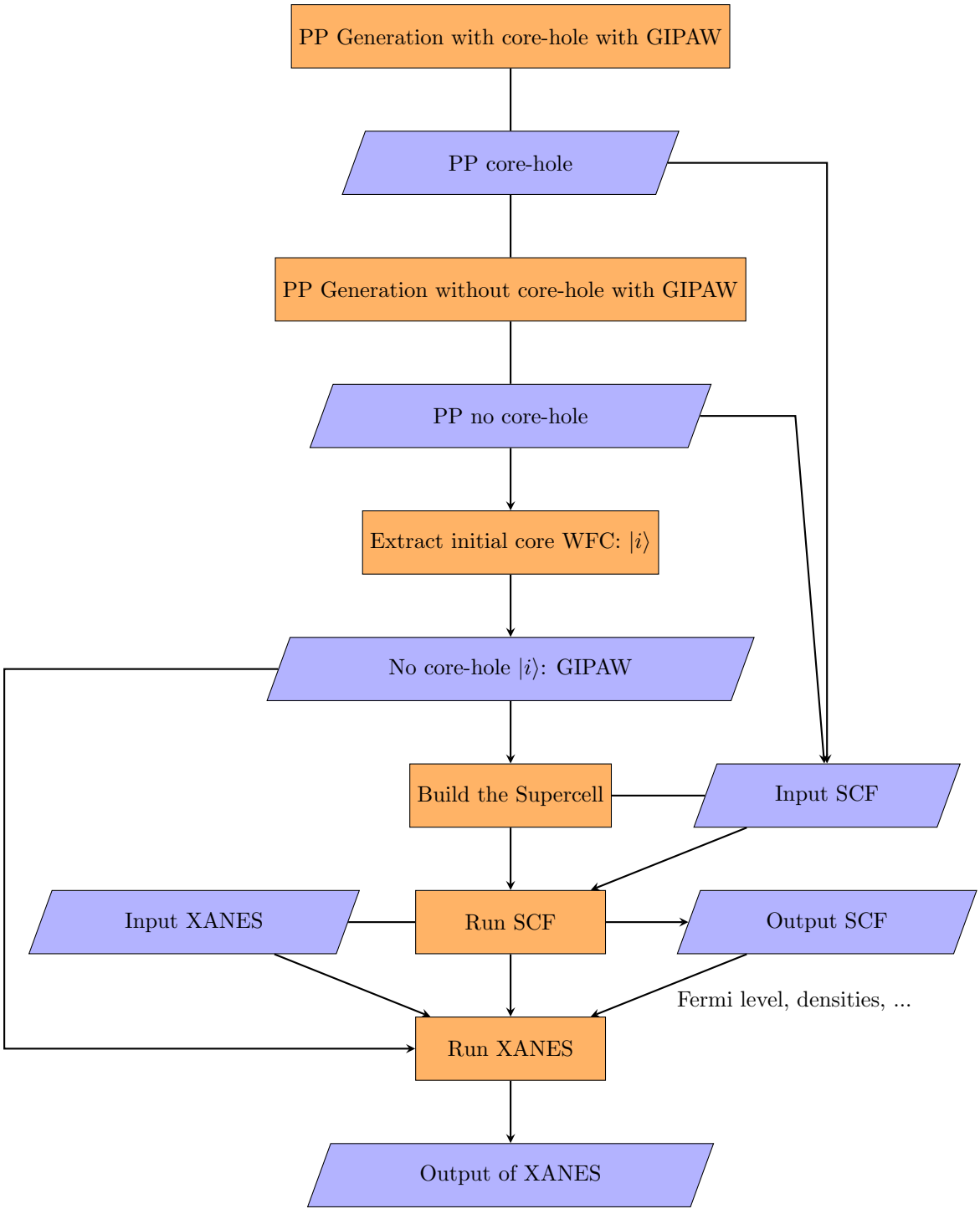

Figure 3.3: Flowchart shows us the required steps to perform a XANES calculation.

Chapter 4

Dynamical Methods to Atoms and Molecules

In classical molecular dynamics (MD), one wishes to determine both the time evolution of $3N$ atomic coordinates $\{\mathbf{r}\}$ along with the $3N$ atomic momenta $\{\mathbf{p}\}$ of the N atoms composing the system under study. To accomplish this task, one can apply the classical movement law upon the N particles (where $N \sim 10^{23}$, from the classical Hamiltonian of the system. A state of the system is defined by a point in the phase space such that $\left(\mathbf{r}^N, \mathbf{p}^N\right) \equiv (\mathbf{r}_1, \mathbf{r}_2, \mathbf{r}_3, \ldots, \mathbf{r}_N;\ \mathbf{p}_1, \mathbf{p}_2, \mathbf{p}_3, \ldots, \mathbf{p}_N)$, in which $\mathbf{r}_i$ and $\mathbf{p}_i$ are the coordinates and conjugated momenta of the particle i, respectively [138]. The basis of molecular modeling lays on that, by mean of which general process for describing complex systems in terms of realistic atomic model. The goal is to predict macroscopic properties based on the acquired knowledge of the atomic scale (reference manual in [139]).

On the whole, macroscopic properties can be ensemble averages over a representative statistical ensemble of the system at a given temperature. In fact, once the molecular model and the force field $V(\mathbf{r})$ is chosen, a search by a suitable low-energy configurational space is required. Such configurations depend on the type and form of the interaction energy function $V(\mathbf{r})$, on the number of degrees of freedom, and on the type of those degrees (cartisian coordinates, bond lengths, bond angles, among others) [140]. If a system has too many degrees of freedom, a weighted collection of configurations (ensembles) has to be generated. One way to collect those configurations would be through the Monte Carlo method, which is based on a Markovian process that allows us to sample the most probable macrostates without taking into account their time evolution [141]. Another way to gather such configurations would be using the nature's law of motion, which has the advantage that the temporal information of the system is obtained. That type of technique has two major simulation methods: Molecular Dynamics (MD), in which the Newton's equations of motion are solved over time, and Stochastic Dynamics (SD), in which the time evolution of the Brownian motion is integrated through the Langevin equation [140].

Those methods are avalable in GROMACS package [142–149], a software to perform atomic scale simulations. For the representation of those ensembles in equilibrium, two methods are available in GROMACS: Monte Carlo and Molecular Dynamics simulations. Non-equilibrium ensembles and analysis

of the dynamics of events are only possible with the second method, which is the one we have used. So, we will shortly give the fundamentals of both MD and SD along with a brief explanation of the techniques used in the mentioned code, such as interactions among the particles of the system, propagations of the atomic coordinates, calculations of both pressure and temperature, energy minimization scheme, and applied periodic boundary conditions.

4.1 Molecular Dynamics

Molecular dynamics simulations comprise on solving the numerical solutions of the classical equations of motion. Doing so, a trajectory of the molecular system, *i.e.*, the time evolution of the configurations, is obtained. In other words, one must solve the Newton's equations of motion for a system with N interacting atoms:

$$m_i \frac{d^2\mathbf{r}_i}{dt^2} = \mathbf{F}_i, \quad i = 1, \ldots, N. \tag{4.1}$$

where the forces $\mathbf{F}_i$ are given by the potential function $V(\mathbf{r}_1, \mathbf{r}_2, \ldots, \mathbf{r}_N)$:

$$\mathbf{F}_i = -\frac{\partial}{\partial \mathbf{r}_i} V(\mathbf{r}_1, \mathbf{r}_2, \ldots, \mathbf{r}_N). \tag{4.2}$$

Another way to express this equations would be through the Hamilton's equation [150]:

$$\begin{aligned} \dot{\mathbf{r}}_i = \frac{\partial \mathbf{r}_i}{\partial t} &= \frac{\partial H}{\partial \mathbf{p}_i}, \\ \dot{\mathbf{p}}_i = \frac{\partial \mathbf{p}_i}{\partial t} &= -\frac{\partial H}{\partial \mathbf{r}_i}, \quad i = 1, 2, \ldots, N \end{aligned} \tag{4.3}$$

where $H = H(\{\mathbf{r}_i\}, \{\mathbf{p}_i\}, t)$ is the Hamiltonian of the system. If H is explicitly time-independent, then $\dot{H} = 0$, where the dot means time derivative of a function. Hence, H, by extension the total energy, is a conserved quantity. The time-independent Hamiltonian is given by

$$H(\mathbf{r}^N, \mathbf{p}^N) = \sum_{i=1}^{N} \frac{\mathbf{p}^2}{2m_i} + V(\mathbf{r}_i) \equiv K + V(\mathbf{r}_i), \tag{4.4}$$

i.e., it is the sum of the kinetic energy and potential energy of the system. From that equation, the absolute temperature, T, is obtained from the equipartition theorem, $K = \frac{1}{2} N_{df} k_B T$, where N_{df} is the number of degrees of freedom of the system. The pressure, in turn, is defined as

$$P = \frac{2}{3\Omega}\left[K - \Xi\right], \text{ with} \tag{4.5}$$

$$\Xi = -\frac{1}{2}\sum_{i<j}^{N} \mathbf{r}_{ij} \cdot \mathbf{F}_{ij}, \tag{4.6}$$

where $\mathbf{r}_{ij} = \mathbf{r}_i - \mathbf{r}_j$, F_{ij} is the force on atom i due to atom j, and Ω is the volume of the computational box.

The mathematical background that allows us, based on the time evolution of the atoms of the system, to connect the microscopic quantities with the macroscopic physical properties is the statistical mechanics. Once the forces, or the potential energy, is known, one can compute the microstates of the system through the equations of motion, using the initial condition $\left(\mathbf{r}^N(0), \mathbf{p}^N(0)\right)$. The integration of equation (4.1) is performed at small time steps (usually 1 – 10 fs [140]). Thus, both dynamic and static informations can be extracted by averaging over a sufficient large number of representative ensembles of the states of the system. As a technique to search configurational space, temperature, and therefore kinetic energy, plays a key role for the system can be able to surmount energy barries of the order of $k_B T$ per degree of freedom.

However, there is a caveat in such a searching. Even if the energy barries between any two energy minima is low, the required time to pass them over may be too long for a MD simulation. Thus, in that case, new methods have to come into the scene, as the stochastic dynamics method, which will be addressed in section 4.2.

4.1.1 Potential Energy Function (Force Field)

The potential function is a summation of several functions chosen to compose the Force Fields (FF) used in MD simulations. Those functions (interaction potentials) are subdivided into three categories: non-bonded interactions, bonded interactions, restraints, and applied forces. We are not going to address all of the functions belonging to those categories here, but only a few of them. In short, the potential energy function includes short range interaction, namely long-range interaction such as Lennard-Jones potential for van der Waals interaction, and Coulomb interaction, and the intermolecular interaction, such as bond stretching (r), angle deformation (θ), dihedral torsions (φ). The general form of the function is given by

$$V_{total} = \sum_{i,j;\, i<j} \left\{ 4\varepsilon_{ij} \left[\left(\frac{\sigma_{ij}}{r_{ij}}\right)^{12} - \left(\frac{\sigma_{ij}}{r_{ij}}\right)^{6} \right] + \frac{q_i q_j}{r_{ij}} \right\} + \sum_{\text{bond}} k_b \left(r - b_{ij}\right)^2 + \sum_{\text{angle}} k_\theta \left(\theta - \theta_{ijk}\right)^2 + \\ + \sum_{\text{dihedral}} k_\varphi \left[1 + cos(n\varphi - \delta)\right], \tag{4.7}$$

where r_{ij} is the distance between the atoms i and j, with charges q_i and q_j, respectively; b_{ij} is the equilibrium distance between atoms i and j, and θ_{ijk} is the equilibrium bond angle comprising the atoms i, j, and k. The parameters k_b, k_θ, and k_φ from the intramolecular potential, as well as a bit more

detailed description of this harmonic functions will be discussed later. The term in curl brackets in turn is the intermolecular potential.

4.1.2 Intramolecular Potentials

These terms are not exclusively pair potential, but are described by the interactions of bonded atoms indeed. Besides, they can also include a three- or four-body potential. The former is related to the angle deformation, and the latter is given by the dihedral angle torsion. The two-body term is given by the bond stretching, as we will see soon.

Bond Stretching

The bond stretching between two atoms i and j is modelled by the harmonic potential:

$$V_b(r_{ij}) = k_{ij}^b \left(r - b_{ij}\right)^2, \tag{4.8}$$

which describes the bonding between atoms as a simple spring including a harmonic restoring force, where k_{ij}^b is the spring constant, and b_{ij} is the equilibrium bond length.

Angle Deformation

The deformation angle amongst the atoms i, j, and k is described through the potential

$$V_{ang}(\theta) = k_{ijk}^\theta \left(\theta - \theta_{ijk}\right)^2, \tag{4.9}$$

where θ_{ijk} is the equilibrium bond angle $i-j-k$, and k_{ijk}^θ is the angle deformation constant.

Dihedral Torsion Angle

Dihedral (or torsion) angles are defined as the angle between two intersecting planes, where each plane has at least two atoms bonded together. For example, if four atoms i, j, k, and l are bonded such that $i-j$ is in a plane that intersects the plane contaning the bond $k-l$ in a angle φ, then this angle comprises the bond $j-k$ and is the dihedral angle. The potential that describes this interaction is given by

$$V_{dihedral}(\varphi) = k_{ijkl}^\varphi \left[1 + cos(n\varphi - \delta)\right], \tag{4.10}$$

where δ is the equilibrium torsion, and n is an integer.

4.1.3 Intermolecular Potentials

Intermolecular potential, or non-bonded interaction potential, can be splitted into two types: long-range and short-range interactions. The dispersion and repulsion terms are combined together into a Lennard-Jones potential (also known as 6-12 interaction). The (partially) charged atoms of the systems are included into the Coulomb potential.

Lennard-Jones Interaction

The intensity of this interaction diminishes rapidly with the increasing of the distance between the atoms, so that beyond a certain radius the interaction does not present any meaningful effect. Such a distance is called cutoff radius, R_c. The Lennard-Jones potential is given as

$$V_{LJ}(r_{ij}) = 4\varepsilon_{ij}\left[\left(\frac{\sigma_{ij}}{r_{ij}}\right)^{12} - \left(\frac{\sigma_{ij}}{r_{ij}}\right)^{6}\right]. \tag{4.11}$$

Actually, in practical term this potential is truncated at R_c, so that, so equation (4.11) becomes

$$V_{LJ}(r_{ij}) = \begin{cases} 4\varepsilon_{ij}\left[\left(\frac{\sigma_{ij}}{r_{ij}}\right)^{12} - \left(\frac{\sigma_{ij}}{r_{ij}}\right)^{6} - \left(\frac{\sigma_{ij}}{R_c}\right)^{12} + \left(\frac{\sigma_{ij}}{R_c}\right)^{6}\right], & r_{ij} \leq R_c \\ 0, \quad r_{ij} \geq R_c. \end{cases}$$

The terms ε_{ij} and σ_{ij} are parameters related to the potential well and the size of the particles, respectively. In general, they are either determined from *ab-initio* calculations or empirically. The term r_{ij} is defined by the distance between the particles i and j.

Coulomb Interaction

For charged particles interacting among themselves it is necessary the usage of long-range interaction that is the Coulomb interaction. The Coulomb potential is represented by the following equation

$$V^{el}\left(\{\mathbf{r}^N\}\right) = \sum_{i=1}^{N}\sum_{a=1}^{n_i}\sum_{j=1}^{N}\sum_{b=1}^{n_j}\frac{q_{ia}q_{jb}}{r_{iajb}} \tag{4.12}$$

where we define a system with N molecules i, each one containing n atoms with partial charge q_{ia}. We have omitted the factor $1/4\pi\varepsilon_0$ by making $c = e = 1$ for simplicity. In practical calculations, one of the ways to make the computations is to use the Ewald summation, which was first introduced as a method to calculate long-range interactions of the periodic images in crystals [151]. The equation (4.12) is thus replaced by an expansion mathematically equivalent, but that converges more quickly, so that using the Ewald summation method, that equation is given by

$$V^{el}\left(\{\mathbf{r}^N\}\right) = \underbrace{\sum_{i=1}^{N}\sum_{a=1}^{n_i}\sum_{j=1}^{N}\sum_{b=1}^{n_j}\frac{q_{ia}\,q_{jb}\,erf(\alpha r_{iajb})}{r_{ij}}}_{\text{real part}} - \underbrace{\sum_{i=1}^{N}\sum_{a=1}^{n_i} q_{ia}\left[\frac{\alpha}{\pi^{1/2}}q_{ia} + \frac{1}{2}\sum_{b\neq a}^{n_i} q_{ib}\frac{erf(\alpha r_{iaib})}{iaib}\right]}_{\text{sefl-term}} + \underbrace{\frac{2\pi}{V}\sum_{k\neq 0}^{\infty}\frac{exp\left[-k^{2/4\alpha^2}\right]}{k^2}\left|\sum_{i=1}^{N}\sum_{a=1}^{n_i} q_{ia}exp\left[i(\mathbf{k}\cdot\mathbf{r}_{ia})\right]\right|^2}_{\text{reciprocal term}}, \tag{4.13}$$

where α is an adjustable parameter on the order of $L/5$, in which L is the length of the cubic-box side, and V is its volume L^3. The error function, $erf(x)$, is given by $erfc(x) = 1 - erf(x)$, where

$$erfc(x) = \frac{2}{\sqrt{\pi}}\int_x^{\infty} e^{-t^2}dt \tag{4.14}$$

is the complementary error function. Also, $\mathbf{k} = 2\pi/L\,[k_x, k_y, k_z]$ is a vector in reciprocal space. One must tune the parameters α and $\mathbf{k}$ up in order to achieve feasible energy values of the system in a MD simulation. The first term is the real part of the potential, while the last one computes the interactions in reciprocal space. The energy self-term, in turn, includes the interactions among the charges q_{ia} and its images; also, it has a correction factor. More details on the equation (4.14) can be found in [25, 152].

It is important to mention that in large systems the computational cost of the reciprocal part greatly increases. An alternative method was implemented in order to decrease this simulation time. An approach on such methods can be found in [23, 25, 153, 154]. In one of these methods, the Coulomb interactions are computed only in between the particles whose distances r_{ij} is to be within the cutoff radius R_c, being known as a "truncated" or "shifted" Coulomb potential, which is given by

$$\begin{aligned} V^{el}\left(\{\mathbf{r}^N\}\right) = \frac{1}{2}\sum_{i=1}^{N}\sum_{a=1}^{n_i}\sum_{j=1}^{N}\sum_{b=1}^{n_j}\left[\frac{q_{ia}q_{jb}\,erf(\alpha r_{iajb})}{r_{ij}} - \lim_{r_{iajb}\to R_c}\left\{\frac{q_{ia}q_{jb}\,erf(\alpha r_{iajb})}{r_{ij}}\right\}\right] - \\ -\frac{1}{2}\sum_{i=1}^{N}\sum_{a=1}^{n_i} q_{ia}\left[\left(\frac{erf(\alpha R_c)}{R_c} + \frac{2\alpha}{\pi^{1/2}}\right)q_{ia} + \sum_{b\neq a}^{n_i}\left(\frac{erf(\alpha r_{iaib})}{r_{iaib}} + \frac{erf(\alpha R_c)}{R_c}\right)q_{ib}\right], \end{aligned} \tag{4.15}$$

where the forces are computed from equations (4.1) and (4.2).

4.2 Stochastic Dynamics

The system under study evolves according to the potential associated to it. However, due to practical reasons, this potential is an approximation of the real situation. Thus, stochastic dynamics, which is an extension of MD, comes in to fill in the gap between the real and the approximated potential, as the system is subjected to effects of a "noise". Although SD does not define a real potential, it tries

to define a general correlation between those situations, which does not depend on the details of the potential. Therefore, it takes into account the previously neglected degrees of freedom to obtain a more realistic simulation [141].

According to [140], a trajectory of the molecular system is obtained by integrating the stochastic or velocity Langeving equation of motion:

$$\frac{d^2\mathbf{r}_i(t)}{dt^2} = \frac{1}{m_i}\left[\mathbf{F}_i + \mathbf{R}_i\right] - \gamma_i \frac{d\mathbf{r}}{dt}, \tag{4.16}$$

where $\mathbf{R}_i$ is a stochastic force (or a noise process), and γ_i is a friction coefficient, on which the frictional force is proportional to. Those terms are added to equation (4.1). The stochastic term introduces energy, whereas the frictional term removes kinetic energy from the system, so that the condition for zero energy loss is

$$\langle \mathbf{R}_i^2 \rangle = 6\, m_i\, \gamma_i\, k_B\, T_{ref}, \tag{4.17}$$

where T_{ref} is the reference temperature of the system. When γ_i is too large, stochastic dynamics reduces to Brownian dynamics, also known as position Langevin dynamics.

4.3 Energy Minimization

Molecular Dynamics simulations are an essential tool to generate non-equilibrium ensembles and to investigate dynamic events. To perform that, a starting point for the system configuration is required. Sometimes, however, such initial configuration is far from equilibrium, which means that the forces acting on each atom may be excessively large. In such a case, the energy minimization is required. Besides that, energy minimization can be necessary to remove the kinetic energy from the system, since it reduces thermal noises in both the structure and potential energy of the system.

The potential energy function, which describes the energy of an interacting system, can be a very complicated function of the atomic positions. Such a function can have a large number of local minima, and a deepest point, the global minimum, on which the derivate of the potential energy with respect to the coordinates (the forces) are null, and its second derivative (Hessian matrix) are non-negative. For completeness, the Hessian matrix has zero eigenvalues only for a system (an isolated molecule) with collective coordinates that correspond to translation or rotation. Between any two minima there are saddle points, on which the Hessian has one only negative values. Therefore, knowing all the local minima, and possibly the global one, enables us to describe all the system. In practical terms, however, there is no minimization method that is able to find the global minimum of a system in a realistic execution time for any purpose. Nonetheless, given a good starting configuration, it is possible to get to a nearest[1] local minimum. In fact, GROMACS can perform energy minimzation using three methods: steepest descent, conjugate gradients, and the L-BFGS minimizer, which is comparable to the second one. The first two

[1] "Nearest" here means the minimum that can be reached by descending the steepest local gradient, *i.e.* the force.

are based on the gradient of the potential function, while the last one is based on the Newton-Raphson method, which, unlike the former ones, is based on the Hessian of the potential.

In this work, we have used the steepest descent method, which simply takes a step into the direction of the force, not considering the prior history of the system. Its convergence can be very slow in the vicinity of the local minimum, but it will lead the system close to the nearest local minimum faster than the other methods. Thus, if a vector of all the 3N coordinates, $\mathbf{r}$, is defined, an initial maximum displacement h_0 has to be given, otherwise new positions will not feel the effect of the forces. After the calculation of the gradient of the potential energy, V, or negative of the forces, the new positions are given by [139]

$$\mathbf{r}_{n+1} = \mathbf{r}_n + \frac{\mathbf{F}_n}{max(|\mathbf{F}_n|)} h_n, \tag{4.18}$$

where h_n is the maximum displacement, $\mathbf{F}_n$ is the force, and $max(|\mathbf{F}_n|)$ is the largest scalar force on any atom. Then, the forces and energies are again performed for the new position using the following criteria:

If $V_{n+1} < V_n$, the new positions are accepted, and $h_{n+1} = 1.2h_n$.
If $V_{n+1} \geq V_n$, the new positions are rejected, and $h_n = 0.2h_n$.

The energy minimization stops when a maximum of the absolute values of the force components is smaller than a specified value.

4.4 Integration Algorithms

Integration techniques by finite differences are used to generate trajectories of molecular dynamics simulations. Such integrations methods of the Newton's equation of motion have to be time-reversal, as so is the Newton's equation. To perform such a task onto tiny time steps, one uses integration algorithms. The most used are the Verlet, Velocity Verlet, Leap-Frog, and Beeman algorithms [23], which assume a Taylor series expansion of coordinates around the time point t. Hereafter, we will only review the Verlet, and the leap-frog schemes. The latter one is the default MD integrator in GROMACS.

4.4.1 Verlet Algorithm

In 1967, Loup Verlet developed the algorithm [155] that presently carries his name. His method is based on both positions and acceleration at a time t, and on positions at a time $t - \Delta t$. The Taylor series expansion for the coordinate $\mathbf{r}(t)$, around time t, is given by

$$\mathbf{r}(t + \Delta t) = \mathbf{r}(t) + \Delta t\, \mathbf{v}(t) + \frac{1}{2}(\Delta t)^2\, \mathbf{a}(t) + \cdots, \text{ similarly} \tag{4.19a}$$

$$\mathbf{r}(t - \Delta t) = \mathbf{r}(t) - \Delta t\, \mathbf{v}(t) + \frac{1}{2}(\Delta t)^2\, \mathbf{a}(t) + \cdots \tag{4.19b}$$

Adding up the equations (4.19a) and (4.19b), and truncating the resulting summation on the second term, one gets the following result:

$$\mathbf{r}(t+\Delta t) = 2\mathbf{r}(t) - \mathbf{r}(t-\Delta t) + (\Delta t)^2\mathbf{a}(t). \tag{4.20}$$

In all the above relations, Δt is meant to be the numerical integration time step in the MD simulation, which should be less than the molecular relaxation times ($10^{-16} - 10^{-13}$ seconds). Some considerations about the equation (4.20) are relevant: velocities are not required for the trajectory calculations, however they are needed for kinetic energy computations, and by extention for the total energy. The velocity are obtained as

$$\mathbf{v}(t) = \frac{\mathbf{r}(t+\Delta t) - \mathbf{r}(t-\Delta t)}{2\Delta t}. \tag{4.21}$$

This algorithm is a well-established and widely-tested method. Note, also, that the estimate error on the position is of the order Δt^4, and the corresponding velocity error is of the order Δt^2. In the early 1980's, Swope *et al.* [156] proposed an algorithm based on a modification of the Verlet algorithm, in which the position, velocity, and acceleration are calculated in the same time t. The following equations comprise the Velocity Verlet algorithm:

$$\mathbf{r}(t+\Delta t) = \mathbf{r}(t) + \Delta t\,\mathbf{v}(t) + \frac{1}{2}(\Delta t)^2\,\mathbf{a}(t) \tag{4.22a}$$

$$\mathbf{v}(t+\Delta t) = \mathbf{v}(t) + \frac{1}{2}\Delta t\,[\mathbf{a}(t) + \mathbf{a}(t+\Delta t)]\,. \tag{4.22b}$$

4.4.2 Leap-Frog Algorithm

There are many alternatives to the Verlet algorithm. The Euler algorithm, for instance, is obtained by truncating the Taylor expansion beyond the term in Δt^2. Nevertheless, the leap-frog algorithm is the simplest among them [157]. It computes the velocities at $\Delta t/2$ and uses these velocities to compute the new positions. The leap-frog algorithm comes from the Verlet scheme by defining the velocities as

$$\begin{aligned} \mathbf{v}(t-\Delta t/2) &\equiv \frac{\mathbf{r}(t) - \mathbf{r}(t-\Delta t)}{\Delta t}, \text{ and} \\ \mathbf{v}(t+\Delta t/2) &\equiv \frac{\mathbf{r}(t+\Delta t) - \mathbf{r}(t)}{\Delta t}. \end{aligned} \tag{4.23}$$

Using these expressions, we can obtain the expression for the new positions:

$$\mathbf{r}(t+\Delta t) = \mathbf{r}(t) + \Delta t\,\mathbf{v}(t+\Delta t/2), \tag{4.24}$$

and from the Verlet algorithm, one can update the velocities:

$$\mathbf{v}(t + \Delta t/2) = \mathbf{v}(t - \Delta t/2) + \Delta t\, \mathbf{a}(t). \tag{4.25}$$

As one can see, because leap-frog algorithm is derived from the Verlet one, it yields the same trajectories. However, the velocities are not defined at the same time as the positions, which implies the kinetic and potential energies cannot be calculated at the same time, and hence the total energy cannot be directly computed. That is why the velocity Verlet algorithm comes in handy. With no temperature or pressure coupling, these algorithms give identical trajectories.

4.5 Temperature and Pressure Coupling

Direct evaluation of the Newton's equation of motion gives rise to an NVE ensemble (microcanonical one), which means that the number of particle, volume, and energy (adiabatic system) of the system are conserved. However, in real world simulations, one may need to evaluate quantities that require the imposition of external contraints on the system, in order to avoid energy loss by dissipative process, for example. In such a case, constant temperature bath (NVT, or canonical ensemble), or temperature coupling, would be interesting to work with. As one might expect, when temperature or pressure coupling are used the total energy is no longer conserved. Thus, one needs to rescale the equations through the combination of either temperature or pressure coupling, or even both, so that one would be able to simulate a system as "real" as possible. The next two subsections will be based on both the GROMACS user guide [139] and on the review after Van Gunsteren and Barendsen [140].

4.5.1 Temperatute Coupling

There are several ways to perform MD simulations under a constant temperature, which may be based on either the rescaling of the atomic velocities, which in turn is related to the temperature, or on the modification of the equation of motion that pushes the system towards the desired temperature constraint. Different methods that are implemented in GROMACS can perform such a task. The first one we would like to mention is Berendsen scheme [158], which is known as weak-coupling scheme for the deviation from the system temperature is gradually restored to the temperature bath T_0. There is also a constraint method called velocity-rescaling thermostat [159], in which the velocities are updated at each MD time step by a factor $[T_0/T(t)]^{1/2}$, where $T(t)$ is defined using the equipartition theorem. In the stochastic method, in turn, the velocities are stochastically changed. Andersen [160] proposed that the velocities should be selected through the Maxwell-Boltzmann distribution using an adjustable parameter that would cause the re-thermalization of the system. At last, there is also an extended system method in which an extra degree of freedom, the heat bath, is added to the system, which was proposed by Nosé [161] and Hoover [162].

In our calculations, we have used the first two methods. In the Berendsen method, the equations of motion are adapted such that the net results on the system owing temperature changes are a first-order relaxation of the temperature towards the reference value T_0 [158]. Such temperature shifts can be written as

$$\frac{dT(t)}{dt} = \frac{1}{\tau_T}[T_0 - T(t)], \tag{4.26}$$

by which the kinetic energy can change, ΔK, across a MD time step Δt by scaling the atomic velocities $\mathbf{v}_i$ with a factor λ. Such a scaling factor affects the heat flow into or out the system as

$$\Delta K = (\lambda^2 - 1)\frac{1}{2}N_{df}k_B\,T(t). \tag{4.27}$$

The quantity that correlates the energy change of a system with its temperature shift is the heat capacity per degree of freedom of that system. Here, we are going to define $\tau = T_0 - T(t)$, and write

$$\tau = \frac{1}{N_{df}c_V}\Delta K. \tag{4.28}$$

Thus, solving equations (4.26), (4.27), and (4.28) for λ, we get

$$\lambda = \left[1 + c_V(k_B/2)^{-1}\frac{\Delta t}{\tau_T}\left(\frac{T_0}{T(t)} - 1\right)\right]^{1/2}. \tag{4.29}$$

It can also be written as

$$\lambda = \left[1 + \frac{\Delta t}{\tau}\left\{\frac{T_0}{T\left(t - \frac{1}{2}\Delta t\right)} - 1\right\}\right]^{1/2}, \tag{4.30}$$

where we have redefine $\tau = \tau_T\,k_B N_{df}/2c_V$. This coupling can be sufficiently weak (large τ_T), as in a gas phase, but also can be chosen sufficiently strong (small τ_T), as for a damping system like an aquous one. However, for a system with a huge number of atoms this approach may fail in conserving the desired quantities, for it is not associated to a well defined ensemble [159].

The way-out to that is given by the velocity-rescaling temperature coupling [159], which is a Berendsen thermostat with additional stochastic term that ensures a correct kinetic energy distribution [139]. In this method a random force is added, in order to enforce the correct distribution for the kinetic energy according to a constant value, which can be defined and works as a guide to verify how much a generated configuration is close enough to the desired NVT ensemble at each time step.

Roughly, the conventional velocity-rescaling method consist in multiplying the velocities of all particles by the same factor

$$\alpha = \sqrt{\frac{\bar{K}}{K}}, \tag{4.31}$$

where, $\bar{K} = N_{df} k_B T/2$ is the average kinetic energy at a target temperatute. The proposal in this method is to enforce the canonical distribution for K by modifying the scaling factor α to

$$\alpha' = \sqrt{\frac{K}{K_t}}, \tag{4.32}$$

selecting target values K_t with a stochastic procedure through the canonical equilibrium distribution:

$$\bar{P}(K_t)\, dK_t \propto K_t^{\left(\frac{N_{df}}{2}-1\right)} e^{-K_t/k_B T}\, dK_t. \tag{4.33}$$

However, it exhibits fluctuations with relative magnitude $\sqrt{1/N_{df}}$. Therefore, this approach is softened by distributing the rescaling procedure among the number of time steps in the MD run, with the prescription that the distribution in equation (4.33) has to be left unchanged. Because of the arbitrariness of the chosen stochastic dynamics, it imposes that K is described by a first-order differential equation, namely, the Fokker-Planck equation [163], which must exhibit a zero-current solution. Yet, such an equation refers to the evolution of a probability distribution. In fact, a Maxwell-Boltzmann distribution can be a solution for that equation [164]. This equation can be written as

$$dK = \left(D(K) \frac{\partial \log \bar{P}}{\partial K} + \frac{\partial D(K)}{\partial K} \right) dt + \sqrt{2D(K)}\, dW, \tag{4.34}$$

where D(K) is an arbitrary positive definite function of K, and dW, a Wiener noise [163]. By inserting the equation (4.33) into the last one, one gets

$$dK = \left(\frac{N_{df} D(K)}{2\bar{K}K} (\bar{K} - K) - \frac{D(K)}{K} + \frac{\partial D(K)}{\partial K} \right) dt + \sqrt{2D(K)}\, dW, \tag{4.35}$$

where $D(K)$ can be chosen as

$$D(K) = \frac{2K\bar{K}}{N_{df}\,\tau}, \tag{4.36}$$

where τ determines the time-scale of the thermostat as in Berendsen's formulation. Therefore, we arrive to the following clear expression:

$$dK = (\bar{K} - K)\frac{dt}{\tau} + 2\sqrt{\frac{K\bar{K}}{N_{df}}}\frac{dW}{\sqrt{\tau}}, \tag{4.37}$$

which reduces to the standard Berendsen thermostat if one zeroes the stochastic term. Therefore, this thermostat can produce a correct canonical ensemble and still, as in the Berendsen scheme, is a first-order decay of temperature deviations with no oscillations.

4.5.2 Pressure Coupling

The system also can be coupled to a pressure bath. Unlike temperature coupling, pressure change occurs due to scaling the volume of the simulation box and by changing the virial (equation (4.7)) through a scaling of the interatomic distances [140], that is to say, now one can get a NPT ensemble (approximately). As for temperature coupling, pressure coupling also has been implemented in GROMACS, which supports the Berendsen scheme [158] that scales coordinates and box vector at every time step, the extended system method of Parrinello-Rahman [165, 166], which adds an extra degree of freedom, the volume of the box, to the system, and also the velocity-Verlet variante by Martyna-Tuckerman-Tobias-Klein (MTTK) [167]. We will elaborate on the first one.

The Berendsen barostat rescales the coordinates and the simulation box vectors through the modification of the equation of motion, which has the effect of a first-order kinetic relaxation of the pressure towards a reference value P_0 by the following equation

$$\frac{dP(t)}{dt} = \frac{1}{\tau_P}\left[P_0 - P(t)\right]. \tag{4.38}$$

A scaling factor, μ, leads to modifications on the coordinates and box vectors by chaging the volume of the system by

$$\Delta V = (\mu^3 - 1)V, \tag{4.39}$$

by which the pressure difference is strictly related to the change in volume through the following expression

$$\Delta P = -\frac{1}{\beta_T V}\Delta V, \tag{4.40}$$

where β_T is the isothermal compressibility of the system. Thus, solving the equations (4.38), (4.39), and (4.40) for μ one gets

$$\mu = \left[1 - \beta_T \frac{\Delta t}{\tau_P}\left(P_0 - P(t)\right)\right]^{1/3}. \tag{4.41}$$

Although this scaling formulation is done isotropically, it also can be extended to a general anisotropic system. In such a case, virial, kinetic energy, pressure, and scaling factor would become cartesian tensors, and the box volume would become the determinant of a matrix formed by the lattice vectors of the simulation box. The scaling factor, for instance, would be like

$$\boldsymbol{\mu} = \begin{pmatrix} \mu_{xx} & \mu_{xy} + \mu_{yx} & \mu_{xz} + \mu_{zx} \\ 0 & \mu_{yy} & \mu_{yz} + \mu_{zy} \\ 0 & 0 & \mu_{zz} \end{pmatrix}. \tag{4.42}$$

Besides that, the conserved energy quantities need to be modified, since the equation of motion has been as well. Thus, at every step, the work the barostat applies to the system needs to be subtracted from the

total energy:

$$-(\boldsymbol{\mu}-\mathbf{I})\,\mathbf{P}\,V = 2\,(\boldsymbol{\mu}-\mathbf{I})\,\boldsymbol{\Xi}, \tag{4.43}$$

where $\mathbf{I}$ is an identity matrix.

4.6 Periodic Boundary Condition and Minimum Image Convention

Periodic Boundary Condition (PBC) is used in order to solve two problems that arise from the necessity of simulating a system with a high number of particles: the computational unfeasibility that such a system has to work with, and its surface effects. This technique enables the accomplishment of simulations using a small relevant number of particles.

In the application of PBC, the particles are contained inside a simulation box that has images of each particle replicated on every direction. If a particle acquires motion and goes across one of the faces, and its image goes through an opposite face, the number of total particles inside the box is conserved. The figure 4.1 shows the PBC scheme.

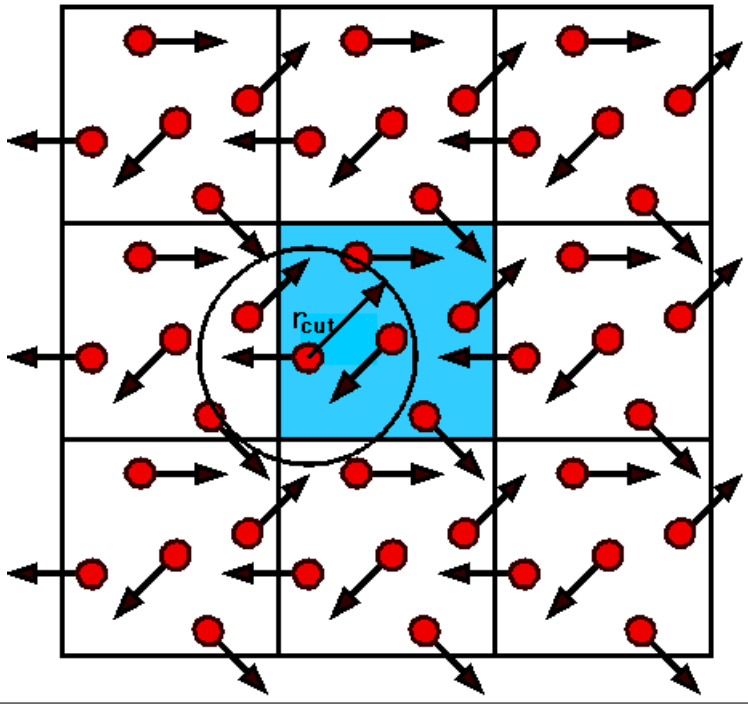

Figure 4.1: Pictorial representation of a system under PBC. The unit cell is painted as blue, the particles as red. The radius of the circle is related with the interaction between the particle in its center and the neighbors inside the circle. This figure was taken from [168].

PBC allows us to choose one region of space inside the simulation box in which the interactions by dissipative forces among the particles are calculated so as not reproduce interactions that have already

been performed. This region is determined by cutoff radius as shown in figure 4.1, and this is known as minimum image convention. By the way, the interactions of the pair of non-bonded atoms are defined within the cutoff radius, and their interaction force and energies are calculated for distances between the closest neighbors, which makes the simulation time decreases, for it would be impracticable to describe all the interactions of the system under investigation. In the Ewald method, a particle interacts with all the other particles inside the simulation box and their images, in a infinity array of periodic cells. Therefore, one can generalize the equation (4.12) into

$$U^{el}(\{\mathbf{r}^N\}) = \frac{1}{2}\sum_{\mathbf{n}}{}' \left(\sum_{i=1}^{N}\sum_{a=1}^{n_i}\sum_{j=1}^{N}\sum_{b=1}^{n_j} \frac{q_{ia}q_{jb}}{|r_{iajb}+\mathbf{n}|} \right) \tag{4.44}$$

where $\sum_{\mathbf{n}}$ indicates the summation over all the cubic images of the main cell, such that $\mathbf{n} = (n_x L, n_y L, n_z L)$, where n_x, n_y, and n_z are integers. The "$\prime$" sign indicates that $\mathbf{n} = \mathbf{0}$, $i = j$ will be omitted.

4.7 Molecular Dynamics Simulation Scheme

The state-of-the-art of MD simulations is rather laborious. The flowchart below in the figure 4.2 shows the summary of the scheme on how the MD algorithm works [139], which is based on GROMACS package. It also can be used as a general sketch on how to perform such simulations in other programs.

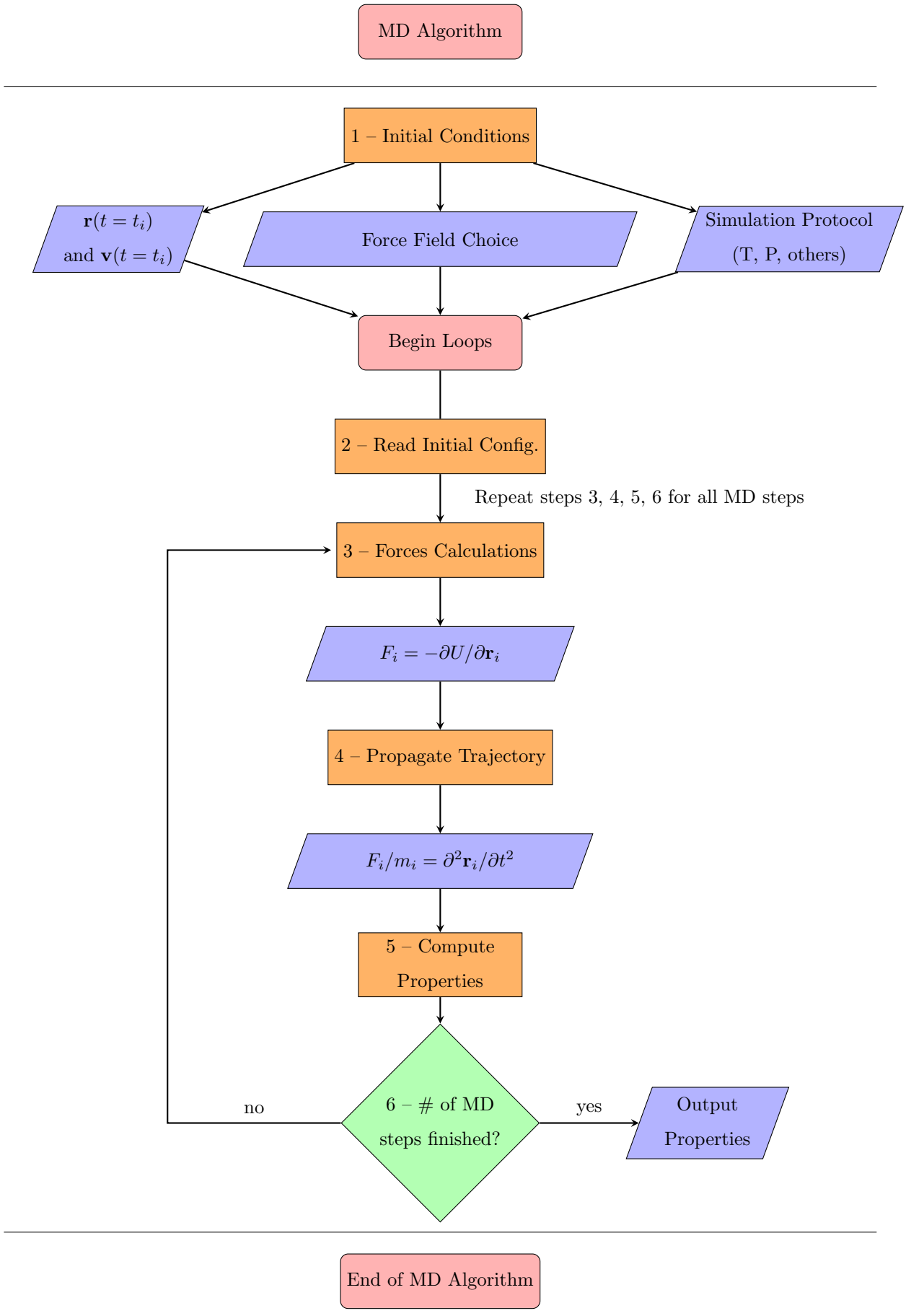

Figure 4.2: Flowchart shows us the required steps to perform a MD simulation.

Chapter 5

Computational Details

To address the proposed problems, we have been using the theoretical methodologies exposed in the chapters 2, 3, and 4. In this chapter, we would like to address the computational details behind the scenes. But, before going ahead, we would like to point out that we have employed the Generalized Gradient Approximation by Perdew, Burke, and Ernzerhof (GGA-PBE) [83] as the exchange-correlation potential function for it is well known that it better describes the structure of the systems. For the contributions from electron-ion interactions we have used two methods: ultrasoft pseudopotential (USPP) method [104] and projector augmented wave (PAW) method [94]. In fact, according to Bunău and Calandra [110], USPP methods are less computational time consuming compared to the NCPP one. This is a good choice for large systems, such as those that need to be simulated as supercells due to the required core-hole model. Also, it requires a smaller representation in terms of plane waves. PAW method, in turn, is well employed in reconstructing the all-electron wavefunction of the empty valence states to describe the properties from core states, which are an essential component for XANES simulations.

PAW method is used along with GIPAW method to reconstruct those AE wavefunctions in the presence an electromagnetic field as is shown in appendix F. Since PAW is a generalization of both the USPP and the linear augmented-plane-wave (LAPW) method[1], it is capable to work directly on the full valence and core wavefuntions, which is an advantage, as it is more efficient at an optimization level [94].

Besides, according to Kresse and Joubert [97] the total energy functional for USPP can be approximated by a linearization of two terms in a modified PAW energy functional, so that the Hamiltonian operator, forces, and stress tensor can be derived from this modified PAW functional. Such methods was shown to work pretty well in both molecular and bulk systems, and those results are closely related to the USPP ones, except in case of magnetic systems, such as Fe, Co, and Ni.

Therefore, in the following we will discuss the computational details according to the systems we have been working with, namely: carbon-based systems, diamond-like systems, and molybdenum-based

[1] You can refer to the chapter 17 from [78] for more information on this method. By now, the prior augmentation leads to basis functions that result in non-linear equations, which is more complicated that the linear ones expressed in fixed energy-denpendent basis, such as plane waves. In a nutshell, the linearization is achieved by defining augmented functions as linear combination of radial function and its derivative, which form a basis. Thus, any augmentation method can be written in a linearized form.

systems along with acetonitrile molecules. This was necessary due to the different parameters used for each required computational simulation, as will be better explained throughout this chapter.

5.1 Carbon-based Systems

To perform the calculations, we have relied on Density Functional Theory (DFT) as implemented in QUANTUM ESPRESSO package [43]. In order to get a better description of the unit cell of all the graphite systems, we have performed the optimization of the unit cells using GGA-PBE along with the PAW method. In XANES calculations we have used USPP and GIPAW approach.

Based on the recent work by Del Grande, Menezes, and Capaz [169], a systematic analysis of non-local van der Waals (vdW) exchange-correlation functionals was performed, in order to obtain the best structural and vibrational properties of multilayer graphene in face of experimental results, we have used the parameters they employed. They found that the vdW-DF1-optB88 functional [170] has the best overall performance. Throughout the calculation of graphite systems, we have used energy cutoff of 60 and 480 Ry for plane-wave expansions of wavefunctions and electronic density, respectively. The atomic and cell optimization were performed within a convergence threshold of 10^{-6}Ry bohr^{-1} on forces, and 10^{-5}Ry on energies.

Initially the Brillouin zone was defined according to the Monkhorst-Pack (MP) scheme [93] used in [169], which was 16x16x16 for graphite. However, to minimize the computational cost in supercells, we did a somewhat different approach. Firstly, for graphite systems, starting from the optimized parameters from the Del Grande's work ($a_0 = 2.47$ Å, and $c_0 = 6.68$ Å), we made a variable cell (VC) calculation, which previded us with the new parameters ($a = 2.46$ Å and $c = 6.68$ Å). Then, with these new parameters, we performed a convergence test of the in-plane k-points. We found 10 k-points. Afterwads, a convergence test on the perpendicular direction led us to 5 k-points. Then, as the supercell is a 3x3 expanded unit cell, we found ourselves with a MP k-point mesh of 4x4x5 k-points.

Secondly, for cubic diamond, we used the experimental parameter found in 1913 [171, 172] (3.55 Å), obtaining $a = 3.57$ Å after variable cell optimization. Then, we performed a convergence test on k-points, which gave us 8x8x8 k-points. Within the 2x2x2 supercell with 64 carbon atoms, it reduced to 4x4x4 k-points. At last but not least, in case of hexagonal diamond, after the VC optimization (getting $a = 2.51$ Å and $c = 4.18$ Å), we found also 8x8x8 k-points after the k-point test. In the 3x3x2 supercell, we got 3x3x4 k-point mesh. The cutoff energies used in these systems ware 50 and 350 Ry for wavefunctions and electronic density, respectively.

Concerning XANES simulations, we really need to have those supercells to perform XANES calculations, since the X-ray absorbing atom, which has core-hole, making the system defective, cannot interact with its periodic images. Using these supercells, the core-hole atoms stay about 7.6 Å far from the images, which is a acceptable value. To such calculations we have changed the grid mesh to 10x10x10

k-points, and used a constant value of 0.5 eV throughout the energy range for the half width at half maximum of a Lorentzian function for the spectral lineshape.

5.2 Diamond-like Systems

Indeed, it is custumary one makes convergence tests of cutoff energies to fill the space out with a plane-waves basis set. However, nowadays we have repositories with available ready-to-use pseudopotentials. One of them that is well-known is the PSlibrary [173,174], which is mantained by Andrea dal Corso, and co-workers, and distributed under GNU licence. He made a detailed description of this repository that is given in [175], using the code ld1.x from QUANTUM ESPRESSO. A series of tests have been made as well, for example, by [176], which can be found in Materials Cloud website [177]. As a matter of fact, we have used the pseudopotentials from PSlibrary version 1.0.0 [178].

The reason why we changed cutoff energies to lower values for diamond systems, as mentioned in the section 5.1, is to lower the computational cost. Following the notes on pseudopotential generation by Dal Corso [179], one can find that the minimum cutoff suggested by the generated pseudopotential can be used, provided that it reproduces well some experiments. Also, we can find a chart contaning convergence plots for each atom, according to the pseudopotential library version in [177]. Nonetheless, for diamond-like systems we have used the same values as the ones used for graphite systems.

The relaxed structures were obtained from [56–58,180]. By employing a MP grid mesh of 3x3x1, as the systems under investigation have a vacuum between the layers of around 20 Å, we also performed optimization relaxation of the atomic positions on all the structures using QUANTUM ESPRESSO package.

Regarding XANES calculations, we have used a grid of 6x6x1, and also used a constant value of 0.5 eV throughout the energy range for the half width at half maximum of a Lorentzian function for the spectral lineshape.

5.3 Molybdenum-Based Systems and Acetonitrile

The systems under discussion in the following is composed by acetonitrile molecules interacting with Mo-based systems: MoO_3 and MoS_2. To address such systems, we have treated the huge combined systems (more than ten thousand atoms) using Molecular Dynamics (MD) to visualize the atomic time evolution of each system through the solution of the Newton's motion law, followed by the DFT-based QM method, on which we take into account the influence of the quantum behavior of the electrons of the systems. For this latter method, we cannot deal with a system with $\sim 10^4$ atoms. Instead, we narrow what we want to investigate down, which lead us to a bit more than one-hundred atoms.

For the aforementioned solids, we have used the parameters found in the Aflowlib repository

[181,182]. We have used energy cutoff of 50 and 330 Ry for plane waves and electronic density, respectively, and a Monkhorst-Pack mesh of k-point of 13x13x3 (12x7x3) k-points for MoO_3 (MoS_2) unit cell. We also used PBE-GGA exchange-correlation functional, employing PAW method for suitable description between ionic and valence electrons. By treating the composed system during the MD simulations, we have used the Generalized Amber Force Field (GAFF) [183] for the liquid phase of acetonitrile (ACN) molecules, which was obtained from [184]. For the force field of the solid, in turn, we have used a Universal Force Field (UFF) [185] for MoO_3, which was obtained from the web-based server OBGMX [186, 187] that generates topologies using UFF force field. It is based on Open Babel suite [188] and is able to deal with periodic systems; for the MoS_2, we have used the force field employed in the work by Sresht *et al.* [189]. All the simulation boxes used to perform MD simulations on systems composed by one of the solids and by acetonitrile molecules, or just by acetonitrile, were built using PACKMOL package [190].

To study the charge transfer of the composed system, we have used both the localized density approximation exchange-correlation functional by Perdew and Zunger [85] (PW-LDA) and the PBE-GGA functional [83]. For atomic relaxation purpose within the scope of the GGA approximation, we have used the same van der Waall functional [170] used in section 5.1. We also used PAW method to express the interaction between the valence electrons and the ionic ones. Since the computational cost becomes dense for such a huge system, we have used small slices of the composed system, as will be explained later in section 7.2. A MP grid mesh of 2x2x1 was employed for the charge analysis in the cell extracted from the MD simulations.

5.4 Water and oxygen molecules

We also performed MD simulations on the ACN simulation boxes containing 0.1 mole fraction of either H_2O or O_2 (55 molecules), which can be seen as "contaminants" of the ACN, since in the exfoliation process pointed out by the reference [73] the solid was thermally treated in an inert ambient, but the dispersion agent (liquid acetonitrile) was not. For the H_2O molecules, we have used the force field (FF) indicated by [191], which was derived from TIP3P parametrization class [192], that was used to simulate liquid-phase exfoliation of MoS_2 using N-methyl-2-pyrrolidone (NMP) as solvent, and also 0.1 mole fraction of H_2O. According to that reference, it was found to be crucial for stabilization of MoS_2 nanosheets in NMP dispersions. For the O_2 molecules, we have employed a force field used to simulate its absorption on solids, such as silica and zeolites [193]. This FF was constructed as a three sites molecules: two oxygen atoms connected via a massless point charge (a virtual site).

Chapter 6

XANES simulations in diamond-like two-dimensional materials

It was asserted that the diamond hexagonal phase (also known as londasleite[1]) would come from asteroidal impact due to the huge pressure involved in the process. However, it was never found as a discrete material, as occurs with cubic diamond [196]. In fact, it was discovered as faulted and twinned cubic diamond, and, actually, the londasleite meteorite sample would be a disordered stacking of the hexagonal and cubic phases [197]. However, shock experiments [47, 198] have shown that it is feasible to create a relatively pure londasleite in a high-pressure environment. Thus, we will discuss both the cubic and the hexagonal phases, the former one being the most stable as shown by theoretical studies [199, 200]. Our results have shown that the energy difference per atom between them is around 28 meV.

As XANES simulations can be used to probe empty states in solids [39], such a method along with DFT calculations can be a powerful tool to probe local environment of an atom (either a bare atom, or a functionalized one). In fact, that can happen whenever a X-ray photon strikes the atom, which can be probed by XANES simulations using the steps we have outlined in the section 3.3.4. These simulations were performed on the materials shown in figure 6.1, and also on the ones shown in figure 6.16. As a matter of fact, as diamondol (shown in figure 6.16-a) is formed from the pressurization of graphite layers [56], and bi-F-diamane (figure 6.16-d) from the fluorination of AB-stacked bilayer graphene grown in a chemical vapor deposition (CVD) experiment on a CuNi-(111) surface [57], we thought it would be interesting to firstly do an analysis of the precursor layers, namely, hexagonal graphite (HG), also known as Bernal graphite (figure 6.1-c), and bilayer graphene (BLG), as well as an analysis on both the cubic and hexagonal diamonds (CD and HD, respectively). Since diamond consists of carbon atoms bonded by sp^3 hybridization, whereas graphite systems are made up by planes of carbon atoms bonded through sp^2 hybridization, which are stacked by van der Waals forces, we would like to compare results of the diamond-like systems to those mentioned carbon allotropes phases. By doing so, we expect to verify

[1] Hexagonal diamond is named this way in honor of Dame Kathleen Lonsdale, an Irish crystallographer who was the first to use Fourier spectral methods for solving the structure of hexachlorobenzene. In addition to it, she also worked on the synthesis of diamonds, and its study using X-rays [194, 195].

whether such material remains close to which hybridization configuration, the former or the latter ones, in order to provide a theoretical characterization of these systems.

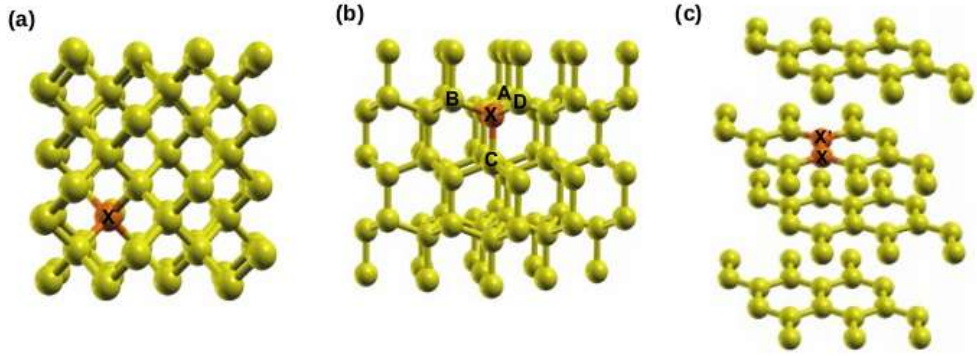

Figure 6.1: Pictorial representation of (a) and (b), cubic and hexagonal diamonds, respectively, and (c) Bernal graphite. Yellow sphere represent carbon atoms. The orange ones represent the non-equivalent carbon atoms probed by XANES simulations.

In the following, the experimental results for the precursor materials are shown. Our simulated peaks, shown in table 6.1, are in good agreement to the experimental data, which are shown in parenthesis. These experimental values can be checked out in the figure 6.2, which are the results for the diamonds (CD and HD) and both Bernal graphite (HG) and bilayer graphene (BLG). Just for completeness, the theoretical result shown in figure 6.2-(b) was performed based on a cluster model calculation using DV-Xα method [201], which is based on the first-principle molecular-orbital (MO) calculations [202] implemented in the package SCAT [203]. All the simulated values are within the energy resolution of some experiments [204, 205], being the major difference 1.5 eV for HD, whereas the minor one is 0.2 eV for σ-transition of BLG, with around 0.1% of relative error.

Table 6.1: Comparison between our XANES simulations and the experimental results (in parenthesis) for CD (cubic diamond), HD (hexagonal diamond), HG (hexagonal, or Bernal, graphite), and few-layers graphene (bilayer graphene, BLG). These values are given in eV. A figure with the C(K)-edge photoabsorption spectra for each of these systems can be seen in Fig. S1.

System	**π-transition**	**σ-transition**
CD	–	289.0 (289.5 [2])
HD	–	288.4 (289.9 [206])
HG	284.7 (285.5 [204])	291.2 (292.5 [204])
BLG	284.8 (285.5 [205])	291.3 (291.5 [205])

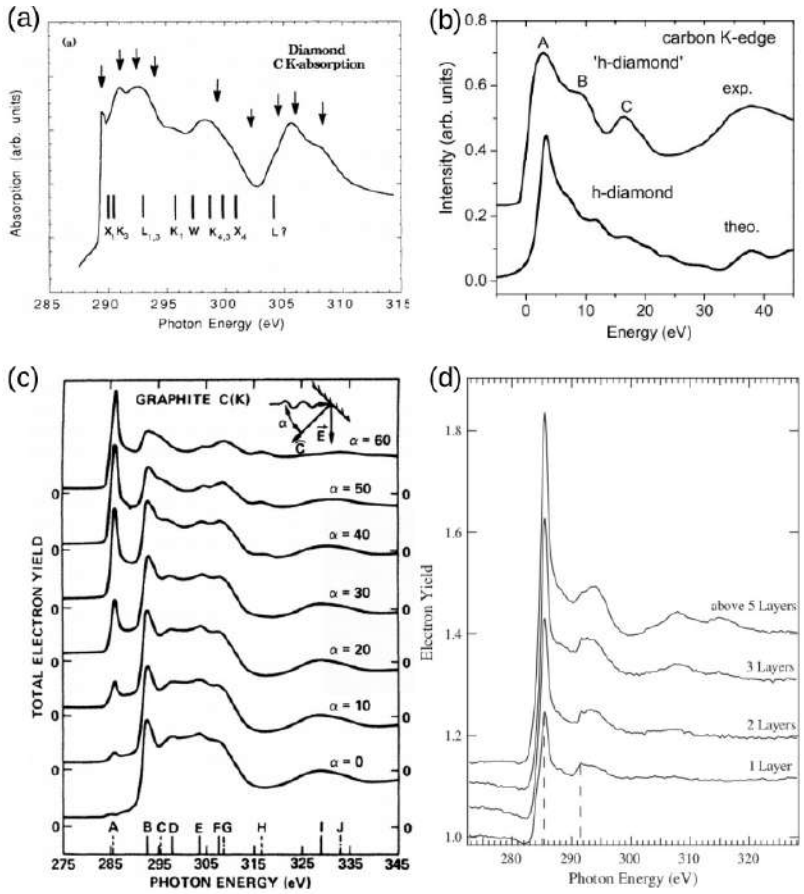

Figure 6.2: Experimental results for (a) CD [2] (b) HD [207], with experimental result from [206], (c) HG [204], and (d) few-layers graphene (FLG) [205].

So, the following sections will be presented as follows: in section 6.1 cubic and hexagonal diamonds will be addressed so that we can understand the spectra of a sp^3-hybridized material; in section 6.2, in turn, we will do a systematic study on the Bernal graphite along with the BLG system under XANES investigation, performing an angular-dependence analysis of the carbon K-edge spectra; finally, the X-ray probing of the diamond-like materials will be studied in section 6.3.

6.1 Probing Diamond Materials

6.1.1 Cubic Diamond

Because diamondol seems to present an admixture of sp^3- and sp^2-hybridization characters on its carbon atoms, it is important to analyze the XANES spectra of the cubic diamond phase. Electronic properties was analysed in figure 6.3, which shows the projected density of states (PDOS) for the cubic

system without core-hole (left-hand side) and with core-hole (right-hand side)[2]. PDOS for systems with core-hole mean that one electron has been removed from the atomic core, specifically from the 1s-orbital, due to the X-ray incidence. Henceforward, as in figure 6.3, the Fermi level is set to 284.2 eV, which is the 1s core-level binding energy of the electron struck by the X-ray photon [208]. Such a value is adopted by the XSpectra code in the QUANTUM ESPRESSO suite in computing XANES spectra for carbon atoms.

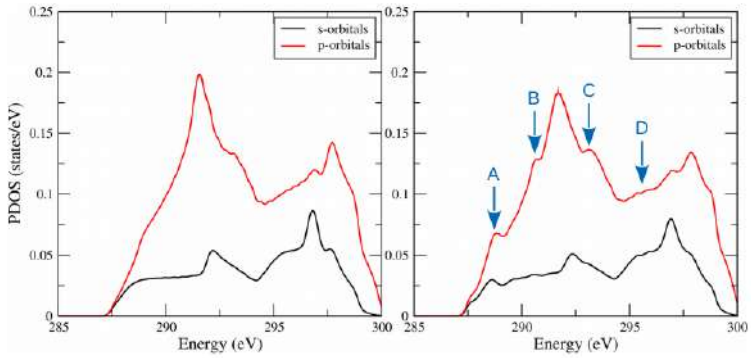

Figure 6.3: Projected density of states (PDOS) for cubic diamond without (left) and with (right) core-hole. The blue arrows highlight the main differences in comparison to the bare system.

Electronic features of both bare system and core-hole one can be compared through figure 6.3, by which we can see small differences between them. They are pointed out by blue arrows on the right-hand side of that figure. Indeed, there appear kinks at 288.6 eV for both s- and p-states. Also, there are new p-states at 290.6 eV and 293.1 eV, as well as around 295.0 eV. The labels are to be regarded as relevant states to the equally labeled peak in XANES spectra, as explained below[3].

By comparing XANES simulation with experimental results in figures 6.4(a) and 6.4(b), respectively, one can see a general good agreement. Because of the symmetry of the cubic diamond, both the perpendicularly polarized spectrum and the parallely polarized one are the same. Moreover, features in the spectra can be attributed to the PDOS in figure 6.3 (right-hand side), as explained in [2], where there are critical points, which were discussed in the last paragraph and pointed by blue arrows. For example, the first peak in figure 6.4(a) (labeled with the letter A) is strongly related to the newly-mentioned p-states at 288.8 eV in figure 6.3. Besides, the less prominent peak, the B one at 290.6 eV can be matched to the B-labeled states in the PDOS. If we slide down through the spectra up to around 295 eV, we can see two very tiny ripple, peaks C and D at 293.3 and 295.3 eV, respectively. However, the p-states related to the D peak can barely be distiguished from the bare system on the left-hand side of the figure 6.3. Finally, the decreasing of the XANES intensity around 300 eV can be explained through the lack of p-states in figure 6.3.

[2]From now on, we will refer systems without core-hole, i.e., system in which the atoms have all core-electrons untouched as a bare system. This system is said to be found on its ground state.

[3]In fact, all the following analysis will be performed observing how the core-hole system changes as compared to their counterpart bare system. The most important changes will be labeled according to the same labels used in XANES spectra, in order to make connections between the newly-generated states and the peaks of the spectra.

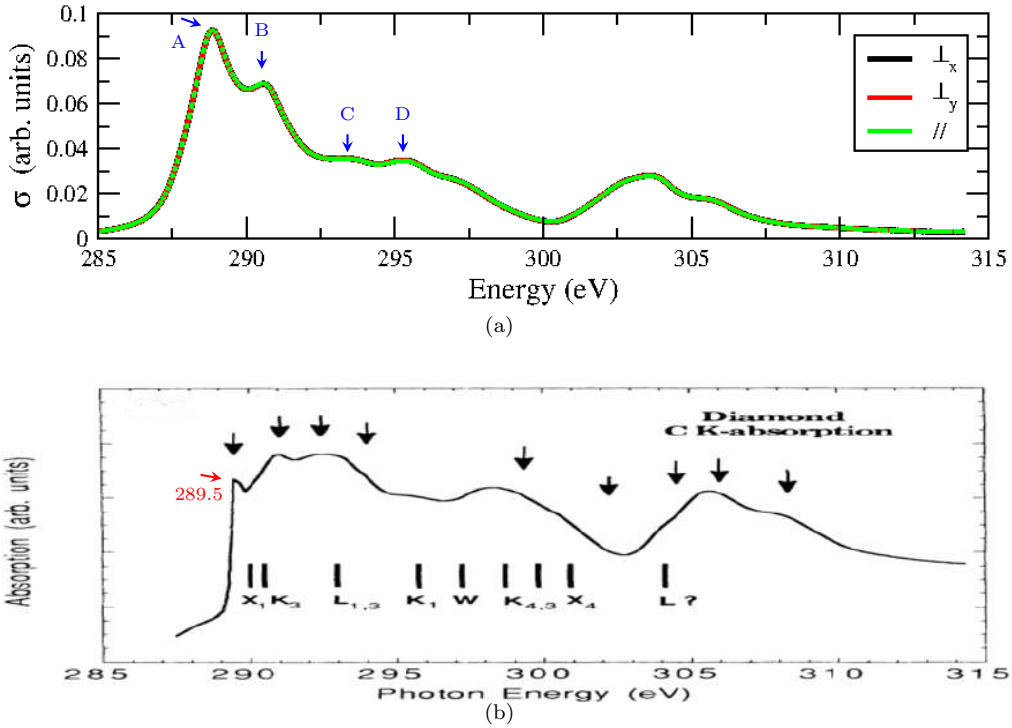

Figure 6.4: (a) Calculated XANES spectra for cubic diamond: black and red curves represent X-ray polarization perpendicular to the material; green curve represents X-ray polarization parallel to diamond. (b) Experimental results from [2] for C K-edge absorption spectrum of cubic diamond. The letters underneath the spectrum refer to special points within the Brillouin zone, and its values were calculated in [209], which are listed in table I after [2].

According to Ma *et al.* in [2], 1 s core excitation is assigned to 289.5 eV, which is 5.5 eV above the valence band maximum (VBM), and is related to the 1 s-σ transition. That value is close to the high symmetry critical point X_1 (red arrow on the bottom of the figure 6.4(b)), which is 5.91 eV above the VBM [209]. Interestingly, an indirect energy gap of 5.5 eV was experimentally found [210] with the VBM at Γ, and the CBM along the $\Gamma - X$ path in the Brillouin zone [210, 211], which is the value assigned to the 1s-σ^* transition. Our calculation shown an indirect energy gap of 4.16 eV, whose value, compared to other calculations we have found (4.12 eV [212], and 4.34 eV [213]), is in good agreement. The underestimation with respect to the experimental value shown above is expected for this GGA-PBE functional we have employed. The first peak in XANES spectrum is around 288.8, which is 5.6 eV above the VBM. Indeed, it agrees very well with the results after Ma *et al.*.

Through the figure 6.5, which shows the PDOS of both the first-neighboring atoms (figure 6.5(a)) of the X-ray absorbing one (figure 6.5(b)), one can see how those atoms contribute for the XANES spectra. The first-neighboring atoms have the same PDOS due to the symmetry of the system. The projected density of states on the absorbing atom comes both from the valence electron orbitals and from the orbitals of the required projectors (6.5(b)) to perform the XANES simulations. As one can see, those PDOS fairly correspond to the aforementioned peaks, especially those of 288.8 eV and 303.75 eV, which come mainly from the absorbing atom. Furthermore, the peak at 295.3 eV (labeled as D), which could not clearly be matched through the s- and p-orbitals of the figure 6.3, can be assigned to the first-neighboring atoms.

Also, we can see that 3 s- and 3 p-orbitals mostly contribute to the shoulder-like part of the spectrum, around 303.75 eV. In fact, the XANES simulation is in accordance with the experimental results of [2], which are also reported in [39].

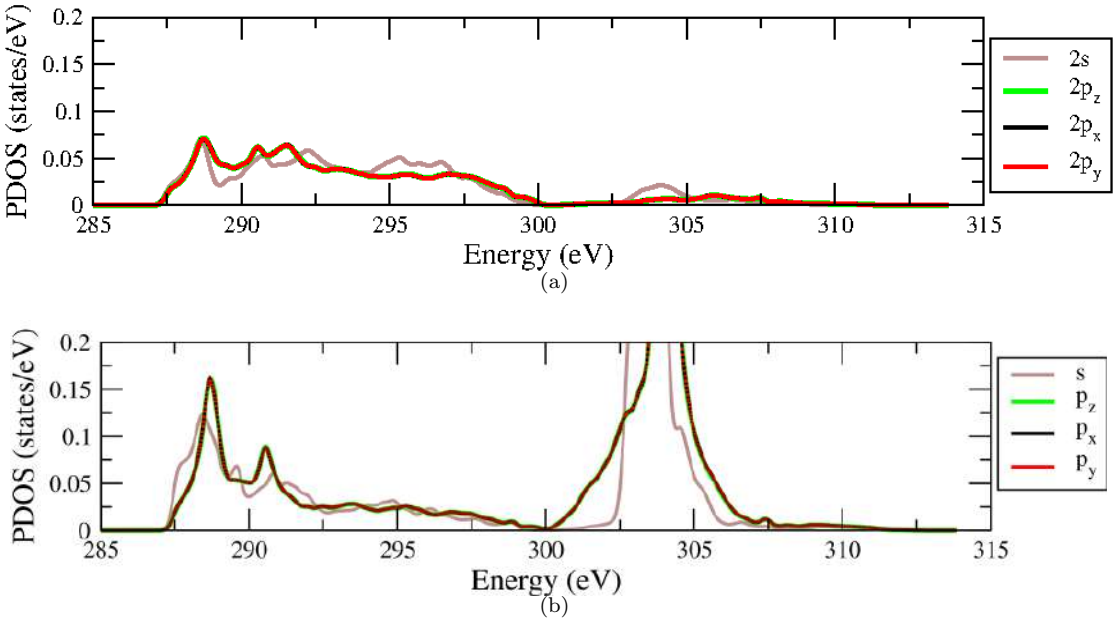

Figure 6.5: Projected density of states on: (a) the first-neighboring atoms of the X-ray absorbing one. All three first-neighbors have the same PDOS due to the symmetry of the system; (b): X-ray absorbing atom, where we have the combination of 2 s and 3 s orbitals, as well as 2 p and 3 p orbitals in the plot. Both the 3 s and 3 p orbitals are required to perform XANES simulations, as explained in the section 3.3.1. From now on, all the following figures regarding the absorbing atom will have the same labels.

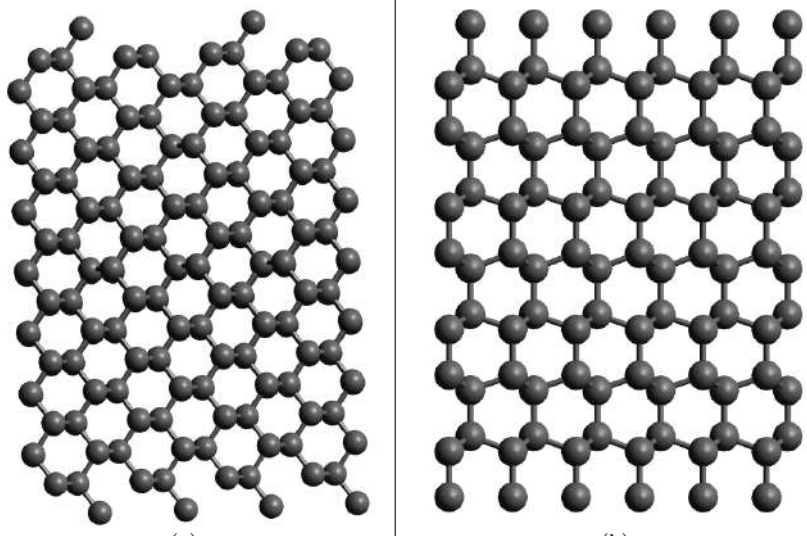

Figure 6.6: (a) Cubic diamond is the arrangement of the six-membered carbon atoms layers with a shift half-way the diagonal of a ring; (b) In the hexagonal diamond each layers is a mirror image of the previous one. The first structure is seen from the top-view of the [101] crystalographic direction. The latter one is seen from [0100] direction.

6.1.2 Hexagonal Diamond

The difference between the cubic and the hexagonal diamonds relies on how those layers of carbon atoms are stacked. Through the figure 6.6 we can visualize the slight difference between these phases. The former one has its six-membered rings shifted by half-way across the diagonal of a ring, whereas the hexagonal one has its rings mirrored from the neighboring layer [197]. Therefore, it is expected that the landasleite spectrum becomes different from the cubic one.

However, before analysing its spectrum, it is important to see the electronic properties through the PDOS for the systems with and without core-hole. By looking at the figure 6.7, we can see that a kink also appear at 288 eV for the p-states PDOS curve of cubic diamond (labeled as A). Nonetheless, above it, both with and without core-hole PDOS curves are alike in many aspects. Figure 6.8 shows its XANES simulation and the experimental EELS[4] results [196]. Looking at the energy scale of the figure 6.8(b) we can see that our results (shown in figure 6.8(a)) is pretty much the same. For instance, around 287.5 eV, we can see that there is a tiny shoulder due to contributions from the in-plane polarization (overlaid red and black curves), while around 297 eV another shoulder arises, this time due mostly to the parallel component (green curve).

The local PDOS on the first-neighbor atoms of the absorbing one are shown in figure 6.9. The peak A from XANES simulation, which has contributions from both perpendicular and parallel X-ray polarizations, has larger contribution from p_x orbital of the in-plane atoms, as well as an even larger contribution the p_z orbital from the out-of-plane one. Similarly, from figure 6.9(c), we can see that the absorbent one itself also contributes for the peak in the region of 288 eV. Although there are other two observed peaks related to the differences observed in the figure 6.7, the local PDOS does not show a straightforward contribution from the first-neighbors of the absorbent.

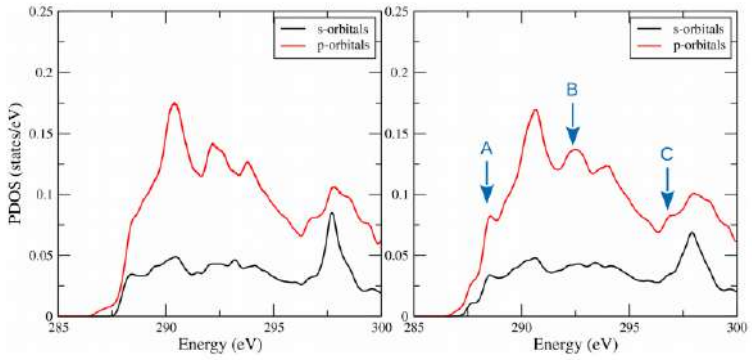

Figure 6.7: Projected density of states (PDOS) for hexagonal diamond without (left) and with (right) core-hole. The blue arrows highlight the main differences in comparison to the bare system.

[4]It stands for Electron Energy Loss Spectrum.

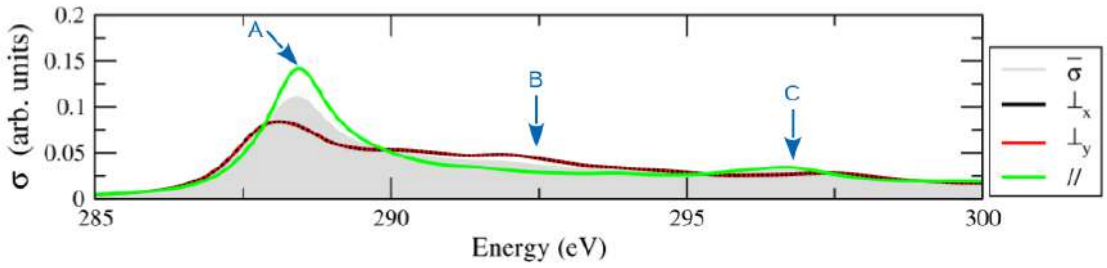

(a)

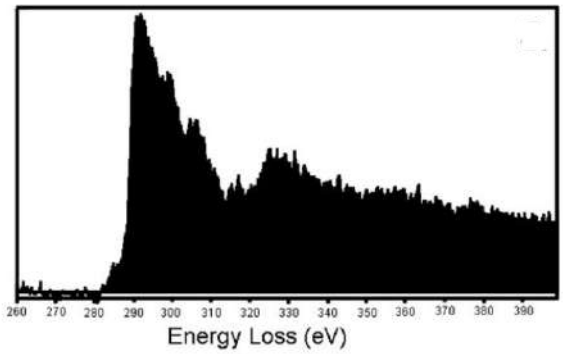

(b)

Figure 6.8: Simulated XANES for hexagonal diamond (a), and its experimental EELS result (b) from [196] (figure 4a from supplementary information of that reference) in a natural londasleite sample of the Canyon Diablo's meteorite. The grey, shaded area, $\bar{\sigma}$, refers to the mean of the polarized ones (black, red, and green curves). See text for more information. The Fermi level is set to 284.2 eV.

However, one could wonder about the EELS spectrum from figure 6.8(b). In fact, this result was published in 2014 by Németh and co-workers [196] when they were engaged at showing the necessity for re-evaluating the interpretation of londasleite material. In their study, they used a natural sample from the Canyon Diablo's meteorite, from which the londasleite was first discribed [195, 214] more than 50 years ago, as well as a synthetized one [215]. Actually, according to [35], in its section 2.5, we can learn that 100–300 keV eletron beams can be used to probe core level of atoms in a material. Within those energies, electrons can be approximated as plane-waves, so that the cross-section would be proportional to

$$\sigma \propto \left|\langle \Phi_f | e^{i\mathbf{q}\cdot\mathbf{r}} | \Phi_i \rangle\right|^2 \delta(E_f - E_i - \Delta E), \tag{6.1}$$

where ΔE is the electron energy loss. With the expansion given by the equation (3.13), one can certify the EELS spectrum is proportional to the XAS cross section:

$$\sigma_{EELS} \propto \sigma_{XAS} \propto \left|\langle \Phi_f | \mathbf{q}\cdot\mathbf{r} | \Phi_i \rangle\right|^2 \delta(E_f - E_i - \Delta E) \tag{6.2}$$

In fact, in case of high-energy X-ray beam, the X-ray can also be approximated as a plane-wave. That is

the reason for us to compare the figure 6.8(a) to the figure 6.8(b).

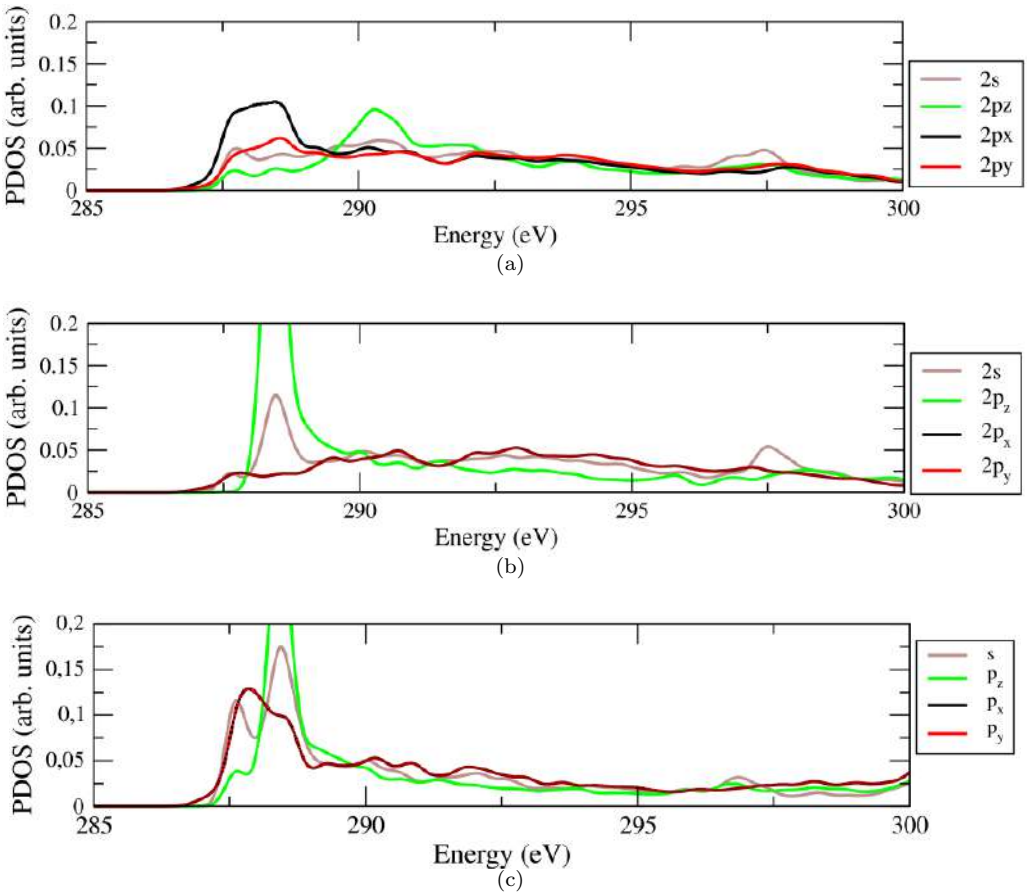

Figure 6.9: Projected density of states on: (a) the in-plane first-neighboring atoms of the X-ray absorbing one. All three first-neighbors have similar PDOS due to the symmetry of the system; (b) the out-of-plane carbon atom, and (c) the X-ray absorbing one.

6.2 Hexagonal Graphite and Bilayer Graphene

Electronic properties, and XANES spectra analysis will be addressed for these layered systems, whose atoms are bonded together by sp^2-hybridization throughout the in-plane directions, while those planes interact weakly by van der Waals forces through π-orbitals, which are perpendicular to them. Several works have reported the transition from graphite into diamond [215–223] mostly through either shock-induced or pressure-dependence phase conversion from hexagonal graphite (HG) to hexagonal diamond (HD), and also from rhombohedral graphite (RG) to cubic diamond (CD). That is the reason why we are going to treat graphite systems in this section. Indeed, Rosenberg *et al.* reported in 1986 a study showing that the C(K) near-edge X-ray absorption fine structure (NEXAFS) of highly oriented pyrolytic graphite (HOPG) changes dramatically with the X-ray incidence angle α [204], which we are going to define as the angle between the incident X-ray polarization vector, $\hat{\varepsilon}$, and the direction perpendicular to

the material surface, $\hat{c}$, that can be seen in the schematic figure 6.10.

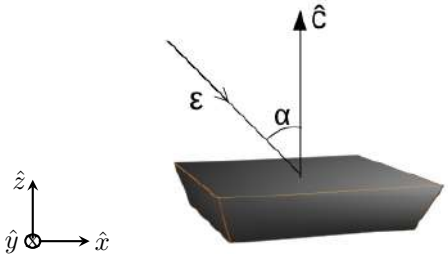

Figure 6.10: A sketch of the angle α between the incident X-ray polarization vector ε and the direction perpendicular to the crystal surface $\hat{c}$.

According to Rosenberg *et al.* [204], angular variations of the spectra depends on the X-ray polarization vector. Indeed, in HOPG the σ-bonding symmetry is lifted when the $\hat{\varepsilon}$ is aligned with the bonding axis, otherwise π-symmetry is probed when $\hat{\varepsilon}$ is perpendicular to the interatomic bonding axis. So, in a nutshell, for carbon K-near-edge structure, we have the following transitions:

$$\begin{aligned} 1\,\mathrm{s} &\rightarrow \sigma, \text{ for } \hat{\varepsilon} \perp \hat{c}, \\ 1\,\mathrm{s} &\rightarrow \pi, \text{ for } \hat{\varepsilon} \,//\, \hat{c}, \end{aligned} \tag{6.3}$$

One should be aware that, in the Rosenberg's results, the angle values (α) shown on the left side of the figure 6.11(a) do not correspond to the inset shown therein. It must have been typo errors, so that we would like to draw your attention to that. Their results assigned $1\,\mathrm{s} \rightarrow \pi$ transition to the peak at 285.5 eV, 2.0 eV above the Fermi level [204], marked with a letter A at the bottom of the figure 6.11(a). The σ-resonance, in turn, is observed at around 292.5 eV[5], letter B at the same figure. Besides, for dipole transitions, the intensity of a pure $1\,\mathrm{s} \rightarrow \pi$ transition is proportional to $sin^2(\alpha)$, as shown in figure 6.11(b).

Figure 6.12(a) shows how the angle dependence of the incident X-ray polarization influences the form of the spectra. As the incident X-ray angle becomes perpendicular to the normal direction to the material surface, $\hat{c}$, the $1s \rightarrow \pi$ transition (blue arrows) is turned off – please, refer to the figure 6.10 for a better understanding. Therefore, in that case, the $1s \rightarrow \sigma$ trasitions becomes more apparent, which are displayed as brown arrows. As seen in figure 6.12(a), an outstanding feature of this X-ray angle-dependence analysis is that the peak A loses almost completely its intensity as α increases. Besides, we have noticed that as long as the perpendicularly polarized curve drops down, the parallel polarized spectrum seems to compesate it at 293.8 eV, which is linked to the states on the right-side inset of the figure 6.13. One last thing to observe is the linearity of the intensity of the peak A with $sin^2(\alpha)$, as displayed in figure 6.12(b). It does resembles the trending observed in [204], which asserts the π-character of that peak.

[5]It was also noted this peak at 292 eV for C−C intermolecular bond length of 1.42 Å, 7.3 eV above the binding energy 284.7 eV [204, 224].

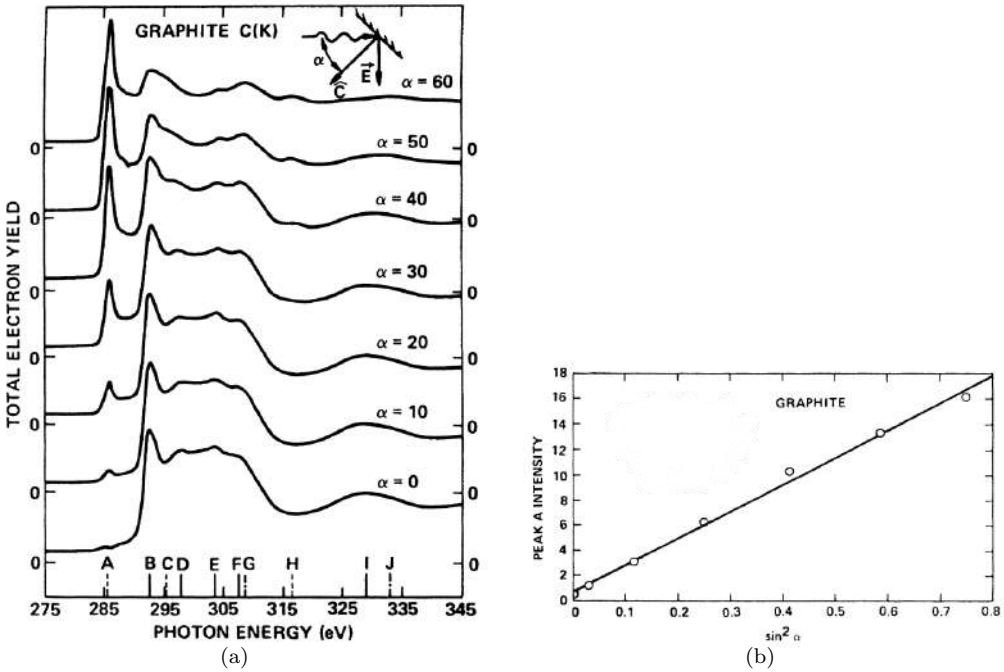

Figure 6.11: Experimental results after Rosenberg *et al.* (a) showing the carbon K-edge photoabsorption spectra of HOPG for various incident X-ray angles α. At the bottom of the figure, dashed lines represent π-symmetrized states, and solid line represent states with σ symmetry. The study of those correspondences can be found in [225]. The dependence of the relative intensity of peak A with $sin^2(\alpha)$.

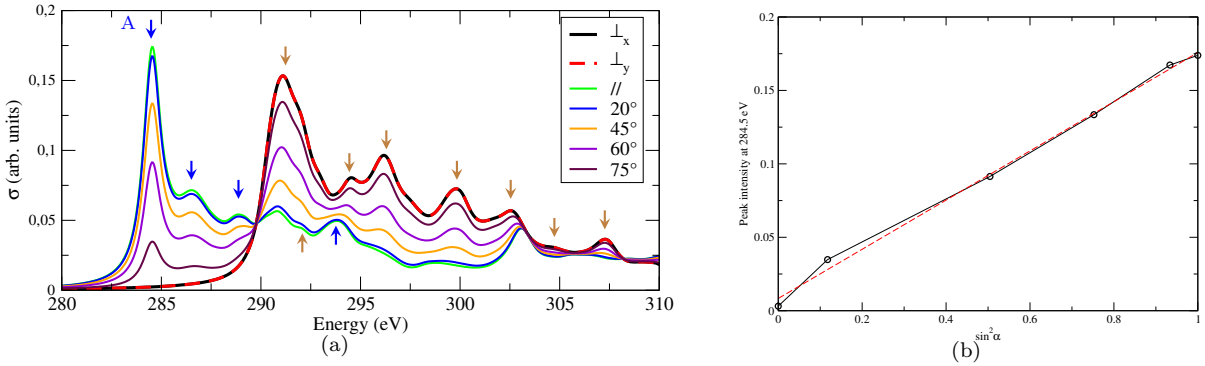

Figure 6.12: (a) Angle-denpendece of XANES for HG strucure, where the X-ray incidence angle is defined between the X-ray direction relative to the crystal coordinates of the material and the axis perpendicular to the material surface. (b) Plot of the peak intensities around 284.5 eV (peak A) versus $sin^2(\alpha)$, where α is the angle between the incident X-ray and the direction perpendicular to the crystal.

Here, we will investigate the electronic properties of both Bernal graphite and AB-stacked bilayer graphene (BLG), along with the projected DOS on the atoms, as it was done in section 6.1 for diamond systems. We will analyze them in the following along with the XANES simulations.

Electronic properties of both systems are shown in figure 6.13, wherein the PDOS on p-orbitals of bare ones are displayed on the left-hand side, and the systems with core-hole, on the right-hand side. By comparing both the bare systems, they present almost the same p-states (within our work's theoretical

level), except for the states within the 286 – 290 eV range, where one can see a ridge-like form of the states related to the BLG. When it comes to the core-hole systems (right-hand side), the major differences one can notice are pointed out by blue arrows. Their labels are linked to the XANES peaks observed in figure 6.14, whose spectra are taken as the mean of the contribution from the non-equivalent atoms, considering also the polarization contributions. Firstly, the states spotted by the A label (at 284.8 eV for BLG) are around 0.15 eV above the ones for HG system. Sencondly, at B (285.6 eV) there are also states related to the promoted core-electron. Those are states that noticeably differ from the bare system and have influence on the XANES spectra owing to the dipole trasition rule ($\Delta l = 1$), as one can see in the aforementioned figure. Other states that contribute for the D and E XANES peaks are also shown in the figure: 291.3 eV and 292.1 eV, respectively. Although the PDOS associated to the BLG system are higher, they do not influence on the XANES peaks as much as the HG-related states. This is observed owing to the orbital hybridizations, although for 1s-π^* transitions only p_z orbitals are accounted for. Moreover, there is the C peak, which is related to a shoulder-like curve of states (at 287 eV) shown in figure 6.13. These reflect on the form of the XANES curve for BLG system (figure 6.14).

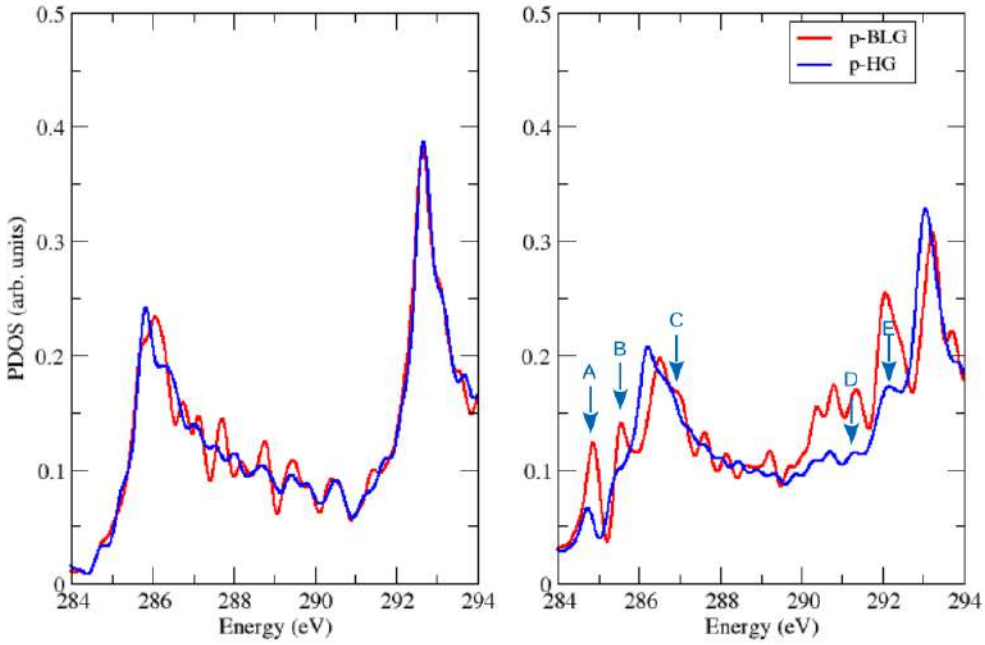

Figure 6.13: Projected density of states (PDOS) on p-orbitals per atom for HG and BLG without (left) and with (right) core-hole. The Fermi level is set to 284.2 eV, which is under the vertical, violet, dashed line.

First of all, it is important to note that the peak A is related to the $1s \rightarrow \pi$ transition, which occurs at 284.7 eV (284.8 eV) for HG (BLG), 0.8 eV below that reported by Rosenberg in [204] (285.5 eV), and 0.3 eV below that after Fischer *et al.* [226] (285.0 eV). Overall, it is an acceptable value. The second main peak (peak D) is related to the $1s \rightarrow \sigma$ transition, which is around 291.3 eV. In fact, the value reported by both aforementioned references is 292 eV. One can see that there is no shift in the peak associated with the π transitions as the angle α diminishes, whereas the peaks D undergoes a tiny shift from 291.3 eV to 290.8 eV as α cuts down (refer to the figure 6.12(a)). It is important to mention that

the difference on the XANES contributions from the two inequivalent sublattice is practically null.

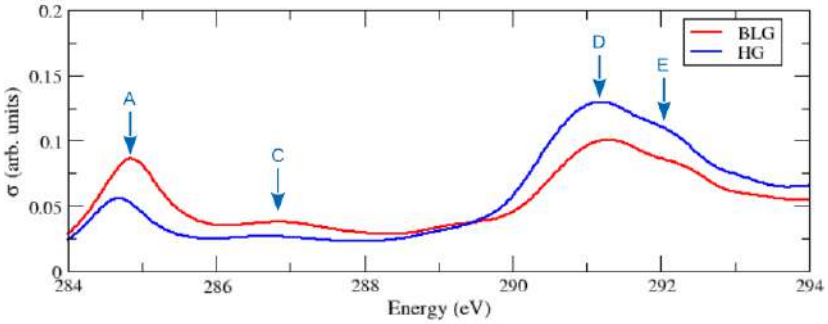

Figure 6.14: XANES simulations for both hexagonal graphite (HG) and bilayer graphene (BLG).

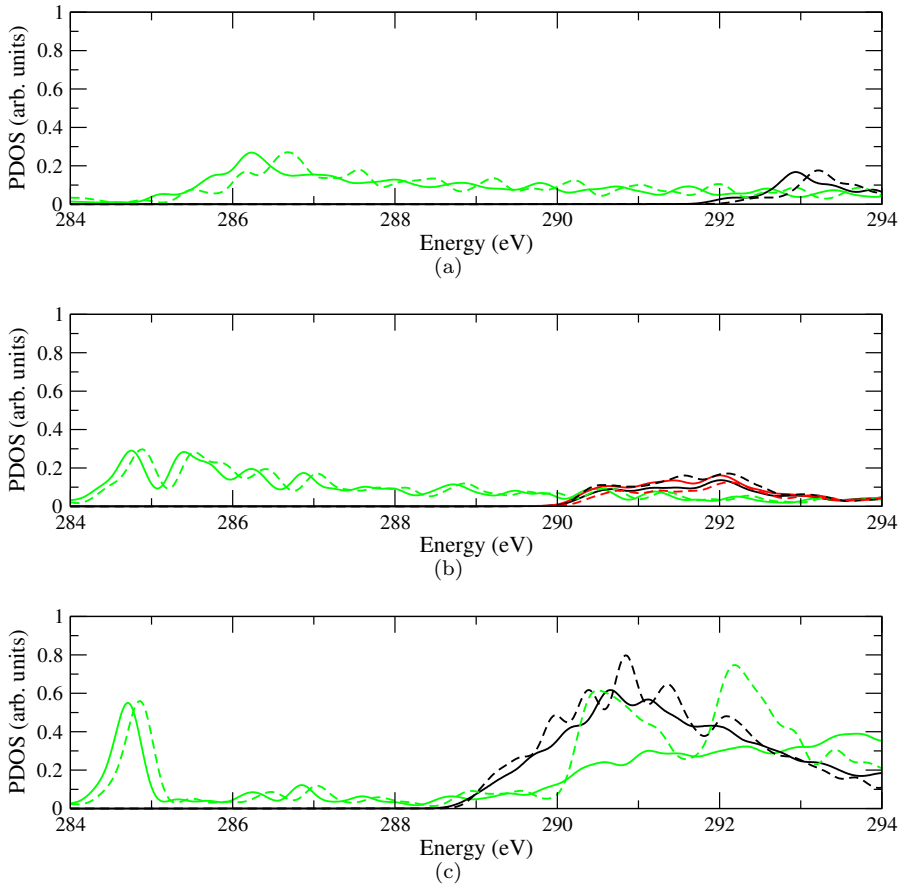

Figure 6.15: Local projected density of states (PDOS) on first-neighbor atoms, and the absorbent one itself for both HG (solid lines) and BLG (dashed lines). The top plot corresponds the perpendicularly positioned atoms w.r.t. the absorbent one, the middle plot refers to the parallel first-neighbors, and the bottom plot regards the absorbing atom. Green, black and red lines are indication of states decomposed on p_z-, p_x-, and p_y-orbitals. The plots that present only black lines do not show the red ones because they have the same quantitative contribution.

In order to investigate how the first-neighboring atoms of the X-ray absorbing one, as well as itself, take part in this process, an analysis of the PDOS on each of them is necessary. Since both systems present two non-equivalent carbon atoms, it is importante to point out that the analysis performed on

both atoms did not bring out relevant differences between them. It consisted on investigating how the local PDOS on each atom, and its first-neighbors (positioned in- and out-of-plane) took part in the observed XANES peaks. Those PDOS are shown in figures 6.15. One can see that the peak A (figure 6.14) is linked to the p_z states from both the parallel (in-plane) positioned neighbors w.r.t. the X-ray-absorbent atom and itself of both systems (figure 6.15(c)). Peak C, in turn, has higher contribution from the perpendicular and parallel positioned neighbors (figures 6.15(a) and 6.15(b), respectively). Peaks D and E of XANES spectrum comes mainly from the absorbent atom (bottom figure), in fact an admixture of the three components of p orbitals.

6.3 XANES investigation on diamond-like materials

Concerning the diamond-like structures shown in figures 6.16-a to 6.16-d, we have performed both structural relaxation and XANES simulations. Essentially, the same type of analysis we have made in the previous sections were performed. As one knows, diamondol formation comes from the fact that the presence of hydroxyl groups on either a bi- or fewlayer graphene [56,58,180], can enforce sp^3-hybridization due to the formation of C−OH bonds, and three C−C interlayer covalent bonds. Also, the fluorination of graphene sheets in Bernal stacking [57], forming C−F bonds, took place by chemical vapor deposition (CVD) on a CuNi(111) crystal, nurturing the formation of interlayer carbon bonds.

Therefore, in the following, an analysis of the chemical environment of carbon atoms in such structures, along with their electronic properties was performed. We have also calculated the work function (WF) of those materials, and the 1s-core-level binding energy (BE) for each of their non-equivalent carbon atoms. These information can be a source of data for experimentalists in the field.

6.3.1 Atomic arrangement of the materials

Both *ab-initio* calculations and experimental techniques [56–58] confirmed the atomic structures shown in figure 6.16. The table 6.2, in turn, shows the atomic disposition, namely bond length and angle between the atoms, for those structures. According to that table, the bond length between the carbon atom (X) and the oxygen atom is 4.2% larger than the same bond w.r.t. the fluorinated systems. Also, the distance between atoms X' and Y of the single-covered systems is found 6.1% larger than the corresponding double-covered ones. Considering the angles amongst the atoms participating in such bonds, one can notice that φ_{YXF} is slightly smaller for both flourinated systems than φ_{YXO} from the hydroxylated ones. Furthermore, $\varphi_{A(C)XO}$ is found to be 2.4% smaller than φ_{YXO} for both diamondol and bidiamondol structures. It indicates, along with the value of $\varphi_{X'YX}$, that the groups are slightly tilted outwards the direction perpendicular to the plane of the material. Conversely, that is not observed for both F-diamane and bi-F-diamane systems.

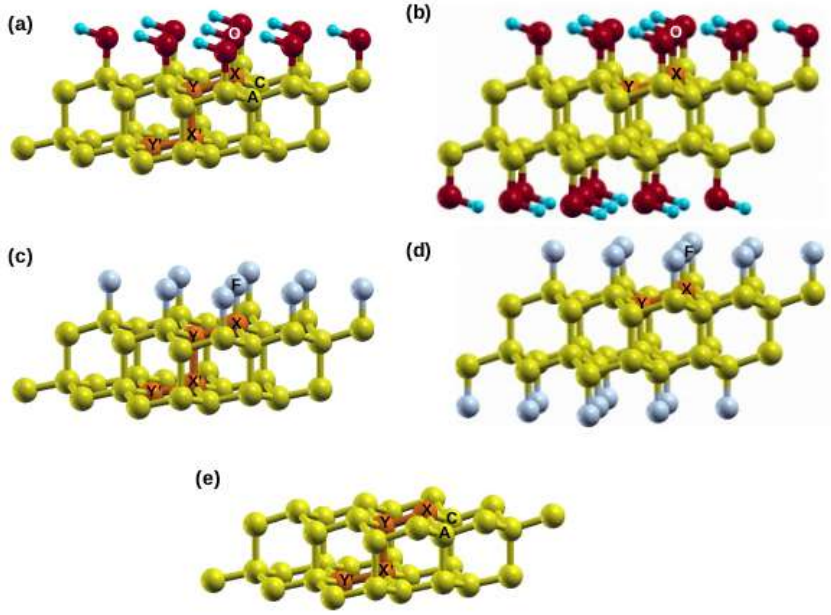

Figure 6.16: Crystal structures of (a) diamondol, (b) bidiamondol, (c) F-diamane, (d) bi-F-diamane, and (e) diamondene*. This last one is obtained by removing the hydroxyl groups from the diamondol structure. The orange spheres refer to the X-ray absorbent atoms, which are non-equivalent carbon atom. Hydrogen, oxygen, carbon, and fluorine atoms are depicted as light blue, red, yellow, and gray spheres.

For the sake of comparison, it is important to confront those information with those of the diamonds and the Bernal graphite, which are also in the caption of the table 6.2. The former ones, which are the cubic (CD) and hexagonal diamond (HD) have their bond length given by 1.55 Å, and $d_{X-C} = 1.57$ Å and $d_{X-A(B,C)} = 1.54$ Å, respectively. With respect to the angles between the bonds, the cubic diamond atoms are disposed in an angle of approximately 109.5°, and the HD shows their bonds in angles of $\varphi_{CXD} = 109.9°$ and $\varphi_{BXA} = 109.0°$. Bernal graphite, in turn, has bond length and angles of 1.42 Å and 120°, respectively. The in-plane bonds of the diamondized structures, such as d_{X-Y} and $d_{X'-Y'}$, have the same length as those of the diamonds structures. Besides, the bonding $d_{Y-X'}$ of both diamondol and F-diamane are longer than the ones from bidiamondol and bi-F-diamane, whose bond lengths are of the same order as that of the cubic diamond. The angular arrangement of the in-plane atoms are around the same as the diamonds ones, whereas the arrangement of the out-of-plane atoms may vary by about ±1°. By these information, therefore, the diamondized structures have been shown to be sp^3–hybridized materials.

Table 6.2: Bond length, d (in Å), and angles, ϕ (in °), between atoms of the systems shown in figure 6.16 according to the labels depicted therein. For the diamonds (CD, and HD), the values are 1.55 Å, and $d_{X-C} = 1.57$ Å and $d_{X-A(B,C)} = 1.54$ Å, respectively. Their angles are given as 109.5°, and for HD, $\varphi_{CXD} = 109.9°$ and $\varphi_{BXA} = 109.0°$. Regarding HG, we have 1.42 Å and 120°, respectively. Refer to the figure 6.1 for these labels.

	Diamondol	**Bidiamondol**	**F-diamane**	**Bi-F-diamane**
$d_{X-O(F)}$	1.44	1.43	1.38	1.37
d_{X-Y}	1.55	1.57	1.54	1.56
$d_{Y-X'}$	1.64	1.55	1.66	1.55
$d_{X'-Y'}$	1.51	1.57	1.51	1.56
$\varphi_{YXO(F)}$	110.24	110.82	108.26	108.85
$\varphi_{YXC(A)}$	110.27	109.78	110.65	110.09
φ_{AXC}	110.32	109.99	110.65	110.09
$\varphi_{A(C)XO(F)}$	107.84	108.19	108.26	108.85
$\varphi_{X'YX}$	108.54	108.69	108.26	108.85

6.3.2 XANES simulations

In the following, we show our results concerning the XANES simulations performed on the diamond-like structures. The bottom plot of the figure 6.17 shows each of the spectra, which were calculated as an average over all non-equivalent carbon atom, for the structures depicted in the figure 6.16. In the upper chart one can see the spectra for the carbon-layered systems and the diamond ones. As we have already seen, the peak labeled as A for the HG has lower intensity than that of BLG, which occurs due to the lower density of p-state, as was shown in figure 6.13. In fact, the p-DOS of BLG is twice as high as that of HG in the $284 - 286$ energy region.

In the bottom chart, diamondol (magenta line) presents a peak at 284.5 eV (0.3 eV above the Fermi level), close to the peak A from HG π-transition. On this region, the diamondol's peak closely resembles to the F-diamane peak (turquoise line), roughly at the same energy. Moving forward in the energy scale, close to the D peak, diamondol presents a peak (at 288.1 eV) ∼0.3 eV below that one and ∼0.95 eV below the D' peak. F-diamane, in turn, presents a peak 0.1 eV above that of diamondol, and another one ∼1.0 eV below it (at 287.2 eV). Also, diamondol presents another peak (at 290.0 eV) 0.95 eV above the D' one, and 1.23 eV below the peak B. F-diamane has a similar peak 0.5 eV above this one of diamondol. Therefore, diamondol and F-diamane have spectral features from other carbon structures, including the HG π-feature. Concomitantly, they also have peaks that give similar signatures to the diamond structures.

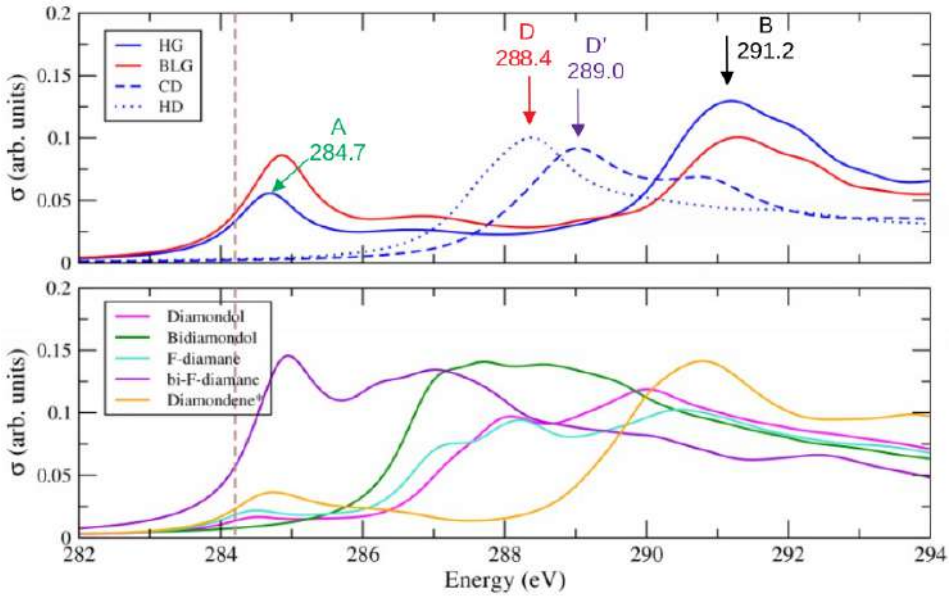

Figure 6.17: Carbon K-edge X-ray absorption spectra for: Upper: HG (solid, blue line), CD (dashed, blue line), HD (dotted blue line), BLG (red line). Bottom: diamondol (magenta line), bidiamondol structure (dark green line), F-diamane (turquoise line), bi-F-diamane (purple line), and diamondol structure without the hidroxyl group, which we called diamondene* due to the fact that it resembles the diamondene structure [58] (orange line). The vertical, dashed, brown line spots the Fermi level. The green, red, purple, and black arrows indicate the HG π-, HD σ-, CD σ-, and HG σ-trasition, respectively.

By removing the -OH group of diamondol, the diamondene* (orange line in figue 6.17) shows a more intensified peak near the A one compared to both diamondol and F-diamane, but shifted to higher energy value. It has a peak at 290.8 eV, 0.4 eV below the peak B of HG, even with similar intensity. Regarding the doubly-covered structures, bidiamondol (dark green line) and bi-F-diamane (purple line), in turn, present higher intensities within 284–289 eV range. However, only the latter has the π-feature, showing a peak at approximately 285 eV. It also has contributions at 287 eV (so as bidiamondol), a peak similar to what F-diamane shows. Conversely, bidiamondol does not show π-transition. Instead, it has a group of wavelet-like peaks on the region of the diamond ones. These peaks are endowed with higher intensity compared to the diamondol ones.

It is well-known that experimentally one is able to perform polarization-dependent X-ray absorption spectra by changing the angle between the X-ray beam and the sample [227]. Such possibility of probing a determined material gives rise to drastic changes in the spectra, which is related to the prediction of the symmetry of the final states (σ or π) associated with that spectral feature [204]. In figure 6.18, we have simulated the XANES spectra decomposed into perpendicular and parallel X-ray polarization with respect to the direction perpendicular to the solid surface, according to the inset shown on the left-hand side of the chart. Peaks a* of both diamondol and F-diamane (at 284.5 eV) have mostly contributions from parallel polarized spectrum (green line), which are found 0.2 eV below the energy of peak A for HG π-transition. As hydroxyl group is removed, the system (diamondene*) becomes characterized by the peak a (bottom figure, orange line), which is exactly at the HG π-transition, with majoritary contribution from parallel polarization. Bi-F-diamane presents a peak of π-feature at $\sim$285

eV as well. Besides, all the systems, but diamondene*, have the peak d* (~287.2 eV). They have mostly parallel polarized contributions, except for the bi-F-diamane, whose d* has major contributions from the perpendicular polarization. They are found 1.2 eV below the D peak from HD. Furthermore, the peak d (at 288 eV) is located 0.4 eV below the peak D and has contribution from both parallel and perpendicular polarized spectra. It is observed for Diamondol and F-diamane higher contribution from parallel polarization for this peak. Also, bidiamondol and bi-F-diamane present d peaks at 288.5 eV (0.1 eV above D peak), but they have mostly perpendicular contributions. There is a shoulder-like peak in d' exactly at the energy of the CD σ-transition, whose contribution in diamondol and F-diamane come out from perpendicular spectrum. Another shoulder-like peak, d'* in diamondol (at 290 eV), is related to CD σ-transition as well. This shoulder shape appears due to the parallel polarized X-ray. This peak also is observed in diamondene*, but it has higher parallel contribution. Peak b*, in turn, is straightforwardly linked to the HG σ-transition. Its contribution comes mainly from perpendicularly polarized spectrum both in F-diamane and in diamondene*.

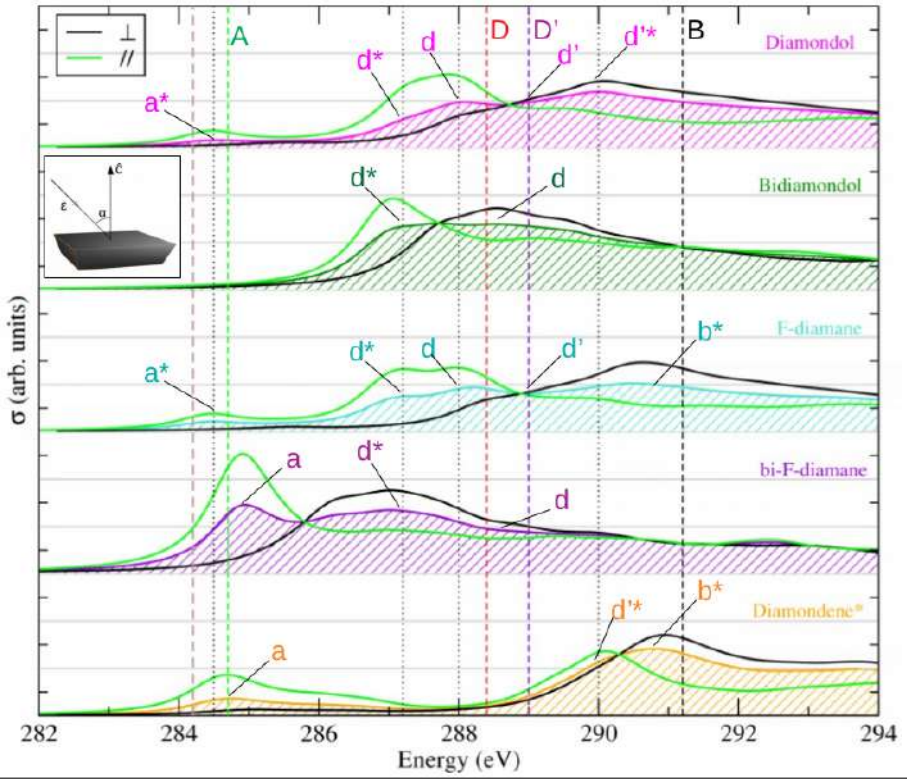

Figure 6.18: C(K)-edge XANES spectra decomposed into polarized X-ray beam. The lines and the colors represent the same systems as the ones from Fig.6.17. The green lines refer to the spectra parallel to $\hat{c}$ (inset on the left-hand side) while the black ones refer to the perpendicularly polarized spectra. $\hat{c}$ represents the direction perpendicular to the solid surface (depicted as a black solid). The dashed, vertical lines are colored as the arrows shown in Fig.6.17. Fermi level is represented by a thicker dashed, brown line. Lowercase letters stand for the peaks related to the ones from the other carbon allotropes, which are shown as vertical, dashed-thin lines. The asterisk sign is to indicate the peak is nearby those ones.

By decomposing those spectra into the non-equivalent carbon atoms, one can see that the peaks a* from both diamondol and F-diamane originate uniquely from the Y atom. The figures 6.19-a and -c show the spectra for the single-covered systems. The atoms of these systems present almost the same

spectra, except the F-diamane's X atom, which shows higher intensity for the parallel spectrum. In fact, although both the C−O and C−F bonds in these systems were found almost the same (1.44 and 1.38 Å), this can be explained be Löwdin total charge analysis, which showed that the charge in the X atom increases by 1.57 and 1.64e, respectively, with respect to the calculation with no core-hole included. Besides, due to the different electronegativities, fluorine presented about 0.7e more than the oxygen atom. Furthermore, Y atom presents a parallel polarized peak near the Fermi level for both the systems. The observed difference in intensity of the peaks around 290 eV is due to the fact that the spectra of their Y and X' components show tiny displacements one w.r.t. each other. The perpendicular components of these atoms for F-diamane are shifted 0.5 eV higher than the ones of diamondol. Despite the fact that the bond lengths of the involved atoms are very similar, the angle φ_{YXO} for diamondol is 2 higher than the angle φ_{YXF} between the atoms in question. Since the Löwdin analysis for both atoms does not draw any significant difference, this small angle difference can be interfering in the way the hybridization between the p-orbital take place. By looking at the figures H.1, we can see that the p_y orbitals from the Y's in-plane first-neighbors, and p_x orbitals from the X' in-plane first-neighbors of diamondol participate in the bonds, whereas in the case of F-diamane, only the p_y orbitals of the Y's in-plane first-neighbors are accounted for it, as shown in figure H.3.

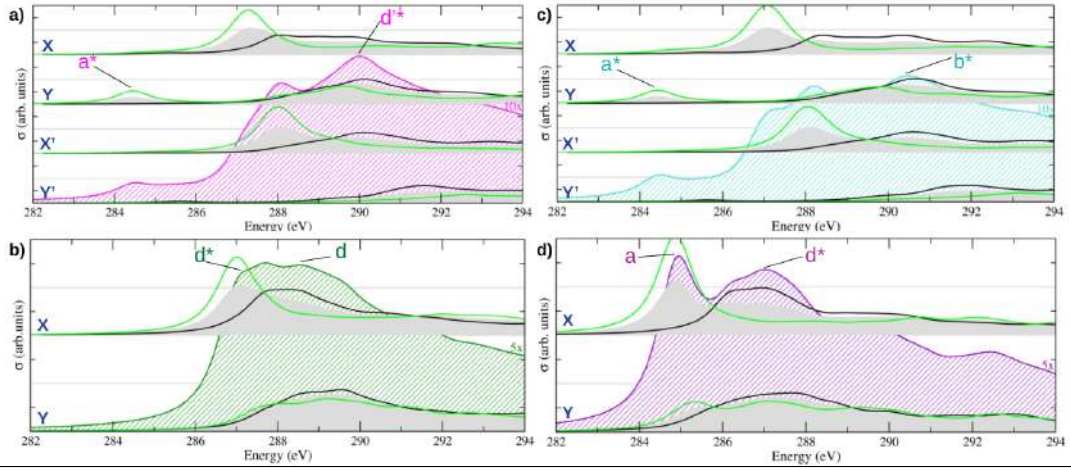

Figure 6.19: XANES spectra of (a) diamondol, (b) bidiamondol, (c) F- diamane, and (d) bi-F- diamane. The black and green solid lines refer to the perpendicular and parallel polarized spectra, respectively. Each of them are assigned to an atom of the unit cell, shown by blue letters on the left-hand side (refer to the figure 6.1). The gray, shaded areas show the mean for each atom.

Besides, figures 6.19-b and -d show, in turn, spectra of the double-covered systems. Atoms X' and Y' present the same spectra by symmetry. Although the bidiamondol and bi-F-diamane are similar in terms of their structures, it is important to notice that the peak a (shown in figure (d)), which has contributions from both X and Y atoms, does not appear in the bidiamondol case at the same energy value. In fact, both are to be regarded as π-transition peaks, as can be seen in figures H.2 and H.4, which show the local PDOS of the addressed atoms, whose p_z states are shifted. Diamondol and F-diamane, in turn, show a rather less intense, but alike peaks on the same energy region (peak a*). Unlike the bi-F-diamane case, these peaks come only from the Y atom, as already mentioned. Such as bi-F-diamane,

the bidiamondol structure also presents a pronounced parallel polarized peak (peak d* in 6.19-b), but it has contributions mostly from the X atom.

One can also see that perpendicularly polarized peaks have their contribution to the spectra coming mainly from around 288 eV. Lastly, it is worth to mention that in some cases, such as the d, d* (bidiamondol and bi-F-diamane), d'*, and b*, the resulting peaks are contribution from a mixture of perpendicular and parallel spectra from different atoms. Furthermore, around 290 eV, diamondol spectrum shows higher intensity than the latter one. Considering the double-covered materials, bi-F-diamane shows a high-intensity peak at ∼285 eV, which comes mainly from X atom (with lower contribution from Y atom). In spite of that, there is no such a peak for the bidiamondol system.

6.3.3 Analysis of the electronic structure of the spin-polarized systems

Since the structures' peaks have been assigned, we should turn our attentions into the spin-polarized systems. We have seen through the Fig.6.18 in the previous section that the Y atom plays an important role on both diamondol and F-diamane systems. These system were found to be spin-polarized, both showing magnetization per unit cell of $\sim 9.0\,\mu_B$, which agree very well with [56].

The structure of those systems, on the ground state, are shown in Fig.6.20-a, which depicts their spin-polarization as an isosurface of 0.0005 e/bohr^3, with the spin-up region spotted by red color. One can see that the bottom of both structures (around the atom X') are spin-down polarized (blue region). The magnetic moment per carbon site, μ, are also shown in the first column of table 6.3 for both systems, which do not change too much from one system to the other. However, that situation undergoes some variations depending on the carbon atom that is simulating the absorption of the incident X-ray, as one can see in table 6.3. In fact, it shows how those quantities change with respect to their corresponding ground state value. There are a few pieces of information we can extract from that table. μ increases by $\sim 50\%$ for atom Y when it is simulated as the absorbing one. Indeed, the atoms X and Y, that undergo the X-ray absorption, show increasing values of μ, except for the X' and Y' atoms: instead of increasing, they decrease their values, being the Y' the one that changed the most (71% for diamondol, and 97% for F-diamane). Another observation connected to the last ones is that while μ are decreased, their first neighbors Y' and X', respectively, increase their μ.

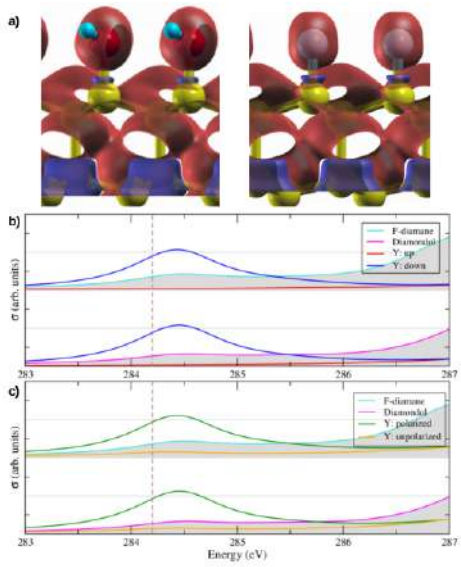

Figure 6.20: (a): Spin density of diamondol (left) and F-diamane (right). Red regions refer to spin-up polarization. The isosurface was set to 0.0005 e/bohr^3. The values of the magnetic moment per site in units of μ_B are shown in the first column of table 6.3. Light-blue, red, yellow, and grey spheres indicate hydrogen, oxygen, carbon, and fluorine atoms, respectively. (b) and (c): XANES spectra for atom Y of diamondol (magenta line) and F-diamane (turquoise line). The former shows spin-polarized spectra, and the latter shows the mean of the perpendicular and parallel spectra for both spin-polarized system (dark-green line) and for unpolarized system (orange line).

Table 6.3: Magnetic moment per carbon site, μ, for diamondol and F-diamane. The most left-hand column indicates the non-equivalents carbon atoms as shown in Fig.1.1. "c.h." stands for core-hole, which means that "no c.h." represents the system with no core-hole at any carbon atom whatsoever, as the systems depicted in Fig.6.20. The colored-cell backgrounds indicate whether the magnetic moment increased (red hue) or decrease (blue hue), according to the calculation performed on the atom with electronic core-hole, w.r.t. the "no c.h." system.

Diamondol					
	no c.h.	c.h. at X	c.h. at Y	c.h. at X'	c.h. at Y'
X	**0.0035**	0.0050	0.0017	0.0030	0.0012
Y	**0.0814**	0.0831	0.1178	0.0643	0.0499
X'	**-0.0234**	-0.0328	-0.0258	-0.0308	-0.0191
Y'	**0.3097**	0.3328	0.3273	0.3396	0.0114
F-diamane					
	no c.h.	c.h. at X	c.h. at Y	c.h. at X'	c.h. at Y'
X	**0.0020**	0.0080	0.0009	0.0018	0.0004
Y	**0.0801**	0.0791	0.1201	0.0666	0.0455
X'	**-0.0262**	-0.0318	-0.0219	-0.0332	-0.0180
Y'	**0.3032**	0.3090	0.3039	0.3177	0.0092

In Fig.6.20-b shows the peak a* for the Y atom of diamondol and F-diamane, as well as their spin-polarized decomposition. It indicates that the system is spin-down polarized, and that the Y atom is the sole accounted for this character. Just for completeness, by turning off the polarization of the system (orange lines), the peak vanishes, as shown in Fig.6.20-c. To investigate the origin of those peaks near

the Fermi level, the Fig.6.21 shows us the Local PDOS on p_z orbitals for the carbon atoms positioned perpendicularly ($C_\perp$, top graph) and parallel ($C_{//}$, medium graph) to the absorbent one (C^*, bottom graph), which is the Y atom. We also shown the p_z-DOS for Bernal graphite (GR), bilayer graphene (BLG), and diamondene*.

It is important bearing in mind that in both GR and BLG, the distance between the absorbent atom and the atoms positioned above it is about 3.37 Å, whereas in the case of the diamondol and F-diamane the bond lengths between the Y atom and its neighbor are 1.64 Å and 1.66 Å, respectively. Hence, we have observed that the lower the distance, the higher the hybridization between the s-orbitals (not shown) and the p_z-orbitals, as one can see at the top of the figure. This is so because of the selection rule for XANES dipole transition is $\Delta l = 1$. The same occurs with respect to the absorbent atoms, but this time, p_z orbitals of HG and BLG play a more important role compared to the other systems. Regarding the in-plane atoms (middle plot), the systems have the same contributions, except that F-diamane has a smaller contribution, and diamondol do not show any relevant contribution. For the local PDOS regarding the other peaks shown in figure 6.18, please refer to the supplementary results in the appendix H.1.

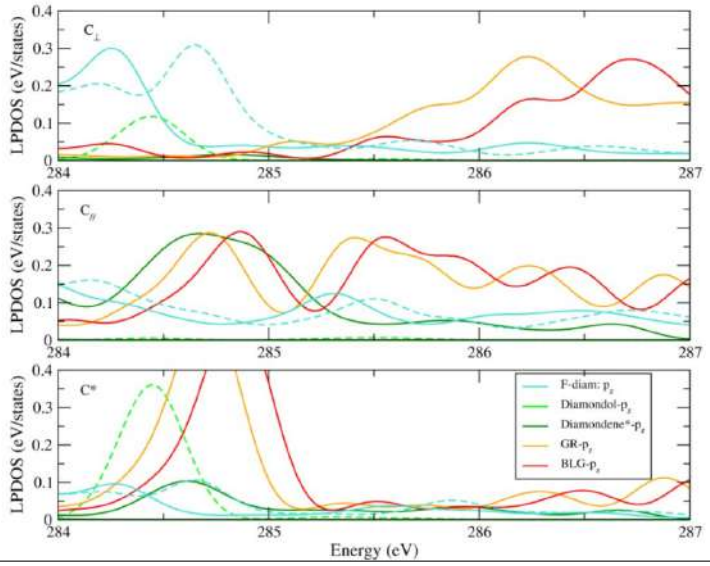

Figure 6.21: Local projected DOS on p_z-orbitals for Y absorbent atom w.r.t. diamondol, F- diamane, diamondene*, Bernal graphite (GR), and bilayer graphene (BLG). The top plot shows the PDOS of the atoms positioned out-of-plane w.r.t. the absorbent one. The middle plot refer to the in-plane atoms (in all directions), and the bottom plot, to the absorbent one itself. The dashed lines indicate spin-down polarized orbitals.

As we have already pointed out, the diamondol is a spin-polarized semiconductor [56]. So, in the following, we will show how the electronic band structure changes as a core-electron is pulled out of the carbon core region (1s orbital). In Fig.6.22-a one can see the electronic band structure of the bare diamondol system, whose direct band gap (0.75 eV) between the VBM (spin-down) and the CBM (spin-down) changes to a indirect band gap (0.2 eV) in the atom Y's core-hole system (b). The VBM (spin-up) now is at the K-point. Our calculated band gap is in agreement with the result shown in the inset [56], which is 0.6 eV: calculated by Siesta code. Bare F-diamane band gap of spin-down states (at Γ-point)

shown in Fig.6.22-c, in turn, increases w.r.t. the diamondol one by 0.65 eV. Nonetheless, the system now presents an indirect bandgap of 0.8 eV, with the VBM at the middle-point within the $K-M$ path. Looking at the F-diamane Y-probed atom (Fig.6.22-d) we can see that the indirect band gap remains with the same size as the diamondol case (Fig.6.22-b), but the VBM is now located within the halfway of $K-M$ path, unlike the diamondol Y-probed atom case. One can also notice that the spin-down VBM (at Γ-point) is shifted-down. Also, states close to 288 eV (and above) undergo an up-shift of approximately 0.35 eV compared to the diamondol counterpart (green arrow). Besides, black arrows in Fig.6.22-b and -d indicate the states that contribute for the peaks around 288 eV in Fig.6.20. In both cases, they are located on the border of Brillouin Zone (K-point).

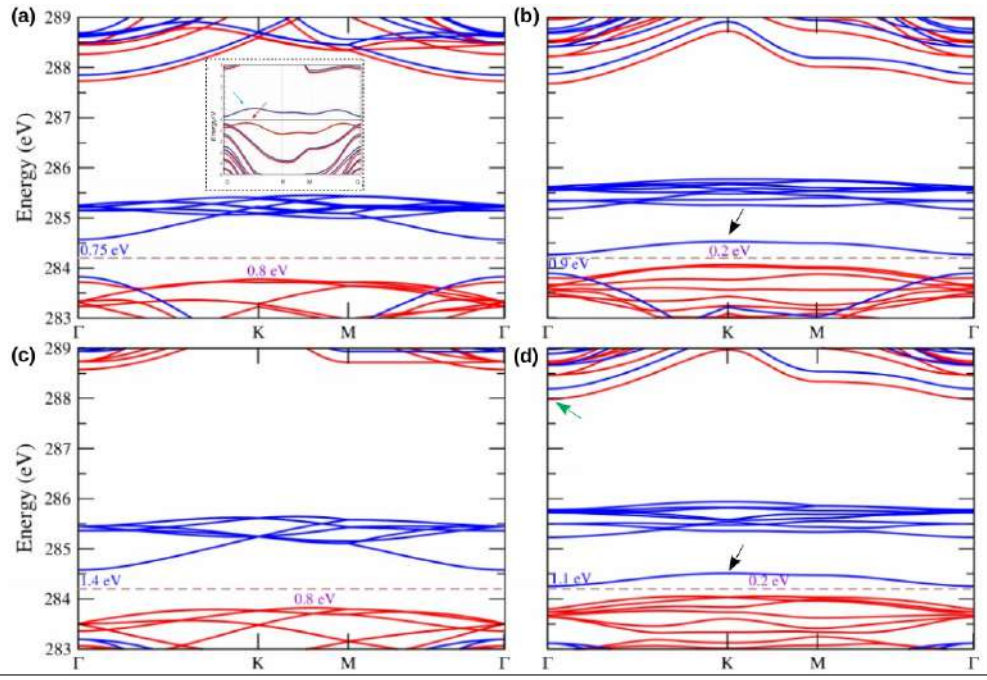

Figure 6.22: Electronic band structure for (a) bare diamondol (no core-hole), (b) probed diamondol's Y atom, (c) bare F-diamane, and (d) probed F-diamane's Y atom. Red lines refer to spin-up energy levels, and the blue ones indicate spin-down energy levels. The colored values indicate the energy gap between the spin-down conduction band minimum and spin-down valence band maximum (blue), or spin-up valence band maximum (purple). The Fermi level is shown by a dashed, brown line in each plot. The inset in (a) shows the band structure of the diamondol primitive cell calculated by [56].

Notwithstand the results of w.r.t. the Y atom, when the X atom is probed, the indirect band gap (0.2 eV in b) is increased to 0.7 eV, as shown in figure 6.23-a. One can see that in the diamondol system presents band gap of 0.7 eV when the X atom is probed. It is now indirect between the VBM (spin-up) and the CBM (spin-down), unlike the bare diamondol system. The gap between the spin-down states at Γ-point is 0.9 eV. Regarding the X-probed atom of F-diamane, the indirect band gap is increased from 0.2 (Fig.d) to 0.6 eV. The same increasing occurs for spin-down band gap at the Γ-point: from 1.1 eV (Fig.d) to 1.6 eV. By comparing it with F-diamane case (b), one can see that the indirect band gap is diminished by 0.1 eV, and the gap between spin-down states at Γ-point is increased by 0.7 eV w.r.t. the diamondol case (a). Black arrows in the figures indicate the states that contribute for the peaks within the 287–288 eV range in the figure 6.18. In both cases, they are located on the border of Brillouin Zone

(K-point), contrary to the F-diamane case (figures 6.22-c and -d).

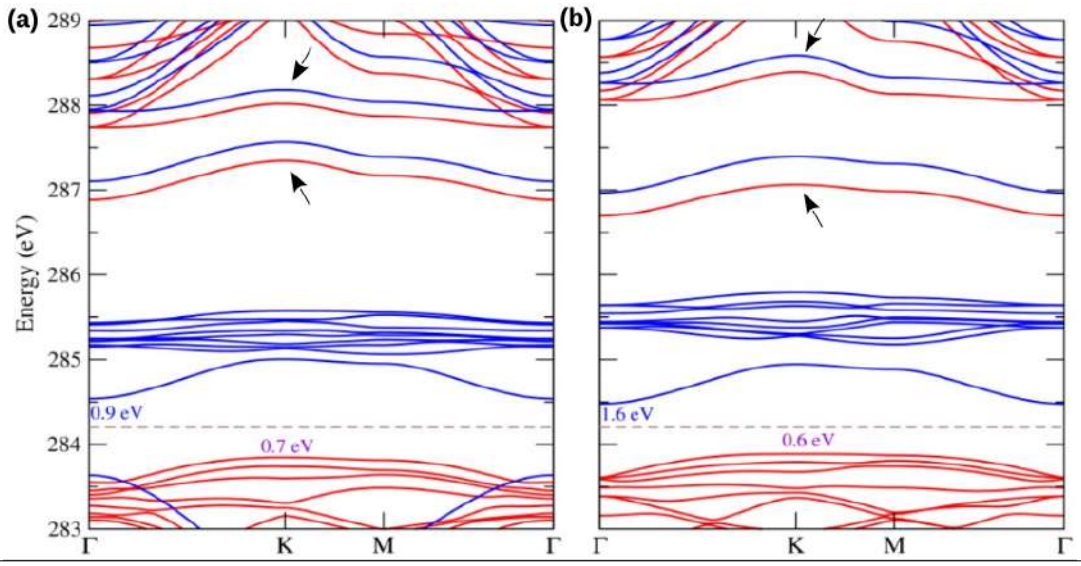

Figure 6.23: Electronic band structure for (a) diamondol?s X probed atom, and (b) F-diamane's X probed atom. Red lines refer to spin-up energy levels, and the blue ones indicate spin-down energy levels. The colored values indicate the energy gap between the spin-down conduction band minimum and spin-down valence band maximum (blue), or spin-up valence band maximum (purple). The Fermi level is shown by a dashed, brown line in each plot.

6.3.4 1s-core binding energy for carbon atoms

Complementarily, X-ray photoelectron spectroscopy (XPS) can be a way to provide insights on the chemical environment of the systems under discussion. However, experimentally, one might not have a direct interpretation of the acquired results after extracting the core-electron by an incident X-ray photon. Therefore, Density Functional Theory (DFT) total energy calculations can be an ally in such interpretations, by calculating the total energies differences between the ground and excited states [228]. In table 6.4 we show the core excitation binding energies (BE) as calculated by:

$$BE_{C_{1s}} = \Delta E_{System} - \Delta E_{PPA} + \Delta E_{AEA}, \tag{6.4}$$

where the excited state here refers to the DFT calculations performed with explicit creation of an electronic core-hole on the pseudopotential of the carbon atom, whereas the ground state refer to the DFT calculations using unaltered pseudopotential. Here, the subscripts stand for the total energy of the system, the pseudopotential approximation (PPA), and the all-electron approximation (AEA) of the carbon atom. If the local environment is weakly perturbed due to Pauling electronegativity, core-level shifts (CLS) can also be computed [228] from differences between those values, choosing one of them as a reference (inside square brackets).

Therefore, by looking at the table 6.4, the first thing one can notice is that the diamonds have almost the same core BE. Notwithstand this result matches qualitatively with an experimental one [229],

Table 6.4: 1s Core-level binding energies (BE) calculated as $E_{C_{1s}} = \Delta BE_{System} - \Delta E_{PPA} + \Delta E_{AEA}$ [228]. The shown BE for diamonds, graphite (HG) and BLG systems are very far from the experimental ones (spotted by parenthesis). Nonetheless, by correcting the system with a positive charge of 0.5e, the BE values improved greatly: 285.85 eV (CD), 285.92 (HD), 287.01 (HG), and 291.52 (BLG). The values in parenthesis were obtained from experiments [229]. The values written within square brackets are the Core Level Shift (CLS) energies w.r.t. the X' atom. In the cases of bidiamondol and bi-F-diamane, the X' atoms is equivalent to the X one.

Atom / System	X	Y	X'	Y'
Diamondol	294.76	293.35	293.91	291.79
	[0.85]	[-0.56]	[0.00]	[-2.12]
Bidiamondol	294.20	292.90	–	–
	[0.00]	[-1.30]	–	–
F-diamane	296.34	294.53	295.20	293.23
	[1.14]	[-0.64]	[0.00]	[-1.96]
bi-F-dimanane	297.02	295.33	–	–
	[0.00]	[-1.69]	–	–
CD	277.19	–	–	–
	(286.92*)			
HD	277.32	–	–	–
HG	283.42	–	–	–
	(284.40*)			
BLG	293.11	–	–	–

their values are way distant from the one measured by the experiment. Nonetheless, by adding 0.5e to the system, the results improved greatly, as shown in the caption of the table. In the setup of the mentioned experiment, they submit the silicon substrate to a negative bias "to simulate the conditions used in physical vapor deposition" [229]. Besides, the dimaondol's Y atom has almost the same BE as the BLG one, with a tiny difference of 0.24 eV. In general, the overall core BE for diamodol is larger than those of both the diamonds and the Bernal graphite. Similar observation can be done for the other diamondize systems. Moreover, the energy difference between the X atom of diamondol and F-diamane is around 0.56 eV, and for Y atom is 0.45 eV. But, the same comparison between F-diamane and bi-F-diamane give us -0.68 eV and -0.77 eV for X and Y atoms, respectively.

Finally, by using the 1s-core BE from table 6.4 along with the calculated workfunctions of the materials, as shown in figure 6.24, one is able to calculate the electron kinetic energy a detector is able to measure in the laboratory through the following expression:

$$h\nu = BE_{C_{1s}} + K_e + \phi \longrightarrow K_e = h\nu - BE_{C_{1s}} - \phi \tag{6.5}$$

where $h\nu$ is the X-ray photon energy, K_e is the kinetic energy of the electron, and ϕ is the workfunction of the material. These are worthy note informations, for experimentalists can have them to characterize the material they are probing. Through the aforementioned figure, one can see that the diamondol's workfunction is larger than the bidiamondol's one, and both are smaller than those of F-diamane and bi-

F-diamane. These latter ones, in turn, have almost the same workfunction values, being the workfunction of bi-F-diamane 70 meV higher than the F-diamane one.

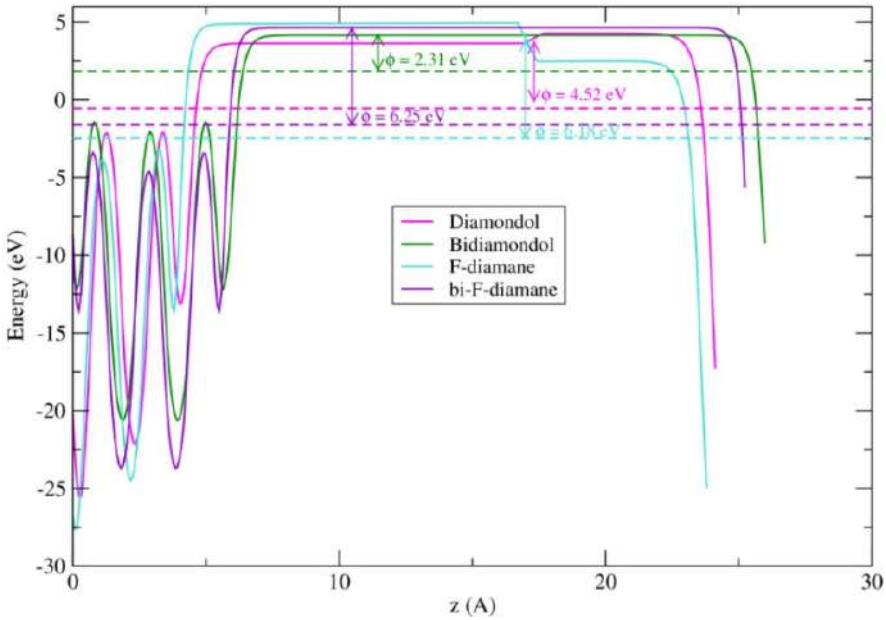

Figure 6.24: Diamondol (magenta line), bidiamondol (dark green line), F-diamane (turquoise line), and bi-F-diamane (purple line) workfunction calculated using dipole correction added to the bare ionic potential [230]. A tiny electric field of 0.0001 a.u. was added to both diamondol and F-diamondol systems to correct the error throughout the vacuum space. The z variable refer to the unit cell length along the direction perpendicular to the solid surface.

6.4 Main conclusions of this chapter

We saw that the results for the diamond systems agree very well with the experimental analysis, as one can see in section 6.1. Moreover, performing a polarization-dependent carbon K-edge analysis on HG and BLG, we have been able to access the symmetry of both the σ and π final states of the 1s-core electron that has been struck by the X-ray photon. Our results, which can be found in section 6.2, show that 1s–π transitions for Bernal graphite occurs at 284.5 eV, which agree very well with the ones reported by Rosenberg [204] (285.5 eV) and Fischer *et al.* [226] (285.0 eV). Regarding the 1s–σ transition, we have found that it is assigned to the peak at 291.1 eV in figure 6.12(a), while the value reported by both aforementioned references is 292.0 eV. Besides, π-transition-related peak increases its intensity as the polarization angle, α, goes to zero, which means that the X-ray polarization is parallel to the normal direction to the material surface. On the other hand, the σ-transition-related peak rises under the same condition. Those results also agree with the references just cited. Yet, we have also observed the linearity of the intensity of the 1s–π trasition peak with $sin^2(\alpha)$, as one can see in figure 6.12(b), as also was observed by Rosenberg *et al.* in [204]. Therefore, our simulations performed on those materials have corresponded very well to the experimental ones within the energy resolution of their respective

experiments. The major error lies on the HD within 1.5 eV.

With respect to the diamondized structures, both the single-convered systems (diamondol and F-diamane) present spin-polarized electronic band structure, whose electronic band gap of the first material agrees well with the theoretical study by Barboza *et al.* [56]. Also, we have shown that they presented almost the same spectral character, which are similar to the diamond ones. On the other hand, by removing the hydroxyl group from diamondol, the intensity of the peak near the Fermi level increases compared to the diamondized structures, resembling the spectral shape of the HG. Regarding the doubly-covered materials, only the bi-F-diamane presents π-transition (at 285 eV), whereas the bidiamondol only presents σ transition. Moreover, we have shown that polarization-dependent X-ray absorption spectra confirm the signature of the peaks in terms of orbital dependence. In general, the peaks near the Fermi level present π feature, which are characterized by the parallel polarized X-ray with respect to the direction perpendicular to the solid surface, while the other peaks have mixed contributions, where, at times, perpendicular contributions exceed over the parallel ones. Furthermore, the Y atom (see figure 6.16) is the main accounted for the peak near the Fermi level. In fact, we have observed that after the removal of the core-electron, the magnetic moment at the site Y was increased by $\sim$50%, while the sites X' and Y' decrease their values. The local PDOS on the Y atoms, and on its first neighbors, have shown that p_z are the responsible for the π-character peaks.

Regarding the electronic band structure, bare diamondol presents direct band gap between spin-down states at Γ point in the PBE-GGA flavor for exchange-correlation functional (0.75 eV), whereas F-diamane presents an indirect band gap (0.80 eV) between Γ point (spin-down state) and a k-point in the half-way of the $K - M$ path. The Y-probed site shows an indirect band gap of 0.2 eV for both the systems, the difference between them relies on the location of the VBM k-point: the former has its VBM at K-point, while the later one has its VBM in the middle of the $K - M$ path. Besides, we have also provided a theoretical core excitation binding energy for a core-electron to be removed from a carbon nucleus, which can be employed to calculate the core-level shifts between carbon atoms of a material. Interestingly, the ill predicted results for diamonds were circumvent by adding 0.5e to the system. With the 1s-core BE energies, experimentalists can have the core-electron kinetic energy calculated, which can characterize the material under investigation.

In summary, our results show that DFT calculations along with XANES simulations can be allied tools to probe local environment of carbon atoms in diamond-like bidimensional materials that have as their precursor layered carbon materials, such as bi- or few-layers graphene. We have seen through their electronic properties that they maintain the 2D features in many aspects while the 3D ones are recovered due to the re-hybridization between the sp_z and sp^2 orbitals.

Chapter 7

The interaction of acetonitrile with molybdenum-based layered materials: A computational investigation

In reference [73], it was reported a simple and efficient route to synthesize, disperse, exfoliate, and process molybdenum-based two-dimensional materials using acetonitrile (ACN) as a tri-functional agent, which acts as a separator, exfoliator, and stabilizer of the mixture composed of molybdenum disulfide (MoS_2) and molybdenum oxide (MoO_3) in thermal-controlled inert atmosphere. The result of this liquid-liquid interfacial route (LLIR) is the formation of both layered MoS_2 and agglomerated MoO_3 solid.

The high stability of the dispersed material should be due to electrostatic repulsion. Electrokinetics experiments (figure 3, supplementary material from [73]) have shown an accumulation of the dispersed MoS_2 onto the positive electrode, as an electric field was applied, indicating that it is negatively charged. They argue that the origin of those charges could be due to the electron transfer from the solvent itself or from the product of the degradation of acetonitrile under sonication process [74, 231], which can increase the polarity of the medium. Also, based on the work by Jawaid *et al.* [75], whose work showed that the products obtained by ultrasonication of N-methyl-2-pyrrolidone and acetonitrile are responsable for the stabilization of the sample due to charge transfer, charged MoS_2 are able to be dispersed, whereas MoO_3 should not be dispersed because no charge have been observed on it.

So, as long as acetonitrile interacts with the solids, charge may be tranferred to them, which has to be better explored. Thus, we have performed MD simulations followed by DFT-based calculations on acetonitrile (ACN) interacting both with MoO_3 and MoS_2, in order to simulate the conditions under which the materials were found. Firstly, the former method was employed to observe how the system evolve over the time, whereas the latter method was used to sort out the charge-transfer problems.

7.1 MD simulations

Our model consists of the Mo-based solid surrounded by liquid acetonitrile as shown in the figure 7.2. Firstly, an appropriate equilibration of the subsystem containing liquid ACN was necessary. It is shown in figure 7.1. To accomplish it, we performed an energy minimization on a simulation box with liquid acetonitrile in it using the steepest descent method (section 4.3). This minimization was accomplished in 600 steps, with an initial displacement of 0.001 nm, which accounts for the calculation of the new atomic positions through both the equation 4.18 and its subsequent criteria therein. The adopted convergence criterium was 20 kJ $mol^{-1}nm^{-1}$, under which the minimization is halted. The box size is initially $(36.95 \times 39.41 \times 32.03)$ $Å^3$, containing 500 molecules of acetonitrile (3000 atoms). After the minimization, we performed a MD simulation in NPT ensemble, using the leap-frog algorithm for integration of the Newton's equations of motion. The ensemble was kept at 1.0 bar and 298.15 K, with 0.1 ps coupling time. The time evolution of the MD simulation is 5.0 ns, with 0.001 ps time steps. After this procedure we got a new box with size $(35.71 \times 41.62 \times 31.50)$ $Å^3$, whose average density was found to be 730.3 kg/m^3, which is within about 6% error from the value found in [232, 233].

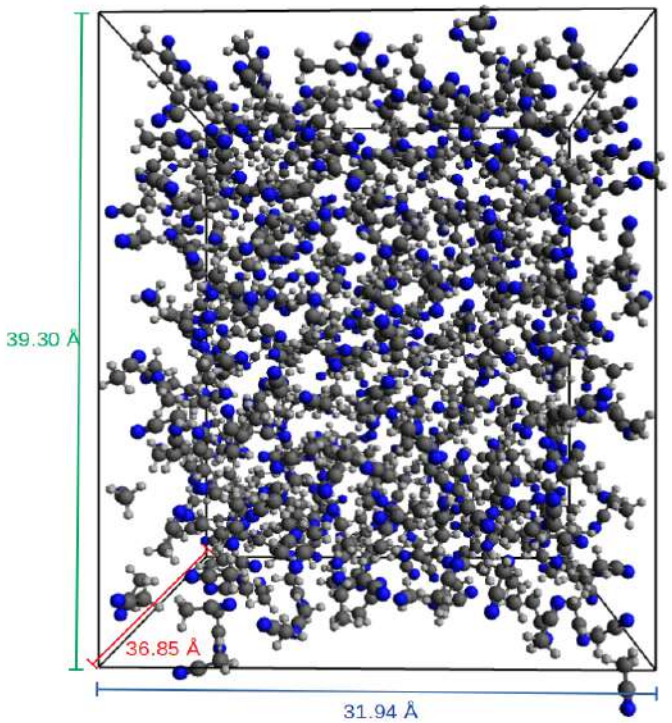

Figure 7.1: A simulated box containing 500 acetonitrile molecules after energy minimization and molecular dynamics simulations viewed in perspective. The box dimensions are colored in the figure, where blue, green, and red mean z, y, and x directions, respectively. Carbon, nitrogen, and hydrogen atoms are represented as dark gray, blue, and light gray, respectively.

Then, we performed a DFT-based variable-cell (VC) optimization on $MoO_3(MoS_2)$ orthorhombic unit cell containing four Mo atoms and twelve(eight) O(S) atoms. In other words, the unit cells have 16 and 12 atoms, respectively. After the optimization, we got unit cells with size $(3.695 \times 3.941 \times 15.349)$

Å^3 and $(3.167 \times 5.486 \times 12.215)$ Å^3. In order to simulate the experimental conditions in [73], we built a composed system consisting of either (MoO_3 or MoS_2) and two portions of liquid acetonitrile enfolding it on each of its surface. The resulting simulation box is shown in figure 7.2, which presents periodic boundary condition. To perform such a task, we did the following subtasks. Firstly, the newly-relaxed unit cell of the solid was turned into a 10x10x3 supercell (4800 atoms for MoO_3), and into a 12x7x3 supercell (3024 atoms), which have dimensions $36.950 \times 39.410 \times 46.050$ Å^3 and $38.004 \times 38.402 \times 36.645$ Å^3, respectively. These supercell dimensions in the directions that form the solid plane differ from the respective dimensions of the acetonitrile box. As the dimensions of both the solids and the acetonitrile box are incommensurable, we changed the dimensions of the acetonitrile box into those of the solids. Then, we performed another simulation run on the acetonitrile. It is important to mention that the acetonitrile box dimensions were changed accordingly, in order to keep the same density as the prior one. By doing so, we got a simulation box for ACN with appropriate dimensions so it fits well the supercell of the solid surface: $36.85 \times 39.30 \times 31.95$ Å^3 for MoO_3, and $37.97 \times 38.37 \times 31.94$ Å^3 for MoS_2. One of the acetonitrile boxes is displayed in figure 7.1. After those steps, we stacked the two acetonitrile boxes with the supercell of the solid together along the [001] direction [60], so that the new systems now have 10800 atoms (1000 acetonitrile molecule and 4800 atoms from the MoO_3 solid) and 9024 atoms (1000 acetonitrile molecules and 3024 atoms from MoS_2). This arrangement of a group of molecules making an interface contact with other group of molecules, atoms, or solid, periodically in x- and y-direction is called a slab. In our case, we have a slab of liquid acetonitrile adjoined the solid slab, and both, in turn, linked to another slab of acetonitrile. Each acetonitrile slab were kept around about 2.0 Å away from the solid before the simulations.

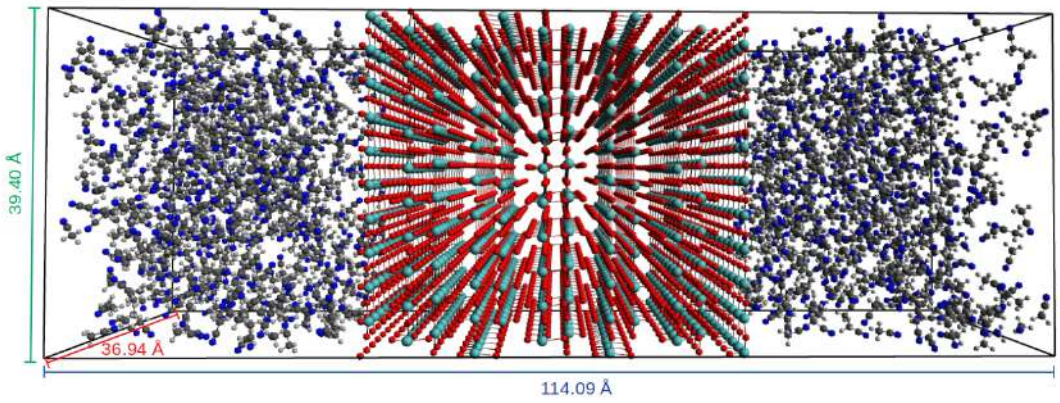

Figure 7.2: Simulation box containing slabs of acetonitrile, and MoO_3 solid. That system contain 10800 atoms, which is composed by 1000 ACN molecules and 4800 atoms of the solid. Each ACN slab were kept 2.0 Å away from the solid before the simulation. The box dimensions are colored in the figure, where blue, green, and red mean z, y, and x directions, respectively. Carbon, nitrogen, hydrogen, molybdenum, and oxygen atoms are represented as dark gray, blue, light gray, turquoise, and red spheres, respectively.

For this slabbing system of figure 7.2, we performed the energy minimization using 500 steps, with a initial maximum step size of 0.01 nm within a tolerance of 200 kJ mol^{-1}nm^{-1}, under which the minimization is halted. The solids slab were kept frozen, in the sense that we wanted only observe

how the acetonitrile slabs would evolve through the time steps in the presence of the solids. After this minimization procedure, we performed a leap-frog Stochastic Dynamics (SD) integration in a NVT ensemble at T=298.15 K. The time evolution of the simulation was 1 ns, within which 10^6 steps were performed. For the same reason as mentioned before (see the last paragraph of section 4.1, and section 4.2), for the SD procedure we also kept the solid slab frozen. It is important to mention that in this phase of the study all the atoms of the solid were with no charges, but including Lennard-Jones potential, and also the intramolecular components of the force fields, as explained in the subsection 4.1.2.

Then, on having the simulation of that system finished, we also performed other two simulations (energy minimization and SD simulations): the atoms of the solid with charges extracted from DFT calculations (Bader charges[1]) with the same SD parameters as the no-charged case; the other one is the same as before, but with different SD parameters of the simulations, as shown in table 7.1. We will call the no-charged solid atoms simulation as S1. The other two mentioned simulations will be called as S2 and S3, consecutively.

Table 7.1: Different parameters used for the SD calculations of the system composed by ACN and MoO_3. The simulation "S1" was performed with no charge for the atoms of the solid, whereas the simulations "S2" and "S3" present charges. The distinction between these latter two simulations is in the different parameters employed. The neighbor list r_{cutoff} is the distance for short-range neighbor list within which non-bonded forces (LJ interactions, for instance) are calculated; Coulomb r_{cutoff} is the cutoff distance for Coulomb interactions; LJ r_{switch} indicates where one starts switching the LJ forces; LJ r_{cutoff} is the cutoff distance for LJ interactions.

	time step (ps)	neighbor list r_{cutoff} (nm)	Coulomb r_{cutoff} (nm)	LJ r_{switch} (nm)	LJ r_{cutoff} (nm)	bond constraints
S1/2	0.001	1.2	1.2	1.0	1.2	none
S3	0.002	1.5	1.5	1.3	1.5	h-bonds

Therefore, we proceeded in analysing the region near the solid surface (just for MoO_3) for each aforementioned simulation type. To have an insight at what is going on in there, we extract the number-density colormap of ACN molecules, which provides a time average of the measurement of the density of molecules on small planes (perpendicular to the page) along the z direction (towards the right-side of the reader) of the figure 7.2 for the simulations "S1", "S2", and "S3". Furthermore, we also evaluated the number density of the ACN molecules across the simulation box for the three simulation types. The simulations "S1" and "S2" are displayed in figure 7.3. Since the last simulation ("S3") shows small differences relative to the second one ("S2"), we put it on the appendix H, figure H.5, whereby one can check it out.

The density maps of figures 7.3(a) and 7.3(c) have a color scale, on which the red refers to the maximum. Both the maxima of the maps were set to the same value (122 nm^{-3}), which is the maximum value of the system "S1". Through those results we see that the charged atoms of the solid induce a

[1]QUANTUM ESPRESSO do not perform such charge evaluation. However, a post-processing tool can be used to extract the all-electron valence charge density from PAW calculations. So, by using a code by the Henkelman Group from Texas University [234] one can extract the total charge associated with each atom enclosed in a Bader's volume [235–238]. A brief explanation on this method is given in appendix G.

small agglomeration of the molecules near the surface, which is shown by the red spots in figure 7.3(c). These density maps also work as a guidance for the eyes when analysing how is the trend of the average density of molecules near the surface. In the figures 7.3(b) and 7.3(d), one can notice that the maxima are the same, but there are different oscillations of the density of ACN molecules as moving away from the surface. The higher oscillation near the surface for the simulation "S2" indeed confirms what have already been expecting. Looking at those figures, it seems that the charged atoms of the solid induces an ordering on the ACN molecules near the surface.

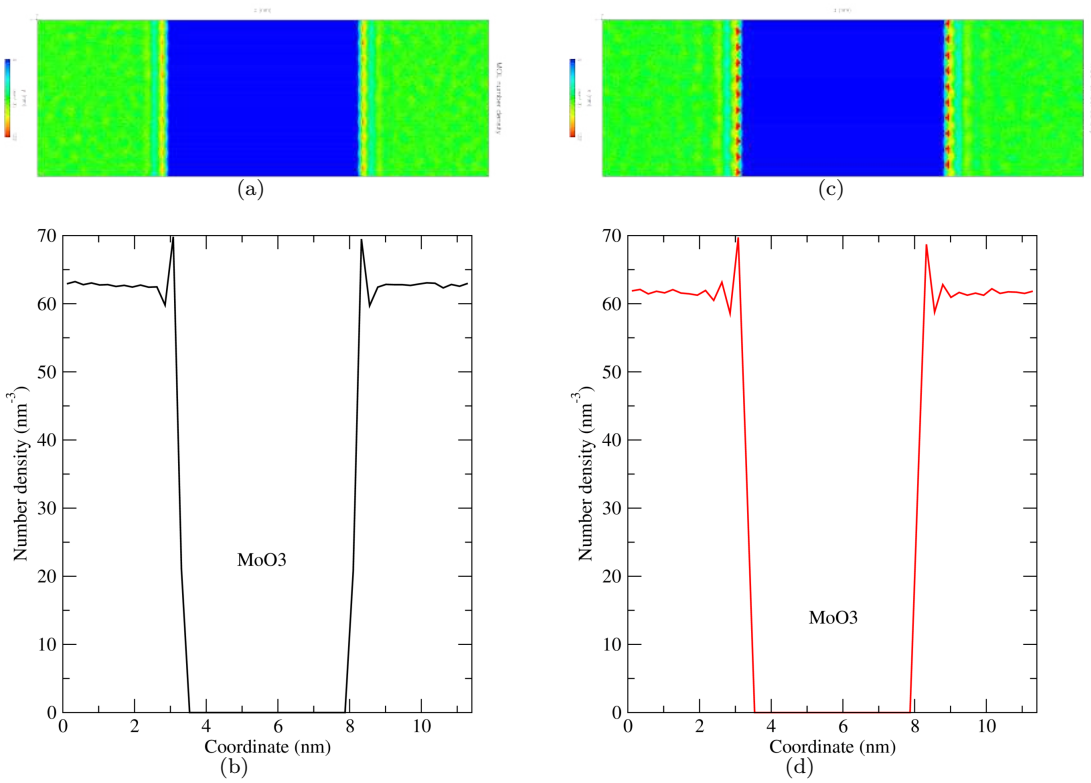

Figure 7.3: Number-density colormaps ('a' and 'c') along the z direction (to the right side of the page), and number density ('b' and 'd') for ACN molecule interacting with the MoO_3 solid. In figures 'a' and 'c', the color scale indicates that the red refers to the maximum value, while the blue color refers to the minimum value, which means that all the blue region is related to the solid.

As both simulations "S2" and "S3" are very similar, the following results were performed within the scheme "S3". We evaluated the time average of the energy of the interactions per acetonitrile molecule as depicted in figure 7.4. The bars in the figure 7.4-a are in log-scale. The labels across the horizontal axis are related with the way the interactions take place (see figure 7.4-b). The "ACN" label means that there is no solid, and that those evaluations are taken only from the interaction among acetonitrile molecules. The "1-4" interactions, violet and black bars, mean that the interactions are calculated for third neighbors of an atom i (atoms $i + 3$). 'SR' stands for Short Range interactions. As one can see in the columns hatched with 'o', there is no practical difference with respect to the intra-interactions, so that ACN molecules behave the same way regardless the solid. Considering the inter-interactions though, there appear differences depending on the solid, with increasing of the LJ interaction as ACNs interplay

with MoS_2 by almost an order of magnitude. The Coulomb interaction, in turn, has decreased by an order of magnitude.

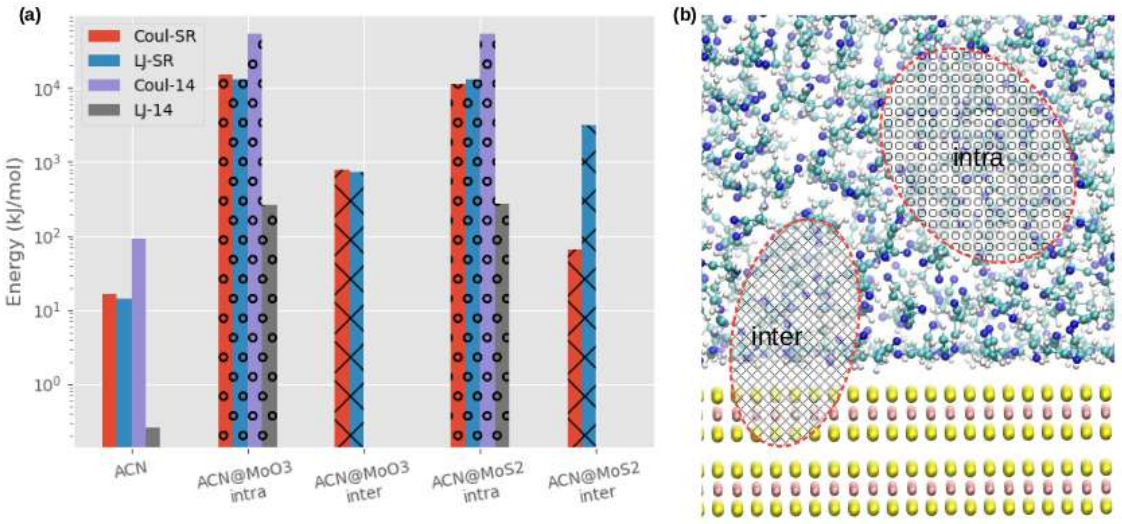

Figure 7.4: **(a)** Energy profile of the system for Lennard-Jones and Coulomb potentials. The 'o' and 'x' marks in the hatched figures refer to the interactions between the ACN molecules themselves ("intra"), and the interactions between the ACN molecules and the solid ("inter") as shown in **(b)**. The energy scale is set as logarithmic. The ACN columns indicate that there is no solid present. The bars are in log-scale. The red bar refers to the Coulomb short-range interaction; the blue one means Lennard-Jones short-range interaction; the violet bar refers to 1-4 Coulomb interaction (see text); and, lastly, the black bar is related to 1-4 Lennard-Jones interaction. As usual among MD code users, the energy units are given in kJ/mol. As a reminder: $1.0\,kJ/mol = 1.036 \times 10^{-2}$ eV.

In the figure 7.5-b, one can see the 2D colormaps of the number density of ACN molecules, similar the ones shown in figure 7.3. However, now we have defined a different scale based on the maximum density of the system composed by of ACN in the presence of MoS_2 solid (figure 7.5-a). This value has been used to normalize the result for the MoO_3 (figure 7.5-b). As a result, this colormap is lighter than before. This results show that the presence of MoS_2 induces a certain accumulation of the molecules along the surface, which is also observed, although in lesser intensity, as one moves away from the surface. It can be seen in the zoomed-in regions (bottom part of the figures 7.5-a and -b), where we can see that there are a few ripples (greenish regions) intercalated by a blueish region. In the figure 7.5-b one can see that in the presence of the MoO_3 solid there is also an accumulaton of molecules, but with lower intensity, contrary to the system with MoS_2, whose ACN molecules are ordered and spread throughout the solid surface. Also, one can notice a more diffusive ordering of molecules by moving away from the surface compared to the MoS_2 case.

The arrangement of the acetonitrile molecules on the solid surface is evaluated through the Radial Distribution Functions (RDF) [139], $g_{AB}(r)$:

$$\begin{aligned} g_{AB}(r) &= \frac{\langle \rho_B(r) \rangle}{\langle \rho_B \rangle_{local}} \\ &= \frac{1}{\langle \rho_B \rangle_{local}} \frac{1}{N_A} \left\langle \sum_{i \in A}^{N_A} \sum_{j \in B}^{N_B} \frac{\delta(r_{ij} - r)}{4\pi r^2} \right\rangle , \end{aligned} \tag{7.1}$$

where N_A and N_B are the number of particles within the system composed of atoms A and B, respectively, $\langle \rho_B(r) \rangle$ is the number density of particles B at a distance r from particles A, and $\langle \rho_B \rangle_{local}$ is the density of particles B averaged over all spheres around particles A within a maximum radius r_{max}, which is defined as the half of the box length. r here is the radial position that matches the center of mass of the ACN molecules. Figure 7.6(a) displays a pictorial representation of the definition (7.1). Figure 7.6(b), in turn, shows the normalization factor $\langle \rho_B \rangle_{local}$. In fact, $g_{AB}(r)$ is a function that describes the spherically average local organization around any given molecule (or specific atom) [150], which reflects the relative amount of molecules as a function of their distance from other molecules (or specific atoms). The definition 7.1 inform us that

$$n(r) = \int_0^r g_{AB}(r')\, 4\pi r'^2 dr' \tag{7.2}$$

is proportional to the probability of finding a particle B in the volume element $d\mathbf{r}$ at a distance r from a particle A. This is known as cumulative distribution, or Cumulative Number (CN) function [239].

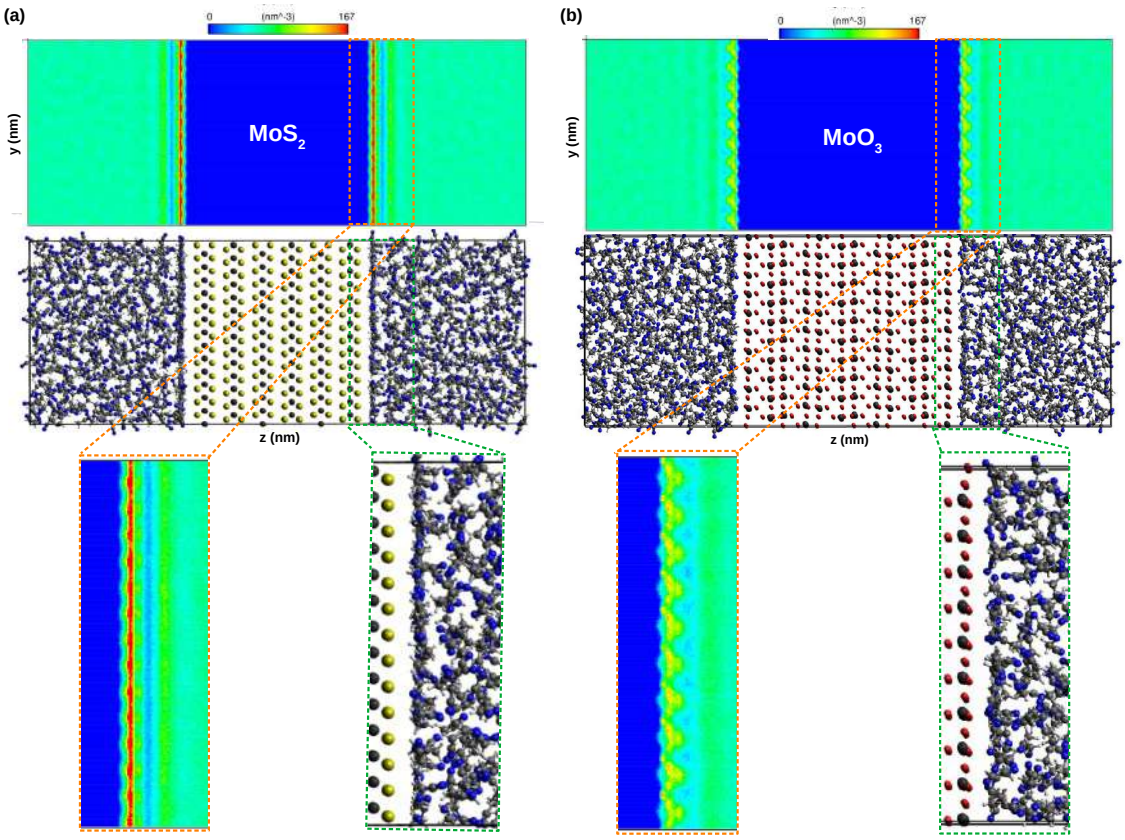

Figure 7.5: Number-density colormap of the ACN molecules averaged over all the simulation time in the presence of the solid of **(a)** MoS_2 and **(b)** MoO_3 (upper part of the picture). The respective systems are shown as a guide for the eyes. The counting was performed along the z-direction (towards the right side of the page). The scales are the same for comparison, but are larger than that of figure 7.3. Specific regions of both the colormaps (orange dashed rectangle) and the system (green dashed rectangle) were zoomed in on the bottom of the figure.

We calculated RDFs between ACN molecules for all the simulation box (figure 7.7-a), and also for small slices (5nm long) of the simulation box: near the solid surface, in the middle of the ACN slab, and away from the solid (figures 7.7-b, -c and -d). The left-side scales refer to the normalized RDFs, and the right-sided ones refer to the CNs. By integrating $n(r)$ up to its first minimum, and multiplying its result by $\langle \rho_B \rangle_{local}$, we have the first coordination number, which is the first set of molecules shell around a given particle (right-hand side scales of the figure 7.7-a and -b). If we look at the first minimum, which is around 0.67 nm, we have a cumulation number of approximately 12. This is the result expected for 3D solids and liquid, being the difference between the two phases the ordering of the atoms within the first coordination shell [138].

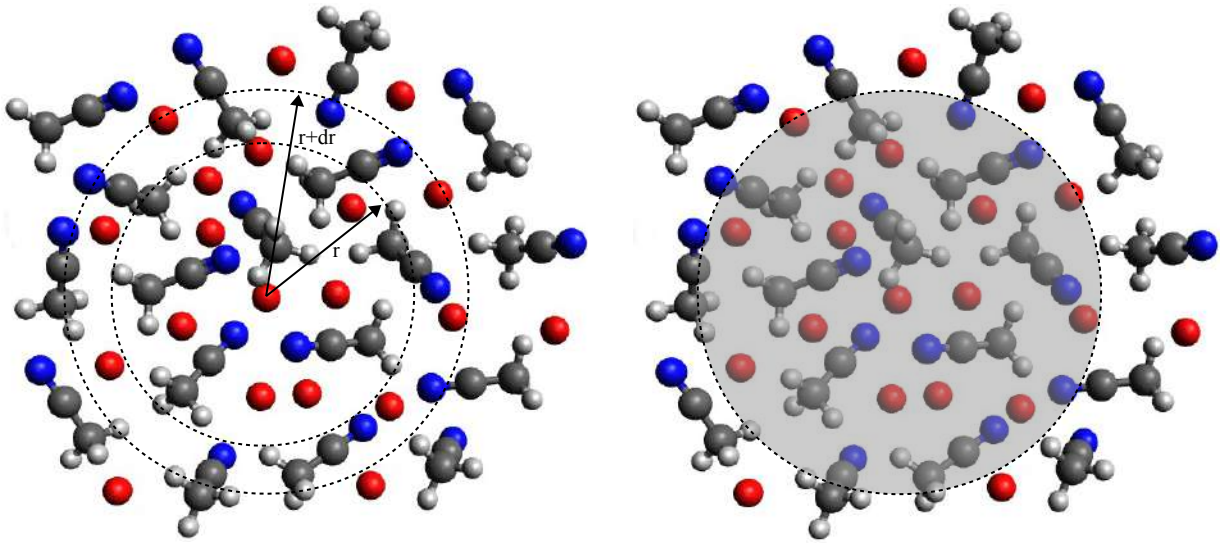

Figure 7.6: (a) Visual representation of the equation 7.1, where particles A can be considered as the oxygen atoms (red spheres), while ACN molecules would represent the particles B. (b) Normalization volume, $\langle \rho_B \rangle_{local}$, shown as a transparent gray circle.

In figure 7.7-a, the RDFs between ACN molecules in the presence of MoS_2 shows a tiny difference compared to the MoO_3 case, as pointed by a black arrow. Besides, there is a shoulder-like peak at $r \simeq 0.4$ nm. That feature is still under investigation, but we believe that it could be assigned to the molecular ordering of the first coordination shell mentioned in the previous paragraph in the sense that a few molecules may be oriented differently than the others within this shell; or it could be assigned to the proximity of a few molecules of the shell to the reference molecule. We found in the literature a similar shoulder-like tendency in the reference [240], when Macchiagodena *et al.* calculated the RDF between the center of one of the three carbon rings of the DPAP (4-(diphenylamino)phthalonitrile) and the center of mass of ACN. However, no explanation was given therein.

Near the solid surface (7.7-b), one can see that difference is more pronounced, including in CN. At about $r \simeq 0.5$ nm, g(r) for MoS_2 is 4.1% higher than the MoO_3 one, which is almost 3.4 times more intense than the case of figure 7.7-a. Likewise, at $r \simeq 0.4$ nm it is around 3.7% higher than that value depicted in the figure 7.7-a. Moreover, we can see that the first minimum of $g(r)$ around $r \simeq 0.67$ nm

presents a difference of 0.3 nm between the MoS_2 and MoO_3 cases. So, regarding the CN of ACN ($\sim$ 12.0 for the case of figure 7.7-a), at $r \simeq 0.67$ nm we have calculated 7.8 for MoS_2 case, and 6.5 for MoO_3 at $r \simeq 0.7$ nm. Moving away from the surface to the middle of the ACN slab (figure 7.7-c), at $r \simeq 0.4$ nm there is no disparity between the RDFs, but both are 3.9 times higher than that of figure 7.7-a. Regarding the peaks around $r \simeq 0.5$ nm, they present no difference with respect to those of figure 7.7-b. The CN for both systems were found to be 5.8 at $r \simeq 0.67$ nm. These results compared to the ones away from the surface (figure 7.7-d) do not show any relevant differences.

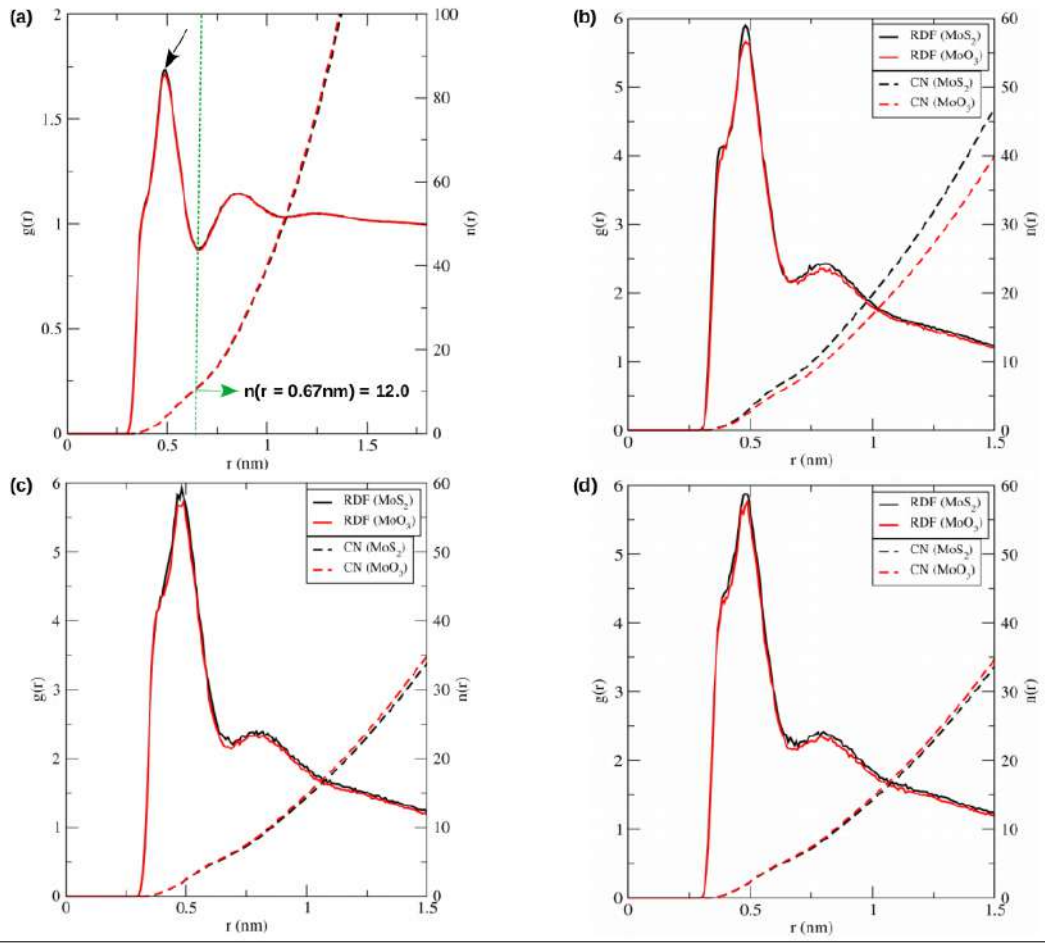

Figure 7.7: Radial Distribution Function (RDF) between ACN molecules for the whole system on the left scale (solid lines), and Cumulation Number (CN) on the right scale (dashed lines) in **(a)**. Black lines refer to MoS_2 and red ones to MoO_3. Figures **(b)**, **(c)**, and **(d)** show the RDF and CN for a 5nm slice of the ACN box near the solid surface, in the middle of the ACN slab, and away from the solid surface, respectively. The vertical, dashed green line in (a) indicates the first coordination shell as explained in the text.

In order to see how the molecules are oriented along the simulation box with respect to the solid, we calculated the probability of finding a molecule at a given angle formed by its C−N bond (cyanide anion) and the axis perpendicular to the solid surface, as shown in figure 7.8-a. Figures 7.8-c and 7.8-d show the results for ACN molecules in the presence of MoS_2 and MoO_3, respectively. The lines' colors refer to the small slices shown in the figure 7.8-b. It is remarkable the relatively higher probability of finding ACN molecules positioned parallel to the surface ($\sim$90°) near the MoS_2 surface (black line in figure

7.8-c) compared to MoO_3 solid (figure 7.8-d). This can also be seen a little far from the surface (blue line). This result corroborates with the investigation of the interactions between ACN molecules using *ab-inition* molecular dynamics [241]. It showed they tend to organize themselves in an anti-parallel disposition due to the dipole-dipole interaction, taking into account van der Waals contributions. Although we can visually notice in figure 7.6 how ACN molecules are disposed with respect to each other, a more detail investigation is needed. Besides, as one moves away from the surface, our results show that the molecules can have similar probabilities within the 60° – 150° range regardless of the solid, as seen in figure 7.8-c and -d.

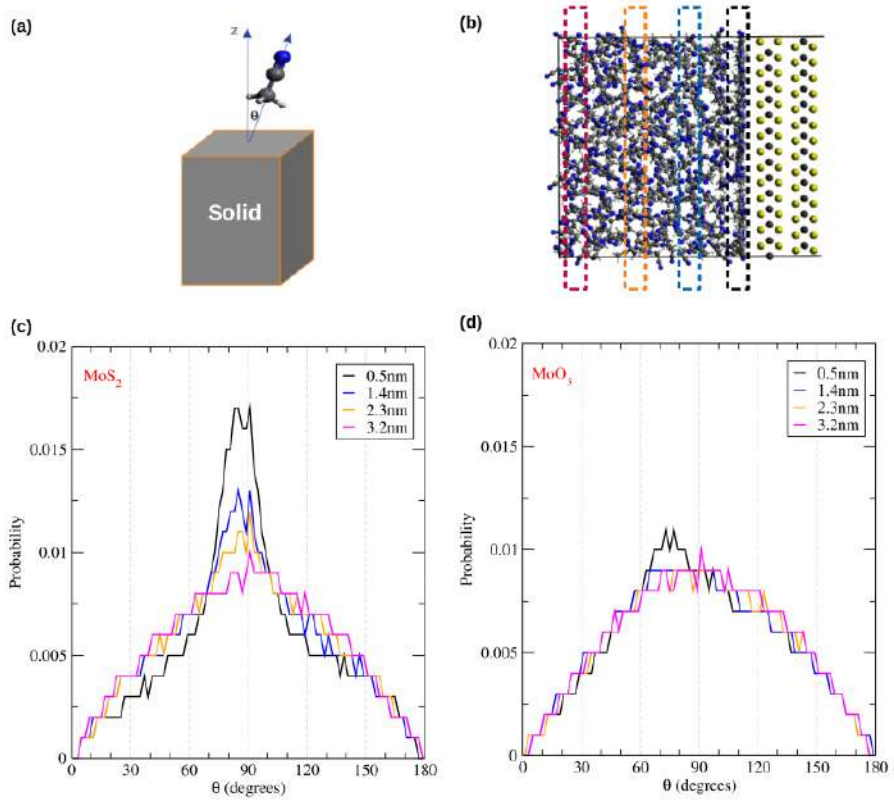

Figure 7.8: Orientation of the ACN molecules through the probability of finding a molecule in an angle θ w.r.t. the axis perpendicular to the solid surface (see the figure **(a)**). The colored lines refer to the dashed rectangles on the figure **(b)**. It shows small slices of 0.3nm width each, located at the referred distance from the solid surface as shown in the legends of the figures **(c)** and **(d)** for MoS_2 and MoO_3, respectively.

In the exfoliation process pointed out in the reference [73], the solid was thermally treated in an inert ambient, but the dispersion agent (liquid acetonitrile) was not. Since, as long as the manipulations was performed in an airy environment, it is reasonable to think of water and oxygen molecules as "contaminants" of the ACN molecules. Therefore, we also performed MD simulations on the ACN simulation boxes containing 0.1 mole fraction of either H_2O or O_2 (55 molecules each) explicitly, whose force fields and motivations for using this model were treated in section 5.4. The new simulation box can be seen in figure 7.9.

On equilibrating those new simulation boxes (NPT ensemble), we coupled them to the respective solids, the same way as done previously, and performed another MD simulation (NVT ensamble). The

results can be seen in figure 7.10, whose $r_z = 0$ is set in the middle of the solid, so that we are here analysing the region near the solid surface. The plot for the whole system can be seen in figure H.6. The vertical, dashed-dotted lines indicate the point at which the differences will be analysed. The orange and purple ones refer to the MoS_2 solid, while the blue one refers to the MoO_3 solid. For the case where we have MoS_2 solid, at $r_z \simeq 2.0$ nm (vertical orange line) the difference between the n_{ACN} for the system with ACN and oxygen (water) and pure ACN is $\simeq 16.0$ nm^{-3} ($\simeq 15.3$ nm^{-3}). At $r_z \simeq 2.4$ nm (vertical purple line), the same analysis returns $\simeq -6.6$ nm^{-3} ($\simeq -5.7$ nm^{-3}). For the MoO_3 solid (vertical blue line), the differences calculated were $\simeq -11.1$ nm^{-3} ($\simeq -10.9$ nm^{-3}). Negative values denote higher density of pure ACN with respect to the "contaminated" case. Therefore, these results indicate that the presence of O_2 and H_2O induces modifications on the way ACN molecules are organized near the MoS_2 surface (region near the vertical orange line). By going away from solid surface, the density of pure ACN becomes higher. Regarding the MoO_3 solid, near its surface (vertical blue line) the density of pure ACN is higher than either the density for ACN with O_2, or the density for ACN with H_2O.

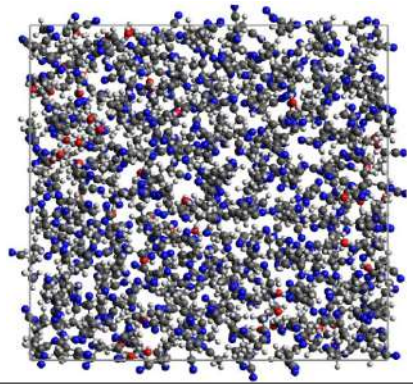

Figure 7.9: Simulation box containing 500 molecules of acetonitrile and 55 molecules of water. After simulation in the NPT ensamble, a new slabbing simulation box, as the one shown in figure 7.2, is built.

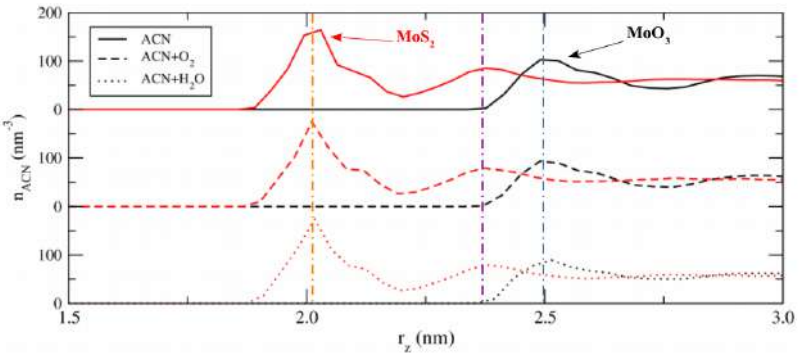

Figure 7.10: ACN molecule density in simulation boxes containg only pure ACN (solid lines), O_2 (dashed lines), and H_2O (dotted lines). Black and red lines refer to the MoO_3 and MoS_2 solids, respectively. The $r_z = 0$ is set in the middle of the solid, so that it shows the region near the solid surfaces. The plot for the whole systems is depicted in figure H.6. The vertical, dashed-dotted lines are used to indicate differences of n_{ACN} between the pure case and the case with either oxygen or water.

By analysing and evaluating the ACN properties in the interface with the Mo-solids, we can have

an idea of how the liquid behave in the presence of the solid. With this information, we can move on to the quantum mechanical calculations.

7.2 DFT-based Calculations

In this section we would like to address the quantum nature of the systems, delving into the charge transfer problem. In order to evaluate whether there is charge transfer, we had to elaborate a way to turn the calculation more feasible, since DFT calculation is impossible for systems with about ten thousand atoms. So, to circumvent such a heavy system, we cut out part of the system, which turns out to be a smaller one composed of 942 atoms (for the case of MoO_3). However, it is still a huge system for DFT calculation purpose. Then, we again cut this sub-system into an even smaller one, which has 144 atoms of the solid, plus a few ACN molecules. That is a system that can be managed by plane-wave based calculations. Afterwards, the charge analysis is performed by increasing the number of ACN molecules.

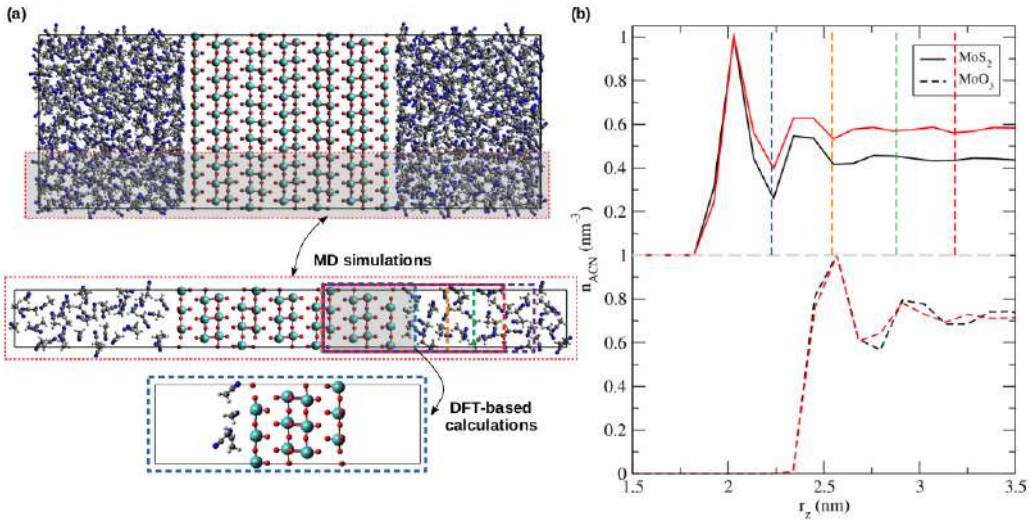

Figure 7.11: Sketch showing the steps performed to achieve the feasibility of the QM calculations mentioned in the text. **(a)** shows the ACN molecules coupled to the MoO_3 solid (top part of the chart). The shaded area, limited by an orange-dashed rectangle, shows part of the system upon which another MD simulation was performed (942 atoms – too big for QM calculations). In the middle part of the chart, one can see another shaded area, limited by a few colored, dashed rectangles, each color indicating different number of "layers" of ACN molecules. One of them is shown in the bottom part of the chart: a system composed of one layer (1L) of ACN molecules and 144 atoms of the MoO_3 solid. The just mentioned different number of layers were devised from the figures **(b)**. It shows the normalized ACN number density, n_{ACN}, of the systems containing MoS_2 (solid lines) and MoO_3 (dashed lines). Black lines refer to the larger system, which contains 1000 ACN molecules (top part of the figure **(a)**), whereas red lines indicate systems containing 85 (96) ACN molecules in the smaller system with MoO_3 (MoS_2). Each peak in n_{ACN} is linked to the aforementioned colored, dashed rectangles of the figure **(a)**.

A sketch of these steps is depicted in the figure 7.11-a. It is important to notice that, regarding the QM calculations, the number of ACN molecules (or "layer" of ACN molecules) follows the peaks

shown in the normalized ACN number density n_{ACN} of the figure 7.11-b, as the vertical dashed lines have the same colors as the dashed rectangles in the middle of the figure 7.11-a. One can still see in this figure that for the system containing MoS_2 (top part of the figure 7.11-b), the n_{ACN} values are higher for the small system (red line) than for the big one (black line), which contains 1000 ACN molecules. On the other hand, this is not observed for the systems containing MoO_3 (bottom part of the figure 7.11-b). The same approach discussed above and shown in figure 7.11-a was used for the systems containing H_2O or O_2.

In the following, we would like to address the charge transfer analysis on those systems, both with and without the contaminants. To perform such a task, we integrated the change density of the solid up to a certain height h, defined by the halfway between the closest atoms of the solid region and the liquid region, as it is shown by a dashed, purple line in the figure 7.12. The volume of the region within which the integral is performed is $V = A \cdot h = a \cdot b \cdot h$, where a and b are the in-plane lattice parameters, and $A = a \cdot b$ is the area formed by them. The difference of electrons in this volume, Δq_e, between the self-consistent calculated electrons and the valence ones is given by

$$\Delta q_e = \int_0^h \rho^{SCF}(\mathbf{r})\, A\, dz - \sum_i^{N_{solid}} q_i^{valence} \tag{7.3}$$

where $\rho^{SCF}(\mathbf{r})$ is the self-consistently calculated electronic density, $\mathbf{r}$ is the electronic positions, N_{solid} is the number of atoms inside the volume V, and $q_i^{valence}$ is the number of valence electrons of the i-th atom in the volume V. If this quantity is null, the presence of ACN molecules does not influence anything. If it is positive, we have accumulation of electrons in the volume V, otherwise we have depletion of them.

The figure 7.13 shows the difference Δq_e on each of the systems composed by different number of ACN molecules, both for pure ACN (figure 7.13(a)) and contaminated ACN (figure 7.13(b)). In the latter case, the calculation was performed for four layers of ACN molecules, as defined in figure 7.11, either with or without non-local vdW functional (vdW-DF-ob86 [242]). As it can be seen in figure 7.13(a), MoS_2 solid has lost on average ~ 0.9 more electron to ACN than the MoO_3 solid: 2.4 electrons for MoS_2 compared to 1.5 of MoO_3. That trending seems ignore the number of ACN molecules. For example, in the case of 1L of ACN, the difference of electrons lost is $0.7e$, whereas for 3L is $\sim 1.1e$.

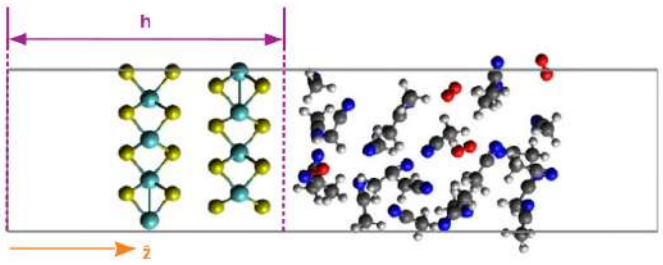

Figure 7.12: System composed by MoS_2 solid and the liquid part, which is made up by ACN and O_2 molecules. The $\hat{z}$ direction shown in the bottom of the figure indicates the direction perpendicular to the solid surface. The charge density is integrated within the volume of the solid, depicted by the letter h. Cyan, yellow, grey, blue, white, and red spheres represent molybdenum, sulfur, carbon, nitrogen, hydrogen, and oxygen atoms.

In considering the vdW functional on the system composed by 4L of ACN in figure 7.13(b), we

observe that for pure ACN the difference on the lost of electrons is very small from both the solids (left- and right-hand side of the figure). For ACN with O_2, MoO_3 almost does not lose any charge, whereas for MoS_2, it loses more electrons than the case with pure ACN. Lastly, regarding ACN molecules with H_2O, the case for MoO_3 shows the inverse trending compared to the one with O_2: it doubles with respect to the pure ACN case. However, for MoS_2 the number of electron lost for ACN also increases, but too few compared to the pure case. Furthermore, the vdW functional makes some difference on the number of electrons calculated that left the solid. In spite of these results, experimentally [73], it was observed that the dispersed MoS_2 solid was found negatively charged, and the aggregated MoO_3 solid was not. Notwithstanding those evidences, our analysis within the theoretical level we have employed did not provide us with the results we believed we would get. However, there can be other routes to deal with this problem. We will delve into it in the chapter 8, where we will show some perspectives.

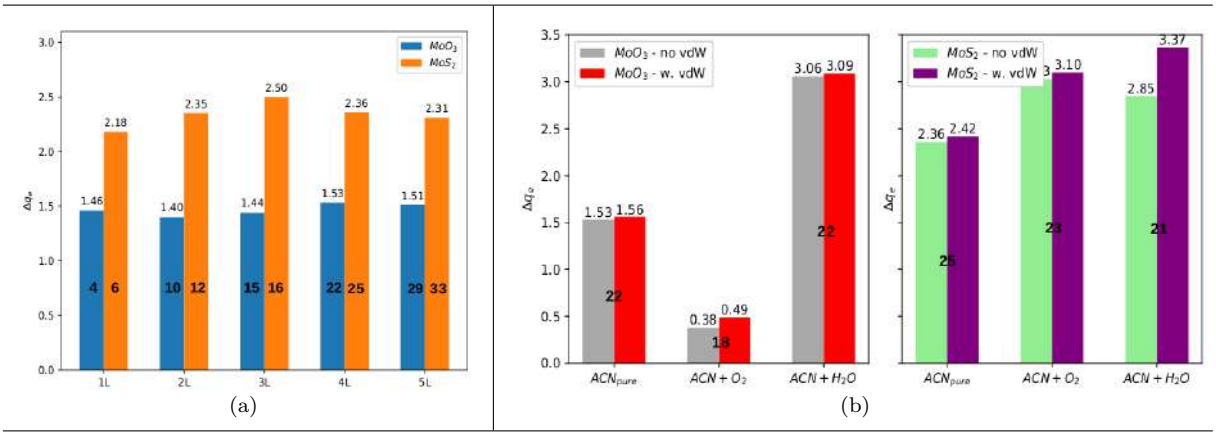

Figure 7.13: Difference in the number of electrons within the Mo-based solids for the system comprising **(a)** pure ACN or **(b)** non-pure ACN (containg either water or oxygen). In figure **(a)** this evaluation was performed for 5 ACN layers (1L, ..., 5L) as defined in figure 7.11, whereas in figure **(b)** we performed the calculations only for 4L of ACN taken into account non-local vdW functional (vdW-DF-ob86 [242]). In both the figures, the numbers inside the bars are the number of ACN molecules considered during the QM calculation.

7.3 Main conclusions of this chapter

In conclusion, we have performed Molecular Dynamics (MD) simulations followed by *ab-initio* Quantum Mechanics (QM) calculations based on DFT, whereby the first method was able to show the time evolution of the ACN molecules interacting classically with the solid systems. Then we performed DFT calculations in order to investigate the electronic interactions in the liquid-solid interface.

Our MD simulations have shown that, whether the atoms of the solid present charges or not in its force field (the solid is neutral overall), the atomic interactions remain the same. In fact, for all the situations studied in section 7.1, where the ACN molecules is put into contact with the solid surface, we have seen that the average energy per molecule interacting among themselves in the presence of the solid does not change regardless the solid. Considering the interaction betweem the ACN molecules and

the solids, the energetic profiles show higher values for MoS_2 than for MoO_3 for LJ interaction. An opposite trending is observed with respect to the Coulomb interaction. By analysing the region near the solid surface, we saw that there are a higher concentration of ACN molecules spread over it. In fact, we have seen that the MoS_2 induces a certain accumulation of the molecules along the surface, which is also observed, although in lesser intensity, as one moves away from the surface, as shown in figure 7.5. This result is supported by the normalized radial distribution function (RDF) shown in figure 7.7, which shows a higher intensity for MoS_2 in the main RDF peak at $r \simeq 0.5$ nm. Also, it shows a peculiar shoulder-like peak before the main one. Although it is still under investigation, it can be assigned to either the molecular ordering or position with respect to the reference molecules within the first coordination shell. Moreover, simulations containing explicitly $\sim 0.1M$ of H_2O or O_2 were performed at the same previously mentioned conditions. They show that the system composed by ACN and O_2 in face of the MoS_2 solid presents higher density of ACN molecules near the solid surface compared to the system with both the pure ACN molecules and ACN with H_2O. However, for the solid MoO_3 the differences are the same either with H_2O or with O_2.

Afterwards, on integrating the charge density in the region comprising the solids, we obtained the number of electrons within this region, which could be compared to the valence electrons of the solid used to perform the DFT-based SCF calculation. Our results have shown (until this moment) that, in the systems containing pure ACN, both the solids for each number of ACN layers analysed have lost electrons to the molecules, which are not expected in face of the aforementioned experimental results. Considering the systems comprising either H_2O or O_2, the quantitative results were similar despite the number of electrons calculated. In fact, for four layer of ACN molecules the system containing MoO_3 solid and O_2 showed sharper decrease of the loss of electrons compared to the pure ACN case, whereas for MoS_2 this number is larger. Considering H_2O molecules, the number of electrons increases with respect to the pure ACN case.

In summary, through MD simulations we were able to evaluate how acetonitrile molecules behave in the presence of both MoS_2 and MoO_3 solids. Also, despite the incongruence between the calculated difference in the number of electrons inside regions comprising the solids and the experimental verification, we were able to get a glimpse of how the MoS_2 influenced our results compared to the MoO_3 solid ones. Qualitatively, the charge transfer due to the MoS_2 solid is higher than that of MoO_3. Lastly, in the chapter 8 we elaborate on a complementing way to deal with this problem, which can handle environmental effects implicitly.

Chapter 8

Conclusions and Prospects

In this thesis we have addressed two problems. The first one concerns the carbon K-edge probed by X-ray absorption near-edge spectroscopy (XANES) simulations of the newly-synthesized diamond-like material called diamondol [56], which is a bidimensional hydroxilated structure, where the hydroxyl groups are attached to carbon atoms as shown in figure 6.16-a. Systematically, we have also performed simulations on fluorinated materials as shown in the same chart, as well as on both cubic and hexagonal diamonds (CD and HD, for short), and also on both Bernal graphite and bilayer graphene (HG and BLG). In the second problem, we have performed theoretical simulations using both molecular dynamics and quantum mechanics approaches to better contribute to the understanding of the results reported in [73], wherein they performed a simple and efficient method to synthesize, disperse, exfoliate, and process molybdenum-based two-dimensional materials using acetonitrile (ACN), which stabilizes the mixture of MoS_2 and MoO_3. The result of such a method, which was coined as Liquid-Liquid Interfacial Route(LLIR), is the formation of both layered MoS_2 and agglomerated MoO_3 solid. Actually, uncertainties are drawn when it comes to charge transfer because the mentioned study reported that MoS_2 becomes negatively charged, whereas the MoO_3 does not. Our aim was to address those charge transfer, as well as the detailed description of the interaction between ACN molecules and the solid surface.

In the first problem, we have done DFT calculations along with XANES simulations to probe carbon atoms in the aforementioned materials. We have seen that the results for the diamond systems, as well as for the Bernal graphite agree very well with the experimental analysis accomplished in [209] and in [204], respectively. as shown in sections 6.1 and 6.2. In this latter case, we were able to select the symmetry of both the σ and π final states of the 1s-core electron that has been struck by the X-ray photon. Regarding the diamond-like materials (section 6.3), both the single-covered systems (diamondol and F-diamane) present spin-polarized electronic band structure. Also, we have shown that their spectral character are similar to the diamond ones due to the hybridization of sp_z and sp^2 orbitals caused by the functionalization of hydroxyl group and fluorine atoms, respectively. However, the π character is more pronounced for diamond-like systems due to the higher contribution of p_z orbitals with spin-down character. Moreover, our results for the theoretical core excitation binding energy can help experimentalists on having the core-electron kinetic energy calculated, which can characterize the material under study.

Concerning the second problem, the charge transfer issue between acetonitrile (ACN) molecules and molybdenum-based system after liquid exfoliation, we have performed Molecular Dynamics (MD) simulations followed by *ab-initio* Quantum Mechanics (QM) calculations based on DFT, whereby the first method was able to show the time evolution of the ACN molecules interacting classically with the solid systems. Then we performed DFT calculations in order to investigate the quantum interaction in the liquid-solid interface. Our MD simulations have shown that the contribution of Lennard-Jones potential in the energetic profiles for ACN molecules is higher for MoS_2 solid than for MoO_3, whereas the contribution due to Coulomb interactions shows an opposite trend. Also, MoS_2 induces more ordering and accumulation of ACN molecules near its surface compared to the other solid. This was verified by RDF analysis, by profiles of the density of ACN molecules in the simulation boxes, and by the angle formed between the C–N bond in the ACN molecules and the axis perpendicular to the solid surface. DFT calculations resulted in unmatched results compared with the experimental verification. Nonetheless, in the level of theory we have used, we were able to see that MoS_2 induced on average higher charge transfer compared to MoO_3, which qualitatively agree with the experimental outcome.

Concerning our perspectives, we would like to start with the second problem studied. It is important to mention that, accorging to [73], the solid precursors were thermally treated in an inert atmosphere. However, the realization of the processes where liquid acetonitrile was employed was not, which drove us to perform the simulations involving either water or oxygen molecules. Despite the unexpected results concerning the applied atomistic models, we keep on the electron transfer analysis using the Environ module [243] from the Quantum Espresso package [43,244], which handles environment effects in *ab-initio* calculations. We believe that the charge transfer in the aforementioned solid-liquid interface can be better addressed by taking into account continuum models for the environment that is embedding the system under discussion. To realize such a task, it is also important to well describe the interface between the embedding system (the environment) and the embedded system (ions comprising the system), as well as to provide the required interactions to feature all system properly.

Finally, regarding the diamond-like systems, we also intend to perform XANES simulations on multilayer diamond-like systems, as multilayer graphene systems can be used as precursors in their synthesis. Moreover, some efforts have been put on exploration of electronic and mechanical properties of the aforementioned diamond-like materials under nitrogen-vacancy centers, which have a great spectrum of application that goes from biosensors to quantum information [245]. Therefore, we also would like to perform XANES simulations at the level of DFT for, as far as we know, such systems lack this kind of analysis at the atomic core level.

Appendix A

Orthogonalized Plane Waves (OPWs) Method

Before the interest in pseudopotentials have been brought up in 1950s by Emil Antoncik [102,103], and James Phillips and Leonard Kleinman [101], Conyers Herring [99,246], in 1940, introduced the basis for the firts quantitative calculations of bands in materials ([78], chapter 11). OPW calculations attested that Si is an indirect-band material [247, 248]. USPP and PAW methods are based on OPW method, which is a general approach to build basis functions for valence electrons:

$$\chi_{\mathbf{q}}^{OPW}(\mathbf{r}) = \frac{1}{\Omega}\left\{ e^{i\mathbf{q}\cdot\mathbf{r}} - \sum_j \langle u_j|\mathbf{q}\rangle u_j(\mathbf{r}) \right\}, \tag{A.1}$$

where,

$$\langle u_j|\mathbf{q}\rangle \equiv -\int d\mathbf{r}\; u_j(\mathbf{r})\, e^{i\mathbf{q}\cdot\mathbf{r}}, \tag{A.2}$$

so that $\chi_{\mathbf{q}}^{OPW}$ is orthogonal to each function u_j, which are required to be localized around each nucleus.

If the localized part are well chosen, then equation (A.1) divides into a smooth part and a localized part. This is conviente for crystals, whose former part may be represented by plane waves, as emphasized by Herring's words [99]:

> "It would be practical to try to appoximate the eigenfunctions in a crystal by a linear combination of a few plane waves, plus a linear combination of a few functions centered about each nucleus and obeying wavefunctions of the form"

$$\frac{1}{2}\nabla^2 u_j + (E_j - V_j)\, u_j = 0. \tag{A.3}$$

As this definitions is rather broad, taking into account $V_j = V_j(r)$ and u_j to be chosen optimal for the problem, OPW method is the startpoint of all the modern pseudopotential and PAW methods.

One should consider the orthogonalized form of the valence states in an atom, labeled by angular momentum, lm, as well as the added functions. The general form of the OPW-like function, based on the equations (A.1) and (A.2), is

$$\psi^v_{lm}(\mathbf{r}) = \tilde{\psi}^v_{lm}(\mathbf{r}) + \sum_j B_{lmj} u_{lmj}(\mathbf{r}), \tag{A.4}$$

where ψ^v_{lm} is the valence function, $\tilde{\psi}^v_{lm}$ is the smooth part, and all functions can be expressed in terms of the original OPWs by Fourier transform:

$$\psi^v_{lm}(\mathbf{r}) = \int d\mathbf{q}\, c_{lm}(\mathbf{q})\, \chi^{OPW}_{\mathbf{q}}(\mathbf{r}), \tag{A.5}$$

$$\tilde{\psi}^v_{lm}(\mathbf{r}) = \int d\mathbf{q}\, c_{lm}(\mathbf{q})\, e^{i\mathbf{q}\cdot\mathbf{r}}, \tag{A.6}$$

$$B_{lmj} u_{lmj}(\mathbf{r}) = \int d\mathbf{q}\, c_{lm}(\mathbf{q})\, \langle u_j|\mathbf{q}\rangle. \tag{A.7}$$

By the way, it is interesting to express the OPW relation, (A.4), as a transformation

$$|\psi^v_{lm}\rangle = \mathcal{T}|\tilde{\psi}^v_{lm}\rangle. \tag{A.8}$$

It means that one can always recover the full solution ψ^v_{lm} using a linear transformation, $\mathcal{T}$, on a smooth solution $\tilde{\psi}^v_{lm}$. This is the approach used in the PAW method, as we will see later (2.5.2).

Concerning the localized states, they are chosen to be core orbitals, $u_{lmi} = \psi^c_{lmi}$, and the potential is chosen to be the actual potential (spherical near the nucleus), so that ψ^c_{lmi} are the lowest eigenstates of the Hamiltonian

$$H\psi^c_{lmi} = \epsilon^c_{li}\psi^c_{lmi}. \tag{A.9}$$

The radial part of ψ^v_l must have as many nodes as there are core orbitals with angular momentum lm, because the valence states ψ^v_{lmi} must be orthogonal to the core states ψ^c_{lmi}. One can show that the choice $u_{li} = \psi^c_{li}$ leads to a smooth function $\tilde{\psi}^v_l(\mathbf{r})$ that has no radial node, and that is indeed smoother than $\psi^v_l(\mathbf{r})$. Furthermore, the core states of an atom can be assumed to be the same in either a molecule or solid composed by those atom.

Another relevant point is that the set of OPWs is not orthonormal, which means that each function has norm less than unity:

$$\langle \chi^{OPW}_{\mathbf{q}} | \chi^{OPW}_{\mathbf{q}} \rangle = 1 - \sum_j |\langle u_j|\mathbf{q}\rangle|^2. \tag{A.10}$$

This means that equations for the OPWs have the form of a generalized eigenvalue problem with an overlap matrix.

Phillips and Klienman [101], and Antoncik [102, 103], in turn, proposed the pseudopotential transformation, which is the insertion of (A.4) for $\psi_i^v(\mathbf{r})$ into the equation for valence eigenfunctions:

$$\hat{H}\psi_i^v(\mathbf{r}) = \left[-\frac{1}{2}\nabla^2 + V(\mathbf{r})\right]\psi_i^v(\mathbf{r}) = \epsilon_i^v\psi_i^v(\mathbf{r}), \tag{A.11}$$

where V is the total effective potential, which leads to an equation for the smooth functions, $\tilde{\psi}_i^v(\mathbf{r})$,

$$\hat{H}^{PKA}\tilde{\psi}_i^v(\mathbf{r}) \equiv \left[-\frac{1}{2}\nabla^2 + \hat{V}^{PKA}\right]\tilde{\psi}_i^v(\mathbf{r}) = \epsilon_i^v\tilde{\psi}_i^v(\mathbf{r}). \tag{A.12}$$

Here

$$\hat{V}^{PKA} = V + \hat{V}^R, \tag{A.13}$$

where $\hat{V}^R$ is a non-local operator that acts upon $\tilde{\psi}_i^v(\mathbf{r})$ as

$$\hat{V}^R\,\tilde{\psi}_i^v(\mathbf{r}) = \sum_j \left(\epsilon_i^v - \epsilon_j^c\right)\langle\psi_j^c|\tilde{\psi}_i^v\rangle\psi_j^c(\mathbf{r}). \tag{A.14}$$

which is the formal transformation of (A.11), the OPW expression, and the summation runs over core states. It has both advantages and disadvantages. First of all, $\hat{V}^R$ is repulsive since $\epsilon_i^v - \epsilon_j^c$ are always positive in equation (A.14). Besides, a stronger attractive nuclear potential would lead to deeper core-states, which makes (A.14) yet more repulsive. Thus, $\hat{V}^{PKA}$ is much weaker than $V(\mathbf{r})$, but is more complicated and is a non-local operator. Furthermore, the smooth pseudo-function, $\tilde{\psi}_i^v(\mathbf{r})$, are not orthonormal because the core orbitals is contained in the full function, ψ_i^v, as well as a smooth potential is not obtained by this transformation, as one can see in equation (A.14). This problem, (A.12), is, therefore, a generalized eigenvalue problem[1].

In spite of the potential operator is more complex than a simple local potential, it has its advantages, conceptually and computationally, because the weaker and smoother the potential is, the smaller will be the number of Fourier components in its expansion. It resolves the contradiction that the valence bands, $\epsilon_{n\mathbf{k}}^v$, are nearly-free-electron-like in some materials, whereas the wavefunctions, $\psi_{n\mathbf{k}}^v$, must be non-free-electron-like as they must be orthogonal to the core states. This occurs because the bands are determined by the secular equation for the smooth $\tilde{\psi}_{n\mathbf{k}}^v$, whose weak potential $\hat{V}^{PKA}$, or $\hat{V}^{model}$, is included.

Based on these foundations, the theory of pseudopotentials has led to two different approaches: definition of either an ionic pseudopotential, or a total pseudopotential. The former is a more general approach in the sense that the pseudopotential could be transferable. The latter, in turn, are very useful for describing band structure accurately, as they can be treated as adjustable empirical potentials. As a matter of fact, we will focus on the ionic potentials (or model potential) that give the same properties as

[1] Norm-conserving potential solves the non-orthogonality intricacy. But, this problem resurfaces in ultrasoft pseudopotentials.

the operators in equations (A.13) and (A.14). The model potential is spherically symmetric, as it replaces the potential of a nucleus and its core electrons. Also, this symmetry turns angular momentum (l, m) to be treated separately, which leads to non-local l-dependent model pseudopotentials $V_l(r)$. Outside the core region, the potential is Z_{ion}/r, a Coulomb potential between the nucleus and the core electrons. The repulsiveness inside the core region is tuned according to angular momentum l.

The l-dependence of a pseudopotential means that it is a non-local operator that can be written in "semilocal" (SL) form:

$$\hat{V}_{SL} = \sum_{lm} |Y_{lm}\rangle V_l(r) \langle Y_{lm}|, \tag{A.15}$$

where $Y_{lm}(\theta, \phi) = P_l\left(cos(\theta)\right) e^{im\phi}$ are the spherical harmonics. It is semilocal, actually, because it is local in radial variable, such that if $\hat{V}_{SL}$ acts on a function $f(r, \theta', \phi')$, then

$$\left[\hat{V}_{SL}\ f\right]_{r,\theta,\phi} = \sum_{lm} Y_{lm}(\theta, \phi) V_l(r) \int d(cos\theta') d\phi'\ Y_{lm}(\theta', \phi')\ f(r, \theta', \phi'). \tag{A.16}$$

As one can imagine, electronic structures involves the matrix elements between states ψ_i and ψ_j:

$$\langle \psi_i | \hat{V}_{SL} | \psi_j \rangle = \int dr\ \psi_i(r, \theta, \phi)\ \left[\hat{V}_{SL}\ \psi_j\right]_{r,\theta,\phi}. \tag{A.17}$$

Appendix B

Norm-conserving Pseudopotentials (NCPPs)

Norm-conserving pseudopotentials [100] preserve the fundamentals of *ab-initio* pseudopotentials. They are termed in this fancy way because they are not fitted to experiment. Compared to the PKA approach outlined in equation (A.4), norm-conserving method has advantage, at first, because the norm-conserving pseudofunctions, $\psi^{PS}(\mathbf{r})$, are normalized and are solutions of a model potential chosen to reproduce the valence properties of an all-electrons calculation. For complex systems, as the ones already described, the valence pseudofunctions satisfy the usual orthonormality conditions as in equation (2.36):

$$\langle \psi_i^{\sigma,\,PS} | \psi_j^{\sigma',\,PS} \rangle = \delta_{i,j}\,\delta_{\sigma,\sigma'}, \tag{B.1}$$

so that the Kohn-Sham equations have the same form as in:

$$\left(H_{KS}^{\sigma,\,PS} - \epsilon_i^{\sigma}\right)\psi_i^{\sigma,\,PS} = 0, \tag{B.2}$$

with $H_{KS}^{\sigma,\,PS}$ given by equations (2.39) and (2.40), and the external potential will be derived soon.

The definition of an *ab-initio* norm-conserving pseudopotential needs a list of requirements proposed by D. R. Hamann, M. Schlüter, and C. Chiang (HSC) [100], which are the following (extracted from [78], section 11.4):

1. All-electron and pseudo valence eigenvalues agree for the chosen atomic reference configuration.
2. All-electron and pseudo valence wavefunctions agree beyond a chosen core radius R_c.
3. The logarithmic derivatives of the all-electron and pseudo wavefunctions agree at R_c.
4. The integrated charge inside R_c for each wavefunction agrees (norm-conserving).
5. The first energy derivative of the logarithmic derivatives of the all-electron and pseudo wavefunction agrees at R_c.

Both points 1 and 2 assert that NCPPs equal the atomic potential outside the core region. Concerning the point 3, a dimentionless logarithmic derivative, D, is defined by

$$D_l(\epsilon, r) \equiv r\psi_l'(\epsilon, r)/\psi_l(\epsilon, r) = r\frac{d}{dr} ln\left[\psi_l(\epsilon, r)\right], \tag{B.3}$$

and it follows that if $\psi_l(r)$ and its radial derivative, $\psi_l'(r)$, are continuous at R_c for any smooth potential. One step forward, even though one knows that inside R_c both the pseudopotential and the radial pseudo-orbital, ψ_l^{PS}, differ from their all-electron peers, point 4 asserts that the integrated charge,

$$Q_l = \int_0^{R_c} dr\, r^2 \left|\psi_l(r)\right|^2 = \int_0^{R_c} dr\, \phi_l(r)^2, \tag{B.4}$$

is the same for ψ_l^{PS}, or ϕ_l^{PS}, as for the all-electron radial orbital ψ_l (or ϕ_l) for valence states. There are two consequences from the conservation of Q_l: firstly, it ensures that the core charge in the core region is correct and, secondly, unlike the smooth orbital from equation (A.6), the normalized pseudo-orbital is equal to the true orbital outside of R_c. This ensures that the bonding between atoms can be thought as reliable, even because the potential outside R_c is to be correct since the potential outside a spherically symmetric distribution depends on the total charge inside the sphere bounded by R_c. The point 5, in turn, is essential for building a good pseudopotential, which means that it could be generated in a spherical-like atomic environment, and then to be used on a more complex environment.

In fact HSC showed that point 5 is implied by point 4 [100]. Since the model potential is spherically symmetric, one can write the radial equation for spherical atom (or ion) as

$$-\frac{1}{2}\phi_l''(r) + \left[\frac{l(l+1)}{2r^2} + V_{eff}(r) - \epsilon\right]\phi_l(r) = 0, \tag{B.5}$$

where a prime means derivative with respect to r. Defining the variable $x_l(\epsilon, r)$ as

$$x_l(\epsilon, r) \equiv \frac{d}{dr} ln\phi_l(r) = \frac{1}{r}\left[D_l(\epsilon, r) + 1\right], \tag{B.6}$$

the following non-linear first-order differential equation is gotten by substituing (B.6) into (B.5):

$$x_l'(\epsilon, r) + \left[x_l(\epsilon, r)\right]^2 = \frac{l(l+1)}{r^2} + 2\left[V(r) - \epsilon\right]. \tag{B.7}$$

Differentiating it with respect to energy, one has

$$\frac{\partial}{\partial\epsilon} x_l'(\epsilon, r) + 2x_l(\epsilon, r)\frac{\partial}{\partial\epsilon} x_l(\epsilon, r) = -1. \tag{B.8}$$

For any function $f(r)$ and any l, one would get

$$f'(r) + 2x_l(\epsilon, r) f(r) = \frac{1}{\phi_l(r)^2}\frac{\partial}{\partial r}\left[\phi_l(r)^2 f(r)\right], \tag{B.9}$$

and, in multiplying this by $\phi_l(r)^2$ and integrating, one finds at radius R:

$$\frac{\partial}{\partial\epsilon}x_l(\epsilon,R) = -\frac{1}{\phi_l(R)^2}\int_0^R dr\phi_l(r)^2 = -\frac{1}{\phi_l(R)^2}Q_l(R). \tag{B.10}$$

or, making usage of the dimensionless logarithmic derivative, $D_l(\epsilon,R)$:

$$\frac{\partial}{\partial\epsilon}D_l(\epsilon,R) = -\frac{R}{\phi_l(R)^2}\int_0^R dr\phi_l(r)^2 = -\frac{R}{\phi_l(R)^2}Q_l(R). \tag{B.11}$$

This shows that if ϕ_l^{PS} seems like the all-electron function ϕ_l at R_c and obeys norm-conserving (Q_l are the same), then $x_l(\epsilon,R)$, and in turn $D_l(\epsilon,R)$, is the same as for the all-electron wavefunction.

The generation of the l-dependence norm-conserving pseudopotential embraces two aspects. An usual all-electron atomic calculation ([78], chapter 10) is performed for each state (l,m), accompanied by a self-consistent calculation regarding the exchange-correlation functional of the given atomic configuration. Then, the valence states is identified in order to generate both the pseudopotential $V_l(r)$ and the pseudo-orbitals $\psi_l^{PS}(r) = r\phi_l^{PS}(r)$. By finding the "screened" pseudopotential acting on valence electrons, an "unscreening" has to be made such that

$$V_l(r) \equiv V_{l,total}(r) - V_{Hxc}^{PS}(r), \tag{B.12}$$

which means that a subtraction has been made on the total potential by the sum of the Hartree and exchange-correlation potentials, $V_{Hxc}^{PS}(r) = V_{Hartree}^{PS}(r) + V_{xc}^{PS}(r)$, and, still, $V_{Hxc}^{PS}(r)$ is defined for valence electrons in their pseudo-orbitals.

In fact, if the effective exchange-correlation potential were a linear function of density, then we could unreservedly write the equation (B.12) as:

$$V_{l,total} = V_l(r) + V_{Hartree}\left([n^{PS}],\mathbf{r}\right) + V_{xc}\left([n^{PS}],\mathbf{r}\right), \tag{B.13}$$

where $[n^{PS}]$ means the quantity is evaluated as a function of n^{PS}. However, as V_{xc} is a non-linear, and probably non-local, functional of n, the equation (B.13) becomes more difficult to be treated. So, the unscreening of the potential is directly related to the effective exchange-correlation funtional, which, by (B.12), can be written as

$$\tilde{V}_{xc}(\mathbf{r}) = V_{xc}\left([n^{PS}],\mathbf{r}\right) + \left[V_{xc}\left([n^{PS}+n^{core}],\mathbf{r}\right) - V_{xc}\left([n^{PS}],\mathbf{r}\right)\right]. \tag{B.14}$$

According to [105], the term in brackets is a core corrections that increases the transferability of the pseudopotential. Nonetheless, the core charge density must be stored along with the pseudodensity. Moreover, the variation of the core density comes to be a drawback in plane wave methods. This obstacle

was overcome by Louie, Froyen, and Cohen [105], who defined a smooth "partial core density", $n^{core}_{partial}(r)$, as[1]

$$n^{core}_{partial}(r) = \begin{cases} \frac{A\,sin(Br)}{r}, & r < r_0, \\ n^{core}(r), & r > r_0, \end{cases} \tag{B.15}$$

where A and B are determined by the value and gradient of the core charge density at r_0, a radius chosen where n^{core} is about $1 \sim 2$ times $n^{valence}$.

By separating the ionic pseudopotential of (B.12) into a local l-independent part plus non-local terms as

$$V_l(r) = V_{local}(r) + \delta V_l(r), \tag{B.16}$$

one can find the analysis useful within $r > R_c$. Because the eigenvalues and the orbitals are required to be the same for both pseudo and all-electron potential, $\delta V_l(r) \to 0$ and $V_l(r) \to -\frac{Z_{ion}}{r}$ when $r \to \infty$. So, all the long-range effect of Coulomb potential are included in the local potential, $V_{local}(r)$. Therefore, the semilocal operator, (A.15), can be written as

$$\hat{V}_{SL} = V_{local}(r) + \sum_{lm} |Y_{lm}\rangle \delta V_l(r) \langle Y_{lm}|. \tag{B.17}$$

As a matter of fact, there is no "best" pseudopotential for any given element. What there exists is the "best" choice for each particular problem. As cited in [78], there are two overall competing factors:

- The smaller cutoff radius, R_c, the harder will be the developed potentials, since the wavefunctions are to be better described near the atom. This leads to better accuracy and transferability.
- The larger cutoff radius, R_c, the softer will be the pseudopotential. The smoothness of the pseudopotential is a consequence of fewer basis functions (plane waves, for instance) needed for describing the wavefunctions.

An example for Mo [100] is shown in the figure B.1 below.

Christiansen et al. [249], and Kerker [250] defined a pseudo-wavefunction, $\phi^{PS}_l(r)$, with the desired properties for each l and were able to find the potential $V_l(r)$, for which $\phi^{PS}_l(r)$ is solution with energy ϵ, by inverting the Schrödinger equation. For this nodeless functions, for each l, the potential is

$$V_{l,total}(r) = \epsilon - \frac{\hbar^2}{2m_e}\left[\frac{l(l+1)}{2r^2} - \frac{\frac{d^2}{dr^2}\phi^{PS}_l(r)}{\phi^{PS}_l(r)}\right]. \tag{B.18}$$

[1] A discontinuity in the second derivative at r_0 arises in GGA functionals. But, it can be circumvented by using a more flexible functional.

At R_c the wavefunction is matched to a parameterized analytic function. Conveniently, Kerker chose $\phi_l^{PS}(r) = e^{p(r)}$, $r < R_c$, where $p(r) =$ polynomial to fourth power with coefficients chosen by continuous first and second derivatives at R_c and norm-conservation. Considering smoothness, Bachelet, Hamann, and Schlüter (BHS) [251] used gaussian expansion to build what can be called as "standard reference pseudopotentials" from H to Pu elements. And it is called so because they are hard and are used for comparison. Vanderbilt [252] also made use of the same approach, but changing parameters until the wavefunction reaches the desired property. A bit later, Troullier and Martins [253] developed a higher order polynomial in order to make smoother potentials than the Kerker's ones. The interesting figure below, B.2, shows the comparison among those generated pseudopotential.

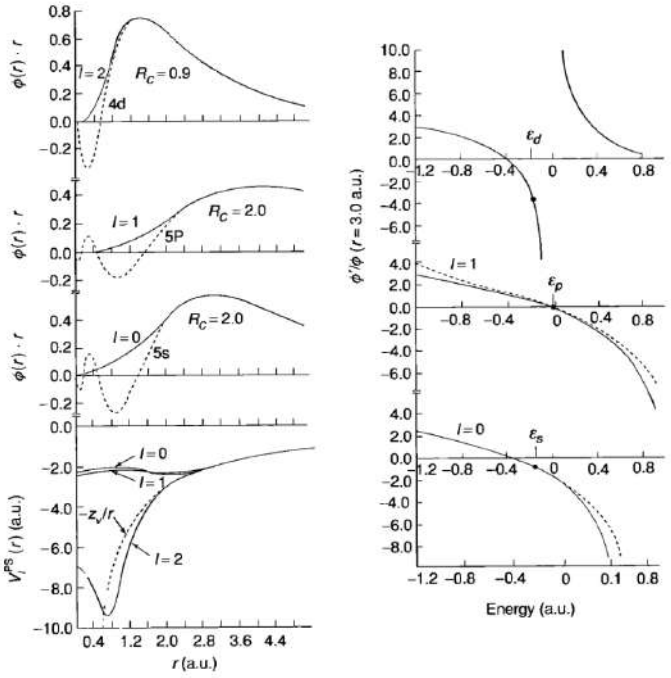

Figure B.1: Example of norm-conserving pseudopotential, pseudofunctions, and logarithmic derivative for Mo. Left Bottom: $V_l(r)$ in Ry for $l = 0, 1, 2$ compared to Z_{ion}/r (dashed line). Left top: All-electron valence radial functions, $\phi_l(r) = r\phi_l(r)$ (dashed line), and norm-conserving pseudofuntions. Right: Logarithmic derivative of the pseudopotential compared to the full atom calculation; the points indicate the energy where they are fitted. Figure extracted from [78], page 216.

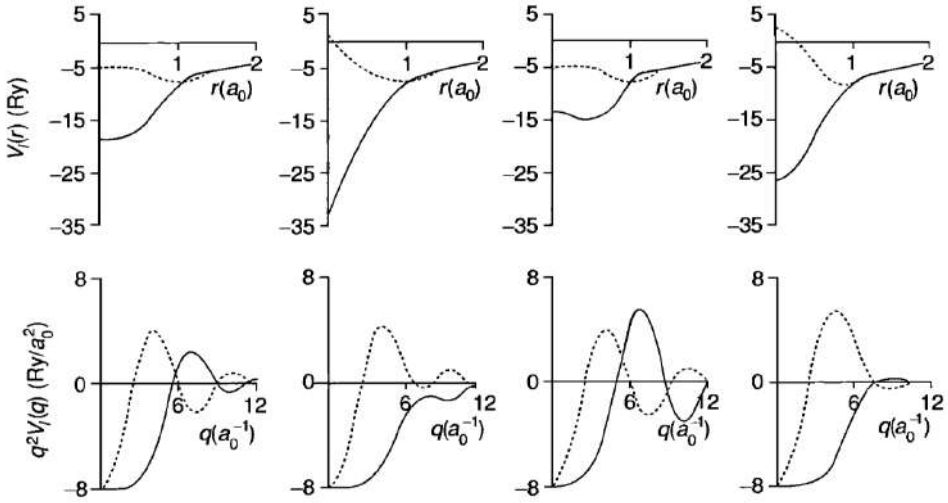

Figure B.2: Comparison of pseudopotential for carbon in both real and reciprocal space. Dotted lines mean s state, and solid lines mean p state. All the potentials shown are norm-conserving potentials. From left to right: Troullier and Martins [253]; Kerker [250]; BHS [251]; Vanderbilt [252]. Regarding the differences among them, please refer to the text and the reference [78], page 217, where the figure was extracted from.

Optimization can be done to turn a pseudopotential as reliable as possible through convergence as, for example, by minimizing the kinetic energy of the pseudopotential for the chosen radius core [254,255]. This can be quantified by examination of the Fourier transform and its behavior at large momentum q. Once this optimization is accomplished, the resulted pseudopotential can be carried over to molecules and solids, since the convergence as a function of q_{max} is the same whatever is the case.

B.1 Separable Pseudopotential Operators and Projectors

Kleinmann and Bylander (KB) [256] found out a way to construct a separable pseudopotential operator, i.e., $\delta V(\mathbf{r},\mathbf{r}') \equiv \sum_i f_i(\mathbf{r})g_i(\mathbf{r}')$. They showed that the semilocal $\delta V_l(r)$ of (B.16) can be replaced by a non-local separable operator $\delta\hat{V}_{NL}$. Thus, the total pseudopotential would be

$$\hat{V}_{NL} = V_{local}(r) + \sum_{lm} \frac{|\psi_{lm}^{PS}\delta V_l\rangle\langle\delta V_l\psi_{lm}^{PS}|}{\langle\psi_{lm}^{PS}|\delta V_l|\psi_{lm}^{PS}\rangle}, \tag{B.19}$$

where the second term, with the form $\delta\hat{V}_{NL}(\mathbf{r},\mathbf{r}')$, is fully non-local in angles θ, ϕ, and r. The projectors $\langle\delta V_l\psi_{lm}^{PS}|$ are defined as functions that operate on a wavefunction:

$$\langle\delta V_l\psi_{lm}^{PS}|\psi\rangle = \int d\mathbf{r}\,\delta V_l(r)\psi_{lm}^{PS}(\mathbf{r})\psi(\mathbf{r}). \tag{B.20}$$

Independently of the extent of the functions $\psi_{lm}^{PS} = \psi_{lm}(r)P_l\,(cos(\theta))\,e^{im\phi}$, the projectors are only non-zero inside the cutoff region. The advantage of this form is that one only has to calculate products of projectors (B.20) to express the matrix elements:

$$\langle\psi_i|\delta\hat{V}_{NL}|\psi_j\rangle = \sum_{lm}\langle\psi_i|\psi_{lm}^{PS}\delta V_l\rangle\frac{1}{\langle\psi_{lm}^{PS}|\delta V_l|\psi_{lm}^{PS}\rangle}\langle\delta V_l\psi_{lm}^{PS}|\psi_j\rangle, \tag{B.21}$$

which can be contrasted with the radial integration of the equation (A.17) for this saves computational time for large systems.

However, it is possible to construct the separable pseudopotential directly, as Vanderbilt showed [104]. Through the same method used to build norm-conserving pseudopotential, ψ_{lm}^{PS} and $V_{local}(r)$ are chosen smooth within $r > R_c$. One can define functions χ_{lm}^{PS}, such that

$$\chi_{lm}^{PS}(\mathbf{r}) \equiv \left\{\epsilon_l - \left[-\frac{1}{2}\nabla^2 + V_{local}(r)\right]\right\}\psi_{lm}^{PS}(\mathbf{r}), \tag{B.22}$$

so that $\chi_{lm}^{PS}(\mathbf{r}) = 0$ outside R_c. Also the operator

$$\delta\hat{V}_{NL} = \sum_{lm}\frac{|\chi_{lm}^{PS}\rangle\langle\chi_{lm}^{PS}|}{\langle\chi_{lm}^{PS}|\psi_{lm}^{PS}\rangle} \tag{B.23}$$

has the same properties as the KB operator in (B.19); in other words, ψ_{lm}^{PS} is a solution of $\hat{H}\psi_{lm}^{PS} = \epsilon_l\psi_{lm}^{PS}$, with $\hat{H} = -\frac{1}{2}\nabla^2 + V_{local} + \delta\hat{V}_{NL}$.

Appendix C

Gauge Freedom

The Maxwell's equations are defined as [257]

$$\nabla \cdot \mathbf{E} = \frac{1}{\epsilon_0}\rho, \tag{C.1}$$

$$\nabla \cdot \mathbf{B} = 0, \tag{C.2}$$

$$\nabla \times \mathbf{E} = -\frac{\partial \mathbf{B}}{\partial t}, \tag{C.3}$$

$$\nabla \times \mathbf{B} = \mu_0 \mathbf{J} + \mu_0 \epsilon_0 \frac{\partial \mathbf{E}}{\partial t}, \tag{C.4}$$

so that given $\rho(\mathbf{r}, t)$ and $\mathbf{J}(\mathbf{r}, t)$, the fields $\mathbf{E}(\mathbf{r}, t)$ and $\mathbf{B}(\mathbf{r}, t)$ could be found. As a reminder, ρ and $\mathbf{J}$ are the charge density and the current density, respectively. These are a set of coupled first-order partial differential equations. However, certainly, it would be better if this number of equations were diminished, even if they turn out to be second-order equations, satisfying the Maxwell's equations. Thus, with this intention, it is convinient to introduce potentials: a scalar potential Φ, and a vector potential $\mathbf{A}$ [258].

Since equation (C.2) holds, $\mathbf{B}$ can be defined in term of the vector potential:

$$\mathbf{B} = \nabla \times \mathbf{A}. \tag{C.5}$$

Then the equation (C.3), Faraday's law, can be written as

$$\nabla \times \mathbf{E} = -\frac{\partial}{\partial t}\left(\nabla \times \mathbf{A}\right), \tag{C.6}$$

$$\nabla \times \left(\mathbf{E} + \frac{\partial \mathbf{A}}{\partial t}\right) = \mathbf{0}. \tag{C.7}$$

Because a curl of a vector is null, one can write equation (C.7) as a gradient of some scalar function, a scalar potential Φ:

$$\mathbf{E} = -\nabla\Phi - \frac{\partial \mathbf{A}}{\partial t} \tag{C.8}$$

which recovers $\mathbf{E} = -\boldsymbol{\nabla}\Phi$ when $\mathbf{A}$ is a constant. The definintion of the fields $\mathbf{E}$ and $\mathbf{B}$ in terms of the potentials Φ and $\mathbf{A}$, as defined in equations (C.5) and (C.8), satisfies both the aforementioned Maxwell's equations. The other two inhomogeneous equations would determine the dynamic behavior of the potentials. In the vacuum, these two equations can be written in terms of the potentials as

$$\nabla^2\Phi + \frac{\partial}{\partial t}\left(\boldsymbol{\nabla}\cdot\mathbf{A}\right) = -\frac{\rho}{\epsilon_0}, \tag{C.9}$$

$$\nabla^2\mathbf{A} - \frac{1}{c^2}\frac{\partial^2\mathbf{A}}{\partial t^2} - \boldsymbol{\nabla}\left(\boldsymbol{\nabla}\cdot\mathbf{A} + \frac{1}{c^2}\frac{\partial\Phi}{\partial t}\right) = -\mu_0\mathbf{J}, \tag{C.10}$$

where c is the light velocity.

Even though we have reduced the Maxwell's equations into a set of two equations, they are still coupled. The uncoupling can be accomplished by exploint the arbitrariness of the definition of the potentials. This arbitrariness is called *gauge freedom*, which means that we can impose extra condition to the potentials, as long as nothing happens to $\mathbf{E}$ and $\mathbf{B}$ [257].

So, supposing we have two set of potentials $(\Phi, \mathbf{A})$ and $(\Phi', \mathbf{A}')$, which correspond to the same fields. Writting them as

$$\mathbf{A}' = \mathbf{A} + \boldsymbol{\alpha} \tag{C.11}$$

$$\Phi' = \Phi + \beta \tag{C.12}$$

The curls of the potentials $\mathbf{A}'$ and $\mathbf{A}$ must be equals since they give the same $\mathbf{B}$. Hence

$$\boldsymbol{\nabla}\times\boldsymbol{\alpha} = \mathbf{0}. \tag{C.13}$$

Therefore, $\boldsymbol{\alpha}$ can be written as a gradient of some scalar:

$$\boldsymbol{\alpha} = \boldsymbol{\nabla}\lambda. \tag{C.14}$$

Also, Φ' and Φ give the same $\mathbf{E}$:

$$\boldsymbol{\nabla}\beta + \frac{\partial\boldsymbol{\alpha}}{\partial t} = \mathbf{0}, \tag{C.15}$$

or

$$\boldsymbol{\nabla}\left(\beta + \frac{\partial\lambda}{\partial t}\right) = \mathbf{0}. \tag{C.16}$$

Calling the term in parenthesis as $k(t)$, we have

$$\beta = -\frac{\partial \lambda}{\partial t} + k(t). \tag{C.17}$$

Therefore,

$$\begin{cases} \mathbf{A}' &= \mathbf{A} + \boldsymbol{\nabla}\lambda, \\ \Phi' &= \Phi - \frac{\partial \lambda}{\partial t}. \end{cases} \tag{C.18}$$

Therefore, for any scalar function $\lambda(\mathbf{r}, t)$, one can add $\boldsymbol{\nabla}\lambda$ to $\mathbf{A}$, assuming $\partial\lambda/\partial t$ is subtracted from Φ. Under such changes in Φ and $\mathbf{A}$, the fields $\mathbf{E}$ and $\mathbf{B}$ will not be changed. These gauge transformations can be used to symplify the equations (C.9) and (C.10) through an adjustment to the $\boldsymbol{\nabla} \cdot \mathbf{A}$.

C.1 Coulomb Gauge

In magnetostatic, the best choice is

$$\boldsymbol{\nabla} \cdot \mathbf{A} = 0 \tag{C.19}$$

so that the equation (C.9) becomes

$$\nabla^2 \Phi = -\frac{\rho}{\epsilon_0}. \tag{C.20}$$

which is the Poisson's equation, whose solution is

$$\Phi(\mathbf{r}, t) = \frac{1}{4\pi\epsilon_0} \int d\mathbf{r}' \frac{\rho(\mathbf{r}', t)}{\mathfrak{r}}, \tag{C.21}$$

where $\mathfrak{r} = \sqrt{\mathbf{r} - \mathbf{r}'}$, with $\mathbf{r}$ and $\mathbf{r}'$ being the distance to a point in space whereby the source charges in $\mathbf{r}'$ are "felt". Its advantage lies at that the scalar potential is easily calculated. On the flip side, the vector potential is particularly difficult to calculate. The differential equation for $\mathbf{A}$, equation (C.10), in the Coulomb gauge is

$$\nabla^2 \mathbf{A} - \mu_0 \epsilon_0 \frac{\partial^2 \mathbf{A}}{\partial t^2} = -\mu_0 \mathbf{J} + \mu_0 \epsilon_0 \boldsymbol{\nabla} \left(\frac{\partial \Phi}{\partial t} \right). \tag{C.22}$$

C.2 Lorenz Gauge

The Lorenz[1] gauge is

$$\boldsymbol{\nabla} \cdot \mathbf{A} = \mu_0 \epsilon_0 \frac{\partial V}{\partial t}. \tag{C.23}$$

The idea is to sweep out the middle term in equation (C.10), so that it becomes

$$\nabla^2 \mathbf{A} - \mu_0 \epsilon_0 \frac{\partial^2 \mathbf{A}}{\partial t^2} = -\mu_0 \mathbf{J}, \tag{C.24}$$

while the differential equation for Φ becomes

$$\nabla^2 \Phi - \mu_0 \epsilon_0 \frac{\partial^2 \Phi}{\partial t^2} = -\frac{\rho}{\epsilon_0}. \tag{C.25}$$

Actually, the equations (C.24) and (C.25) can be written in terms of a common differential operator:

$$\nabla^2 - \mu_0 \epsilon_0 \frac{\partial^2}{\partial t^2} \equiv \Box^2, \tag{C.26}$$

which is called *d'Alembertian*. So, these equations can also be written as

$$\begin{aligned} \Box^2 V &= -\tfrac{\rho}{\epsilon_0} \\ \Box^2 \mathbf{A} &= -\mu_0 \mathbf{J}. \end{aligned} \tag{C.27}$$

[1] Until recently, it was spelled "Lorentz", in honor of the Dutch physicist H. A. Lorentz, but is now attibuted to L. V. Lorenz, the Dane ([257], page 441).

Appendix D

Proof of Equation (3.39)

According to the reference [41], for $x \in \mathbb{R}$, we have

$$\pi \sum_f |\tilde{\psi}_f\rangle \delta(E_f - x) \langle \tilde{\psi}_f| = \lim_{\gamma \to 0} \mathfrak{Im} \left[\hat{S}^{-1/2} \frac{1}{x - \hat{S}^{-1/2} \tilde{H} \hat{S}^{-1/2} - i\gamma} \hat{S}^{-1/2} \right]. \tag{D.1}$$

Further, if

$$\pi \sum_f |\tilde{\psi}_f\rangle \delta(E_f - x) \langle \tilde{\psi}_f| = \lim_{\gamma \to 0} \mathfrak{Im} \left[\sum_f |\tilde{\psi}_f\rangle \frac{1}{x - E_f - i\gamma} \langle \tilde{\psi}_f| \right], \tag{D.2}$$

then we have

$$\begin{aligned} \sum_f |\tilde{\psi}_f\rangle \frac{1}{x - E_f - i\gamma} \langle \tilde{\psi}_f| = & \sum_f \hat{S}^{-1/2} \frac{1}{x - E_f - i\gamma} \hat{S}^{1/2} |\tilde{\psi}_f\rangle \langle \tilde{\psi}_f| = \sum_f \hat{S}^{-1/2} \frac{1}{x - \hat{S}^{-1/2} \tilde{H} \hat{S}^{-1/2} - i\gamma} \hat{S}^{1/2} |\tilde{\psi}_f\rangle \langle \tilde{\psi}_f| \\ = & \hat{S}^{-1/2} \frac{1}{x - \hat{S}^{-1/2} \tilde{H} \hat{S}^{-1/2} - i\gamma} \hat{S}^{-1/2} \sum_f \hat{S} |\tilde{\psi}_f\rangle \langle \tilde{\psi}_f| = \hat{S}^{-1/2} \frac{1}{x - \hat{S}^{-1/2} \tilde{H} \hat{S}^{-1/2} - i\gamma} \hat{S}^{-1/2}. \end{aligned} \tag{D.3}$$

where we have used the following property of (2.84):

$$\mathbb{1} = \sum_f |\tilde{\psi}_f\rangle \langle \tilde{\psi}_f| \hat{S} = \sum_f \hat{S} |\tilde{\psi}_f\rangle \langle \tilde{\psi}_f|. \tag{D.4}$$

Appendix E

$\hat{S}^{-1}$ Matrix Calculation

According to [96], $\hat{S}$ can be written as

$$\hat{S} = \mathbb{1} + \sum_{i,j} q_{ij} |\tilde{p}_i\rangle\langle\tilde{p}_j|, \tag{E.1}$$

and the matrix $\hat{S}^{-1}$ as

$$\hat{S}^{-1} = \mathbb{1} + \sum_{ij} a_{ij} |\tilde{p}_i\rangle\langle\tilde{p}_j|. \tag{E.2}$$

The condition $\hat{S}\hat{S}^{-1} = \mathbb{1}$ must be satisfied, so that

$$\begin{aligned} \hat{S}\hat{S}^{-1} = & \left(\mathbb{1} + \sum_{i,j} q_{ij}|]ep_i\rangle\langle\tilde{p}_j|\right)\left(\mathbb{1} + \sum_{l,m} a_{lm}|\tilde{p}_l\rangle\langle\tilde{p}_m|\right) \\ = & \quad \mathbb{1} + \sum_{i,j} |\tilde{p}_i\rangle\langle\tilde{p}_j| \left(q_{ij} + a_{ij} + \sum_{l,m} q_{ij} P_{jl} a_{lm}\right), \end{aligned} \tag{E.3}$$

where $P_{jl} = \langle\tilde{p}_j|\tilde{p}_l\rangle$. In matrix form, we have

$$q + a + qPa = 0, \tag{E.4}$$

whose solution is $a = -(1+qP)^{-1}Q$. Therefore, S^{-1} can be calculated by inverting the matrices of size $N_p \times N_p$, where N_p is the number of ultrasoft projectors.

Appendix F

Gauge-Including Projector Augmented-Wave Method

This method has its origin in the look for understanding atomic structure of systems under Nuclear Resonance Magnetic (NMR), whose chemical shift spectra give unambiguous determination of the microscopic structure [111]. Concerning first-principle calculations based in all-electron Hamiltonian [259, 260], up to 1996 only norm-conserving pseudopotentials have been used. In fact, pseudowave functions are properly chose because in the core region because of pseudopotential methods, and many properties, such as NMR chemical shifts, depend critically on the all-electron wavefunctions at the nucleus. As one knows, PAW approach gives an overall technique to calculate all-electron properties from pseudopotential-based scheme. For example, core-level [261] spectra and electric-field gradient [262] have been calculated using PAW method.

As in all works mentioned, an X-ray absorbing atom is in presence of an electromagnetic field, an extension of the Blöchl's PAW approach called Gauge-Including Projector Augmented Wave (GIPAW) is needed. This is necessary because the Hamiltonian constructed using GIPAW would have the demanded transational invariance in the presence of a magnetic field [111]. So, as PAW method has already been discussed in section 2.5.2, the single-augmentation region in a uniform magnetic field will be discussed, followed by the consequences under which translations under such fields could make rise. Afterwards, the GIPAW method will be introduced and, then, the GIPAW Hamiltonian. We will be based on the main work on this subbject [111].

F.1 The All-Electron Hamiltonian

In the presence an external magnetic field $\mathbf{B}$, the all-electron Hamiltonian is

$$H = \frac{1}{2}\left(\mathbf{p} + \frac{1}{c}\mathbf{A}(\mathbf{r})\right)^2 + V(\mathbf{r}), \tag{F.1}$$

where c is the speed of light, $V(\mathbf{r})$ is the all-electron local potential, and $\mathbf{B} = \boldsymbol{\nabla} \times \mathbf{A}(\mathbf{r})$. The aim is to construct a pseudo-Hamiltonian for a system, which will contain many augmentation region. To begin with, considering a simplest system with only one augmentation region around the atomic site.

The symmetric gauge is $\mathbf{A}(\mathbf{r}) = \frac{1}{2}\mathbf{B} \times (\mathbf{r} - \mathbf{d})$, where $\mathbf{d}$ indicates the gauge origin, from which the expectation values of the observables do not depend. Nonethless, the number of partial waves to describe the valence all-electron eigenstates do depends on $\mathbf{d}$. Putting $\mathbf{d} = \mathbf{0}$ (atomic site of that region) that number of partial waves is minimized, as well as the effect of the magnetic field on all-electron wavefunctions in the augmentation region [111]. Also, and this may be the most important aspect as we are using pseudopotential approximation, that choice of gauge results in diminishing the interaction between the valence and core states of the augmented atom.

Thus, if

$$\mathbf{A}(\mathbf{r}) = \frac{1}{2}\mathbf{B} \times \mathbf{r}, \tag{F.2}$$

the equation (**??**) becomes

$$H = \frac{1}{2}\mathbf{p}^2 + V(\mathbf{r}) + \frac{1}{2c}\mathbf{L} \cdot \mathbf{B} + \frac{1}{8c^2}\left(\mathbf{B} \times \mathbf{r}\right)^2, \tag{F.3}$$

where $\mathbf{L} = \mathbf{r} \times \mathbf{p}$ is the angular-momentum operator computed within the augmentation region.

Now, using the equation (2.96) rewritten here:

$$\tilde{\mathcal{O}} = \mathcal{O} \sum_{\mathbf{R},n,m} |\tilde{p}_{\mathbf{R},n}\rangle \left[\langle \phi_{\mathbf{R},n}|\mathcal{O}|\phi_{\mathbf{R},m}\rangle - \langle \tilde{\phi}_{\mathbf{R},n}|\mathcal{O}|\tilde{\phi}_{\mathbf{R},m}\rangle\right] \times \langle \tilde{p}_{\mathbf{R},m}|, \tag{F.4}$$

and supposing that the norms within $\Omega_{\mathbf{R}}$ of $|\tilde{\phi}_{\mathbf{R}}, n\rangle$ and $|\phi_{\mathbf{R}}, n\rangle$ coincide, we can recover the norm-conserving formalism of KB [263]. Thus, the pseudo-wave functions that correspond to the all-electron valence eigenstates of the H are eigenstate of the $\tilde{H}$ with the same eigenvalues. Thus,

$$\tilde{H} = \mathcal{T}^\dagger H \mathcal{T} = \frac{1}{2}\mathbf{p}^2 + V^{loc}(\mathbf{r}) + \sum_{\mathbf{R}} V^{nl}_{\mathbf{R}}, \tag{F.5}$$

where $V^{loc}(\mathbf{r})$ is the local part of the pseudopotentials, and its non-local part at the atomic site $\mathbf{R}$ is given by

$$V^{nl}_{\mathbf{R}} = \sum_{n,m} |\tilde{p}_{\mathbf{R},n}\rangle a^{\mathbf{R}}_{n,m} \langle \tilde{p}_{\mathbf{R},m}|, \tag{F.6}$$

where $a^{\mathbf{R}}_{n,m}$ depend on $\mathbf{R}$ because each atomic site may be occupied by a different chemical species [111].

The pseudo-Hamiltonian is obtained by using (F.4), (F.5) and (F.3):

$$\tilde{H} = \frac{1}{2}\mathbf{p}^2 + V^{loc}(\mathbf{r}) + V_{\mathbf{0}}^{nl} + \frac{1}{2c}\mathbf{L}\cdot\mathbf{B} + \frac{1}{8c^2}\left(\mathbf{B}\times\mathbf{r}\right)^2 + \sum_{n,m}|\tilde{p}_{\mathbf{0},n}\rangle\left(b_{n,m}^{(1)} + b_{n,m}^{(2)}\right)\langle\tilde{p}_{\mathbf{0},m}|, \tag{F.7}$$

where

$$b_{n,m}^{(1)} = \frac{1}{2c}\mathbf{B}\cdot\left[\langle\phi_{\mathbf{0},n}|\mathbf{L}|\phi_{\mathbf{0},m}\rangle - \langle\tilde{\phi}_{\mathbf{0},n}|\mathbf{L}|\tilde{\phi}_{\mathbf{0},m}\rangle\right], \tag{F.8}$$

and

$$b_{n,m}^{(2)} = \frac{1}{8c^2}\left[\langle\phi_{\mathbf{0},n}|\left(\mathbf{B}\times\mathbf{r}\right)^2|\phi_{\mathbf{0},m}\rangle - \langle\tilde{\phi}_{\mathbf{0},n}|\left(\mathbf{B}\times\mathbf{r}\right)^2|\tilde{\phi}_{\mathbf{0},m}\rangle\right]. \tag{F.9}$$

We can see that, as in norm-conserving case, if only one projector is used per angular momentum [100, 253], then $b_{n,m}^{(1)}$ vanishes, since both all-electron and pseudo wavefunctions are the same within the augmentation region, and also they are both eigenstates of L and L_z. Also, in the center of the augmentation region, $\left(\mathbf{B}\times\mathbf{r}\right)^2$ goes to zero. Therefore, with one augmentation region centered at the gauge origin, the coupling with the magnetic field in the pseudo- and all-electron Hamiltoninans has the same form:

$$\tilde{H} = \frac{1}{2}\mathbf{p}^2 + V^{loc}(\mathbf{r}) + V_{\mathbf{0}}^{nl} + \frac{1}{2c}\mathbf{L}\cdot\mathbf{B} + \frac{1}{8c^2}\left(\mathbf{B}\times\mathbf{r}\right)^2. \tag{F.10}$$

F.2 Translation Invariance

For systems with several augmentation region, the last derivation is not appropriated, since the gauge origin can coincide with just one augmentation region. Thus, the number of projectors of the other augmentation regions would have to increase for those regions [111]. The description of a system under a uniform magnetic field should be invariant upon atomic translation $\mathbf{t}$, however this does not occur in PAW approach.

The new potential for translated atoms is $V'(\mathbf{r}) = V(\mathbf{r}-\mathbf{t})$, and so the corresponding Hamiltonian:

$$H' = \frac{1}{2}\left(\mathbf{p} + \frac{1}{c}\mathbf{A}(\mathbf{r})\right)^2 + V(\mathbf{r}-\mathbf{t}), \tag{F.11}$$

where $\mathbf{A}(\mathbf{r})$ is given by equation (F.2).

The eigenenergies of H and of H' are the same because of the translational invariance, but the eigenstates $|\Psi'_n\rangle$ and $|\Psi_n\rangle$ are not. Actually, they need an additional phase owing to magnetic field:

$$\langle \mathbf{r}|\Psi'_n\rangle = e^{(i/2c)\mathbf{r}\cdot(\mathbf{t}\times\mathbf{B})}\langle \mathbf{r}-\mathbf{t}|\Psi_n\rangle, \tag{F.12}$$

which is not achieved by the transformation (2.95) according the PAW approach.

F.3 GIPAW Method

A PAW-like approach need to be constructed to restore the translation invariance. To do so, a new field-dependet transformation operator $\mathcal{T}_{\mathbf{B}}$ is defined as

$$\mathcal{T}_{\mathbf{B}} = \mathbf{1} + \sum_{\mathbf{R},n} e^{(i/2c)\mathbf{r}\cdot(\mathbf{R}\times\mathbf{B})}\left[|\phi_{\mathbf{R},n}\rangle - |\tilde{\phi}_{\mathbf{R},n}\rangle\right]\langle \tilde{p}_{\mathbf{R},n}|e^{-(i/2c)\mathbf{r}\cdot(\mathbf{R}\times\mathbf{B})}, \tag{F.13}$$

so that the GIPAW pseudo-wave functions and the GIPAW operators obtained with $\mathcal{T}_{\mathbf{B}}$ are read as $|\bar{\Psi}\rangle$ and $\bar{\mathcal{O}}$, respectively. The pseudo-eigenstate $|\bar{\Psi}\rangle = \mathcal{T}_{\mathbf{B}}|\Psi\rangle$, thus, satisfies the same translation relation as that of equation (F.12). And the GIPAW pseudo-operator $\bar{\mathcal{O}} = \mathcal{T}^{\dagger}_{\mathbf{B}}\mathcal{O}\mathcal{T}_{\mathbf{B}}$ is given by

$$\begin{aligned}\bar{\mathcal{O}} = \mathcal{O} + \sum_{\mathbf{R},n,m} & e^{(i/2c)\mathbf{r}\cdot(\mathbf{R}\times\mathbf{B})}|\tilde{p}_{\mathbf{R},n}\rangle \\ & \times \Big[\langle\phi_{\mathbf{R},n}|e^{-(i/2c)\mathbf{r}\cdot(\mathbf{R}\times\mathbf{B})}\mathcal{O}e^{(i/2c)\mathbf{r}\cdot(\mathbf{R}\times\mathbf{B})}|\phi_{\mathbf{R},m}\rangle \\ & - \langle\tilde{\phi}_{\mathbf{R},n}|e^{-(i/2c)\mathbf{r}\cdot(\mathbf{R}\times\mathbf{B})}\mathcal{O}e^{(i/2c)\mathbf{r}\cdot(\mathbf{R}\times\mathbf{B})}|\tilde{\phi}_{\mathbf{R},m}\rangle\Big] \\ & \times \langle\tilde{p}_{\mathbf{R},m}|e^{-(i/2c)\mathbf{r}\cdot(\mathbf{R}\times\mathbf{B})}.\end{aligned} \tag{F.14}$$

F.4 GIPAW Hamiltonian

From equation (F.14), using the identity

$$e^{-(i/2c)\mathbf{r}\cdot(\mathbf{R}\times\mathbf{B})}\left(\mathbf{p}+\frac{1}{c}\mathbf{A}(\mathbf{r})\right)^n e^{(i/2c)\mathbf{r}\cdot(\mathbf{R}\times\mathbf{B})} = \left(\mathbf{p}+\frac{1}{c}\mathbf{A}(\mathbf{r}-\mathbf{R})\right)^n, \tag{F.15}$$

where n is an integer, and the results from section F.1 for $b^{(1)}_{n,m}$ and $b^{(2)}_{n,m}$, we get the GIPAW pseudo-Hamiltonian:

$$\bar{H} = \frac{1}{2}\mathbf{p}^2 + V^{loc}(\mathbf{r}) + \sum_{\mathbf{R}} e^{(i/2c)\mathbf{r}\cdot(\mathbf{R}\times\mathbf{B})}\, V^{nl}_{\mathbf{R}}\, e^{-(i/2c)\mathbf{r}\cdot(\mathbf{R}\times\mathbf{B})} + \frac{1}{2c}\mathbf{L}\cdot\mathbf{B} + \frac{1}{8c^2}\left(\mathbf{B}\times\mathbf{r}\right)^2. \tag{F.16}$$

If one makes $\mathbf{B} = \mathbf{0}$ the GIPAW Hamiltonina recovers the PAW Hamiltonian of equation (F.5), and for $\mathbf{B} \neq \mathbf{0}$ it recovers the PAW Hamiltoninan of equation (F.10) for systems with a single augmentation region centered at the origin [111]. Also, indeed, the GIPAW eigenenergies are invariant upon translation, unlike the PAW ones. Therefore, with such an instrument, one is able to obtain the expectation values of the desired operators.

Appendix G

Bader Charge Analysis

Following [234], an intuitive way of saparating molecules into atoms is called Quantum Theory of Atoms in Molecules (QTAIM)[1]. An atom participating in a molecular bonding is defined based purely on its electronic charge density within a specific volume. Each atom is separated by a bidimensional zero-flux surface, where the charge density is a minimum between the atoms, and their maxima are located on each of them, as one can see in figure G.1.

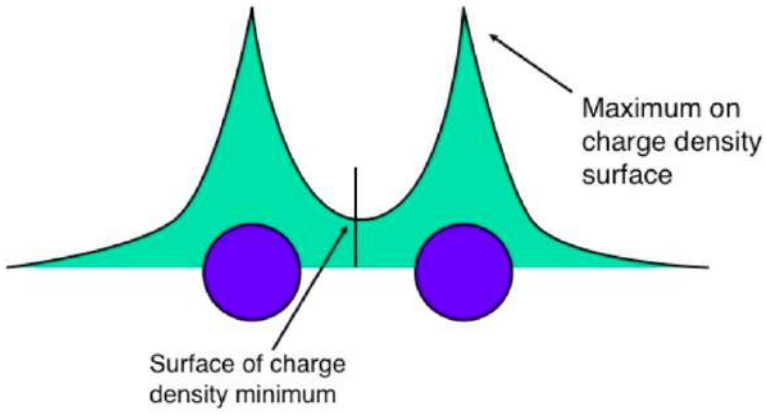

Figure G.1: A sketch of the region comprised by two bonding atoms (blue circles), which is shown by light green color. The surface charge density and the maximum charge density are shown in the figure (extracted from [234]).

The surface density defined as a surface that separated the volume comprising each atom, or the Barder volumes, has the minima of the scalar function, the charge density in this case. It is, in turn, defined in a grid of points, whose values are evaluated and assigned to define a path (arrows in figure G.2-a) towards which a maximum is found. Whenever two maxima is found (see figure G.2-b), the minima between them define the zero-flux surface, which separetes the Bader volumes (red line in that figure) [235]. Therefore, integrating all the charge density within the Bader volume one is able to get the Bader charge for that atom.

[1] It was devised by Richard Bader from McMaster University [264].

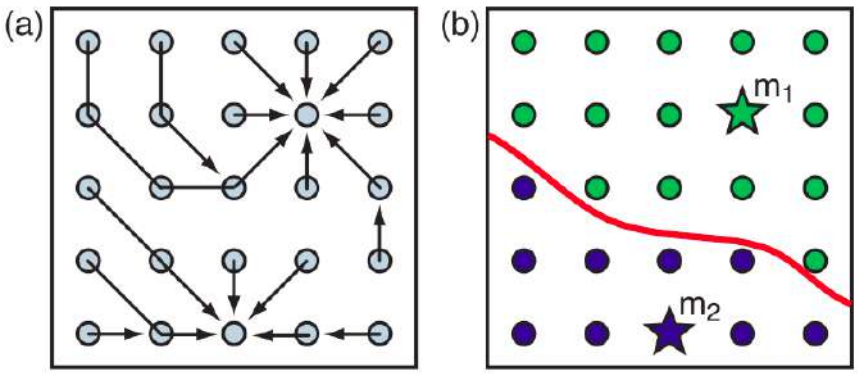

Figure G.2: Partitioning of the charge density grid into Bader volumes around the atomic site. Each point in figure (a) composes the grid of charge density function, and each arrow points to its maxima following certain criteria, such as if the point was already assigned or if it has a higher value than the previous one. After the assignment of every point of the grid, the set of point close to each maximum (m_1 in green, and m_2 in blue) determines the Bader volume. The minimum between these two volumes (two atoms) defines the Bader surface that separates the two volumes, which is shown in figure (b) by a red line. Figure from [235].

Appendix H

Supplementary Results

H.1 Local PDOS for XANES contributions shown in figure 6.18

The peak a* in Fig.H.1 has contributions from spin-down p_z orbitals from Y and X' (smaller contribution) atoms, as well as the out-of plane atoms (2nd line in the plot), and the in-plane atom w.r.t. X? atom. Regarding the d* peak, we have contribution from p_z orbital from both X and O atoms.

Peak d, in turn, has p_z orbitals from out-of-plane atom w.r.t. the X and X' atoms, and also from p_y orbitals from in-plane atoms w.r.t. the X and Y atoms. Also, there are contribution from p_z and p_x orbitals from the X and X' atoms themselves.

Concerning the d' peak, we have that p_y orbitals from X atoms contribute. p_x orbitals from in-plane atoms w.r.t. the X atom, and p_y orbital w.r.t. the Y atom play their role. Regarding the out-of-plane ones, p_z orbitals from Y and X atoms contribute, the former contributes mostly. Peak d'* has a strong mixture of contributions from different atoms when it comes to the in-plane atoms and absorbent ones themselves. Nonetheless, the out-of-plane atoms w.r.t. Y and X' atoms strongly contributes with p_z orbitals.

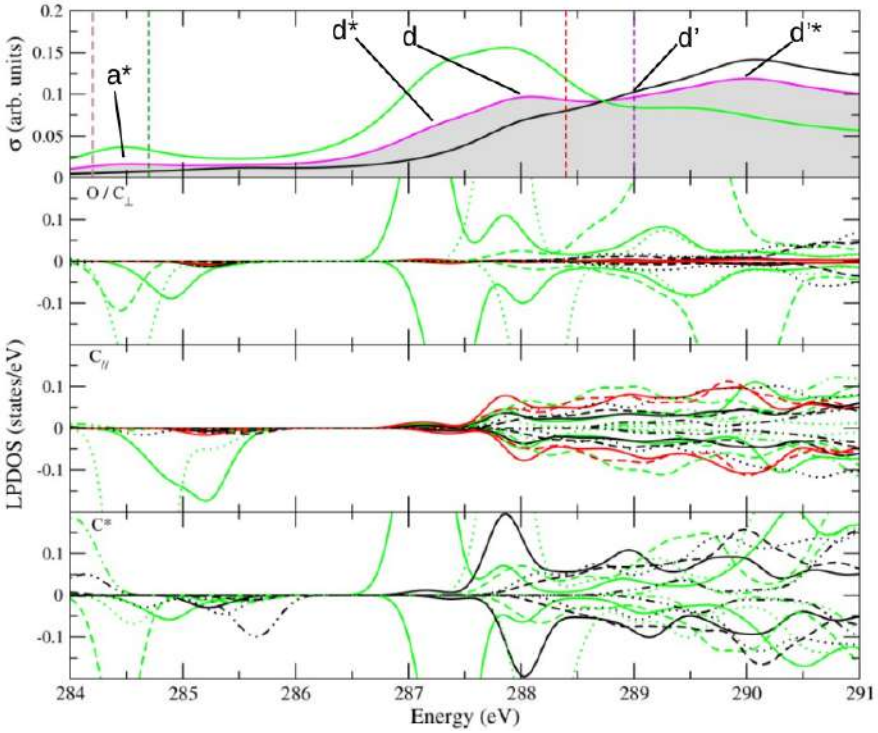

Figure H.1: First line: XANES of diamondol (magenta line) lines green and black (armchair direction), or red (zingzag direction), refer to parallel and perpendicular XANES polarization. Second line refer to PDOS of the atoms that lay perpendicularly the absorbent one. Third line: atoms that lay in-plane w.r.t. the absorbent one. Last line: absorbent ones. The solid, dashed, dotted, and dashd-dotted lines refer to the atoms X, Y, X', and Y', respectively.

Regarding the bidiamondol system (Fig.H.2), peak d* has contribution from p z orbitals of both the X atom itself and oxygen atom attached to it. There is also a tiny contribution from p_x and p_y orbitals of X atom and its parallel neighbors. Likewise, the peak b has also the same kind of contributions, added to them also the p_x and p_y states from parallel atoms w.r.t. both the X and Y atoms. It is important to notice that the atoms X' and Y' are equivalents to their counterparts, the X and Y ones. Therefore, they present the same contributions.

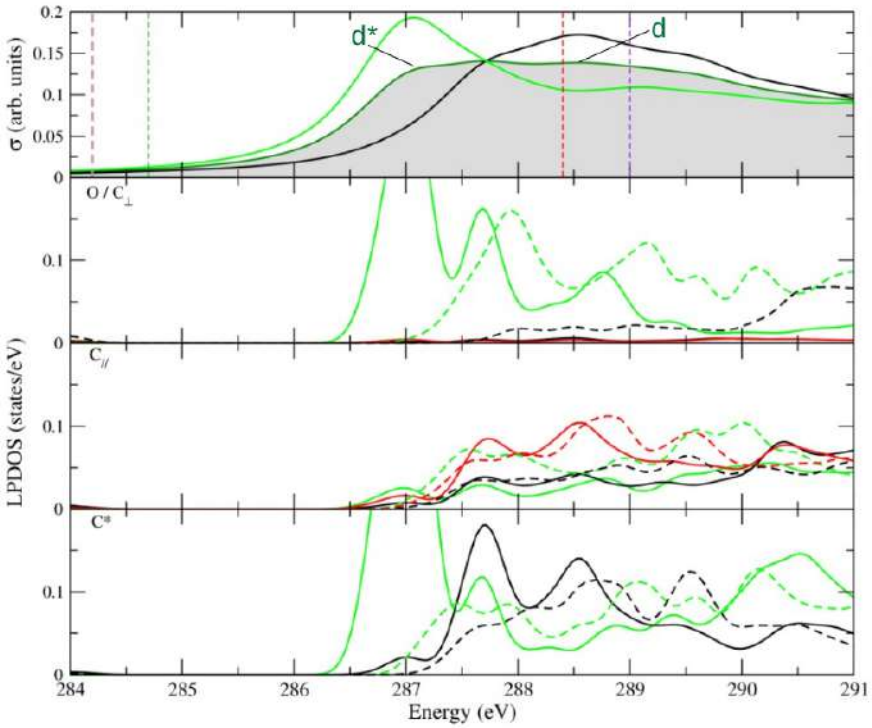

Figure H.2: First line: XANES of bidiamondol (dark green line) lines green and black (armchair direction), or red (zingzag direction), refer to parallel and perpendicular XANES polarization. Second line refer to PDOS of the atoms that lay perpendicularly the absorbent one. Third line: atoms that lay in-plane w.r.t. the absorbent one. Last line: absorbent ones. The solid and dashed lines refer to the atoms X and Y, respectively. Atoms X' and Y' are equivalent to them.

The F-diamane's peak a*, as shown in Fig.H.3, has contributions from spin-down p_z orbitals from Y atom, as well as the out-of plane atoms (2nd line in the plot), and the in-plane atom w.r.t. X and X' atom. Regarding the d* peak, we have contribution from p_z orbital from both X and F atoms, just as in the diamondol case. Peak d has p_z orbitals from out-of-plane atom w.r.t. the X and X' atoms, and also from p_y orbitals from in-plane atoms w.r.t. the X and Y atoms. Also, there are contribution from p_z and p_x orbitals from the X and X' (smaller in comparison) atoms themselves. It is important to notice that there is no contribution from p_z orbitals of perpendicular atoms to the X at 288 eV, as observed in diamondol. Concerning the d' peak, the contributions are very similar to those of diamondol. Concerning the peak b* the strong mixture of contributions comes mainly from p_x and p_y orbitals of different atoms when it comes to the in-plane atoms and absorbent ones themselves. Nonetheless, the out-of-plane atoms w.r.t. Y (2nd line) and X' (4th line) atoms strongly contributes with $acep_z orbitals$.

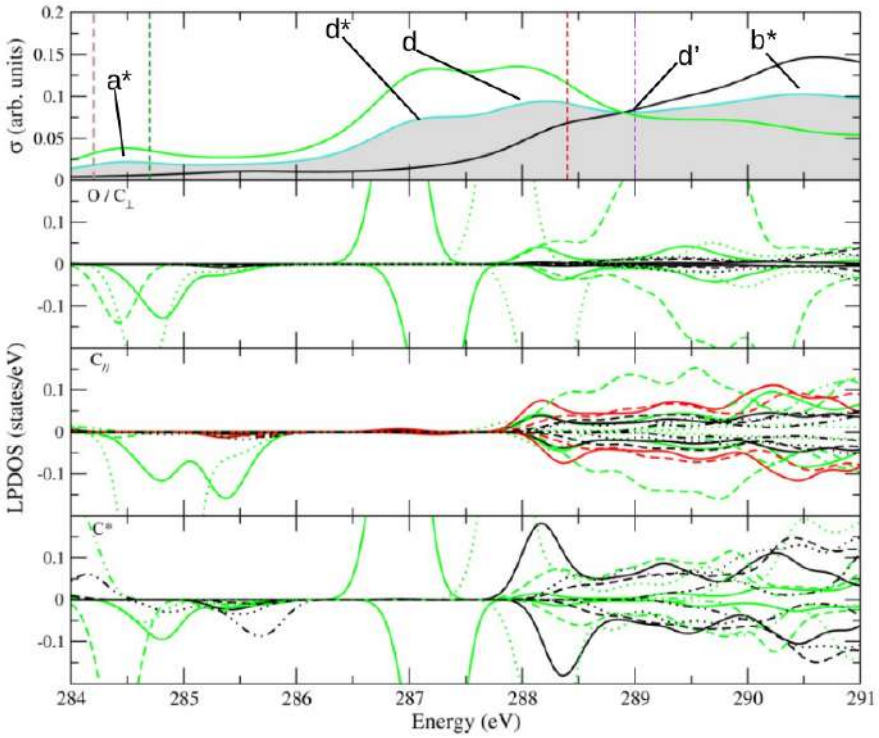

Figure H.3: First line: XANES of F-diamane (turquoise line) lines green and black (armchair direction), or red (zingzag direction), refer to parallel and perpendicular XANES polarization. Second line refer to PDOS of the atoms that lay perpendicularly the absorbent one. Third line: atoms that lay in-plane w.r.t. the absorbent one. Last line: absorbent ones. The solid, dashed, dotted, and dashd-dotted lines refer to the atoms X, Y, X', and Y', respectively.

Concerning peak a of bi-F-diamane (Fig.H.4, p_z orbitals from X atom and perpendicular first-neighbor have the most important contribution. Also, p_z orbitals from Y atom and its first-neighbors contribute to the continuity of the observed spectrum. Regarding the peak d*, one has mainly contribution from p_z orbitals from Y atom and its perpendicular neighbor, and also p_x and p_y orbitals from X and Y atoms and their parallel neighbors. Peak d, in turn, despite the same kind of contributions compared to the d* peak, it is found that the p_z ones are less intense compared with the others.

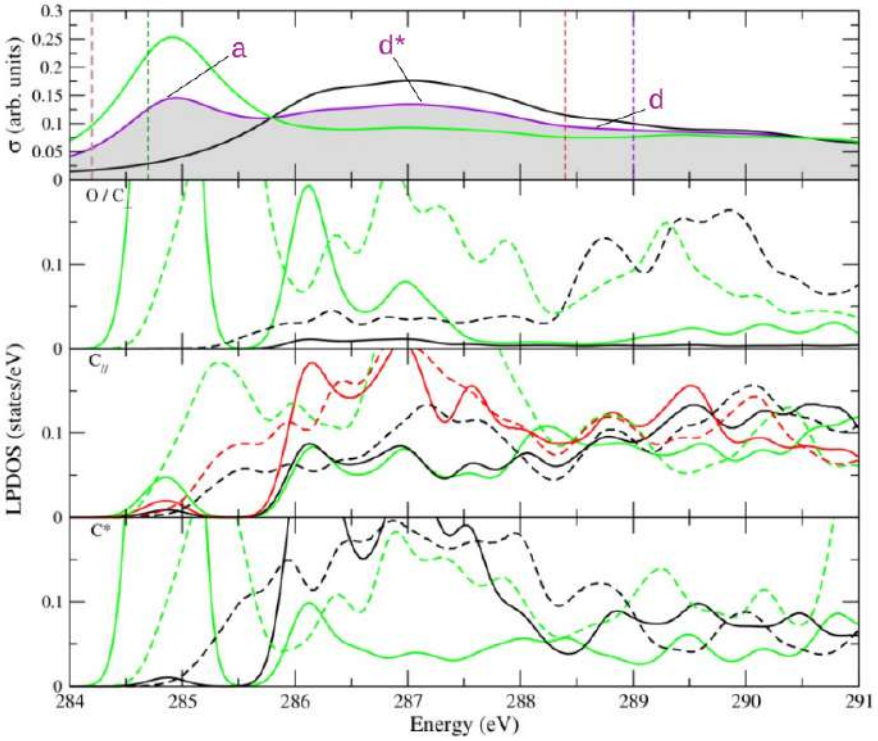

Figure H.4: First line: XANES of bi-F-diamane (purple line), green and black (armchair direction), or red (zingzag direction), lines refer to parallel and perpendicular XANES polarization, respectively. Second line refer to PDOS of the atoms that lay perpendicularly the absorbent one. Third line: atoms that lay in-plane w.r.t. the absorbent one. Last line: absorbent ones. The solid and dashed lines refer to the atoms X and Y, respectively. Atoms X' and Y' are equivalent to those.

H.2 Mo-based Systems, and Their Interaction with Acetonitrile

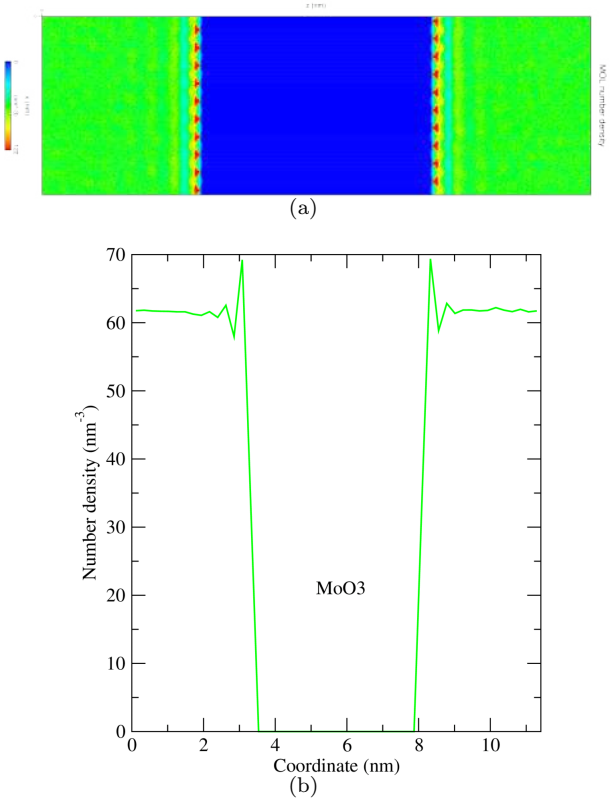

Figure H.5: Number-density color map along the z direction, number density, and charge density for ACN molecule interacting with the MoO_3 solid. All the figures refer to the simulation "S3". In figure (a), the color scale indicates that the red refers to the maximum value, while the blue color refers to the minimum value, which means that all the blue region is related to the solid.

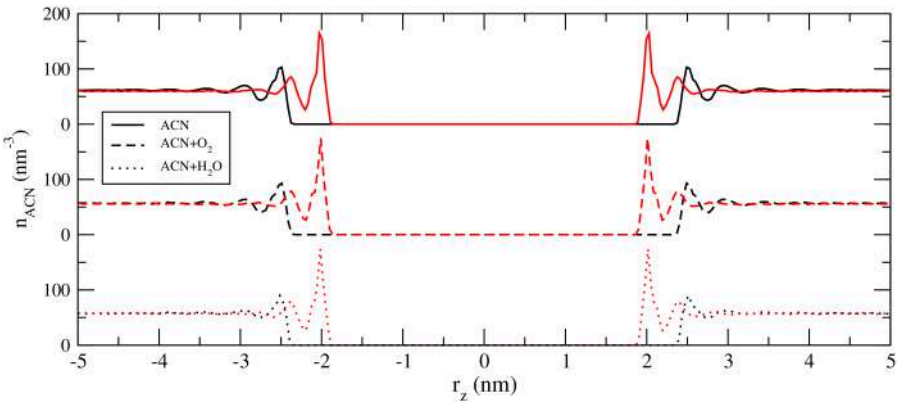

Figure H.6: Number density of ACN molecules in simulation boxes containg only pure ACN (solid lines), O_2 (dashed lines), and H_2O (dotted lines). Black and red lines refer to the MoO_3 and MoS_2 solids, respectively. The $r_z = 0$ is set in the middle of the solid.

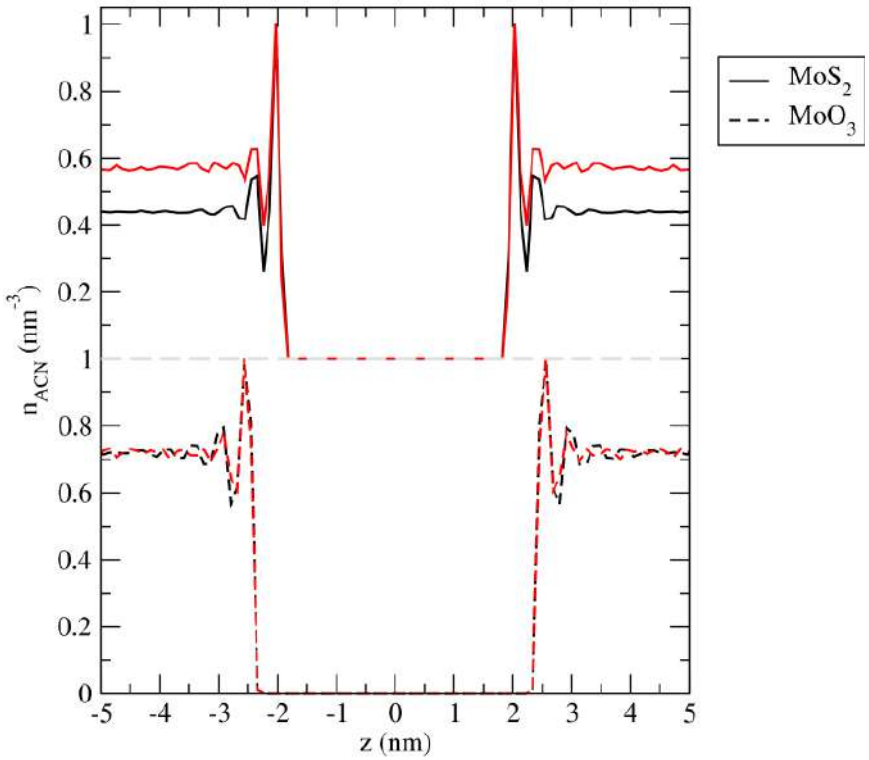

Figure H.7: Normalized ACN number density, n_{ACN}, of the systems containing MoS_2 (solid lines) and MoO_3 (dashed lines). Black lines refer to the larger system, which contains 1000 ACN molecules (top part of the figure **(a)**), whereas red lines indicate systems containing 85 (96) ACN molecules in the smaller system with MoO_3 (MoS_2), as depicted in figure 7.11.

Bibliography

[1] BUNDY, F.; HALL, H. T.; STRONG, H.; WENTORF, R. Man-made diamonds. *nature*, v. 176, n. 4471, p. 51–55, 1955.

[2] MA, Y.; WASSDAHL, N.; SKYTT, P.; GUO, J.; NORDGREN, J.; JOHNSON, P.; RUBENSSON, J.; BOSKE, T.; EBERHARDT, W.; KEVAN, S. Soft-x-ray resonant inelastic scattering at the c k edge of diamond. *Physical review letters*, v. 69, n. 17, p. 2598, 1992.

[3] ABBASCHIAN, R.; ZHU, H.; CLARKE, C. High pressure–high temperature growth of diamond crystals using split sphere apparatus. *Diamond and related materials*, v. 14, n. 11-12, p. 1916–1919, 2005.

[4] YARNELL, A. The many facets of man-made diamonds. *Chemical & engineering news*, v. 82, n. 5, p. 26–31, 2004.

[5] Synthetic diamond - wikipedia. https://en.wikipedia.org/wiki/Synthetic_diamond. (Accessed on 03/06/2020).

[6] JACKSON, D.; ARACNE-RUDDLE, C.; MALBA, V.; WEIR, S.; CATLEDGE, S.; VOHRA, Y. Magnetic susceptibility measurements at high pressure using designer diamond anvils. *Review of scientific instruments*, v. 74, n. 4, p. 2467–2471, 2003.

[7] DENISENKO, A.; KOHN, E. Diamond power devices. concepts and limits. *Diamond and related materials*, v. 14, n. 3-7, p. 491–498, 2005.

[8] SALEHPOUR, M.; SATPATHY, S. Comparison of electron bands of hexagonal and cubic diamond. *Physical Review B*, v. 41, n. 5, p. 3048, 1990.

[9] ROBERTS, R.; WALKER, W. Optical study of the electronic structure of diamond. *Physical Review*, New York, v. 161, n. 3, p. 730, 1967.

[10] KHOUNSARY, A. M.; SMITHER, R. K.; DAVEY, S.; PUROHIT, A. Diamond monochromator for high heat flux synchrotron x-ray beams. In: . c1993. v. 1739. p. 628–642.

[11] J. HÃ¤RTWIG, P. VAN VAERENBERGH, I. G. J. H. A. R. A. C. G. C. S. C. M. R. R. S. D. D. L. M. R. B. J. H. Diamonds for modern synchrotron radiation sources. http://www.esrf.eu/UsersAndScience/Publications/Highlights/2005/Imaging/XIO5. (Accessed on 03/06/2020).

[12] Semiconductor - wikipedia. https://en.wikipedia.org/wiki/Semiconductor#Germanium_and_silicon_semiconductors. (Accessed on 08/25/2021).

[13] BERNAL, J. D. The structure of graphite. *Proceefings of the Royal Society of London. Series A, Containing Paper of a Mathematical and Physical Character*, v. 106, n. 740, p. 749–773, 1924.

[14] NOVOSELOV, K. S.; GEIM, A. K.; MOROZOV, S. V.; JIANG, D.; ZHANG, Y.; DUBONOS, S. V.; GRIGORIEVA, I. V.; FIRSOV, A. A. Electric field effect in atomically thin carbon films. *science*, v. 306, n. 5696, p. 666–669, 2004.

[15] LIN, Y.; WILLIAMS, T. V.; CONNELL, J. W. Soluble, exfoliated hexagonal boron nitride nanosheets. *The Journal of Physical Chemistry Letters*, v. 1, n. 1, p. 277–283, 2010.

[16] CHHOWALLA, M.; SHIN, H. S.; EDA, G.; LI, L.-J.; LOH, K. P.; ZHANG, H. The chemistry of two-dimensional layered transition metal dichalcogenide nanosheets. *Nature chemistry*, v. 5, n. 4, p. 263, 2013.

[17] HUANG, X.; ZENG, Z.; ZHANG, H. Metal dichalcogenide nanosheets: preparation, properties and applications. *Chemical Society Reviews*, v. 42, n. 5, p. 1934–1946, 2013.

[18] XU, M.; LIANG, T.; SHI, M.; CHEN, H. Graphene-like two-dimensional materials. *Chemical reviews*, v. 113, n. 5, p. 3766–3798, 2013.

[19] CHHOWALLA, M.; LIU, Z.; ZHANG, H. Two-dimensional transition metal dichalcogenide (tmd) nanosheets. *Chemical Society Reviews*, v. 44, n. 9, p. 2584–2586, 2015.

[20] OSADA, M.; SASAKI, T. Exfoliated oxide nanosheets: new solution to nanoelectronics. *Journal of Materials Chemistry*, v. 19, n. 17, p. 2503–2511, 2009.

[21] WANG, Q.; Oâ€™HARE, D. Recent advances in the synthesis and application of layered double hydroxide (ldh) nanosheets. *Chemical reviews*, v. 112, n. 7, p. 4124–4155, 2012.

[22] JI, Z.; ZHANG, L.; XIE, G.; XU, W.; GUO, D.; LUO, J.; PRAKASH, B. Mechanical and tribological properties of nanocomposites incorporated with two-dimensional materials. *Friction*, v. 8, n. 5, p. 813–846, 2020.

[23] FRENKEL, D.; SMIT, B. *Understanding molecular simulation: from algorithms to applications*. Elsevier, 2001. v. 1.

[24] ZHANG, H. Ultrathin two-dimensional nanomaterials. *ACS nano*, v. 9, n. 10, p. 9451–9469, 2015.

[25] ALLEN, M. P.; TILDESLEY, D. J. *Computer simulation of liquids*. Oxford university press, 2017.

[26] FRIEDERICH, P.; HÄSE, F.; PROPPE, J.; ASPURU-GUZIK, A. Machine-learned potentials for next-generation matter simulations. *Nature Materials*, v. 20, n. 6, p. 750–761, 2021.

[27] HOHENBERG, P.; KOHN, W. Inhomogeneous electron gas. *Physical review*, v. 136, n. 3B, p. B864, 1964.

[28] KOHN, W.; SHAM, L. J. Self-consistent equations including exchange and correlation effects. *Physical Review*, New York, v. 140, n. 4A, p. A1133, 1965.

[29] SCHLEDER, G. R.; PADILHA, A. C.; ACOSTA, C. M.; COSTA, M.; FAZZIO, A. From dft to machine learning: recent approaches to materials science–a review. *Journal of Physics: Materials*, v. 2, n. 3, p. 032001, 2019.

[30] OZBOYACI, M.; KOKH, D. B.; CORNI, S.; WADE, R. C. Modeling and simulation of protein–surface interactions: achievements and challenges. *Quarterly reviews of biophysics*, v. 49, 2016.

[31] KOHN, W. Nobel lecture: Electronic structure of matterâ€"wave functions and density functionals. *Reviews of Modern Physics*, Woodbury, v. 71, n. 5, p. 1253, 1999.

[32] POPLE, J. A. Nobel lecture: Quantum chemical models. *Reviews of Modern Physics*, Woodbury, v. 71, n. 5, p. 1267, 1999.

[33] BURKE, K. Perspective on density functional theory. *The Journal of chemical physics*, v. 136, n. 15, p. 150901, 2012.

[34] IORI, F.; CORNI, S.; DI FELICE, R. Unraveling the interaction between histidine side chain and the au (111) surface: a dft study. *The Journal of Physical Chemistry C*, v. 112, n. 35, p. 13540–13545, 2008.

[35] DE GROOT, F.; KOTANI, A. *Core level spectroscopy of solids*. CRC press, 2008.

[36] VAN BOKHOVEN, J. A.; LAMBERTI, C. *X-ray absorption and x-ray emission spectroscopy: theory and applications*. John Wiley & Sons, 2016. v. 1.

[37] SAYERS, D. E.; STERN, E. A.; LYTLE, F. W. New technique for investigating noncrystalline structures: Fourier analysis of the extended x-rayâ€"absorption fine structure. *Physical review letters*, v. 27, n. 18, p. 1204, 1971.

[38] VAN NORDSTHAND, R. A. The use of x-ray k-absorption edges in the study of catalytically active solids. In: *Advances in catalysis*. Elsevier, 1960. v. 12, p. 149–187.

[39] TAILLEFUMIER, M.; CABARET, D.; FLANK, A.-M.; MAURI, F. X-ray absorption near-edge structure calculations with the pseudopotentials: Application to the k edge in diamond and α-quartz. *Physical Review B*, v. 66, n. 19, p. 195107, 2002.

[40] BROUDER, C. Angular dependence of x-ray absorption spectra. *Journal of Physics: Condensed Matter*, Bristol, v. 2, n. 3, p. 701, 1990.

[41] GOUGOUSSIS, C.; CALANDRA, M.; SEITSONEN, A. P.; MAURI, F. First-principles calculations of x-ray absorption in a scheme based on ultrasoft pseudopotentials: From α-quartz to high-t c compounds. *Physical Review B*, v. 80, n. 7, p. 075102, 2009.

[42] DE OLIVEIRA, I.; KAGIMURA, R.; VENEZUELA, P.; MIWA, R. Investigating the preservation of π–conjugation in covalently functionalized carbon nanotubes through first principles simulations. *The Journal of chemical physics*, v. 150, n. 20, p. 204701, 2019.

[43] GIANNOZZI, P.; BARONI, S.; BONINI, N.; CALANDRA, M.; CAR, R.; CAVAZZONI, C.; CERESOLI, D.; CHIAROTTI, G. L.; COCOCCIONI, M.; DABO, I.; Dal Corso, A.; DE GIRONCOLI, S.; FABRIS, S.; FRATESI, G.; GEBAUER, R.; GERSTMANN, U.; GOUGOUSSIS, C.; KOKALJ, A.; LAZZERI, M.; MARTIN-SAMOS, L.; MARZARI, N.; MAURI, F.; MAZZARELLO, R.; PAOLINI, S.; PASQUARELLO, A.; PAULATTO, L.; SBRACCIA, C.; SCANDOLO, S.; SCLAUZERO, G.; SEITSONEN, A. P.; SMOGUNOV, A.; UMARI, P.; WENTZCOVITCH, R. M. Quantum espresso: a modular and open-source software project for quantum simulations of materials. *Journal of Physics: Condensed Matter*, Bristol, v. 21, n. 39, p. 395502 (19pp), 2009. http://www.quantum-espresso.org.

[44] International year of light - lightsources of the world. http://www.light2015.org/Home/LearnAboutLight/Lightsources-of-the-world.html. (Accessed on 03/06/2020).

[45] SALLOUM ABOU JAOUDE, G. *In situ investigation by x-ray radiography of microstructure evolution during solidification of binary alloys*. 2014. Tese (Doutorado em Física) - Aix-Marseille, 2014.

[46] BERGER, C.; SONG, Z.; LI, T.; LI, X.; OGBAZGHI, A. Y.; FENG, R.; DAI, Z.; MARCHENKOV, A. N.; CONRAD, E. H.; FIRST, P. N. et al. Ultrathin epitaxial graphite: 2d electron gas properties and a route toward graphene-based nanoelectronics. *The Journal of Physical Chemistry B*, v. 108, n. 52, p. 19912–19916, 2004.

[47] TURNEAURE, S. J.; SHARMA, S. M.; VOLZ, T. J.; WINEY, J.; GUPTA, Y. M. Transformation of shock-compressed graphite to hexagonal diamond in nanoseconds. *Science advances*, v. 3, n. 10, p. eaao3561, 2017.

[48] DECARLI, P. S.; JAMIESON, J. C. Formation of diamond by explosive shock. *Science*, Washington, v. 133, n. 3467, p. 1821–1822, 1961.

[49] NETO, A. C.; GUINEA, F.; PERES, N. M.; NOVOSELOV, K. S.; GEIM, A. K. The electronic properties of graphene. *Reviews of modern physics*, v. 81, n. 1, p. 109, 2009.

[50] MCCANN, E. Asymmetry gap in the electronic band structure of bilayer graphene. *Physical Review B*, v. 74, n. 16, p. 161403, 2006.

[51] OHTA, T.; BOSTWICK, A.; SEYLLER, T.; HORN, K.; ROTENBERG, E. Controlling the electronic structure of bilayer graphene. *Science*, Washington, v. 313, n. 5789, p. 951–954, 2006.

[52] PARK, S.; RUOFF, R. S. Chemical methods for the production of graphenes. *Nature nanotechnology*, v. 4, n. 4, p. 217–224, 2009.

[53] ELIAS, D. C.; NAIR, R. R.; MOHIUDDIN, T.; MOROZOV, S.; BLAKE, P.; HALSALL, M.; FERRARI, A. C.; BOUKHVALOV, D.; KATSNELSON, M.; GEIM, A. et al. Control of graphene's properties by reversible hydrogenation: evidence for graphane. *Science*, Washington, v. 323, n. 5914, p. 610–613, 2009.

[54] PRADO, M. C.; NASCIMENTO, R.; MOURA, L. G.; MATOS, M. J.; MAZZONI, M. S.; CANCADO, L. G.; CHACHAM, H.; NEVES, B. R. Two-dimensional molecular crystals of phosphonic acids on graphene. *ACS nano*, v. 5, n. 1, p. 394–398, 2011.

[55] ZHOU, J.; WANG, Q.; SUN, Q.; CHEN, X.; KAWAZOE, Y.; JENA, P. Ferromagnetism in semihydrogenated graphene sheet. *Nano letters*, v. 9, n. 11, p. 3867–3870, 2009.

[56] BARBOZA, A. P.; GUIMARAES, M. H.; MASSOTE, D. V.; CAMPOS, L. C.; BARBOSA NETO, N. M.; CANCADO, L. G.; LACERDA, R. G.; CHACHAM, H.; MAZZONI, M. S.; NEVES, B. R. Room-temperature compression-induced diamondization of few-layer graphene. *Advanced Materials*, v. 23, n. 27, p. 3014–3017, 2011.

[57] BAKHAREV, P. V.; HUANG, M.; SAXENA, M.; LEE, S. W.; JOO, S. H.; PARK, S. O.; DONG, J.; CAMACHO-MOJICA, D. C.; JIN, S.; KWON, Y. et al. Chemically induced transformation of chemical vapour deposition grown bilayer graphene into fluorinated single-layer diamond. *Nature nanotechnology*, v. 15, n. 1, p. 59–66, 2020.

[58] MARTINS, L. G. P.; MATOS, M. J.; PASCHOAL, A. R.; FREIRE, P. T.; ANDRADE, N. F.; AGUIAR, A. L.; KONG, J.; NEVES, B. R.; DE OLIVEIRA, A. B.; MAZZONI, M. S. et al. Raman evidence for pressure-induced formation of diamondene. *Nature communications*, v. 8, n. 1, p. 1–9, 2017.

[59] KALANTAR-ZADEH, K.; TANG, J.; WANG, M.; WANG, K. L.; SHAILOS, A.; GALATSIS, K.; KOJIMA, R.; STRONG, V.; LECH, A.; WLODARSKI, W. et al. Synthesis of nanometre-thick moo 3 sheets. *Nanoscale*, v. 2, n. 3, p. 429–433, 2010.

[60] SCANLON, D. O.; WATSON, G. W.; PAYNE, D.; ATKINSON, G.; EGDELL, R.; LAW, D. Theoretical and experimental study of the electronic structures of moo3 and moo2. *The Journal of Physical Chemistry C*, v. 114, n. 10, p. 4636–4645, 2010.

[61] RAMADOSS, A.; KIM, T.; KIM, G.-S.; KIM, S. J. Enhanced activity of a hydrothermally synthesized mesoporous mos 2 nanostructure for high performance supercapacitor applications. *New Journal of Chemistry*, v. 38, n. 6, p. 2379–2385, 2014.

[62] LOU, X. W.; ZENG, H. C. Hydrothermal synthesis of α-moo3 nanorods via acidification of ammonium heptamolybdate tetrahydrate. *Chemistry of materials*, v. 14, n. 11, p. 4781–4789, 2002.

[63] ZHAN, Y.; LIU, Z.; NAJMAEI, S.; AJAYAN, P. M.; LOU, J. Large-area vapor-phase growth and characterization of mos2 atomic layers on a sio2 substrate. *Small*, v. 8, n. 7, p. 966–971, 2012.

[64] ABDELLAOUI, A.; MARTIN, L.; DONNADIEU, A. Structure and optical properties of moo3 thin films prepared by chemical vapor deposition. *physica status solidi (a)*, v. 109, n. 2, p. 455–462, 1988.

[65] UZCANGA, I.; BEZVERKHYY, I.; AFANASIEV, P.; SCOTT, C.; VRINAT, M. Sonochemical preparation of mos2 in aqueous solution: replication of the cavitation bubbles in an inorganic material morphology. *Chemistry of materials*, v. 17, n. 14, p. 3575–3577, 2005.

[66] YOGANANDA, H.; NAGABHUSHANA, H.; NAIK, R.; PRASHANTHA, S. Calcination temperature dependent structural modifications, tailored morphology and luminescence properties of moo3 nanostructures prepared by sonochemical method. *Journal of Science: Advanced Materials and Devices*, v. 3, n. 1, p. 77–85, 2018.

[67] KARADE, S. S.; DUBAL, D. P.; SANKAPAL, B. R. Mos 2 ultrathin nanoflakes for high performance supercapacitors: room temperature chemical bath deposition (cbd). *RSC advances*, v. 6, n. 45, p. 39159–39165, 2016.

[68] SALVATIERRA, R. V.; OLIVEIRA, M. M.; ZARBIN, A. J. One-pot synthesis and processing of transparent, conducting, and freestanding carbon nanotubes/polyaniline composite films. *Chemistry of Materials*, v. 22, n. 18, p. 5222–5234, 2010.

[69] COLEMAN, J. N.; LOTYA, M.; Oâ€™NEILL, A.; BERGIN, S. D.; KING, P. J.; KHAN, U.; YOUNG, K.; GAUCHER, A.; DE, S.; SMITH, R. J. et al. Two-dimensional nanosheets produced by liquid exfoliation of layered materials. *Science*, Washington, v. 331, n. 6017, p. 568–571, 2011.

[70] VARRLA, E.; BACKES, C.; PATON, K. R.; HARVEY, A.; GHOLAMVAND, Z.; MCCAULEY, J.; COLEMAN, J. N. Large-scale production of size-controlled mos2 nanosheets by shear exfoliation. *Chemistry of Materials*, v. 27, n. 3, p. 1129–1139, 2015.

[71] AHMED, H.; REZK, A. R.; CAREY, B. J.; WANG, Y.; MOHIUDDIN, M.; BEREAN, K. J.; RUSSO, S. P.; KALANTAR-ZADEH, K.; YEO, L. Y. Ultrafast acoustofluidic exfoliation of stratified crystals. *Advanced Materials*, v. 30, n. 20, p. 1704756, 2018.

[72] MOHIUDDIN, M.; WANG, Y.; ZAVABETI, A.; SYED, N.; DATTA, R. S.; AHMED, H.; DAENEKE, T.; RUSSO, S. P.; REZK, A. R.; YEO, L. Y. et al. Liquid phase acoustic wave exfoliation of layered mos2: critical impact of electric field in efficiency. *Chemistry of Materials*, v. 30, n. 16, p. 5593–5601, 2018.

[73] SCHMIDT, A.; ZARBIN, A. J. Molybdenum-based two-dimensional materials: Synthesis, dispersion, exfoliation and thin film deposition. *Journal of colloid and interface science*, v. 554, p. 80–90, 2019.

[74] ALARGOVA, R. G.; DEGUCHI, S.; TSUJII, K. Stable colloidal dispersions of fullerenes in polar organic solvents. *Journal of the American Chemical Society*, Washington, v. 123, n. 43, p. 10460–10467, 2001.

[75] JAWAID, A.; NEPAL, D.; PARK, K.; JESPERSEN, M.; QUALLEY, A.; MIRAU, P.; DRUMMY, L. F.; VAIA, R. A. Mechanism for liquid phase exfoliation of mos2. *Chemistry of Materials*, v. 28, n. 1, p. 337–348, 2016.

[76] MADELUNG, O. *Introduction to solid-state theory*. Springer Science & Business Media, 1996.

[77] ASHCROFT, N. W.; MERMIN, N. D. *Solid state physics*. Thomson, 1976.

[78] MARTIN, R. M. *Electronic structure: basic theory and practical methods*. Cambridge University Press, 2004.

[79] MENEZES, M. G. *Electronic and structure properties of graphene*. 2013. Tese (Doutorado em Física) - Universidade Federal do Rio de Janeiro, Instituto de Física, Programa de Pós-Graduação em Física, Rio de Janeiro, 2013.

[80] THOMAS, L. H. The calculation of atomic fields. In: . c1927. v. 23. p. 542–548.

[81] FERMI, E. Statistical method to determine some properties of atoms. *Rend. Accad. Naz. Lincei*, v. 6, p. 602–607, 1927.

[82] KOHN, W. Highlights of condensed matter theory. In: . c1985. p. 1–15.

[83] PERDEW, J. P.; BURKE, K.; ERNZERHOF, M. Generalized gradient approximation made simple. *Physical review letters*, v. 77, n. 18, p. 3865, 1996.

[84] CEPERLEY, D. M.; ALDER, B. Ground state of the electron gas by a stochastic method. *Physical Review Letters*, New York, v. 45, n. 7, p. 566, 1980.

[85] PERDEW, J. P.; ZUNGER, A. Self-interaction correction to density-functional approximations for many-electron systems. *Physical Review B*, v. 23, n. 10, p. 5048, 1981.

[86] HERMAN, F.; VAN DYKE, J. P.; ORTENBURGER, I. B. Improved statistical exchange approximation for inhomogeneous many-electron systems. *Physical Review Letters*, New York, v. 22, n. 16, p. 807, 1969.

[87] BURKE, K.; PERDEW, J. P.; WANG, Y. Derivation of a generalized gradient approximation: The pw91 density functional. In: *Electronic Density Functional Theory*. Springer, 1998. p. 81–111.

[88] BECKE, A. D. Density-functional exchange-energy approximation with correct asymptotic behavior. *Physical review A*, v. 38, n. 6, p. 3098, 1988.

[89] PERDEW, J. P.; WANG, Y. Accurate and simple analytic representation of the electron-gas correlation energy. *Physical Review B*, v. 45, n. 23, p. 13244, 1992.

[90] LIEB, E. H. A lower bound for coulomb energies. *Physics Letters A*, Amsterdam, v. 70, n. 5-6, p. 444–446, 1979.

[91] LIEB, E. H.; OXFORD, S. Improved lower bound on the indirect coulomb energy. *International Journal of Quantum Chemistry*, v. 19, n. 3, p. 427–439, 1981.

[92] WANG, Y.; PERDEW, J. P. Spin scaling of the electron-gas correlation energy in the high-density limit. *Physical Review B*, v. 43, n. 11, p. 8911, 1991.

[93] MONKHORST, H. J.; PACK, J. D. Special points for brillouin-zone integrations. *Physical Review B*, v. 13, n. 12, p. 5188, 1976.

[94] BLÖCHL, P. E. Projector augmented-wave method. *Physical Review B*, v. 50, n. 24, p. 17953, 1994.

[95] BLÖCHL, P. E. Generalized separable potentials for electronic-structure calculations. *Physical Review B*, v. 41, n. 8, p. 5414, 1990.

[96] VANDERBILT, D. Soft self-consistent pseudopotentials in a generalized eigenvalue formalism. *Physical review B*, v. 41, n. 11, p. 7892, 1990.

[97] KRESSE, G.; JOUBERT, D. From ultrasoft pseudopotentials to the projector augmented-wave method. *Physical Review B*, v. 59, n. 3, p. 1758, 1999.

[98] HOLZWARTH, N.; MATTHEWS, G.; DUNNING, R.; TACKETT, A.; ZENG, Y. Comparison of the projector augmented-wave, pseudopotential, and linearized augmented-plane-wave formalisms for density-functional calculations of solids. *Physical Review B*, v. 55, n. 4, p. 2005, 1997.

[99] HERRING, C. A new method for calculating wave functions in crystals. *Physical Review*, New York, v. 57, n. 12, p. 1169, 1940.

[100] HAMANN, D.; SCHLÜTER, M.; CHIANG, C. Norm-conserving pseudopotentials. *Physical Review Letters*, New York, v. 43, n. 20, p. 1494, 1979.

[101] PHILLIPS, J. New method for calculating wave functions in crystals and molecules. *Phys. Rev*, v. 116, p. 287, 1959.

[102] ANTONČÍK, E. A new formulation of the method of nearly free electrons. *Cechoslovackij fiziceskij zurnal*, v. 4, n. 4, p. 439–451, 1954.

[103] ANTONČÍK, E. Approximate formulation of the orthogonalized plane-wave method. *Journal of Physics and Chemistry of solids*, v. 10, n. 4, p. 314–320, 1959.

[104] VANDERBILT, D. Soft self-consistent pseudopotentials in a generalized eigenvalue formalism. *Physical Review B*, v. 41, n. 11, p. 7892, 1990.

[105] LOUIE, S. G.; FROYEN, S.; COHEN, M. L. Nonlinear ionic pseudopotentials in spin-density-functional calculations. *Physical Review B*, v. 26, n. 4, p. 1738, 1982.

[106] KOKALJ, A. Xcrysden: a new program for displaying crystalline structures and electron densities. *Journal of Molecular Graphics and Modelling*, v. 17, n. 3, p. 176–179, 1999.

[107] HANWELL, M. D.; CURTIS, D. E.; LONIE, D. C.; VANDERMEERSCH, T.; ZUREK, E.; HUTCHISON, G. R. Avogadro: an advanced semantic chemical editor, visualization, and analysis platform. *Journal of cheminformatics*, v. 4, n. 1, p. 17, 2012.

[108] X-ray - wikipedia. https://en.wikipedia.org/wiki/X-ray#cite_note-1. (Accessed on 02/16/2020).

[109] SCHNOHR, C. S.; RIDGWAY, M. C. *X-ray absorption spectroscopy of semiconductors*. Springer, 2015.

[110] BUNĂU, O.; CALANDRA, M. Projector augmented wave calculation of x-ray absorption spectra at the l 2, 3 edges. *Physical Review B*, v. 87, n. 20, p. 205105, 2013.

[111] PICKARD, C. J.; MAURI, F. All-electron magnetic response with pseudopotentials: Nmr chemical shifts. *Physical Review B*, v. 63, n. 24, p. 245101, 2001.

[112] LANCZOS, C. Solution of systems of linear equations by minimized iterations. *J. Res. Nat. Bur. Standards*, v. 49, n. 1, p. 33–53, 1952.

[113] HAYDOCK, R.; HEINE, V.; KELLY, M. Electronic structure based on the local atomic environment for tight-binding bands. *Journal of Physics C: Solid State Physics*, v. 5, n. 20, p. 2845, 1972.

[114] HAYDOCK, R.; HEINE, V.; KELLY, M. Electronic structure based on the local atomic environment for tight-binding bands. ii. *Journal of Physics C: Solid State Physics*, v. 8, n. 16, p. 2591, 1975.

[115] HAYDOCK, R. Recursive tridiagonalization of infinite dimensional hamiltonians. *Computer physics communications*, v. 55, n. 1, p. 1–3, 1989.

[116] PROUX, O.; HAZEMANN, J. measured at the fame beam line at the esrf. *private communication*.

[117] OYANAGI, H.; TOKUMOTO, M.; ISHIGURO, T.; SHIRAKAWA, H.; NEMOTO, H.; MATSUSHITA, T.; ITO, M.; KURODA, H. Polarized x-ray absorption spectra of bromine-doped polyacetylene; evidence for highly-oriented polybromine ions. *Journal of the Physical Society of Japan*, v. 53, n. 11, p. 4044–4053, 1984.

[118] LANDAU, L.; LIFSHITZ, E. Quantum mechanics pergamon press, 1977.

[119] SAKURAI, J. J.; COMMINS, E. D. Modern quantum mechanics, revised edition, 1995.

[120] BLINDER, S. M. Foundations of quantum dynamics. 1974.

[121] SOFF, G.; MÜLLER, B. Transition rates of electrons in superheavy elements. *Zeitschrift für Physik A Atoms and Nuclei*, v. 280, n. 3, p. 243–247, 1977.

[122] BRIAND, J. Fundamental processes in energetic atomic collisions, eds. ho lutz, js briggs, h. kleinpoppen, 1983.

[123] EDLABADKAR, V.; MANDE, C. Transition rate calculations of some forbidden lines in x-ray emission spectra. *Journal of Physics B: Atomic and Molecular Physics*, v. 15, n. 15, p. 2339, 1982.

[124] GILFRICH, J.; ROBINSON, J. Handbook of spectroscopy, 1974.

[125] https://www.quantum-espresso.org/doc/input_xspectra.txt. https://www.quantum-espresso.org/Doc/INPUT_XSpectra.txt. (Accessed on 02/18/2020).

[126] JOLY, Y. X-ray absorption near-edge structure calculations beyond the muffin-tin approximation. *Physical Review B*, v. 63, n. 12, p. 125120, 2001.

[127] WENG, X.; REZ, P.; SANKEY, O. Pseudo-atomic-orbital band theory applied to electron-energy-loss near-edge structures. *Physical Review B*, v. 40, n. 8, p. 5694, 1989.

[128] CZYŻYK, M.; POTZE, R.; SAWATZKY, G. Band-theory description of high-energy spectroscopy and the electronic structure of licoo 2. *Physical Review B*, v. 46, n. 7, p. 3729, 1992.

[129] BACEWICZ, R.; WOLSKA, A.; LAWNICZAK-JABLONSKA, K.; SAINCTAVIT, P. X-ray absorption near-edge structure of cuinse2 crystals. *Journal of Physics: Condensed Matter*, Bristol, v. 12, n. 33, p. 7371, 2000.

[130] SHIRLEY, E. L. Ab initio inclusion of electron-hole attraction: Application to x-ray absorption and resonant inelastic x-ray scattering. *Physical review letters*, v. 80, n. 4, p. 794, 1998.

[131] SOININEN, J.; SHIRLEY, E. L. Scheme to calculate core hole–electron interactions in solids. *Physical Review B*, v. 64, n. 16, p. 165112, 2001.

[132] HAYDOCK, R. The recursive solution of the schrödinger equation. *Computer Physics Communications*, v. 20, n. 1, p. 11–16, 1980.

[133] MAHAN, G. D. *Many-particle physics*. Springer Science & Business Media, 2013.

[134] LANCZOS, C. *An iteration method for the solution of the eigenvalue problem of linear differential and integral operators*. United States Governm. Press Office Los Angeles, CA, 1950.

[135] BENEDICT, L. X.; SHIRLEY, E. L. Ab initio calculation of ε 2 (ω) including the electron-hole interaction: Application to gan and caf 2. *Physical Review B*, v. 59, n. 8, p. 5441, 1999.

[136] HASNIP, P.; PICKARD, C. Electronic energy minimisation with ultrasoft pseudopotentials. *Computer physics communications*, v. 174, n. 1, p. 24–29, 2006.

[137] WALKER, B.; GEBAUER, R. Ultrasoft pseudopotentials in time-dependent density-functional theory. *The Journal of chemical physics*, v. 127, n. 16, p. 164106, 2007.

[138] CHANDLER, D. *Introduction to modern statistical*. 1987.

[139] M.J. ABRAHAM, D. VAN DER SPOEL, E. L. B. H.; THE GROMACS´ DEVELOPMENT TEAM. Gromacs user manual version 2019. ftp://ftp.gromacs.org/pub/manual, 2019. (Accessed on 02/21/2020).

[140] VAN GUNSTEREN, W. F.; BERENDSEN, H. J. Computer simulation of molecular dynamics: methodology, applications, and perspectives in chemistry. *Angewandte Chemie International Edition in English*, v. 29, n. 9, p. 992–1023, 1990.

[141] PAQUET, E.; VIKTOR, H. L. Molecular dynamics, monte carlo simulations, and langevin dynamics: a computational review. *BioMed research international*, v. 2015, 2015.

[142] Gromacs - gromacs. http://www.gromacs.org/. (Accessed on 02/21/2020).

[143] BERENDSEN, H. J.; VAN DER SPOEL, D.; VAN DRUNEN, R. Gromacs: a message-passing parallel molecular dynamics implementation. *Computer physics communications*, v. 91, n. 1-3, p. 43–56, 1995.

[144] LINDAHL, E.; HESS, B.; VAN DER SPOEL, D. Gromacs 3.0: a package for molecular simulation and trajectory analysis. *Molecular modeling annual*, v. 7, n. 8, p. 306–317, 2001.

[145] VAN DER SPOEL, D.; LINDAHL, E.; HESS, B.; GROENHOF, G.; MARK, A. E.; BERENDSEN, H. J. Gromacs: fast, flexible, and free. *Journal of computational chemistry*, v. 26, n. 16, p. 1701–1718, 2005.

[146] HESS, B.; KUTZNER, C.; VAN DER SPOEL, D.; LINDAHL, E. Gromacs 4: algorithms for highly efficient, load-balanced, and scalable molecular simulation. *Journal of chemical theory and computation*, v. 4, n. 3, p. 435–447, 2008.

[147] PRONK, S.; PÁLL, S.; SCHULZ, R.; LARSSON, P.; BJELKMAR, P.; APOSTOLOV, R.; SHIRTS, M. R.; SMITH, J. C.; KASSON, P. M.; VAN DER SPOEL, D. et al. Gromacs 4.5: a high-throughput and highly parallel open source molecular simulation toolkit. *Bioinformatics*, v. 29, n. 7, p. 845–854, 2013.

[148] PÁLL, S.; ABRAHAM, M. J.; KUTZNER, C.; HESS, B.; LINDAHL, E. Tackling exascale software challenges in molecular dynamics simulations with gromacs. In: . c2014. p. 3–27.

[149] ABRAHAM, M. J.; MURTOLA, T.; SCHULZ, R.; PÁLL, S.; SMITH, J. C.; HESS, B.; LINDAHL, E. Gromacs: High performance molecular simulations through multi-level parallelism from laptops to supercomputers. *SoftwareX*, v. 1, p. 19–25, 2015.

[150] RAPAPORT, D. C.; RAPAPORT, D. C. R. *The art of molecular dynamics simulations*. Cambridge University Press, 2004.

[151] EWALD, P. P. Die berechnung optischer und elektrostatischer gitterpotentiale. *Annalen der physik*, v. 369, n. 3, p. 253–287, 1921.

[152] FRENKEL, D.; SMIT, B. From algorithms to applications, 1996.

[153] TOUKMAJI, A. Y.; BOARD JR, J. A. Ewald summation techniques in perspective: a survey. *Computer physics communications*, v. 95, n. 2-3, p. 73–92, 1996.

[154] WOLF, M. G.; HOEFLING, M.; APONTE-SANTAMARÍA, C.; GRUBMÜLLER, H.; GROENHOF, G. g_membed: Efficient insertion of a membrane protein into an equilibrated lipid bilayer with minimal perturbation. *Journal of computational chemistry*, v. 31, n. 11, p. 2169–2174, 2010.

[155] VERLET, L. Computer" experiments" on classical fluids. i. thermodynamical properties of lennard-jones molecules. *Physical review*, v. 159, n. 1, p. 98, 1967.

[156] SWOPE, W. C.; ANDERSEN, H. C.; BERENS, P. H.; WILSON, K. R. A computer simulation method for the calculation of equilibrium constants for the formation of physical clusters of molecules: Application to small water clusters. *The Journal of Chemical Physics*, v. 76, n. 1, p. 637–649, 1982.

[157] HOCKNEY, R.; EASTWOOD, J. Computer simulations using particles mcgraw-hill. *New York*, 1981.

[158] BERENDSEN, H. J.; POSTMA, J. V.; VAN GUNSTEREN, W. F.; DINOLA, A.; HAAK, J. R. Molecular dynamics with coupling to an external bath. *The Journal of chemical physics*, v. 81, n. 8, p. 3684–3690, 1984.

[159] BUSSI, G.; DONADIO, D.; PARRINELLO, M. Canonical sampling through velocity rescaling. *The Journal of chemical physics*, v. 126, n. 1, p. 014101, 2007.

[160] ANDERSEN, H. C. Molecular dynamics simulations at constant pressure and/or temperature. *The Journal of chemical physics*, v. 72, n. 4, p. 2384–2393, 1980.

[161] NOSÉ, S. A molecular dynamics method for simulations in the canonical ensemble. *Molecular physics*, v. 52, n. 2, p. 255–268, 1984.

[162] HOOVER, W. G. Canonical dynamics: Equilibrium phase-space distributions. *Physical review A*, v. 31, n. 3, p. 1695, 1985.

[163] GARDINER, C. W. et al. *Handbook of stochastic methods*. springer Berlin, 1985. v. 3.

[164] SALINAS, S. *Introduction to statistical physics*. Springer Science & Business Media, 2001.

[165] PARRINELLO, M.; RAHMAN, A. Polymorphic transitions in single crystals: A new molecular dynamics method. *Journal of Applied physics*, v. 52, n. 12, p. 7182–7190, 1981.

[166] NOSÉ, S.; KLEIN, M. Constant pressure molecular dynamics for molecular systems. *Molecular Physics*, v. 50, n. 5, p. 1055–1076, 1983.

[167] MARTYNA, G. J.; TUCKERMAN, M. E.; TOBIAS, D. J.; KLEIN, M. L. Explicit reversible integrators for extended systems dynamics. *Molecular Physics*, v. 87, n. 5, p. 1117–1157, 1996.

[168] ALEX S. CÃ´TÃ©, BILL SMITH, P. J. D. L. Democritus: A molecular dynamics tutorial. https://www.ccp5.ac.uk/sites/www.ccp5.ac.uk/files/Democritus/Theory/pbc-mi.html, 2001. (Accessed on 02/24/2020).

[169] DEL GRANDE, R. R.; MENEZES, M. G.; CAPAZ, R. B. Layer breathing and shear modes in multilayer graphene: A dft-vdw study. *Journal of Physics: Condensed Matter*, Bristol, v. 31, n. 29, p. 295301, 2019.

[170] KLIMEŠ, J.; BOWLER, D. R.; MICHAELIDES, A. Chemical accuracy for the van der waals density functional. *Journal of Physics: Condensed Matter*, Bristol, v. 22, n. 2, p. 022201, 2009.

[171] BRAGG, W. H.; BRAGG, W. L. The structure of the diamond. *Proceedings of the Royal Society of London. Series A, Containing Papers of a Mathematical and Physical Character*, v. 89, n. 610, p. 277–291, 1913.

[172] SINGH, J. *Physics of semiconductors and their heterostructures*. McGraw-Hill College, 1993.

[173] Github - dalcorso/pslibrary: A library of ultrasoft and paw pseudopotentials. https://github.com/dalcorso/pslibrary. (Accessed on 02/29/2020).

[174] Welcome to pslibrary | a library of ultrasoft and paw pseudopotentials. https://dalcorso.github.io/pslibrary/. (Accessed on 02/29/2020).

[175] DAL CORSO, A. Pseudopotentials periodic table: From h to pu. *Computational Materials Science*, v. 95, p. 337–350, 2014.

[176] LEJAEGHERE, K.; BIHLMAYER, G.; BJÖRKMAN, T.; BLAHA, P.; BLÜGEL, S.; BLUM, V.; CALISTE, D.; CASTELLI, I. E.; CLARK, S. J.; DAL CORSO, A. et al. Reproducibility in density functional theory calculations of solids. *Science*, Washington, v. 351, n. 6280, p. aad3000, 2016.

[177] Sssp efficiency. https://www.materialscloud.org/discover/sssp/table/efficiency. (Accessed on 02/29/2020).

[178] Pseudopotentials - quantumespresso. https://www.quantum-espresso.org/pseudopotentials. (Accessed on 02/29/2020).

[179] GIANNOZZI, P. Notes on pseudopotential generation, 2017.

[180] BARBOZA, A. P.; SOUZA, A. C.; MATOS, M. J.; BRANT, J. C.; BARBOSA, T. C.; CHACHAM, H.; MAZZONI, M. S.; NEVES, B. R. Graphene/h-bn heterostructures under pressure: From van der waals to covalent. *Carbon*, v. 155, p. 108–113, 2019.

[181] CURTAROLO, S.; SETYAWAN, W.; WANG, S.; XUE, J.; YANG, K.; TAYLOR, R. H.; NELSON, L. J.; HART, G. L.; SANVITO, S.; BUONGIORNO-NARDELLI, M. et al. Aflowlib. org: A distributed materials properties repository from high-throughput ab initio calculations. *Computational Materials Science*, v. 58, p. 227–235, 2012.

[182] Aflow - automatic - flow for materials discovery. http://aflowlib.org/. (Accessed on 02/28/2020).

[183] WANG, J.; WOLF, R. M.; CALDWELL, J. W.; KOLLMAN, P. A.; CASE, D. A. Development and testing of a general amber force field. *Journal of computational chemistry*, v. 25, n. 9, p. 1157–1174, 2004.

[184] virtualchemistry.org - gromacs molecule database - acetonitrile. http://virtualchemistry.org/molecule.php?filename=acetonitrile.sdf. (Accessed on 02/29/2020).

[185] RAPPÉ, A. K.; CASEWIT, C. J.; COLWELL, K.; GODDARD III, W. A.; SKIFF, W. M. Uff, a full periodic table force field for molecular mechanics and molecular dynamics simulations. *Journal of the American chemical society*, v. 114, n. 25, p. 10024–10035, 1992.

[186] Obgmx. http://software-lisc.fbk.eu/obgmx/. (Accessed on 03/01/2020).

[187] GARBEROGLIO, G. Obgmx: A web-based generator of gromacs topologies for molecular and periodic systems using the universal force field. *Journal of computational chemistry*, v. 33, n. 27, p. 2204–2208, 2012.

[188] O'BOYLE, N. M.; BANCK, M.; JAMES, C. A.; MORLEY, C.; VANDERMEERSCH, T.; HUTCHISON, G. R. Open babel: An open chemical toolbox. *Journal of cheminformatics*, v. 3, n. 1, p. 33, 2011.

[189] SRESHT, V.; GOVIND RAJAN, A.; BORDES, E.; STRANO, M. S.; PADUA, A. A.; BLANKSCHTEIN, D. Quantitative modeling of mos2–solvent interfaces: predicting contact angles and exfoliation performance using molecular dynamics. *The Journal of Physical Chemistry C*, v. 121, n. 16, p. 9022–9031, 2017.

[190] MARTÍNEZ, L.; ANDRADE, R.; BIRGIN, E. G.; MARTÍNEZ, J. M. Packmol: a package for building initial configurations for molecular dynamics simulations. *Journal of computational chemistry*, v. 30, n. 13, p. 2157–2164, 2009.

[191] GUPTA, A.; ARUNACHALAM, V.; VASUDEVAN, S. Liquid-phase exfoliation of mos2 nanosheets: the critical role of trace water. *The journal of physical chemistry letters*, v. 7, n. 23, p. 4884–4890, 2016.

[192] PRICE, D. J.; BROOKS III, C. L. A modified tip3p water potential for simulation with ewald summation. *The Journal of chemical physics*, v. 121, n. 20, p. 10096–10103, 2004.

[193] VUJIĆ, B.; LYUBARTSEV, A. P. Transferable force-field for modelling of co2, n2, o2 and ar in all silica and na+ exchanged zeolites. *Modelling and simulation in Materials science and Engineering*, v. 24, n. 4, p. 045002, 2016.

[194] LONSDALE, K. Diamonds, natural and artificial, 1944.

[195] FRONDEL, C.; MARVIN, U. B. Lonsdaleite, a hexagonal polymorph of diamond. *Nature*, London, v. 214, n. 5088, p. 587–589, 1967.

[196] NÉMETH, P.; GARVIE, L. A.; AOKI, T.; DUBROVINSKAIA, N.; DUBROVINSKY, L.; BUSECK, P. R. Lonsdaleite is faulted and twinned cubic diamond and does not exist as a discrete material. *Nature Communications*, v. 5, n. 1, p. 1–5, 2014.

[197] SALZMANN, C. G.; MURRAY, B. J.; SHEPHARD, J. J. Extent of stacking disorder in diamond. *Diamond and Related Materials*, Lausanne, v. 59, p. 69–72, 2015.

[198] KRAUS, D.; RAVASIO, A.; GAUTHIER, M.; GERICKE, D.; VORBERGER, J.; FRYDRYCH, S.; HELFRICH, J.; FLETCHER, L.; SCHAUMANN, G.; NAGLER, B. et al. Nanosecond formation of diamond and lonsdaleite by shock compression of graphite. *Nature communications*, v. 7, n. 1, p. 1–6, 2016.

[199] FAHY, S.; LOUIE, S. G.; COHEN, M. L. Theoretical total-energy study of the transformation of graphite into hexagonal diamond. *Physical Review B*, v. 35, n. 14, p. 7623, 1987.

[200] TATEYAMA, Y.; OGITSU, T.; KUSAKABE, K.; TSUNEYUKI, S. Constant-pressure first-principles studies on the transition states of the graphite-diamond transformation. *Physical Review B*, v. 54, n. 21, p. 14994, 1996.

[201] TANAKA, I.; ARAKI, H.; YOSHIYA, M.; MIZOGUCHI, T.; OGASAWARA, K.; ADACHI, H. First-principles calculations of electron-energy-loss near-edge structure and near-edge x-ray-absorption fine structure of bn polytypes using model clusters. *Physical Review B*, v. 60, n. 7, p. 4944, 1999.

[202] TANAKA, I.; ADACHI, H. Calculation of core-hole excitonic features on al l 23-edge x-ray-absorption spectra of α-al 2 o 3. *Physical Review B*, v. 54, n. 7, p. 4604, 1996.

[203] ELLIS, D. E.; ADACHI, H.; AVERILL, F. Molecular cluster theory for chemisorption of first row atoms on nickel (100) surfaces. *Surface Science*, v. 58, n. 2, p. 497–510, 1976.

[204] ROSENBERG, R.; LOVE, P.; REHN, V. Polarization-dependent c (k) near-edge x-ray-absorption fine structure of graphite. *Physical Review B*, v. 33, n. 6, p. 4034, 1986.

[205] PACILÉ, D.; PAPAGNO, M.; RODRÍGUEZ, A. F.; GRIONI, M.; PAPAGNO, L.; GIRIT, Ç.; MEYER, J.; BEGTRUP, G.; ZETTL, A. Near-edge x-ray absorption fine-structure investigation of graphene. *Physical review letters*, v. 101, n. 6, p. 066806, 2008.

[206] SCHMID, H. K. Phase identification in carbon and bn systems by eels. *Microscopy Microanalysis Microstructures*, v. 6, n. 1, p. 99–111, 1995.

[207] GAO, S.-P.; ZHU, J.; YUAN, J. Identification of polymorphs of sp3 bonded carbon and boron nitride using core-level absorption spectroscopy. *Chemical physics letters*, v. 400, n. 4-6, p. 413–418, 2004.

[208] THOMPSON, A. C.; VAUGHAN, D. et al. *X-ray data booklet*. Lawrence Berkeley National Laboratory, University of California Berkeley, CA, 2001. v. 8.

[209] CHELIKOWSKY, J. R.; LOUIE, S. G. First-principles linear combination of atomic orbitals method for the cohesive and structural properties of solids: Application to diamond. *Physical Review B*, v. 29, n. 6, p. 3470, 1984.

[210] CLARK, C.; DEAN, P.; HARRIS, P. Intrinsic edge absorption in diamond. *Proceedings of the Royal Society of London. Series A. Mathematical and Physical Sciences*, v. 277, n. 1370, p. 312–329, 1964.

[211] HIMPSEL, F.; VAN DER VEEN, J.; EASTMAN, D. Experimental bulk energy bands for diamond using h ν-dependent photoemission. *Physical Review B*, v. 22, n. 4, p. 1967, 1980.

[212] LIU, X.; LI, L.; LU, F. Optical properties and mechanical properties of c, si, ge and 3c-sic materials calculated from first principles theory using heyd-scuseria-ernzerhof functional. *Mater. Sci. Semicond. Process*, v. 16, p. 1369–1376, 2013.

[213] PROJECT, T. M. Materials data on c by materials project.

[214] HANNEMAN, R.; STRONG, H.; BUNDY, F. Hexagonal diamonds in meteorites: implications. *Science*, Washington, v. 155, n. 3765, p. 995–997, 1967.

[215] BUNDY, F.; KASPER, J. Hexagonal diamondâ€"a new form of carbon. *The Journal of Chemical Physics*, v. 46, n. 9, p. 3437–3446, 1967.

[216] UTSUMI, W.; YAGI, T. Formation of hexagonal diamond by room temperature compression of graphite. *Proceedings of the Japan Academy, Series B*, v. 67, n. 9, p. 159–164, 1991.

[217] BUNDY, F.; BASSETT, W.; WEATHERS, M.; HEMLEY, R.; MAO, H.; GONCHAROV, A. The pressure-temperature phase and transformation diagram for carbon; updated through 1994. *Carbon*, v. 34, n. 2, p. 141–153, 1996.

[218] KHALIULLIN, R. Z.; ESHET, H.; KÜHNE, T. D.; BEHLER, J.; PARRINELLO, M. Nucleation mechanism for the direct graphite-to-diamond phase transition. *Nature materials*, v. 10, n. 9, p. 693–697, 2011.

[219] LE GUILLOU, C.; BRUNET, F.; IRIFUNE, T.; OHFUJI, H.; ROUZAUD, J.-N. Nanodiamond nucleation below 2273 k at 15 gpa from carbons with different structural organizations. *Carbon*, v. 45, n. 3, p. 636–648, 2007.

[220] NAKAMUTA, Y.; TOH, S. Transformation of graphite to lonsdaleite and diamond in the goalpara ureilite directly observed by tem. *American Mineralogist*, v. 98, n. 4, p. 574–581, 2013.

[221] ISOBE, F.; OHFUJI, H.; SUMIYA, H.; IRIFUNE, T. Nanolayered diamond sintered compact obtained by direct conversion from highly oriented graphite under high pressure and high temperature. *Journal of Nanomaterials*, v. 2013, 2013.

[222] QINGKUN, L.; YI, S.; ZHIYUAN, L.; YU, Z. Lonsdaleite–a material stronger and stiffer than diamond. *Scripta Materialia*, v. 65, n. 3, p. 229–232, 2011.

[223] KULNITSKIY, B.; PEREZHOGIN, I.; DUBITSKY, G.; BLANK, V. Polytypes and twins in the diamond–lonsdaleite system formed by high-pressure and high-temperature treatment of graphite. *Acta Crystallographica Section B: Structural Science, Crystal Engineering and Materials*, v. 69, n. 5, p. 474–479, 2013.

[224] MCFEELY, F.; KOWALCZYK, S.; LEY, L.; CAVELL, R.; POLLAK, R.; SHIRLEY, D. X-ray photoemission studies of diamond, graphite, and glassy carbon valence bands. *Physical Review B*, v. 9, n. 12, p. 5268, 1974.

[225] WILLIS, R.; FITTON, B.; PAINTER, G. Secondary-electron emission spectroscopy and the observation of high-energy excited states in graphite: Theory and experiment. *Physical Review B*, v. 9, n. 4, p. 1926, 1974.

[226] FISCHER, D.; WENTZCOVITCH, R. M.; CARR, R.; CONTINENZA, A.; FREEMAN, A. J. Graphitic interlayer states: A carbon k near-edge x-ray-absorption fine-structure study. *Physical Review B*, v. 44, n. 3, p. 1427, 1991.

[227] HEALD, S. M.; STERN, E. A. Anisotropic x-ray absorption in layered compounds. *Physical Review B*, v. 16, n. 12, p. 5549, 1977.

[228] HAMANN, D.; MULLER, D. A. Absolute and approximate calculations of electron-energy-loss spectroscopy edge thresholds. *Physical review letters*, v. 89, n. 12, p. 126404, 2002.

[229] NAMBA, Y. Attempt to grow diamond phase carbon films from an organic solution. *Journal of Vacuum Science & Technology A: Vacuum, Surfaces, and Films*, v. 10, n. 5, p. 3368–3370, 1992.

[230] BENGTSSON, L. Dipole correction for surface supercell calculations. *Physical Review B*, v. 59, n. 19, p. 12301, 1999.

[231] MCHEDLOV-PETROSSYAN, N. O.; KAMNEVA, N. N.; AL-SHUUCHI, Y. T.; MARYNIN, A. I.; ZOZULIA, O. S.; KRYSHTAL, A. P.; KLOCHKOV, V. K.; SHEKHOVTSOV, S. V. Towards better understanding of c 60 organosols. *Physical Chemistry Chemical Physics*, v. 18, n. 4, p. 2517–2526, 2016.

[232] CALEMAN, C.; VAN MAAREN, P. J.; HONG, M.; HUB, J. S.; DA COSTA, L. T.; VAN DER SPOEL, D. Force field benchmark of organic liquids: Density, enthalpy of vaporization, heat capacities, surface tension, compressibility, expansion coefficient and dielectric constant. 2011.

[233] MARCUS, Y. *The properties of solvents*. 1998.

[234] theory.cm.utexas.edu/henkelman/code/bader/. http://theory.cm.utexas.edu/henkelman/code/bader/. (Accessed on 06/15/2021).

[235] TANG, W.; SANVILLE, E.; HENKELMAN, G. A grid-based bader analysis algorithm without lattice bias. *Journal of Physics: Condensed Matter*, Bristol, v. 21, n. 8, p. 084204, 2009.

[236] SANVILLE, E.; KENNY, S. D.; SMITH, R.; HENKELMAN, G. Improved grid-based algorithm for bader charge allocation. *Journal of computational chemistry*, v. 28, n. 5, p. 899–908, 2007.

[237] HENKELMAN, G.; ARNALDSSON, A.; JÓNSSON, H. A fast and robust algorithm for bader decomposition of charge density. *Computational Materials Science*, v. 36, n. 3, p. 354–360, 2006.

[238] YU, M.; TRINKLE, D. R. Accurate and efficient algorithm for bader charge integration. *The Journal of chemical physics*, v. 134, n. 6, p. 064111, 2011.

[239] 4.7.3. radial distribution functions â€" mdanalysis.analysis.rdf â€" mdanalysis 0.20.1 documentation. https://www.mdanalysis.org/docs/documentation_pages/analysis/rdf.html. (Accessed on 04/08/2020).

[240] MACCHIAGODENA, M.; DEL FRATE, G.; BRANCATO, G.; CHANDRAMOULI, B.; MANCINI, G.; BARONE, V. Computational study of the dpap molecular rotor in various environments: from force field development to molecular dynamics simulations and spectroscopic calculations. *Physical Chemistry Chemical Physics*, v. 19, n. 45, p. 30590–30602, 2017.

[241] DIAS, R. F.; DA COSTA, C. C.; MANHABOSCO, T. M.; DE OLIVEIRA, A. B.; MATOS, M. J.; SOARES, J. S.; BATISTA, R. J. Ab initio molecular dynamics simulation of methanol and acetonitrile: The effect of van der waals interactions. *Chemical Physics Letters*, Amsterdam, v. 714, p. 172–177, 2019.

[242] KLIMEŠ, J.; BOWLER, D. R.; MICHAELIDES, A. Van der waals density functionals applied to solids. *Physical Review B*, v. 83, n. 19, p. 195131, 2011.

[243] ANDREUSSI, O.; DABO, I.; MARZARI, N. Revised self-consistent continuum solvation in electronic-structure calculations. *The Journal of chemical physics*, v. 136, n. 6, p. 064102, 2012.

[244] GIANNOZZI, P.; ANDREUSSI, O.; BRUMME, T.; BUNAU, O.; NARDELLI, M. B.; CALANDRA, M.; CAR, R.; CAVAZZONI, C.; CERESOLI, D.; COCOCCIONI, M. et al. Advanced capabilities for materials modelling with quantum espresso. *Journal of physics: Condensed matter*, v. 29, n. 46, p. 465901, 2017.

[245] SCHIRHAGL, R.; CHANG, K.; LORETZ, M.; DEGEN, C. L. Nitrogen-vacancy centers in diamond: nanoscale sensors for physics and biology. *Annual review of physical chemistry*, v. 65, p. 83–105, 2014.

[246] HERRING, C.; HILL, A. The theoretical constitution of metallic beryllium. *Physical Review*, New York, v. 58, n. 2, p. 132, 1940.

[247] HERMAN, F. Speculations on the energy band structure of geâ€"si alloys. *Physical Review*, New York, v. 95, n. 3, p. 847, 1954.

[248] BASSANI, F. Energy band structure in silicon crystals by the orthogonalized plane-wave method. *Physical Review*, New York, v. 108, n. 2, p. 263, 1957.

[249] CHRISTIANSEN, P. A.; LEE, Y. S.; PITZER, K. S. Improved ab-initio effective core potential for molecular calculations. *The Journal of Chemical Physics*, v. 71, n. 11, p. 4445–4450, 1979.

[250] KERKER, G. Non-singular atomic pseudopotentials for solid state applications. *Journal of Physics C: Solid State Physics*, v. 13, n. 9, p. L189, 1980.

[251] BACHELET, G.; HAMANN, D.; SCHLÜTER, M. Pseudopotentials that work: From h to pu. *Physical Review B*, v. 26, n. 8, p. 4199, 1982.

[252] VANDERBILT, D. Optimally smooth norm-conserving pseudopotentials. *Physical Review B*, v. 32, n. 12, p. 8412, 1985.

[253] TROULLIER, N.; MARTINS, J. L. Efficient pseudopotentials for plane-wave calculations. *Physical review B*, v. 43, n. 3, p. 1993, 1991.

[254] RAPPE, A. M.; RAPPE, K. M.; KAXIRAS, E.; JOANNOPOULOS, J. Optimized pseudopotentials. *Physical Review B*, v. 41, n. 2, p. 1227, 1990.

[255] KRESSE, G.; HAFNER, J.; NEEDS, R. Optimized norm-conserving pseudopotentials. *Journal of Physics: Condensed Matter*, Bristol, v. 4, n. 36, p. 7451, 1992.

[256] KLEINMAN, L.; BYLANDER, D. Efficacious form for model pseudopotentials. *Physical Review Letters*, New York, v. 48, n. 20, p. 1425, 1982.

[257] GRIFFITHS, D. J. *Introduction to electrodynamics*. Prentice Hall New Jersey, 1962.

[258] JACKSON, J. D. *Classical electrodynamics*. John Wiley & Sons, 2007.

[259] MAURI, F.; PFROMMER, B. G.; LOUIE, S. G. Ab initio theory of nmr chemical shifts in solids and liquids. *Physical review letters*, v. 77, n. 26, p. 5300, 1996.

[260] MAURI, F.; LOUIE, S. G. Magnetic susceptibility of insulators from first principles. *Physical review letters*, v. 76, n. 22, p. 4246, 1996.

[261] PICKARD, C.; PAYNE, M. Ab initio eels: beyond the fingerprint. In: . c1997. v. 153. p. 179–182.

[262] PETRILLI, H. M.; BLÖCHL, P. E.; BLAHA, P.; SCHWARZ, K. Electric-field-gradient calculations using the projector augmented wave method. *Physical Review B*, v. 57, n. 23, p. 14690, 1998.

[263] KLEINMAN, L.; BYLANDER, D. Efficacious form for model pseudopotentials. *Physical Review Letters*, New York, v. 48, n. 20, p. 1425, 1982.

[264] BARDER, R. Atoms in molecules: a quantum theory, 1990.